Precision measurements in the beta decay of 6He

Mohamad Kanafani

To cite this version:

Mohamad Kanafani. Precision measurements in the beta decay of 6He. Physics [physics]. Normandie Université, 2023. English. NNT : 2023NORMC257 . tel-04466399

HAL Id: tel-04466399
https://theses.hal.science/tel-04466399v1

Submitted on 19 Feb 2024

THÈSE

Pour obtenir le diplôme de doctorat

Spécialité **PHYSIQUE**

Préparée au sein de l'**Université de Caen Normandie**

Precision measurements in the beta decay of 6He

Présentée et soutenue par

MOHAMAD KANAFANI

Thèse soutenue le 21/11/2023
devant le jury composé de :

MME MURIEL FALLOT	Professeur des universités - UNIVERSITE NANTES	Rapporteur du jury
M. ALEJANDRO GARCIA	Professeur - University of Washington	Rapporteur du jury
M. PIERRE DELAHAYE	Chargé de recherche HDR - 14 GANIL de CAEN	Membre du jury
MME NADEZDA SMIRNOVA	Professeur des universités - UNIVERSITE DE BORDEAUX	Président du jury
M. OSCAR NAVILIAT CUNCIC	Professeur des universités - Université de Caen Normandie	Directeur de thèse
M. XAVIER FLECHARD	Directeur de recherche au CNRS - Université de Caen Normandie	Co-directeur de thèse

Thèse dirigée par **OSCAR NAVILIAT CUNCIC** (Laboratoire de physique corpusculaire (Caen)) et **XAVIER FLECHARD** (Laboratoire de physique corpusculaire (Caen))

Acknowledgements

This thesis represents three years of hard work, filled with challenges and triumphs. I'm thankful for the support and help of many individuals throughout this journey.

I want to express my heartfelt gratitude to my thesis director, M. Oscar Naviliat-Cuncic, for his unwavering support and guidance from the very beginning, even before I set foot in France. I'm genuinely thankful for your consistent rigor and critical feedback regarding my work. This has consistently motivated me to enhance my knowledge and skills. I believe I was very lucky to have the privilege of working under the mentorship of such a distinguished physicist and a great person. In the end, I can only say "Merci Oscar!"

I am deeply thankful to my thesis co-director, M. Xavier Fléchard, who played an essential role in shaping the researcher I've become today. Sharing an office with you was the best part of my thesis journey. I can't thank you enough for always answering all my "uhhh Xavier, J'ai une question!" without hesitation. I truly appreciated our discussions about the problems we faced during the data analysis (and how many there were!), which helped me develop a critical mindset. Working under your supervision made me a better physicist as well as a better person!

I'd also like to thank all the people at LPC Caen, who made my last three years enjoyable and productive. I was told in my first year of PhD that working at LPC Caen is a delight, and honestly, I cannot agree more! I'm especially thankful to my colleagues, fellow PhD students, and postdocs, for their camaraderie. The success of my thesis experiment was a team effort involving many individuals from LPC Caen and GANIL, and I appreciate their contributions.

No words can describe my gratitude to my family, my mother, my father, and my brother, who have been and will always be my strongest supporters, encouraging me to pursue my education and dreams! I want to thank as well my friends for their unwavering support, and especially for putting up with me talking about my thesis for hours on end (:p). Finally, I want to show my appreciation to every person who has ever contributed to my academic journey!

Last but certainly not least, in the context of "exotic" phenomena, my thoughts turn to Lebanon, a country that embodies the essence of "exotic". Throughout the three years of my thesis, Lebanon faced the most severe economic crisis in its history, a devastating explosion in the heart of Beirut, and uncountable other crises. Hopefully, one day, the underlying factors contributing to this country's "exotic" situation could be well constrained!

Abstract

Precision measurements in β decay play an essential role in the search for new physics beyond the standard model (SM), by probing “exotic” phenomena such as scalar and tensor interactions in the electroweak sector. The existence of such interactions induces deviations on certain observables away from their SM predictions. The study of the full β-energy spectrum offers a sensitive property to probe these interactions.

The goal of this work is to perform the most precise measurement of the β-energy spectrum in ^{6}He decay, in order to extract the Fierz interference term b_{GT} with a precision in the order of $4 \cdot 10^{-3}$. This term depends linearly on exotic coupling constants, allowing to search for or to constrain the presence of tensor interactions in nuclear β decay.

The main instrumental effect observed in previous measurements of the β-energy spectrum resides in the energy loss due to electrons backscattering outside the detector volume. A new technique is used to overcome this effect. It consists of using a very low energy beam of ^{6}He$^+$ ions (25 keV) deposited between two scintillation detectors forming a 4π calorimeter. The use of this technique ensures the deposition of the entire energy of the detected β particles. An experiment with this setup was performed at the Grand Accélérateur National d’Ions Lourds (GANIL) in 2021.

This thesis will introduce the general context of the b-STILED project, describe the experimental setup, report the most precise measurement of ^{6}He half-life and the measurement of the shape of the β-energy spectrum with all the challenges that come with such a measurement, and provide preliminary results on the extraction of the Fierz interference term from the β energy spectrum.

Keywords: Beyond the Standard Model, exotic interactions, Fierz interference term, precision measurements, β-decay, half-life measurement, ^{6}He , b-STILED, β-energy spectrum, 4π calorimetry.

Résumé

Les mesures de précision dans la désintégration β jouent un rôle essentiel dans la recherche de nouvelle physique, au-delà du modèle standard (MS), en recherchant des contributions "exotiques" telles que des interactions scalaires et tensorielles au sein de l'interaction faible. L'existence de telles interactions induit des déviations de certaines observables par rapport à leurs prédictions dans le MS. L'étude du spectre en énergie de la particule β permet de sonder ces interactions.

L'objectif de ce travail est d'effectuer la mesure la plus précise du spectre en énergie β dans la désintégration du ^{6}He, afin d'extraire le terme d'interférence de Fierz b_{GT} avec une précision de l'ordre de $4 \cdot 10^{-3}$. Ce terme dépend linéairement des constantes de couplage exotiques, permettant ainsi de rechercher ou de contraindre la présence d'interactions tensorielles dans la désintégration nucléaire β.

L'effet instrumental principal observé dans les mesures précédentes du spectre en énergie β réside dans la perte d'énergie due à la rétrodiffusion des électrons en dehors du volume du détecteur. Une nouvelle technique est utilisée pour s'affranchir de cet effet. Elle consiste en l'utilisation d'un faisceau de ions ^{6}He$^+$ à très basse énergie (25 keV) déposé entre deux détecteurs à scintillation formant un calorimètre 4π. L'utilisation de cette technique garantit le dépôt de toute l'énergie des particules β détectées. Une expérience avec cette configuration a été réalisée au Grand Accélérateur National d'Ions Lourds (GANIL) en 2021.

Cette thèse introduira le contexte général du projet b-STILED, décrira la configuration expérimentale, rendra compte de la mesure la plus précise de la demi-vie de ^{6}He et de la mesure de la forme du spectre d'énergie β avec tous les défis inhérents à une telle mesure, et présentera nos résultats préliminaires sur l'extraction du terme d'interférence de Fierz à partir de la forme du spectre en énergie β.

Mots-clés: Au-delà du Modèle Standard, interactions exotiques, terme d'interférence de Fierz, mesures de précision, désintégration β, mesure de la demi-vie, ^{6}He, b-STILED, spectre d'énergie β, calorimétrie 4π.

Thèse résumée en français

Introduction

Le Modèle Standard (MS) de la physique des particules englobe toute notre compréhension des particules fondamentales qui forment les éléments constitutifs de notre univers et de trois des quatre forces fondamentales. Cependant, malgré son énorme succès, le MS reste à ce jour incomplet. En réalité, de nombreuses questions restent sans réponse dans le cadre de ce modèle, ce qui motive les physiciens à rechercher une physique au-delà du MS. Le terme d'interférence de Fierz, noté b, est l'une des observables qui peuvent être utilisées pour sonder la physique au-delà du MS dans la désintégration β. Il est particulièrement sensible à l'existence de nouvelles formes de l'interaction faible car il dépend linéairement des constantes de couplage tensoriel et scalaire exotiques. La manière la plus directe d'accéder au terme de Fierz consiste en une mesure précise de la forme du spectre en énergie β, car il entre dans l'expression de la distribution d'énergie par le biais d'un facteur $\left(1+b\frac{m}{E}\right)$, où m est la masse de l'électron et E est son énergie totale.

Le projet b-STILED vise à réaliser la mesure la plus précise du spectre en énergie β pour la désintégration de l'^{6}He afin d'extraire le terme d'interférence de Fierz pour les transitions Gamow-Teller avec une precision de l'ordre de $\Delta b_{GT} = 3.9 \times 10^{-3}$. Pour cela, deux expériences garantissant une calorimétrie 4π, mais associées à des sources d'erreur systématique différentes, ont été proposées. La première implique l'utilisation d'un faisceau de basse énergie de $^6\mathrm{He}^+$ fourni par la ligne de faisceau LIRAT au GANIL, tandis que la seconde implique l'utilisation d'un faisceau de haute énergie de $^6\mathrm{He}^+$ fourni par la ligne de faisceau LISE. Ce manuscrit de thèse porte sur l'expérience réalisée sur la ligne LIRAT.

L'experience E815S

L'expérience avec un faisceau de basse énergie (25 keV) d'ions $^6\mathrm{He}^+$ a été réalisée au GANIL en mai 2021. Cette expérience était composée de cycles d'implantation-désintégration, au cours desquels un faisceau de basse énergie d'ions $^6\mathrm{He}^+$ est déposé à la surface d'un détecteur, puis un autre détecteur identique est placé juste en face du premier pour former une géométrie 4π. Les détecteurs utilisés dans cette expérience sont constitués d'un scintillateur en cristal (YAP) entouré d'un scintillateur en plastique

(PVT), couplés à un même tube photomultiplicateur (PMT) (Fig. 1). Le YAP a été choisi pour cette expérience en raison de ses propriétés qui peuvent se résumer en une fonction de réponse linéaire dans l'intervalle d'énergie souhaité, une bonne résolution en énergie (environ 5% à 1 MeV) et une perte d'énergie relativement faible due au rayonnement de freinage Bremsstrahlung.

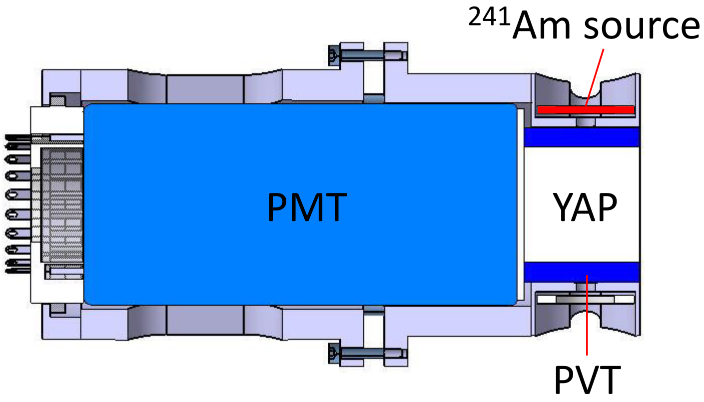

Figure 1: Vue en coupe transversale du détecteur, comprenant les deux scintillateurs couplés à un seul PMT dans une configuration phoswich, et la position de la source de calibration ^{241}Am.

Calibration de premier ordre et mesure de la demi-vie.

Une calibration en énergie très précise des détecteurs n'est pas nécessaire pour une mesure précise de la demi-vie. Néanmoins, il est crucial de contrôler avec haute précision les variations du gain et de la ligne de base des PMT lors de chaque cycle et sur l'ensemble de l'expérience. Cette calibration a été réalisée en utilisant les particules γ de 59,54 keV de la source de ^{241}Am comme point de référence pour corriger les fluctuations du gain et de la ligne de base pour chacun des deux détecteurs, avant de sommer les signaux des deux détecteurs.

Les sources de bruit de fond ont été identifiées, y compris les bruits de fond constants et les contributions induites par l'implantation du faisceau sur le collimateur fixé au détecteur mobile. Ces dernières comprennent une distribution d'événements avec une énergie inférieure à 500 keV, causée par le rayonnement de Bremsstrahlung produit par la désintégration de l'^{6}He sur le collimateur.

La demi-vie de l'^{6}He a été déterminée après correction des effets dépendant du temps, y compris l'effet du temps mort du système de détection et les empilements. La mesure de la demi-vie rapportée ici est la mesure la plus précise qui ait été réalisée pour l'^{6}He . Elle est en accord avec la mesure rapportée dans la référence [1] (Fig. 2), et résout la longue divergence entre deux ensembles de mesures antérieures.

L'analyse du terme de Fierz

La distribution d'énergie des particules β émises par la désintégration de l'^{6}He peut être décrite par l'équation suivante:

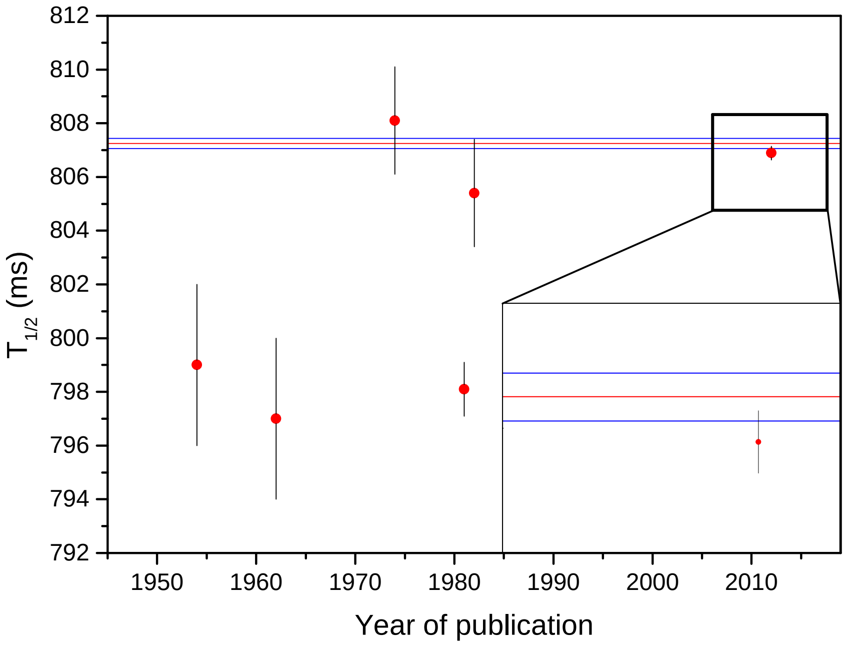

Figure 2: Comparaison entre la valeur de la demi-vie de ^{6}He obtenue dans le présent travail (lignes horizontales) et les mesures précédentes ayant une précision relative inférieure à 1%. Les valeurs représentées sont extraites des références [2, 3, 4, 5, 6, 1].

$$N(W) \propto F(Z,W)pW(W-W_0)^2 \left(\alpha_0 + \alpha_{-1} \cdot \frac{1}{W} + \alpha_1 \cdot W + \alpha_2 \cdot W^2\right), \tag{1}$$

où p est le moment de l'électron émis, W et W_0 représentent respectivement son énergie totale et son énergie limite en unités de la masse de l'électron. $pW(W-W_0)^2$ constitue le facteur d'espace des phases, et $F(Z,W)$ est la fonction de Fermi. α_{-1}, α_0, α_1 et α_2 sont des coefficients qui incluent toutes les corrections théoriques à la forme du spectre β (α_{-1} inclut la contribution de b_{GT}). Le spectre d'énergie déposée peut être décrit avec Eq. (1) après avoir inclus une correction due à la perte d'énergie par rayonnement de Bremsstrahlung et à la production de photons de Bremsstrahlung virtuels et réels. Cette correction a été estimée avec des simulations.

Après la première calibration avec les particules γ de 59,54 keV, une différence non négligeable a été observée entre les spectres β obtenus avec les deux détecteurs pour les événements ayant déposé toute leur énergie à l'intérieur d'un seul des détecteur. Cet écart est du à la différence de collection de lumière issue d'une part des particules γ et de l'autre, des électrons produits par la désintégration de l'^{6}He , qui sont très bien localisés. Par conséquent, une calibration plus précise a été effectuée pour reconstruire correctement l'énergie déposée par chaque événement à l'intérieur des deux détecteurs.

L'énergie déposée pour l'ensemble des événements a été regroupée en histogrammes qui ont été fittés avec une fonction appropriée afin d'extraire le terme d'interférence de Fierz b_{GT}, après soustraction de toutes les sources de bruit de fond, y compris la distribution des événements de rayonnement de Bremsstrahlung en dessous de 500 keV. Les valeurs obtenues pour b_{GT} pour trois ensembles de données indépendants sont présentées dans la Figure 3. L'incertitude statistique pure (hors contribution du Bremsstrahlung) pour la somme des trois lots de données sur la valeur du terme d'interférence de Fierz est de l'ordre de $\Delta b_{GT\ \mathrm{stat}} \simeq 1.6 \times 10^{-3}$, ce qui est conforme à l'objectif d'incertitude de cette expérience.

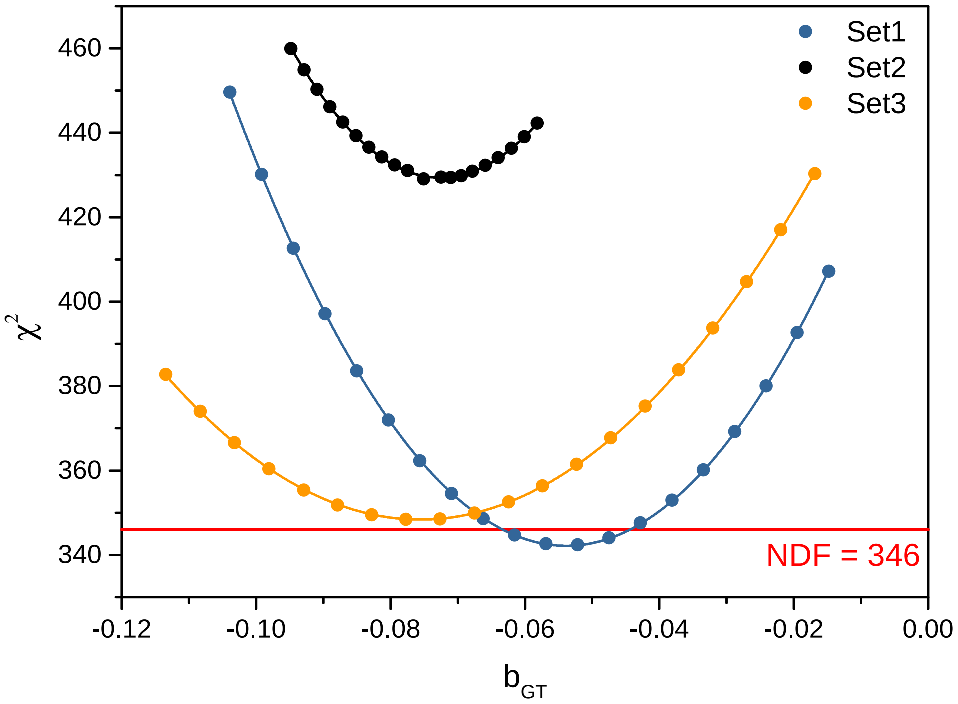

Figure 3: Les valeurs de b_{GT} obtenues par les fits pour les trois ensembles. La ligne rouge représente la valeur de NDF (nombre de degrés de liberté).

Sommaire et conclusions

Cette thèse a présenté la mesure de haute précision de la demi-vie et du spectre d'énergie β pour la désintégration du ^{6}He à partir de l'analyse des données de l'expérience E815S.

La Table 1 résume les effets systématiques qui ont été étudiés ou qui seront étudiés ultérieurement, avec l'incertitude estimée induite par chacun d'entre eux. Les effets systématiques étudiés jusqu'à présent entraînent des erreurs systématiques inférieures ou de l'ordre de 10^{-3}, ce qui reste compatible avec notre objectif de précision.

Systematic effect	Δb_{GT}
EV_{e^-} subtraction	5×10^{-4}
β parameter	$< 2 \times 10^{-3}$
b_{WM}	2.6×10^{-4}
Radiative	3.7×10^{-4}
Bremsstrahlung escape	7×10^{-4}
Pile-ups	?
Selections	?
Calibration offset	?
Non linear response function	?
Total	?

Table 1: Le budget d'erreur pour l'extraction de b_{GT} à partir de la mesure de la forme du spectre β.

Contents

General introduction

The Standard Model (SM) of particle physics is considered one of the biggest achievements of the 20^{th} century. Its success expanded to the beginning of the 21^{st} century culminating with the discovery of the Higgs boson in 2012. It comprises all our understanding of the fundamental particles that form the building blocks of our universe, in addition to three of the four fundamental forces. However, despite its huge success, the SM is so far incomplete. In fact, many questions are still unanswered by the SM (what is the nature of dark matter ?, the reason behind the matter/anti-matter asymmetry ?, ...) and it doesn't include gravity, one of the four fundamental forces. These shortcomings represent a strong motivation for both theoreticians and experimentalists to search for New Physics (NP) beyond the SM. This search can be driven by two main approaches. The first consists in using TeV-scale particle collisions at huge colliders like the LHC, in order to directly look for new particles, while the other consists in looking for hints or signatures of NP through precision measurements at much lower energy scales. The present work belongs to this last approach and is based on the study of β-decay, which proved during the last few decades to be of great importance to test discrete symmetries and to search for the existence of "exotic" interactions.

The Fierz interference term, noted b, is one of the observables that can be used to probe NP within β-decay. It offers sensitive means to search for exotic interactions since it depends linearly on exotic tensor and scalar coupling constants. The most direct way to access the Fierz term is by a precise measurement of the β-energy spectrum shape, as it enters the expression of the energy distribution through a factor $\left(1+b\frac{m}{E}\right)$, with m is the electron mass and E is its total energy. The extraction of b, though, requires a very high precision measurement of the β-energy spectrum, which requires in turn the knowledge with high precision of the theoretical corrections of the spectrum.

The b-STILED project (b-Search for Tensor Interactions in nucLear bEta Decay) aims to perform the most precise measurement of the β-energy spectrum for ^{6}He decay in order to extract the Fierz interference term. For this purpose, two experiments were proposed with different systematic conditions assuring the creation of 4π calorimetry. The first involves the use of a low energy beam of ^{6}He$^+$ delivered by the LIRAT beam line at GANIL, while the second involves the use of a high energy beam of ^{6}He$^+$ delivered by the LISE beam line.

In this manuscript, the low energy experiment of b-STILED project is presented alongside the data analysis for the extraction of the Fierz term and the measurement of ^{6}He half-life, which is a byproduct of this experiment. This document is structured as follows:

- In Chap. 1, the SM and the firmly established V-A nature of the weak interaction and its limitations are presented. It is followed by an introduction to the nuclear β-decay and the possibilities that it offers to search for physics beyond the Standard Model. Finally, the b-STILED project is introduced, with its goals, and the methods to achieve them.
- Chap. 2 is dedicated to the full description of the experimental setup of the E815S experiment that took place at GANIL in May 2021, including the production of the ^{6}He^{+} beam, the double detectors setup, and the tests and simulations that lead to the choice of the scintillators in use.
- Chap. 3 describes in detail the first order calibration accounting for the relative gain and baseline fluctuations, followed by the extraction of the most precise value of ^{6}He half-life and the study of the associated systematic effects.
- Chap. 4 is dedicated to the determination of the Fierz term. First, the theoretical and instrumental components of the experimental energy spectra are introduced. This section is followed by a refined calibration of the detectors based on the signals of the ^{6}He decay. Finally, the details of the analysis are presented, including the subtraction of the backgrounds, the data selections, the fitting of the spectra and the study of systematic effects.
- Chap. 5 gives an overview of the results, the conclusions and perspectives of this work.

CHAPTER 1

Introduction

In this chapter, we give an overview of the Standard Model (SM) of particle physics alongside its limitations and the frontiers at which the search for Beyond the Standard Model physics (BSM) is performed. Afterwards, we introduce nuclear β-decay, and the possibilities it offers in order to probe new physics beyond the SM, by means of low energy (high precision) measurements aiming to probe specific observables e.g. the correlation coefficients such as the Fierz interference term b. Finally, we introduce the b-STILED project, its precision goal, and the instrumental method used to eliminate electron backscattering and outscattering effects distorting the measurement of the β-spectrum.

1.1 The Standard Model... And beyond

The ultimate goal in theoretical physics these days is the attempt to find a unifying theory able to describe nature's laws from the smallest elementary particles to the largest galaxies of the universe. The current status in this matter resides in two very successful big theories. The first, the General Relativity, explains the gravitational interaction, and is used to describe the phenomena at very large scales. The second, The Standard Model of particle physics, describes the elementary particles and their interactions.

The formulation of the Standard Model (SM) is considered one of the greatest achievements of the 20^{th} century. It is the culmination of several decades of scientific research and has been very successful in explaining a wide range of experimental observations. It provided a coherent theoretical framework to understand the building blocks of our universe and their interactions.

1.1.1 The elementary particles and fundamental forces

In the SM, 12 elementary particles of spin $1/2$ and their corresponding anti-particles are needed to explain all nature's processes. These elementary particles consist of 6 quarks and 6 leptons (and their anti-particles). These are the fermions having half-integer spins. Those fermions are classified into three generations of quarks $\big($the up and down quarks (u,d), the charm and strange quarks (c,s), and the top and bottom quarks (t,b)$\big)$, as well as three generations of leptons $\big($the electron and the electron neutrino (e^-, ν_{e^-}), the muon and the muon neutrino (μ, ν_μ), and the tau and the tau neutrino $(\tau, \nu_\tau)\big)$. The generations are arranged according to their masses, where the particles in each generation have larger masses than the previous generation. Table 1.1 shows a schematic summary of the fundamental particles and their properties (their spins, charges and masses). The quarks, having a fraction electrical charge, can never appear free but are bound together to form the hadrons. Oppositely, the leptons having integer electrical charge exist on their own.

		I		II		III
Quarks	u	1/2 +2/3 2.16 MeV	c	1/2 +2/3 1.27 GeV	t	1/2 +2/3 172.69 GeV
	d	1/2 -1/3 4.67 MeV	s	1/2 -1/3 93.4 MeV	b	1/2 -1/3 4.18 GeV
Leptons	e^-	1/2 -1 511 keV	μ	1/2 -1 106 MeV	τ	1/2 -1 1.78 GeV
	ν_{e^-}	1/2 0 <0.8 eV	ν_μ	1/2 0 <0.19 MeV	ν_τ	1/2 0 <18.2 MeV

Table 1.1: Table showing the 12 elementary particles alongside their charges, spins and masses [7].

The four fundamental forces behind the interactions between the elementary particles are the gravitational force, the electromagnetic force, the strong force and the weak force. The particles exchange the force carrying particles called the gauge bosons having integer spins (Table 1.2). In the SM, these are the photons γ, the $W^\pm$ and Z^0 bosons, the gluons g and the gravitons.

The gravitational force is carried by the exchange of gravitons. It is of a feeble strength at the level of particle interactions (except at very extreme conditions i.e. at the boundary of a black hole). It is thus neglected in particle interactions.

The electromagnetic force is currently the best understood of the four. Its source is the electric charge of the particles, it has an infinite range, and it is carried by the exchange of photons. The electromagnetic interaction is described in the classical regime by the famous

Gauge boson	Spin	Charge	Mass	Force
γ	1	0	0	electromagnetic
$W^{\pm}$	1	± 1	80.38 GeV	weak
Z^0	1	0	91.19 GeV	weak
g	1	0	0	strong
$graviton$	2	0	$< 1.76 \times 10^{-23}$ eV	gravitational

Table 1.2: Table showing the gauge bosons, their main properties, and the associated force [7].

Maxwell's equations. The quantum theory describing the interactions of charged particles by electromagnetic fields is called Quantum electrodynamics (QED).

The strong force acts on all the hadrons, it is e.g. the force responsible for the binding of protons and neutrons inside the nucleus. It is also the force responsible for the binding of quarks in hadrons. The strong force acts only at extremely short ranges and is carried by the exchange of gluons. The theory of the strong force is named quantum chromodynamics (QCD).

The weak force is the one responsible for radioactive decay. Similarly to the strong force, it acts at very short ranges. The weak force is carried by the exchange of $W^{\pm}$ bosons when it involves a charge difference, and Z^0 bosons otherwise. The formulation of the weak interaction was done by Fermi in 1934 [8]. One of the most well-known weak processes available for study is β-decay. A unified theory for the weak and electromagnetic interactions (electroweak theory) was formulated by Weinberg, Salam and Glashow in 1968 [9, 10, 11]. This theory describes the interactions of leptons through the exchange of photons, Z^0 and $W^{\pm}$ bosons. The electroweak theory is far more complete than Fermi's description. However, Fermi's formulation is still valid to describe the nuclear β-decay, since the energy scale of the β-decay (few MeV) is much smaller than the mass of the weak interaction gauge bosons.

1.1.2 Not a perfect theory

Despite all the successes of the Standard Model, culminating with the discovery of the famous Higgs boson in 2012 [12], many unanswered questions and observations lead to believe that it is not the perfect theory. For instance, it doesn't have any mention for gravity, one of the four fundamental forces. It doesn't either have a satisfactory explanation for the matter-antimatter asymmetry, nor about the nature of dark matter and dark energy which are known today to form more than 95% of the universe's components according to astronomical observations. In addition, the Standard Model involves 20 fundamental parameters which are all obtained experimentally and not by the theory itself. Because of all of this, the SM can be considered only as a low energy approximation of a more fundamental theory that must be discovered. The search for physics beyond the current limits of the SM is performed with two complementary approaches. The first approach involves experiments at high energy colliders such as the LHC at CERN where the aim is to produce directly new unknown particles and new phenomena. The second approach is based on experiments at very low energies but with very high precision, aiming to look for small deviations of certain observables away from their SM predictions, which can only be caused by the presence of new gauge bosons and new interactions. This thesis belongs to the second approach, and more specifically, aims at a search for BSM phenomena by studying the nuclear β-decay.

1.2 Weak interaction and Nuclear β decay in a nutshell

Nuclear β-decay is a process in which a neutron (proton) is converted into a proton (neutron) with the emission of an electron (positron) and an anti-neutrino (neutrino), ensuring the conservation of the lepton number and of the total angular momentum. During this process, both Z and N are changed by one unit: $Z \rightarrow Z \pm 1$, $N \rightarrow N \mp 1$ so that $A = Z + N$ remains unchanged. The three basic β-decay processes are:

- $n \longrightarrow p + e^- + \overline{\nu_e}$ (β^- decay)
- $p \longrightarrow n + e^+ + \nu_e$ (β^+ decay)
- $p + e^- \longrightarrow n + \nu_e$ (electron capture)

The β-decay is a 4-body interaction, meaning that the decay energy is completely shared between the emitted leptons (considering that the recoil energy of the daughter nuclei is negligible). This explains the continuous shape of the electron energy spectrum that extends up to the endpoint energy, the maximum energy that the emitted electron (or positron) can have. In all that follows we will consider the case of β^- decay.

In 1934, Fermi developed his famous theory for the β decay based on Pauli's neutrino proposition [8]. According to this theory, the decay rate per interval of time can be derived through Fermi's Golden Rule as follows:

$$d\lambda = \frac{g^2 \left|M_{fi}\right|^2}{2\pi^3 \hbar^7 c^3} F(Z_d, p_e) p_e (Q - T_e)^2 \, dp_e \tag{1.1}$$

Where g is the Fermi constant determining the strength of the interaction, Q is the available energy by the decay, T_e and p_e are respectively the kinetic energy and the momentum of the emitted electron, and $F(Z_d, p_e)$ is the Fermi function which accounts for the influence of the nuclear Coulomb field of the daughter nucleus on the emitted electron. M_{fi} is the nuclear matrix element, whose square norm is proportional to the probability of the nuclear transition. It is strictly related to the comparative half-life or ft-value, one of the observables of the β decay, through the following expression:

$$ft = f(Z_d, E_0)t_{1/2} = 0.693\frac{2\pi^3\hbar^7}{g^2 m_e^5 c^4 \left|M_{fi}\right|^2} \tag{1.2}$$

The ft-value can be interpreted as the the nucleus half-life corrected by nuclear effects such as Z_d the charge of the daughter nucleus and E_0 the maximum electron total energy. Thus, it gives a way to compare the β decay probabilities for different nuclei. The ft-values for β decay varies from 10^3 up to 10^{22}. Conventionally, the ft-values quoted is the $\log_{10} ft$. The decays with the shortest comparative half-lives ($\log ft \leq 6$ [13]) are known as allowed decays. For those decays, the outgoing leptons carry no orbital momentum $\ell = 0$, with no change in parity. While the rarest decays ($\log ft > 6$) are known as forbidden decays, and those correspond to $\ell > 0$. Moreover, the allowed transitions are subdivided into three types: pure Fermi, pure Gamow-Teller and mixed transitions. For pure Fermi transitions, for which the total change in the nuclear spin is zero, $\Delta J = 0$, the spins of the electron and the anti-neutrino are anti-parallel. For pure Gamow-Teller transitions, the spins of the emitted leptons can be parallel, which leads to a change in the nuclear spin by zero or one $\Delta J = 0{,}1$ [14]. Mixed transitions satisfy both Fermi and Gamow-Teller selection rules.

1.2.1 Fermi's theory of the β decay

The electromagnetic interaction is described as an interaction between a current ej_μ and the radiation field described by a vector potential A_μ. The Hamiltonian of the electromagnetic interaction is given by:

$$H = \sum_n e j_\mu(\vec{r}_n) A_\mu(\vec{r}_n), \tag{1.3}$$

where $\vec{r}_n$ is the position of the n^{th} particle and e is the electric charge characterizing the strength of the interaction. The transition current is given within a field theory approach by:

$$j_\mu = \bar{\psi}_f \gamma_\mu \psi_i, \tag{1.4}$$

where ψ_i and ψ_f are respectively the spinors for the initial and final states and γ_μ is a 4×4 Dirac γ matrix.

In analogy with the electromagnetic interaction, Fermi described the weak interaction, responsible for β-decay, as an interaction between two currents. In this case a hadronic current J_μ and a leptonic current L_μ, and thus he constructed the Hamiltonian as follows:

$$H = \sum_n g_F J_\mu(\vec{r}_n) L_\mu(\vec{r}_n), \tag{1.5}$$

where g_F is the "elementary charge" that Fermi introduced in analogy to the electric charge e in electromagnetism, which determines the strength of the β decay interaction. J_μ is the current associated with the neutron-proton transition and L_μ is the one associated with the emitted leptons field. In order to make H relativistically invariant, both J_μ and L_μ have the same form and are expressed as

$$\begin{aligned} J_\mu &= \bar{\psi}_p \mathscr{O}_i \psi_n, \\ L_\mu &= \bar{\psi}_e \mathscr{O}_i \psi_\nu, \end{aligned} \tag{1.6}$$

with $\mathscr{O}_i$ the operator, which can be expressed as different combinations of Dirac γ-matrices and could be grouped into five classes according to their transformation properties (Table 1.3).

Operator $\mathscr{O}_i$	Relativistic transformation properties
1	**S**calar S
γ_μ	**V**ector V
$\gamma_\mu \gamma_\lambda$	**T**ensor T
$\gamma_\mu \gamma_5$ (= $\gamma_\nu \gamma_\lambda \gamma_\sigma$)	**A**xial-vector A
γ_5 (= $\gamma_1 \gamma_2 \gamma_3 \gamma_4$)	**P**seudoscalar P

Table 1.3: The different operators that can act in the weak interaction Hamiltonian and their transformation properties.

The only theoretical constraint for the construction of the Hamiltonian describing the β decay is that it should be Lorentz invariant. Thus, it can be written as a linear combination of the five types of interactions (Scalar, Vector, Tensor, Axial-vector and Pseudoscalar) as

$$H_\beta = \sum_{i=S,V,T,A,P} g_i \left(\bar{\psi}_p \mathscr{O}_i \psi_n\right) \left(\bar{\psi}_e \mathscr{O}_i \psi_\nu\right) + h.c., \tag{1.7}$$

with $g_i = g_F C_i$ is the overall coupling constant characterizing the strength of the weak interaction, and C_i are the coupling constants defining the relative strength of the five weak interaction types. The C_i's can only be determined experimentally.

Furthermore, the requirement for the Hamiltonian to be Lorentz invariant while taking into account parity violation in the weak interaction, means that it should be a superposition of a scalar and a pseudoscalar terms. Therefore, the Hamiltonian is given by the combination of a scalar (H_{even}) and a pseudoscalar (H_{odd}) components, which conserve and change of sign under parity transformation. The generalized form of the Hamiltonian is then:

$$\begin{aligned} H_\beta &= H_{even} + H_{odd} \\ &= g_F \sum_i \left(\bar{\psi}_p \mathscr{O}_i \psi_n\right) \left(\bar{\psi}_e \mathscr{O}_i \left(C_i + C_i' \gamma_5\right) \psi_\nu\right) + h.c., \end{aligned} \tag{1.8}$$

or in a more detailed form:

$$
\begin{aligned}
H_\beta = & \frac{G_F}{\sqrt{2}} V_{ud} \Big[\left(\bar{\psi}_p \psi_n\right) \left(\bar{\psi}_e \left(C_S + C'_S \gamma_5\right) \psi_\nu\right) \\
& + \left(\bar{\psi}_p \gamma_\mu \psi_n\right) \left(\bar{\psi}_e \gamma^\mu \left(C_V + C'_V \gamma_5\right) \psi_\nu\right) \\
& + \frac{1}{2} \left(\bar{\psi}_p \sigma_{\lambda\mu} \psi_n\right) \left(\bar{\psi}_e \sigma^{\lambda\mu} \left(C_T + C'_T \gamma_5\right) \psi_\nu\right) \\
& - \left(\bar{\psi}_p \gamma_\mu \gamma_5 \psi_n\right) \left(\bar{\psi}_e \gamma^\mu \gamma_5 \left(C_A + C'_A \gamma_5\right) \psi_\nu\right) \\
& + \left(\bar{\psi}_p \gamma_5 \psi_n\right) \left(\bar{\psi}_e \gamma_5 \left(C_P + C'_P \gamma_5\right) \psi_\nu\right) \Big] \\
& + h.c.,
\end{aligned}
\tag{1.9}
$$

where $\sigma_{\lambda\mu} = -\frac{1}{2} i \left(\gamma_\lambda \gamma_\mu - \gamma_\mu \gamma_\lambda\right)$, C_i are the coupling constants associated to the scalar Hamiltonian (H_{even}), and C'_i are the corresponding ones for the pseudoscalar Hamiltonian (H_{odd}). Equation (1.9) shows that there are 10 coupling constants in the weak interaction.

Concerning the invariance under time-reversal, all the C_i and C'_i must be real. Parity is not violated if only one of C_i or C'_i is null. Maximum parity violation is obtained for $|C_i| = |C'_i|$. Based on the experimental studies that were performed up to now, the Standard Model states that $C_V = C'_V = 1$ and $C_A = C'_A \approx 1.27$, while all the other coupling constants being zero ($C_T = C'_T = C_S = C'_S = C_P = C'_P = 0$). This explains the Vector-Axial-vector (V-A) character of the weak interaction in the Standard Model, while the tensor and scalar interactions are called "exotic" interactions. The search for these exotic currents and constraining their presence represents one of the approaches of the search for physics beyond the Standard Model.

1.2.2 The link with the high energy approach

The existence of scalar and tensor terms in the semi-leptonic weak processes can be studied with an Effective Field Theory (EFT). This enables a connection between the low and high energy sectors, allowing us to compare the sensitivities between these domains to BSM physics. The low energy effective ($\mathcal{O}$(1 GeV)) Lagrangian for the semi-leptonic processes, associated with the Hamiltonian of Eq. (1.9), can be expressed as [15, 16]

$$
\begin{aligned}
&\mathscr{L}_{eff} = \\
&-\frac{G_F V_{ud}}{\sqrt{2}}\Big[(1+\varepsilon_L)\bar{\psi}_e\gamma_\mu(1-\gamma_5)\psi_{\nu_L}\cdot\bar{\psi}_u\gamma^\mu(1-\gamma_5)\psi_d+\tilde{\varepsilon}_L\bar{\psi}_e\gamma_\mu(1+\gamma_5)\psi_{\nu_R}\cdot\bar{\psi}_u\gamma^\mu(1-\gamma_5)\psi_d \\
&+\varepsilon_R\bar{\psi}_e\gamma_\mu(1-\gamma_5)\psi_{\nu_L}\cdot\bar{\psi}_u\gamma^\mu(1+\gamma_5)\psi_d+\tilde{\varepsilon}_R\bar{\psi}_e\gamma_\mu(1+\gamma_5)\psi_{\nu_R}\cdot\bar{\psi}_u\gamma^\mu(1+\gamma_5)\psi_d \\
&+\varepsilon_T\,\bar{\psi}_e\sigma_{\mu\nu}(1-\gamma_5)\psi_{\nu_L}\cdot\bar{\psi}_u\sigma^{\mu\nu}(1-\gamma_5)\psi_d+\tilde{\varepsilon}_T\,\bar{\psi}_e\sigma_{\mu\nu}(1+\gamma_5)\psi_{\nu_R}\cdot\bar{\psi}_u\sigma^{\mu\nu}(1+\gamma_5)\psi_d \\
&+\varepsilon_S\bar{\psi}_e(1-\gamma_5)\psi_{\nu_L}\cdot\bar{\psi}_u\psi_d+\tilde{\varepsilon}_S\bar{\psi}_e(1+\gamma_5)\psi_{\nu_R}\cdot\bar{\psi}_u\psi_d \\
&-\varepsilon_P\bar{\psi}_e(1-\gamma_5)\psi_{\nu_L}\cdot\bar{\psi}_u\gamma_5\psi_d-\tilde{\varepsilon}_P\bar{\psi}_e(1+\gamma_5)\psi_{\nu_R}\cdot\bar{\psi}_u\gamma_5\psi_d\Big] \\
&+h.c.,
\end{aligned}
\tag{1.10}
$$

where ψ_u, ψ_d and ψ_e are the spinors associated respectively to the up quark, down quark and the electron, $\psi_{\nu_{L,R}} = (1 \pm \gamma_5)\psi_\nu/2$ are the left-handed and right-handed neutrino spinors. Moreover, the Wilson coefficients ε_X and $\tilde{\varepsilon}_X$ ($X = L, R, T, S, P$) reflect the effects of BSM physics at a higher energy scale. All the Wilson coefficients are null within the SM ($\varepsilon_X = \tilde{\varepsilon}_X = 0$ for all X).

To make the connection between the low energy description of the β-decay Hamiltonian (Eq. (1.9)) and the high energy quark level Lagrangian (Eq. (1.10)), one can separate the left-handed C_i^+ and the right-handed C_i^- neutrino coupling constants so that $C_i = \left(C_i^+ + C_I^-\right)/2$ and $C_i' = \left(C_i^+ - C_I^-\right)/2$ [16]. The relation between C_i and C_i' and the Wilson coefficients is given by:

$$
\begin{aligned}
C_V^+ &= +\frac{G_F}{\sqrt{2}}V_{ud}\,g_V\sqrt{1+\Delta_R^V}(1+\varepsilon_L+\varepsilon_R) & C_V^- &= +\frac{G_F}{\sqrt{2}}V_{ud}\,g_V\sqrt{1+\Delta_R^V}(\tilde{\varepsilon}_L+\tilde{\varepsilon}_R), \\
C_A^+ &= -\frac{G_F}{\sqrt{2}}V_{ud}\,g_A\sqrt{1+\Delta_R^A}(1+\varepsilon_L-\varepsilon_R) & C_A^- &= +\frac{G_F}{\sqrt{2}}V_{ud}\,g_A\sqrt{1+\Delta_R^A}(\tilde{\varepsilon}_L-\tilde{\varepsilon}_R), \\
C_S^+ &= +\frac{G_F}{\sqrt{2}}V_{ud}\,g_S\varepsilon_S & C_S^- &= +\frac{G_F}{\sqrt{2}}V_{ud}\,g_S\tilde{\varepsilon}_S, \\
C_T^+ &= +\frac{G_F}{\sqrt{2}}V_{ud}\,g_T\varepsilon_T & C_T^- &= +\frac{G_F}{\sqrt{2}}V_{ud}\,g_T\tilde{\varepsilon}_T, \\
C_P^+ &= +\frac{G_F}{\sqrt{2}}V_{ud}\,g_P\varepsilon_P & C_P^- &= +\frac{G_F}{\sqrt{2}}V_{ud}\,g_P\tilde{\varepsilon}_P,
\end{aligned}
\tag{1.11}
$$

where $\Delta_R^{V,A}$ are the short distance radiative corrections, and g_i ($i = V, A, S, P$ and T) are hadronic form factors, among which $g_V = 1$ (universal according to the Conserved Vector Current CVC hypothesis) and the others are determined precisely with lattice QCD calculations. The current most precise values are summarized in Table 1.4 [17]:

	g_A	g_S	g_P	g_T
Value	1.251	1.022	349	0.989
Total uncertainty	0.033	0.1	9	0.033

Table 1.4: Current most precise values of the hadronic form factors determined with lattice QCD calculations [17].

1.2.3 Current limits on exotic scalar and tensor couplings

The constraints on exotic couplings extracted from experiments at high energy or involving nuclear and neutron β-decay are regularly provided in review papers such as e.g. Refs. [16, 18]. They depend on the new physics hypothesis and in particular on scenarios allowing or not right-handed neutrinos. The current constraints on the exotic scalar and tensor couplings are reported in Ref. [18]. Those are obtained by assuming that there are no right-handed neutrinos ($C_i = C'_i$), and that all the couplings are real. This implies that $C_A/C_V = (C_A + C'_A)/(C_V + C'_V)$, $C_S/C_V = (C_S + C'_S)/(C_V + C'_V)$ and $C_T/C_A = (C_T + C'_T)/(C_A + C'_A)$. The coupling constants are obtained by a fit of 17 experimental input data, including the $\mathscr{F}t$-values from superallowed $0^+ \longrightarrow 0^+$ transitions and neutron decay data. The results of the fit are the following:

$$C_S/C_V = 0.0014 \pm 0.0012, \tag{1.12}$$

$$C_T/C_A = 0.0020 \pm 0.0022. \tag{1.13}$$

The results of the fit are illustrated in Fig. 1.1, where the contours represent respectively 1σ, 2σ and 3σ confidence intervals. It can be noticed though that the constraint on the tensor coupling is about twice larger than for the scalar coupling. This weaker constraint for the tensor coupling motivates a new generation of experiments aiming to improve those limits.

1.2.4 Angular distribution and correlation coefficients in β decay

The different coupling constants introduced in Eq. (1.9) influence effectively the angular correlations of the emitted leptons in β decay. The distribution as a function of the electron-neutrino directions, electron polarization and total energy for an allowed β transition of a polarized parent nucleus can be given by [19]:

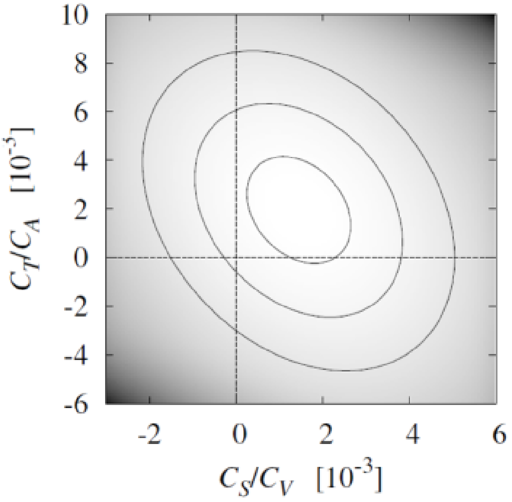

Figure 1.1: Present limits on the scalar (horizontal) and tensor (vertical) couplings extracted from Ref. [18]. The contours around the minimum correspond to 68%, 95% and 99% confidence intervals.

$$\begin{aligned}\omega\left(\langle\vec{I}\rangle,\vec{\sigma}|E_e,\Omega_e,\Omega_\nu\right)dE_e d\Omega_e d\Omega_\nu \propto \\ F(\pm Z,E_e)p_eE_e\left(E_0-E_e\right)^2 dE_e d\Omega_e d\Omega_\nu \times \\ \xi\left\{1+\frac{\vec{p}_e\cdot\vec{p}_\nu}{E_eE_\nu}a+\frac{m_e}{E_e}b+\right. \\ \left.\frac{\vec{I}}{I}\cdot\left[\frac{\vec{p}_e}{E_e}A+\frac{\vec{p}_\nu}{E_\nu}B\right]+\vec{\sigma}\cdot\left[\frac{\vec{p}_e}{E_e}G\right]\right\},\end{aligned} \tag{1.14}$$

where $E_{e,\nu}$, $p_{e,\nu}$ and $\Omega_{e,\nu}$ are respectively the total energy, momentum and angular coordinates of the emitted electron and neutrino, m_e is the electron's mass, $\langle\vec{I}\rangle$ is the polarization of the nuclear state with spin I, E_0 is the endpoint energy of the β spectrum, $\vec{\sigma}$ is the electron polarization direction and $F(\pm Z,E_e)$ is the Fermi function accounting for the Coulomb interaction between the emitted β particle and the daughter nucleus. The factor ξ depends both on the nuclear matrix elements and the coupling constants C_i and C_i'. Furthermore, the correlation coefficients a ($\beta-\nu$ correlation), b (Fierz interference term), A (beta asymmetry), B (neutrino asymmetry) and G (longitudinal beta polarization) are coefficients that are accessed only by experiments and are functions of the coupling constants. In the scope of this work, the parameters a, A, B and G are not important. However, they were used in previous measurements to set the constraints on the Fierz interference term b. It is worthy to note that the two main properties of the weak interaction (the maximal parity violation and the V-A structure) were determined from measurements of these correlation coefficients in β-decay. For the experiment described in this work, which uses non-polarized nuclei and is not sensitive to the spin of the β particles or the $\beta - \nu$ angular correlation, the expression of Eq. (1.14) becomes the following:

$$\omega\left(\langle E_e, \Omega_e, \right) dE_e d\Omega_e \propto F(\pm Z, E_e) p_e E_e \left(E_0 - E_e\right)^2 dE_e d\Omega_e \times \xi \left\{1 + \frac{m_e}{E_e} b\right\}. \tag{1.15}$$

The explicit expressions for ξ and b are given by:

$$\begin{aligned} \xi =& |M_F|^2 \left(|C_S|^2 + |C_V|^2 + |C_S'|^2 + |C_V'|^2\right) \\ &+ |M_{GT}|^2 \left(|C_T|^2 + |C_A|^2 + |C_T'|^2 + |C_A'|^2\right), \end{aligned} \tag{1.16}$$

$$\begin{aligned} b\xi =& \pm 2\gamma Re\Big[|M_F|^2 \left(C_S C_V^* + C_S' C_V'^*\right) \\ &+ |M_{GT}|^2 \left(C_T C_A^* + C_T' C_A'^*\right)\Big]. \end{aligned} \tag{1.17}$$

In these equations, M_F and M_{GT} are respectively the Fermi and Gamow-Teller matrix elements, $\gamma = \sqrt{1 - (\alpha Z)^2}$ with α the fine structure constant and Z the atomic number of the daughter nucleus. The highest sensitivity to scalar and/or tensor coupling constants is obtained for pure Fermi and pure Gamow-Teller transition, since for those transitions the correlation coefficients are independent of the nuclear matrix elements. The b correlation coefficient of (Eq. (1.17)) can be reduced as follows for pure Fermi and Gamow-Teller transitions [20]:

$$b_F \simeq \gamma Re\left(\frac{C_S + C_S'}{C_V}\right) \tag{1.18}$$

$$b_{GT} \simeq \gamma Re\left(\frac{C_T + C_T'}{C_A}\right). \tag{1.19}$$

According to the Standard Model, both the scalar and tensor coupling constants are predicted to be zero. The Fierz interference term, being solely dependent on the scalar and tensor coupling constants respectively for pure Fermi and Gamow-Teller transitions, is expected to be zero for the two types ($b_F = b_{GT} = 0$). The linear dependence of the Fierz term on the exotic tensor and scalar coupling constants, makes b the most appropriate correlation coefficient to be determined by experiments with the highest possible precision in order to set the tightest limits on the exotic scalar and tensor interactions. Further, as b affects the energy distribution of the emitted β particles without any particular directional dependence, the measurement of any other correlation coefficient χ is always affected by b. Such that the experimentally obtained value $\tilde{\chi}$ corresponds to the following:

$$\tilde{\chi} = f\left(\chi, b\right). \tag{1.20}$$

Therefore, the measurement of such correlation coefficients also provides a way to set constraints on b. One should however note that this relation depends strongly on the measurement method and the detection setup [21]. The precise determination of b using other coefficients requires performing appropriate simulations of the setup.

1.3 Current status of the Fierz interference term b

The Fierz interference term, being linearly dependent on exotic tensor and scalar couplings, was extracted previously by many experiments either directly or via indirect measurements (through other measurements such as $\mathscr{F}t$-values and correlations). Ref. [18] provides a summary for 28 measurements in nuclear and neutron β-decay that include measurements of correlations. In the following, a few examples of experiments that contributed to setting the constraints on the Fierz interference term are reported.

Hardy and Towner provided in Ref. [22] a measurement of the Fierz term in Fermi transitions, b_F, with an analysis of the $\mathscr{F}t$-values in superallowed $0^+ \longrightarrow 0^+$ pure Fermi transitions. Their reported value of $b_F = 0.000 \pm 0.002$ provides a strong constraint on the scalar couplings. Another way to set constraints on b_F in pure Fermi transitions is by measurement of the $\beta - \nu$ angular correlation a. For example, the measurement of a in pure Fermi decay of ^{38m}K at TRIUMF reported in Ref. [23], and in pure Fermi decay of ^{32}Ar performed at ISOLDE-CERN reported by Adelberger et al. [24] and by WISArD collaboration [25].

The Fierz term can also be extracted from neutron beta decay, b_n. The most precise value of b_n is reported in Ref. [26] as $b_n = 0.017 \pm 0.021$, which was measured by the PERKEO collaboration at Institule Laue-Langevin (ILL). This value was obtained with a measurement of the β-asymmetry in neutron decay using spin-polarized neutrons.

In pure Gamow-Teller transitions, the Fierz interference term noted b_{GT} can also be constrained through measurements of a. Müller et al. reported in Ref. [27] a measurement of a through β-Nuclear-recoil correlation from ^{6}He . This measurement yielded a value of $0.007 < \frac{C_T}{C_A} < 0.111$ at 90% CL.

Ref. [18] reports the current benchmark uncertainties on the Fierz interference term. The uncertainties are derived from the exotic couplings obtained by fitting the 28 experimental input data, including $\mathscr{F}t$-values from $0^+ \longrightarrow 0^+$ transitions and neutron and nuclear β-decay data. The fit assumes the absence of light right-handed neutrinos. The resulting absolute uncertainties for neutron, Fermi and Gamow-Teller decays are the following:

$$\Delta b_n = 3.2 \times 10^{-3}, \tag{1.21}$$

$$\Delta b_F = 2.3 \times 10^{-3}, \tag{1.22}$$

$$\Delta b_{GT} = 3.9 \times 10^{-3}. \tag{1.23}$$

These uncertainties provide the precision level needed to be achieved by any new measurement in order to improve the current constraints on the exotic couplings. The sensitivities to new physics in low-energy experiments can be compared with those in high-energy experiments with EFT approach. The constraint on the quark level tensor couplings, obtained by the analysis of the data taken at the LHC, provides a 90% confidence level on ε_T of $|\varepsilon_T| \lesssim 0.6 \times 10^{-3}$. This uncertainty corresponds to an uncertainty on the Fierz term of $\Delta b_{GT} \lesssim 2.9 \times 10^{-3}$. This provides the precision level needed for any new low-energy measurement to reach in order to be competitive with the LHC searches.

1.4 Measurements of the β-energy spectrum

1.4.1 Principle and main difficulties

The most sensitive method to measure the Fierz interference term is by direct extraction from the shape of the β-energy spectrum shape. The energy distribution of β particles for allowed pure Gamow-Teller decays is described by the following expression:

$$N(W) \propto (1+\eta(W))\, pW(W_0-W)^2 \left(1+\frac{b_{GT}}{W}\right), \tag{1.24}$$

where p is the momentum of the emitted electron, W and W_0 are respectively its total and end-point energy in unit of electron mass. $pW(W-W_0)^2$ is referred to as the phase space factor. $\eta(W)$ is the product of several theoretical corrections (including the Fermi function) that will be discussed in detail in Chap. 4. Note that such corrections, which can jeopardize the determination of the Fierz term b if the chosen nuclear transition is not appropriate, must be known to sufficiently high precision. $\left(1+\frac{b_{GT}}{W}\right)$ is the distortion to the β-energy spectrum due to the possible presence of the Fierz interference term b_{GT}. The distortion induced by the presence of the Fierz term is so small, that it necessitates a very precise measurement of the β-energy spectrum in order to extract the Fierz term with a relevant precision. In the following, several examples of measurements of the β-energy spectrum for several radioactive isotopes are reported to show the main difficulties accompanying this measurement.

Rustad et al. [28] performed a measurement of the $\beta-\nu$ angular correlation in ^{6}He decay. A part of the experiment was dedicated to the measurement of the β-energy spectrum of ^{6}He in order to investigate the presence of a contaminant with a similar half-life of ^{6}He's but with different endpoint energy. The experimental setup is depicted schematically in the left panel of Fig. 1.2, where the ^{6}He β-active volume and the scintillation spectrometer are placed within the same vacuum volume. The scintillation spectrometer records the energy and the direction of the emitted β particles. The energy spectrum of the β particles detected by the stilbene plastic is shown in the right panel of Fig. 1.2. This experimental setup, with the decay source placed near the detector, encountered instrumental challenges due to the backscattering of β particles from the stilbene plastic that greatly distorted the β-energy spectrum.

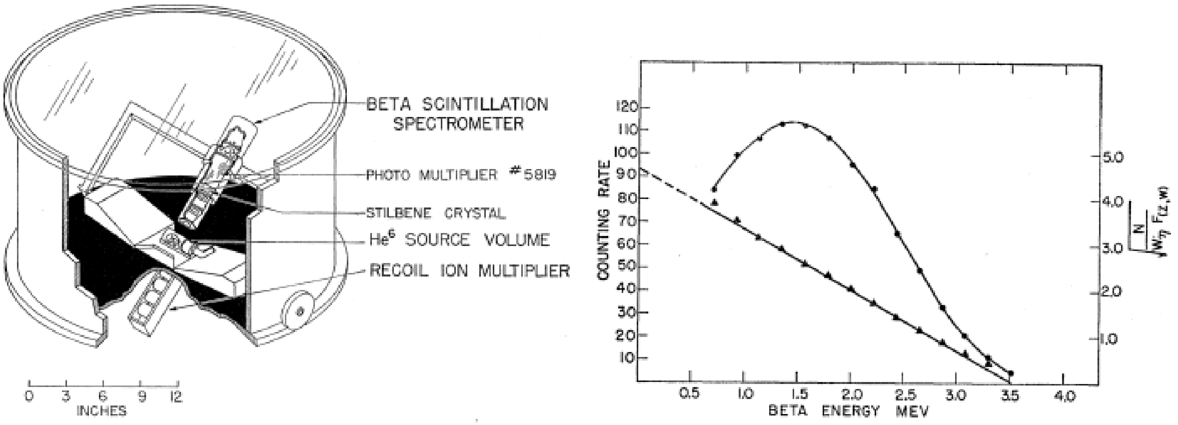

Figure 1.2: Left panel: a schematic sketch of the apparatus used to determine the electron-recoil ion correlation in the decay of ^{6}He . The β-active source volume and the scintillation spectrometer are located in the common vacuum of the “bell-jar”. Right panel: the ^{6}He β-energy spectrum measured with the stilbene scintillation spectrometer. Figures taken from Ref. [28].

A measurement of the β-energy spectrum for ^{20}F decay was performed by Hetherington et al. [29]. During this measurement, the kinetic energy of the β particles was determined with a high purity germanium detector in a high-field superconducting solenoid. The layout of the apparatus is shown in the left panel of Fig. 1.3. The decay was placed outside of the active volume of the detector. The shape of the detected β particles spectrum (dashed line in the right panel of Fig. 1.3) was unfortunately very distorted relatively to the theoretical spectrum shape (solid line in the right panel of Fig. 1.3) due to β particles backscattering and outscattering from the active volume of the detection setup.

Severin et al. [30] conducted a measurement of the β-energy spectrum for the decay of ^{66}Ga. To perform this measurement, they used a superconducting β spectrometer developed at the University of Wisconsin [31], a Wu-type magnetic spectrometer similar to the one detailed in Ref. [32]. The emitted β particles, passing through the annular slits, are detected by a Si(Li) detector. The β-energy spectrum was derived by tallying the counts of detected β particles under several spectrometer currents in sequence. The left panel of Fig. A.2 shows the deposited energy spectrum in the Si(Li) detector at a spectrometer current setting that corresponds to a

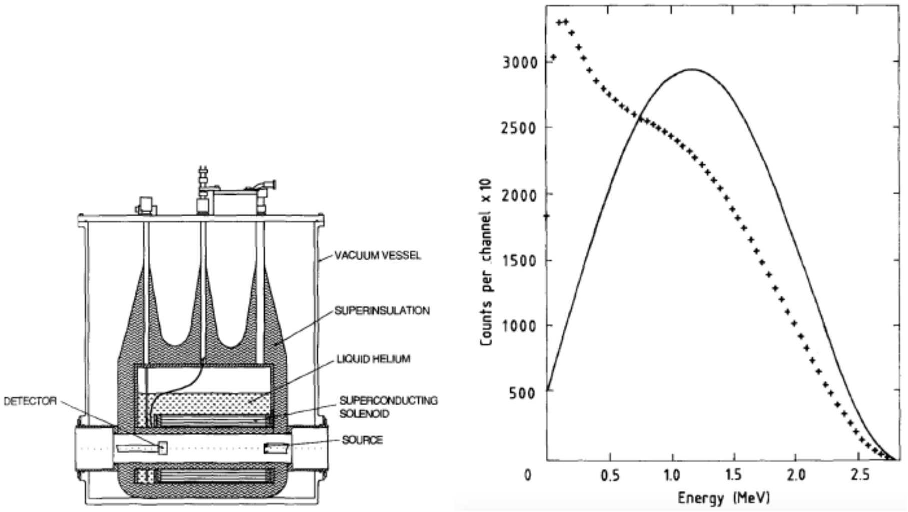

Figure 1.3: Left panel: the layout of the spectrometer used to measure the kinetic energy of particles. It consists of a high-purity germanium detector mounted on the axis in the bore of a superconducting solenoid. Right panel: the theoretical statistical distribution (solid line) and the corresponding response from the detector (dashed line). Figures taken from Ref. [29].

positron kinetic energy of 3.25 MeV. The tail extended below 1.5 MeV was attributed to the energy loss due to positrons backscattering and Bremsstrahlung phenomenon. Additionally, Refs. [33, 34] show that the backscattering events in the ^{66}Ga spectra cannot be accurately reproduced by Monte-Carlo simulations.

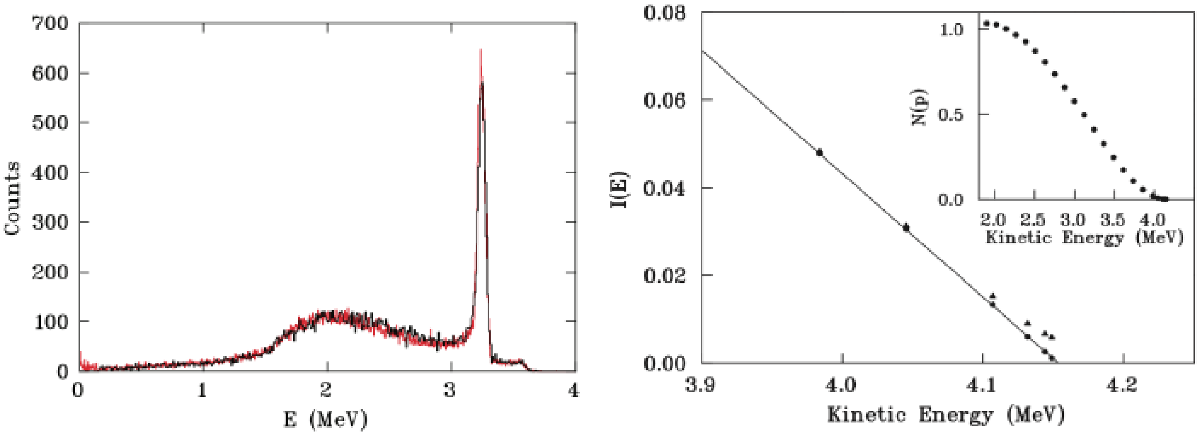

Figure 1.4: Left panel: measured (black) and simulated (red) energy spectra deposited in the Si(Li) detector with a spectrometer current corresponding to a positron kinetic energy of 3.25 MeV. Right panel: the β-energy spectrum in ^{66}Ga decay. Figures taken from Ref. [30].

1.4.2 New generation experiments

All the measurements of the shape of the β-energy spectrum mentioned in the previous section and many others encountered one common main instrumental effect, which is the backscattering of the β particles outside of the active volume of the detector. For the new generation of experiments measuring the β-energy spectra, higher precisions are needed to access any signature of new physics. Therefore, new techniques were introduced in order to suppress or reduce the backscattering effect, which cannot be simulated with enough precision. In the following, several recent experiments that resolved or limited the backscattering problem are reported.

A measurement of the β-energy spectrum in neutron decay was performed by the UCNA collaboration at Los Alamos National Laboratory (LANL) [35]. The UCNA experiment was designed to measure the β-decay asymmetry parameter, A_0, for free neutron decay. The polarized ultra-cold neutrons were transported into a decay trap, where they undergo β-decay. The decay electrons were detected with $\approx 4\pi$ acceptance into two detector telescopes providing the position and the energy of the emitted β particles. This experiment was also sensitive to the Fierz interference term in neutron decay, b_n. Their obtained result of $b_n = 0.067 \pm 0.005_{\text{stat}}\,{}^{+0.090}_{-0.061}{}_{\text{syst}}$ is in agreement with the SM prediction, and is dominated by the systematic uncertainty caused by the energy calibration.

Several experiments are ongoing as well to extract b_{GT} from the shape of the β-energy spectrum. For instance, at the Facility for Rare Isotope Beams (FRIB) at Michigan State University, the β-energy spectra of ^{6}He and ^{20}F were measured with scintillation detectors. For the measurement with ^{20}F, a beam of ^{20}F ions was implanted inside a PVT scintillator for the half-life measurement and in CsI(Na) scintillator for the shape measurement [36]. For the measurement with ^{6}He, a beam of ^{6}He ions was implanted inside a CsI(Na) and a NaI(Tl) scintillators [37]. For the two experiments, the implantation inside the volume of the scintillators solves the electron backscattering problem since the decay electrons cannot escape the detection volume. The total uncertainty is expected to be in the order of $\Delta b_{GT} = 1.0 \times 10^{-2}$ for the measurement with ^{20}F, and in the order of $\Delta b_{GT} = 0.8 \times 10^{-2}$ for the measurement with ^{6}He [38]. In both cases, the uncertainty is dominated by the systematic effects.

The CRES collaboration used a very interesting technique to measure the kinetic energy of electrons/positrons emitted by the β-decay of ^{6}He and ^{19}Ne at the University of Washington, Seattle [39]. This technique consists in determining the energy of the emitted β particles by measuring the frequency of the cyclotron radiation emitted in an external magnetic field provided by a superconducting solenoid. The apparatus, including a cryo-cooler, low noise amplifiers, RF-guides in addition to the superconducting solenoid capable of providing a magnetic field up to 7 T, was able to determine the β particles energies within a range between 5 keV and 2.1 MeV, with the capability to reach 5 MeV. This technique eliminates any distortion due to β

particles backscattering effect or Bremsstrahlung energy escape.

The miniBETA collaboration at KU Leuven also aims to measure the shape of the β-energy spectrum. Their concept is to use a low pressure multi-wire drift chamber (MWDC) with a He/isobutane gas mixture in a hexagonal cell geometry with very thin wires. This geometry ensures the use of a minimum number of necessary wires in order to maximize the detector transparency [40]. The MWDC provides a direct registration of the backscattered β particles from the detector. This offers reference data for the validation of Monte-Carlo simulations. So far, the setup focused on ^{32}P and ^{114m}In decays. The main limitations are electron scattering in the He/isobutane gas in addition to gain variations along the detector surfaces [41].

Another measurement of the β-spectrum was performed by Vanlangendonck et al. [42] for ^{114}In, where a source of ^{114}In was inserted between two scintillation detectors that were placed face-to-face in the high magnetic field of the WISArD setup at ISOLDE/CERN. This experimental setup ensures that the backscattered electrons from one detector are collected by the other. This effectively forms a closed system with a 4π detection geometry, eliminating thus any distortion to the shape of the β spectrum due to the backscattering effect.

1.5 b-STILED project

b-STILED stands for "b-Search for Tensor Interactions in the nucLear bEta Decay". It is a project that aims to search for the presence of exotic tensor couplings in β-decay, by improving the current constraints on these couplings. This is done by extraction of the Fierz interference term b_{GT} for the pure Gamow-Teller transition of ^{6}He .

1.5.1 The uncertainty goal

The left panel of Fig. 1.5 shows the 90% constraining limits (CL) on ε_T and ε_S obtained from the analysis reported in Ref. [18]. The green horizontal band corresponds to the constraints on ε_S extracted from $\mathscr{F}t$-values of superallowed $0^+ \longrightarrow 0^+$ pure Fermi transitions. The orange vertical band shows the constraint on ε_T obtained from radiative pion decay, which represents the most sensitive low-energy probe of ε_T. The blue ellipse shows the constraint from the analysis of $pp \longrightarrow e + MET + X$ at the LHC at a center of mass energy of 8 TeV (20 fb^{-1}) [43]. The black ellipse provides the combined constraints on the two coefficients from β-decay experiments including those from $\mathscr{F}t - values$ of superallowed pure Fermi transitions and from neutron decay.

The improvement of the constraints on the exotic couplings is in play with both the low-energy (β-decay experiments) and high-energy (LHC) approaches. For instance, the analysis performed in Ref. [18] confirmed that the most promising observable to improve the constraint of tensor couplings in β-decay is the Fierz interference term for pure Gamow-Teller transitions

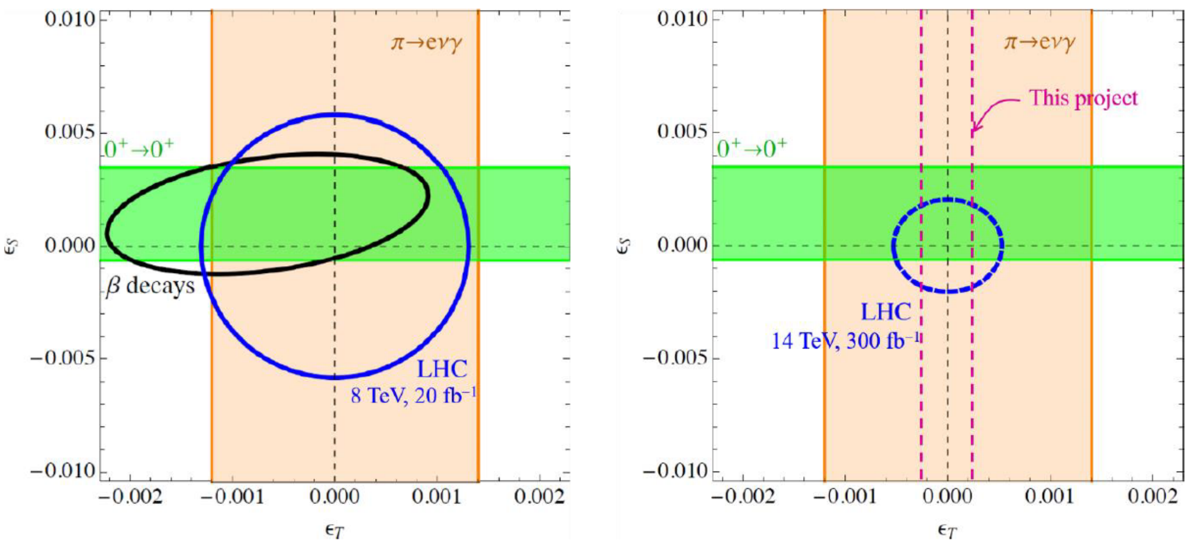

Figure 1.5: 90% CL on the scalar and tensor coefficients from semi-leptonic decays and from LHC. Left panel: current constraints [18]. Right panel: adapted figure from Ref [17] showing the projected sensitivities from the LHC (blue dotted circle) and the final uncertainty goal of b-STILED project (magenta dotted lines)

b_{GT}. The most sensitive way to extract the Fierz interference is from a direct measurement of the β-energy spectrum shape, as it enters the expression of the energy spectrum as shown in Eq. (1.24) through a factor $(1+b_{GT}/W)$. In a pure Gamow-Teller transition, the relation between the Fierz term and the tensor coefficient can be simply given by $b_{GT}=6.2\varepsilon_T$ [18]. The ultimate precision goal for this project is to reach a total uncertainty on the Fierz term of $\Delta b_{GT}=1\times10^{-3}$ at 1σ, which is about a factor 4 improvement of the current limit shown in Eq. (1.23). In the absence of new physics, this uncertainty corresponds to the 90% CL shown in the right panel of Fig. 1.5 with the dotted magenta lines. In the same figure, the blue dotted circle corresponds to the projected sensitivities of the LHC at 14 TeV (300 fb^{-1}). It can be observed in Fig. 1.5 that the projected constraint of b-STILED project provides about a factor of two improvement on the constraints on ε_T in comparison with those projected by the LHC, and about a factor of five improvement in comparison with the constraints obtained by radioactive pion decay.

1.5.2 The candidate ^{6}He

The candidate selected for this project is ^{6}He. The β-decay of ^{6}He already played an essential role in establishing the V-A character of the weak interaction [44, 45]. It decays into the ground state of ^{6}Li in a simple pure Gamow-Teller transition (left panel of Fig. 1.6), which makes it very attractive for BSM studies.

The ^{6}He decay is the most convenient candidate for this project for the several advantages listed below:

- The β-decay of ^{6}He is a 100% pure Gamow-Teller transition, and is thus only sensitive to

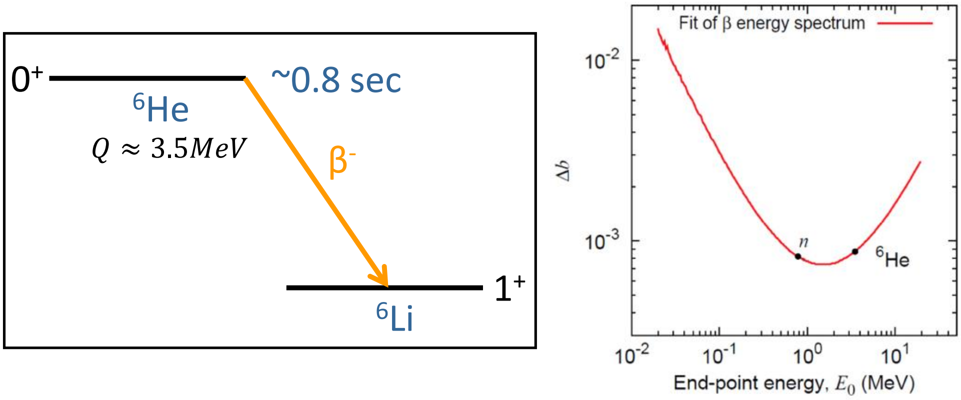

Figure 1.6: Left panel: the decay scheme of the ^{6}He β-decay. Right panel: the 1σ statistical uncertainties of the Fierz interference term obtained by fitting the simulated β-energy spectra with different values of the endpoint energy. Figure taken from Ref. [46].

tensor couplings through a measurement of the Fierz interference term.

- The endpoint energy of ^{6}He decay of $\sim$3.5 MeV results in high sensitivity to the Fierz interference term. This was confirmed by the study performed in Ref. [46] with Monte-Carlo simulations to estimate the impact of the endpoint of the spectrum on the statistical uncertainty on b. The results of this study is shown in the right panel of Fig. 1.6, where the 1σ statistical uncertainties of b are obtained by fitting the β-energy spectrum corresponding for each endpoint value. It is worthy to note that both the nuclear β-decay of ^{6}He and the neutron decay have similar high sensitivities to the extraction of the Fierz term from fits of the energy spectrum.

- The theoretical corrections to the phase space are expressed by the term $(1+\eta(W))$ in Eq. (1.24). The energy dependent functions $\eta(W)$ are known for ^{6}He decay with very high precision (more details in Chap. 4). Table 1.5 lists all the experimental inputs that enter the description of the energy spectrum, alongside the uncertainty on each of them that contributes to the systematic uncertainty on the extracted value of b_{GT}. The total theoretical uncertainty for ^{6}He decay is smaller than the uncertainty goal of this project.

- The ^{6}He decays into the ground state of ^{6}Li with β^- emission, meaning that there are no additional γ rays emission by de-excitation. This is a great advantage for the measurement of the β-energy spectrum.

- The half-life of ^{6}He of $\sim$0.8 sec is convenient for experiments based on beam-on beam-off cycles and decay measurement.

Source	Δb_{GT}
Nuclear charge radius of ^{6}Li	4.6×10^{-5}
Endpoint energy of the transition	1.8×10^{-4}
Weak magnetism form factor	5.7×10^{-4}
Induced tensor form factor	1.9×10^{-5}
Total theoretical uncertainty	6.0×10^{-4}

Table 1.5: Experimental properties that enter the theoretical description of the beta-energy spectrum along with the systematic uncertainty they produce on the extracted Fierz term [47].

1.5.3 The two experimental methods

The most straightforward solution to resolve the problem of electron backscattering observed in previous β-energy spectra measurements resides in using a 4π calorimetric coverage. This prevents energy loss from backscattering in the detector.

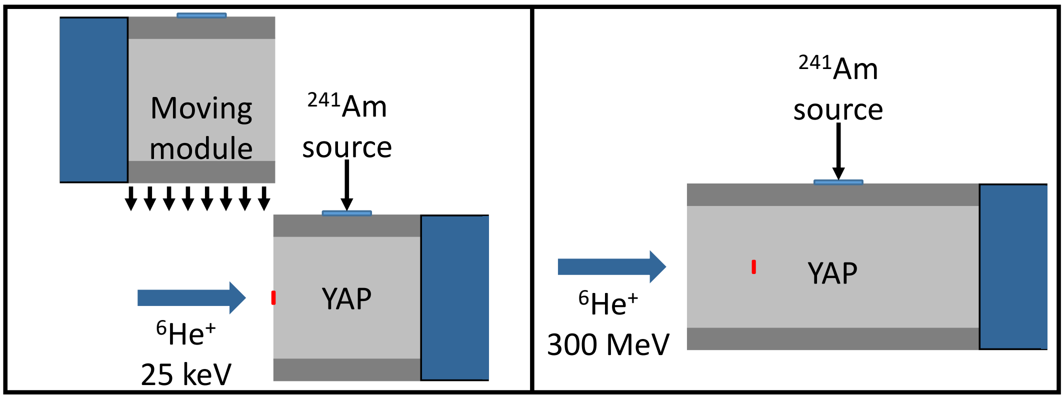

Figure 1.7: Left panel: a sketch of the setup with a low energy beam. The beam is implanted at the surface of the scintillator. A second identical module is sequentially moved in front of the first to achieve a 4π geometry. Right panel: a sketch of the setup with a high energy beam. The beam is implanted deep inside the scintillator. In both setups, the red marks indicate the location of the activity.

To achieve the 4π detection geometry, two techniques were used involving fast and slow beams of ^{6}He produced at the Grand Accélerateur National d'Ions Lourds (GANIL) in Caen, after the LISE fragment separator and at the low energy beam line (LIRAT) of the SPIRAL facility. The first one with the low energy beam (left panel of Fig. 1.7) consists in using two independent detectors. The beam is implanted on the surface of one fixed detector, while the other is free to switch between two positions for beam implantation and β particles energy deposition, ensuring the 4π coverage (details in Chap. 2). The second technique consists in using a single and larger detector (right panel of Fig. 1.7), where the high energy ^{6}He beam is implanted deep inside the volume of the detector, insuring the 4π geometry.

The two experiments involving these two techniques were performed at GANIL, and they both constitute the phase-I of b-STILED project. The total uncertainty goal aimed for the two experiments of phase-I is $\Delta b_{GT} = 3.9 \times 10^{-3}$ at 1σ (including statistical and systematic uncertainties). This level of precision corresponds to the current precision level on the Fierz interference term for pure Gamow-Teller decays shown in Eq. (1.23). Achieving this precision would provide the tightest constraint on the tensor couplings from any single low energy probe. The main goals of phase-I is to validate the level of control of instrumental effects, as well as to look for unforeseen systematic effects and to implement countermeasures. The observations and conclusions of phase-I experiments will be used to chose the ultimate experimental setup for phase-II. The final uncertainty goal of this project ($\Delta b_{GT} = 1 \times 10^{-3}$) will be achieved during phase-II.

CHAPTER 2

E815S experiment

In this chapter, we introduce the experimental setup used during the E815S experiment (low energy experiment) that was performed at the "Grand Accélérateur National d'Ions Lourds" (GANIL), Caen in May 2021. The low energy detection setup, consisting of two identical detectors, was used for this experiment. A 25 keV $^{6}\mathrm{He}^{+}$ beam was deposited on the front face of one fixed detector, while the other one was switching synchronously between two positions for implantation-acquisition cycles. The apparatus, the experimental conditions and the beam transport to the detection setup are fully described in the following sections. A less detailed description can also be found in Ref. [48].

2.1 Beam production and transmission in LIRAT

GANIL produces the highest intensity low energy $^{6}\mathrm{He}^{+}$ ion beams in the world. It is thus the most appropriate facility to host this experiment. The beam of $^{6}\mathrm{He}^{+}$ is delivered by the low energy beam line LIRAT (Ligne d'Ions Radioactifs À Très basse énergies) of GANIL. The production of the high intensity beam of $^{6}\mathrm{He}$ uses the Isotope Separation On-Line (ISOL) technique [49]. A primary beam of $^{13}\mathrm{C}$ is delivered by the GANIL coupled cyclotrons, then directed towards a $^{12}\mathrm{C}$ target at 75 MeV/A with an intensity of 1.6×10^{13} pps. The radioactive products of the fragmentation reaction diffuse through the target and are ionized with an Electron Cyclotron Resonance (ECR) ion source. The ions can be extracted from the source with an energy between 10-30 qkeV, and are separated based on their charge to mass ratio (q/m) with the two sequential magnetic dipoles (ICD1 and ICD3) with a total resolution of $\frac{\Delta m}{m} \approx \frac{1}{300}$ (Fig. 2.1).

The transmission of the beam is measured between two Faraday cages, the first being located right after the ICD1 dipole and the second at the position of the fixed detector. The tuning of the dipoles and quadripoles of the LIRAT line was done first with a stable beam of $^{12}C^{2+}$ at 25 qkeV, since it has the same q/m ratio as $^{6}He^{+}$, before switching to the $^{6}He^{+}$ beam of interest. The high voltage applied to the ECR source was then set to 24890 V, which was found to be the optimal value to limit $^{12}C^{2+}$ contamination while conserving a maximal $^{6}He^{+}$ intensity.

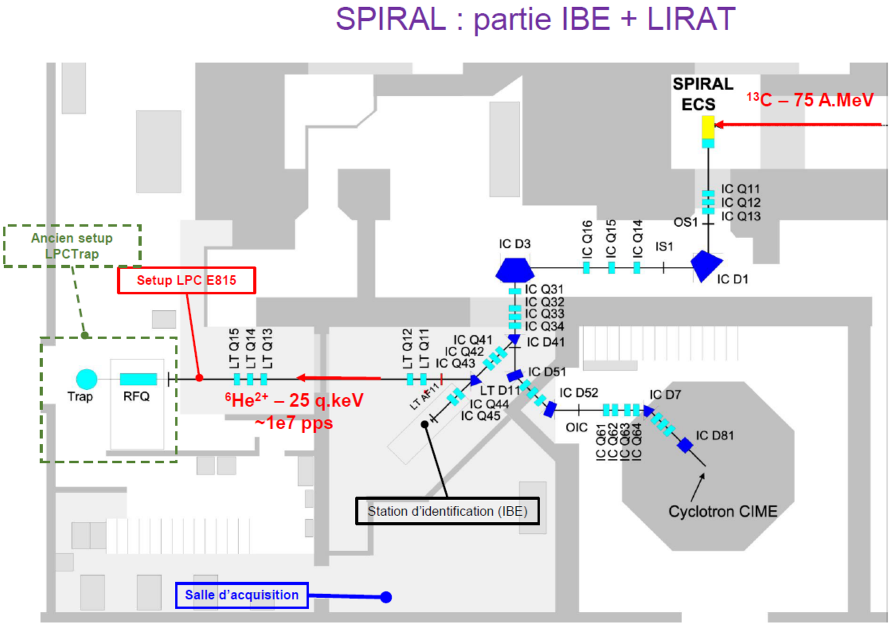

Figure 2.1: Schematic of the low-energy area of the SPIRAL facility. The primary beam impinging the ECS is shown in red in the upper right corner. The detection setup, also indicated in red, is located after the last quadrupoles LTQ13-LTQ15.

2.2 Detection setup

2.2.1 b-STILED chamber

The vacuum chamber containing the two main detectors was placed at the end of the LIRAT line (Fig. 2.2). It is divided into two sections, each having its own pumping system, in order to reduce as much as possible the contamination by ^{6}He atoms.

The two sections are separated by a stainless steel plate with a hole of 35 mm diameter. The first section contains two adjustable collimators with three options for the hole diameter of 4, 6 and 8 mm. The collimators are placed at the entrance and the exit of the first section with a distance of 142 mm between the two of them (Fig. 2.3). The second section houses the two main β-particles detectors, where the $^{6}He^{+}$ ions will be implanted. A movable silicon detector can be inserted at the entrance of this section in order to measure the intensity of the beam before implantation at the surface of the fixed detector. A third and last collimator with a 4 mm diameter aperture was fixed to the movable detector and was located a few millimeters

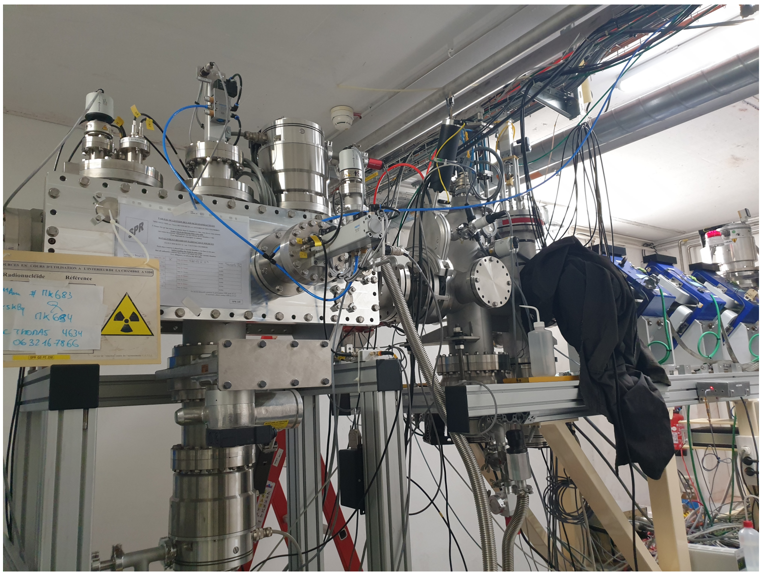

Figure 2.2: The end of LIRAT beam-line with the b-STILED chamber shown on the left.

away from the front face of the fixed detector during the beam implantation phase. The pressure inside the two sections was 2.6×10^{-7} mbar during the experiment. The nominal beam intensity for the implantation was chosen to be below 2.5×10^{4} pps which corresponds to 1.2×10^{5} pps on the silicon detector located before the third collimator. This value was chosen in order to obtain sufficient statistics during the experiment while keeping the gain bias during the cycles below 2%. To achieve this implantation rate, a beam reducer was inserted prior to the ICD31 dipole, which reduced the beam intensity by a factor of 9. The beam was also collimated by the two collimators of the first section using the 6 mm diameter holes. Prior to each data taking, the silicon detector was inserted within the beam trajectory to measure the beam intensity. The $^{6}\mathrm{He}^{+}$ ions were delivered to the implantation position with a kinetic energy of 24.89 keV.

2.2.2 The time sequence

This experiment is based on implantation-acquisition cycles. The time sequence of the cycles is controlled entirely by a Stanford Research Systems DG645 pulse generator. This pulse generator provided three synchronized signals. The first, a TTL signal, is sent to a beam deflector placed right after the ICD1 dipole (Fig. 2.1), which controls the beam passage to the detection setup. The second, another TTL signal, is sent to the mechanical actuator which controls the motion of the movable detector. Lastly, the third is a NIM signal of 20 ns length, and it is sent to the DAQ system in order to save a time reference announcing the beginning of each cycle. The three signals were synchronized in a way that takes into consideration the duration of motion of the movable detector (Fig. 2.4).

As stated in Chap. 1, a 4π calorimetry coverage is needed to ensure the full collection of the

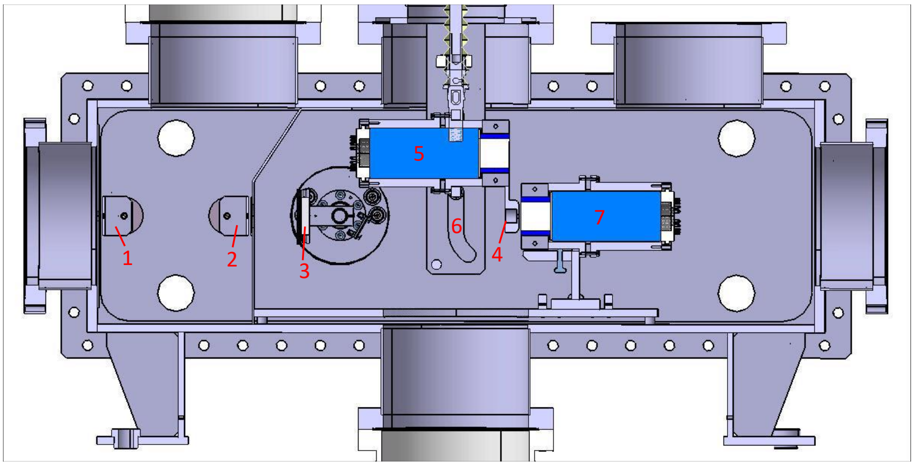

Figure 2.3: Sectional view of the b-STILED vacuum chamber. The labels on the panel are: 1 and 2– the two Ø6 mm collimators in the first section of the chamber; 3– movable Si detector; 4– the third Ø4 mm collimator; 5 and 6– the moving detector and its mechanical guide; 7– the fixed detector.

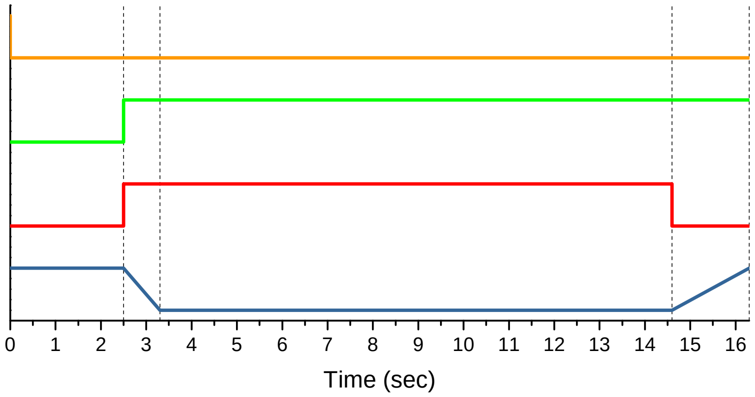

Figure 2.4: Orange: The NIM signal sent to the DAQ. Green: the TTL signal sent to the deflector. Red: The TTL signal sent to the mechanical actuator. Blue: the position of the detector during the cycle. The beam is on during 2.5 sec at the beginning of the cycle.

β-particles energy. A combination of two detectors was used to achieve this goal. The fixed detector is aligned along the beam axis, while the other is mounted on a fast actuator controlled by the DG645 pulse generator. The movable detector is capable of switching between two positions (Fig. 2.5) for beam implantation and events acquisition phases. In the rest of this manuscript, the fixed detector will be referred to as "Det1" and the movable detector will be referred to as "Det2".

The motion of Det2 is synchronized with the beam within well determined cycles of 16.3 sec (Fig. 2.4). Each cycle includes 2.5 sec for the implantation of the 25 keV beam of ^{6}He$^+$. During this phase, Det2 is in the implantation position (left panel of Fig. 2.5) away from the beam trajectory. At the end of the implantation phase, the beam is chopped by the deflector and Det2 starts to move into the acquisition position (right panel of Fig. 2.5). This motion

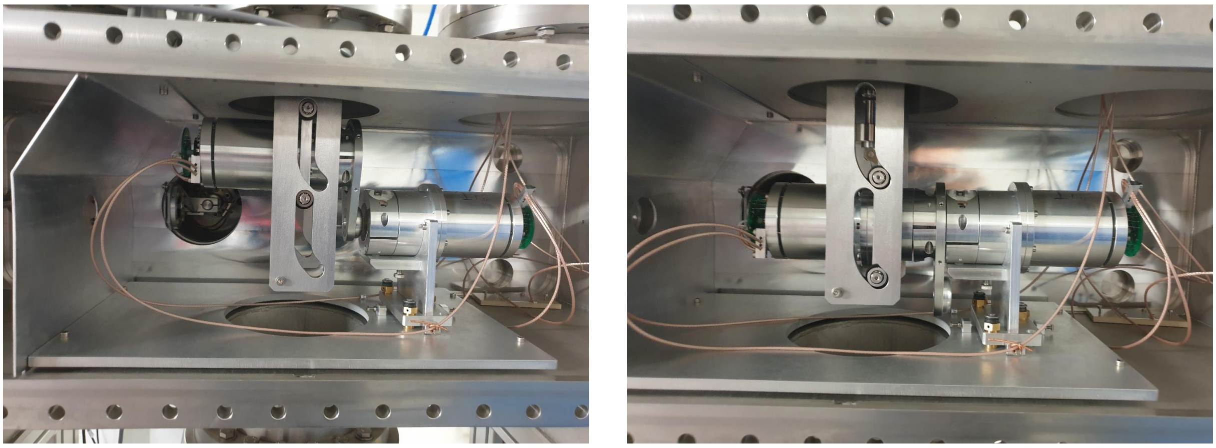

Figure 2.5: The two β-particle detectors during beam implantation phase (left panel) and acquisition phase (right panel).

takes about 0.8 sec. By the time Det2 is in full contact with Det1, the acquisition phase starts allowing the collection of the β-particles energy within the two detectors. This phase lasts for 11.3 sec which corresponds to more than 10 half-lives of ^{6}He, allowing therefore the estimation of the background contribution. After the end of the acquisition phase, Det2 moves back to the implantation position, this motion takes about 1.7 sec. Right after the arrival of Det2 to the implantation position, the beam deflector is switched off for the beginning of the next cycle.

The transit time of Det2 between the implantation and the acquisition phases of 0.8 sec means that the loss of activity during the transition is limited to 50% and does not lead to a very significant loss of statistics. The motion of Det2 was tested intensively for several days with 20 sec duration cycles prior to the experiment, without any signs of degradation of the detector signals. The full contact between the surfaces of the two detectors was periodically checked during the experiment by pinching a 20 µm thickness sheet at different places of the contact surface.

2.3 The β particle detectors

2.3.1 The phoswich configuration

The two detectors, Det1 and Det2, are identical. Each of them is mounted in a "Phoswich" configuration, which consists in using two scintillators with different decay times read out by a single photomultiplier tube (Fig. 2.6). The two scintillators are a cylindrical 3 cm diameter × 3 cm long $YAlO_3$ Ce-doped inorganic scintillator "YAP: Yttrium aluminum perovskite" surrounded by a hollow cylindrical EJ-204 plastic scintillator "PVT: polyvinyl toluene" with an external diameter of 4 cm. The photomultiplier tube (PMT) used for each detector is the R7723 from Hamamatsu which has a diameter of 5.2 cm and a bialkali photocathode [50]. The optical coupling between the PMT and the two scintillators was ensured with a thin layer of optical coupling grease. The entire detector is shielded with an aluminum case that serves as well to keep the pressure between the PMT and the scintillators.

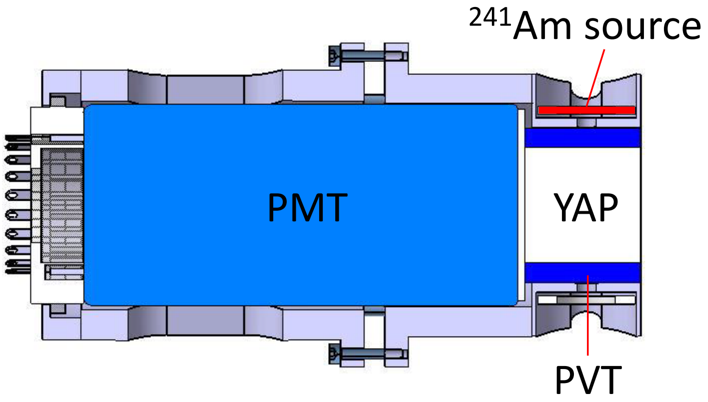

Figure 2.6: Cross sectional view of the detector including the two scintillators coupled to a single PMT in a phoswich configuration, and position of the ^{241}Am calibration source.

An ^{241}Am calibration source with an activity of 5 KBq was permanently mounted on the side of the PVT of each detector (Fig. 2.6). The ^{241}Am decays by emitting a 5.5 MeV α and a 59.54 keV γ. The 59.54 keV photons interact mostly inside the YAP volume and are used as a constant calibration reference. The α particles are completely stopped within the PVT and can be used as well as a calibration reference to monitor the gain and baseline fluctuations. A 225 µm layer of Tyvek is wrapped around the PVT to improve the light collection. A 5 mm diameter hole in the Tyvek is placed in front of the ^{241}Am source to allow the α particles to reach the PVT. The contact surfaces of both detectors are free of any reflector or dead layer. Consequently, the scintillation light generated in one detector is able to cross the surface between the two detectors and be collected by the other detector's PMT. It was observed that about 80% of the light generated in one of the detectors is collected by its own PMT while about 20% is collected by the other detector's PMT (Fig. 2.7).

The PVT is a plastic scintillator with a relatively fast decay time of about 2 ns [51]. It serves mainly as a veto to reduce the background events reaching the YAP. Conversely, The YAP, which is the main scintillator where the ^{6}He decay will happen, is a crystal scintillator with a decay time of about 27 ns [52]. The decay time of the YAP is short enough to limit pileup contributions, but significantly slower than the decay time of the PVT. This allows a clear discrimination between the signals of the two scintillators with pulse shape analysis.

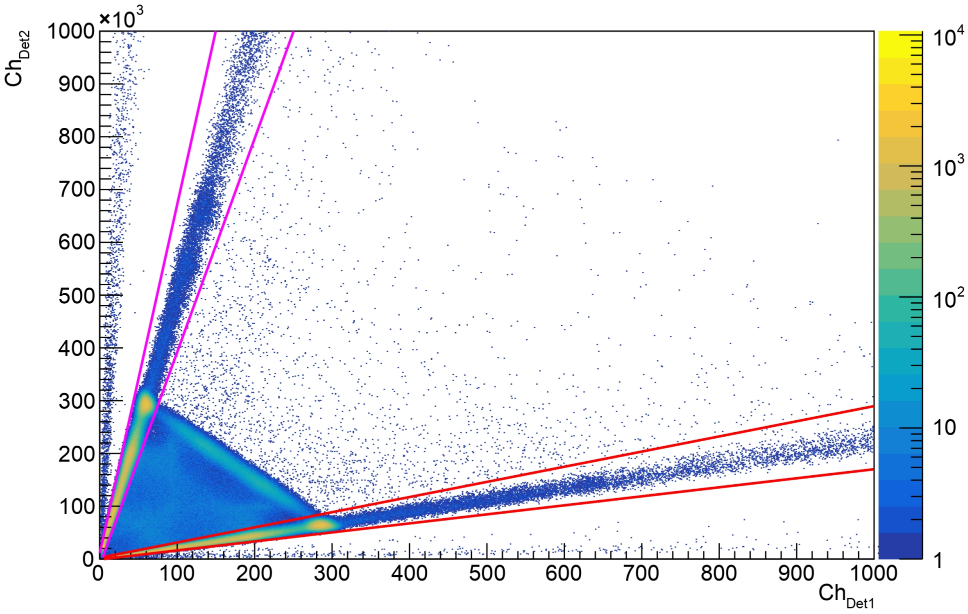

Figure 2.7: Plot showing the collected charge from the PMT of Det2 against the collected charge from the PMT of Det1 during a 1 hour calibration run with a ^{137}Cs source. The events located between the two red lines are those that deposited their entire energy inside the YAP of Det1, while those located between the magenta lines are the ones that deposited their entire energy inside the YAP of Det2. All the other events shown between the red and magenta lines are events that deposited part of their energies in both detectors. For the events that deposited their entire energies in one of the detectors, it can be noticed that ∼80% of the generated scintillation light is collected by this detector's PMT while the rest is collected by the other one. This can be deduced from the slope of the events distributions inside the red and the magenta lines. The events between the lines but above the main ^{137}Cs correspond to the ambient background.

2.3.2 The choice of YAP scintillators

Several inorganic scintillator materials were examined for the measurement of the β-energy spectrum. The first criterion for the selection of the crystal scintillator is the decay time. For this measurement, a relatively fast decay time is necessary in order to reduce as much as possible the pileup effect. Three candidates with relevant decay times appear; The YAP, The Lanthanum Bromide "LaBr$_3$" and the Cesium Iodide "CsI" with a decay time of 16 ns for the last two [53]. While the LaBr$_3$ is considered hygroscopic, the YAP is not, which makes it easier to manipulate and store. The CsI is slightly hygroscopic (must be stored in a well sealed container). In addition, the LaBr$_3$ exhibits a high intrinsic radioactivity. For those reasons, the YAP and CsI seemed to be good candidates for this measurement while the LaBr$_3$ was not taken into consideration.

The second criterion for the choice is the amount of energy escape due to Bremsstrahlung radiations that distort the shape of the detected β-energy spectrum (more details in Chap. 4). These radiations are produced when electrons slow down inside the material. The production

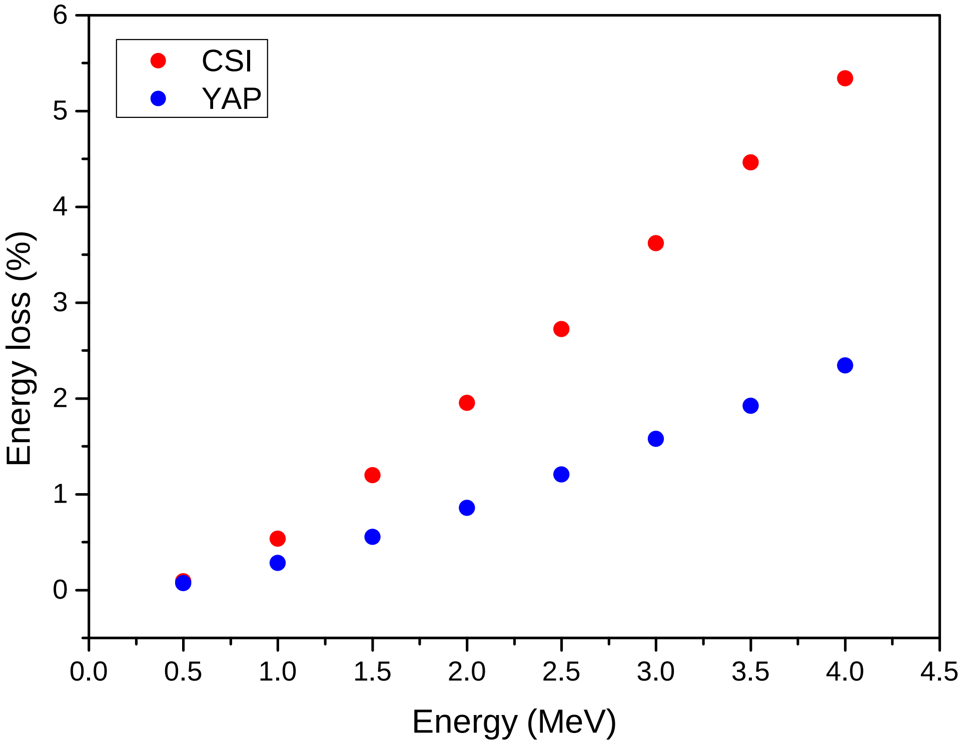

Figure 2.8: The percentage of the energy loss due to Bremsstrahlung escape for different electrons energies up to 4 MeV within the YAP (blue dots) and CsI (red dots) determined with GEANT4 simulation [54]. Electron emission was generated at the center of a 30 mm diameter × 60 mm long YAP volume, corresponding to the chosen experimental configuration when Det1 and Det2 are in contact.

of these radiations is proportional to the square of the effective atomic number of the substance (Z_{eff}^2). This means that the electrons in the YAP (Z_{eff} = 36) produce fewer Bremsstrahlung photons than the same electrons in the CsI (Z_{eff} = 54). However, for electrons with energies below 3.5 MeV (the endpoint energy of the β-spectrum for ^{6}He decay), it is expected that the majority of the produced Bremsstrahlung photons have very low energies [54]. Therefore the absorption of these photons by the material is dominated by the photoelectric effect, which is proportional to $\frac{Z_{eff}^n}{E_\gamma^{3.5}}$ with $4 \leq n \leq 5$ [55], meaning that the Bremsstrahlung photons produced in the CsI have a higher probability to be absorbed by the scintillator than those produced in the YAP.

In order to compare the two materials, a Monte-Carlo simulation was performed for each material with the same configurations (the same geometry, electrons source position and energies), using a detector geometry similar to the one used in the present experiment (a 60 × 30 mm^2 YAP cylinder with the source placed at its center) [54]. Figure 2.8 shows that for this specific geometry, the amount of escaped energy in the YAP is more than two times smaller than that of the CsI. For these reasons, the YAP was the scintillator chosen for this experiment.

The implantation depth of the 25 keV ^{6}He$^+$ inside the YAP was found to be around 140 nm

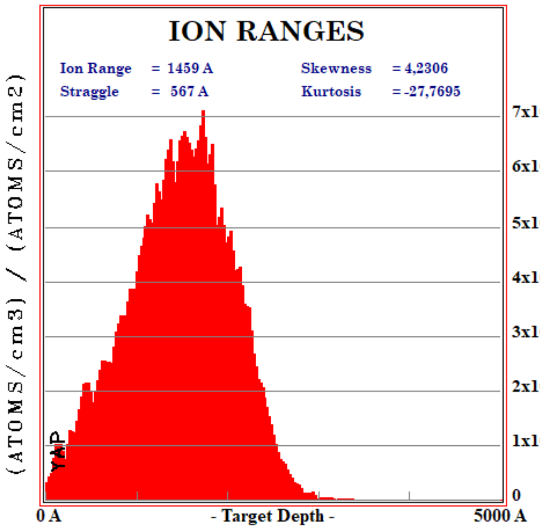

Figure 2.9: The implantation depth of 25 *keV* ^{6}He$^+$ ions inside the YAP scintillator as calculated by TRIM.

by TRIM "TRansport of Ions in Matter" [56] (Fig. 2.9). The average range of 3.5 MeV electrons (the endpoint of the ^{6}He decay) inside the YAP was found to be about 5 mm, this eliminates the possibility of electrons outscattering when the two detectors are in contact. The size of the YAP scintillators was chosen as a compromise between the amount of Bremsstrahlung energy escape and the sensitivity to the ambient background.

Another advantage of the YAP is its fairly linear response function, which was studied in several references [57, 58, 59]. Figure 2.10, which is adapted from Ref [57], shows the normalized light yield per deposited electron energy in the YAP (right panel) and in the CsI(Na) (left panel) for energies between 16 keV and 445 keV. These two plots confirm the linearity of the YAP in comparison with the CsI(Na) within the provided uncertainties of each measurement for energies extending up to 500 keV.

To confirm the linearity of the YAP scintillator in the detection setup up to the endpoint of the ^{6}He β-spectrum, the response function of both detectors was studied with several γ calibration sources (^{22}Na, ^{137}Cs, ^{60}Co and ^{208}Tl) (more details in Appendix B). Figure 2.11 shows that the response function of Det1 is linear between 551 keV and 2614 keV, with deviations smaller than 2 keV from linearity. These deviations are in part due to the fitting procedure of the photopeak that doesn't account for the superposition of the Compton edge tail with the photopeak. The energy resolution was found to be 6.7% at 662 keV and 5.5% at 1332 keV (see Appendix B).

2.4 Data acquisition system

The DAQ system used for this experiment is the FASTER acquisition system developed at LPC Caen [60]. The two signals from the PMTs with the logic pulses from the DG645 generator

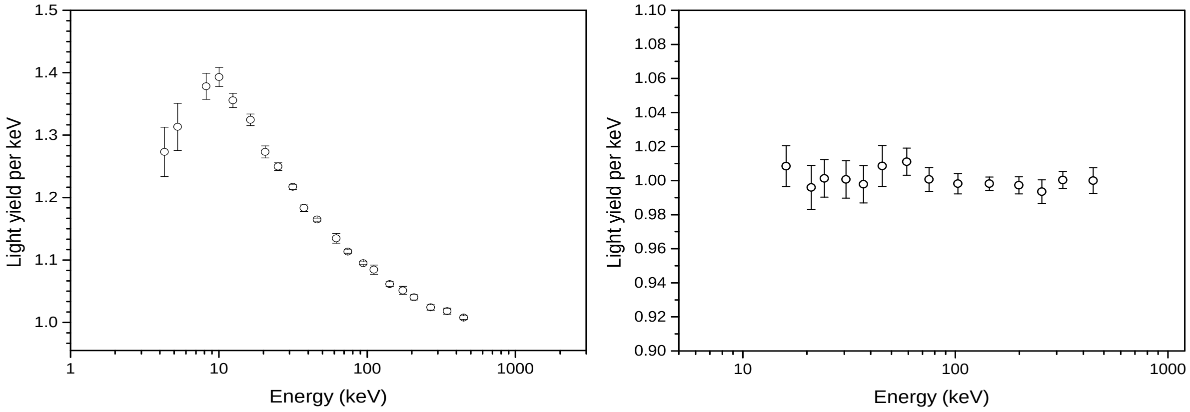

Figure 2.10: Light yield in the YAP (right panel) and the CsI(Na) (left panel) for several electrons energies, values are normalized to unit at 445 keV. Plots are adapted from Ref [57].

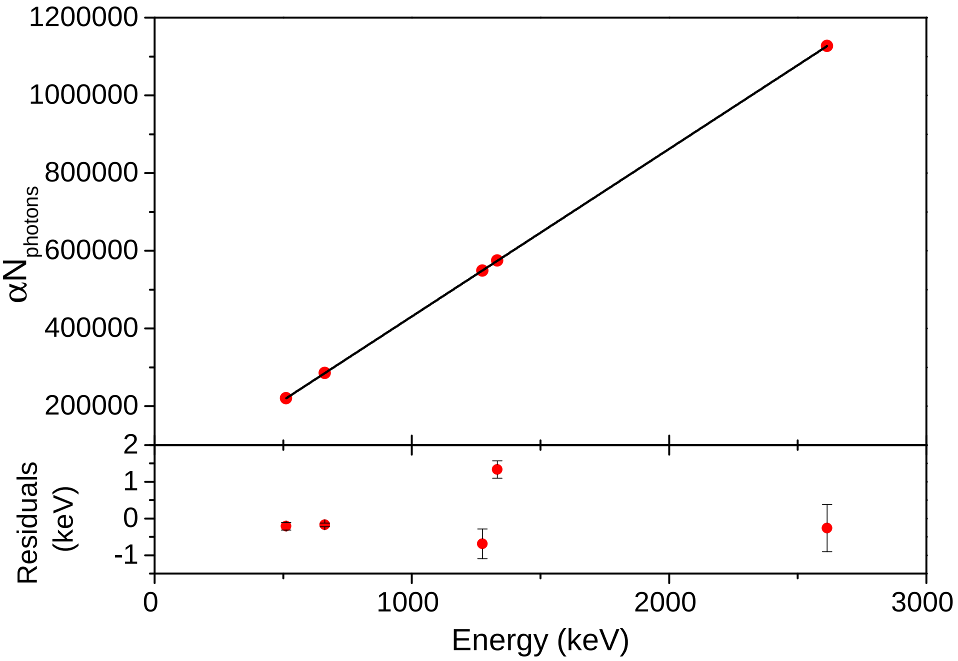

Figure 2.11: The photon yield of the YAP of Det1 against the energy of the γ particles with a linear fit to the points (top) and the residuals of the fit (bottom).

were sent directly to three FASTER CARAS channels. The signals are digitized at a rate of 500 MS/s with a 2.2 Volts range conversion over 12 bits. Each channel has an independent trigger based on individual thresholds. The digitized samples are processed in real time by Field-Programmable Gate Arrays using predefined algorithms adapted to the measurements to be performed [60]. Each collected signal is time stamped with a 2 ns resolution, giving the ability to obtain coincidences either online or offline within user defined time windows.

The chosen algorithm provided the charge integration within four distinct time windows

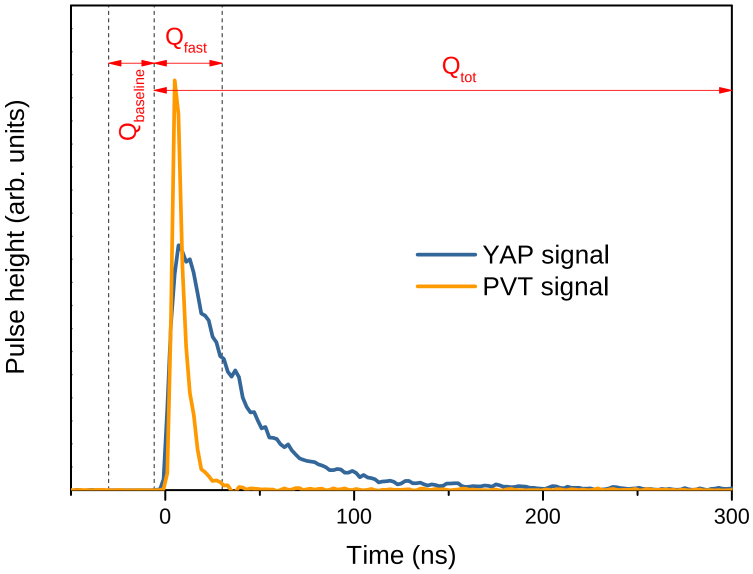

Figure 2.12: Typical signals from the PVT and YAP along with the three charge integration intervals.

relative to the trigger time for both PMTs. The trigger threshold for the PMTs was set to 5 mV, which is equivalent to a deposited energy of 4-9 keV. The first window was set between -30 ns and -6 ns in order to get the charge $Q_{baseline}$ which is used to estimate the baseline level right prior to the signal. The second window was set between -6 ns and 30 ns, while the third was set between -6 ns and 300 ns. Those two windows provided respectively the two charges Q_{fast} and Q_{tot}. Because of the significant difference in the decay time of the YAP (27 ns) and the PVT (2 ns), the typical shape of each one's signal is different (Fig. 2.12). The charge Q_{tot} includes the integration of almost the entire YAP and PVT signals, while Q_{fast} includes only the integration of the entire PVT signals and part of the YAP signals. This means that by calculating the Q_{fast}/Q_{tot} ratio for each signal we can discriminate between the events in the YAP from those in the PVT. Figure 2.13 shows the Q_{fast}/Q_{tot} ratio plotted against Q_{tot}, all the events around Q_{fast}/Q_{tot} value of 1 corresponds to events inside the PVT scintillator while those around Q_{fast}/Q_{tot} value of 0.54 corresponds to the events inside the YAP including the β-particles of the ^{6}He decay. The fourth and last window was set between -30 ns and 1000 ns, and it is used to study after-pulses and pileups effects.

With these settings, the intrinsic dead-time of the acquisition system is equal to the largest time window which is 1030 ns. The baseline for each signal was permanently monitored for the three channels, and corrected for low-frequency variations (below 160 kHz) by the FASTER baseline restoration algorithm. The signals provided by the DG645 generator were used as a time reference to indicate the beginning of each measurement cycle.

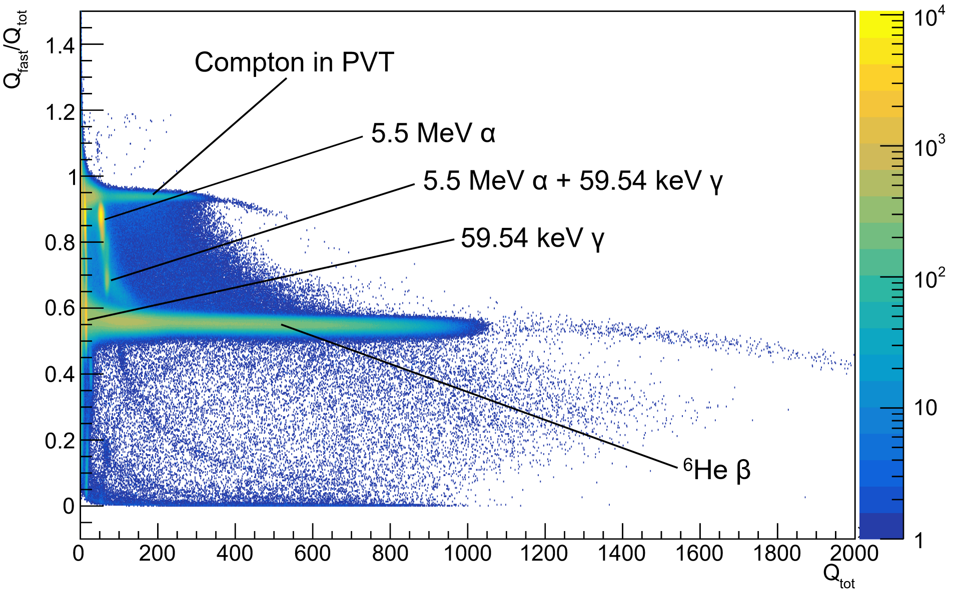

Figure 2.13: A plot of the Q_{fast}/Q_{tot} ratio vs Q_{tot} for a one hour run of the experiment. This plot shows the α and γ particles detected respectively within the PVT and the YAP in addition to the β particles from the decay of ^{6}He inside the YAP. The structures with few counts appearing in blue correspond to pile-up events and to signals with an offset on the baseline.

2.5 Experimental conditions

During the experiment, five sets of measurements were performed to study different systematic effects. For the nominal configuration of the setup, the two PMTs were biased with a polarization voltage of -1620 V and -1420 V respectively for Det1 and Det2. Those values were chosen in order to avoid PMTs saturation for electron events with energies up to the endpoint of the β-spectrum of ^{6}He, as well as in order to reasonably match the gain of the two PMTs. The nominal measurement cycles were set to 16.3 sec including 2.5 sec for the beam implantation, 2.5 sec for the Det2 motion, and 11.3 sec for statistics accumulation. The nominal beam intensity corresponds to an average of about 6000 detected ^{6}He events per cycle. The nominal configuration was used during Set1. For Set2, the length of the measurement cycles was increased to 31.3 sec including the same 2.5 sec for beam implantation and 2.5 sec for Det2 motion, which increased the acquisition phase during this set to 26.3 sec. The beam intensity was also increased during this set in order to increase the number of detected ^{6}He events to about 21000 per cycle. These changes allow us to study the background part of the spectrum to investigate the presence of contaminants with half-lives longer than that of ^{6}He, in addition to the study of pileups due to the increase of the decay rate within the cycles. For Set3, the polarization voltages for both detectors were decreased by 50 V, to study the potential effect of a PMT gain change.

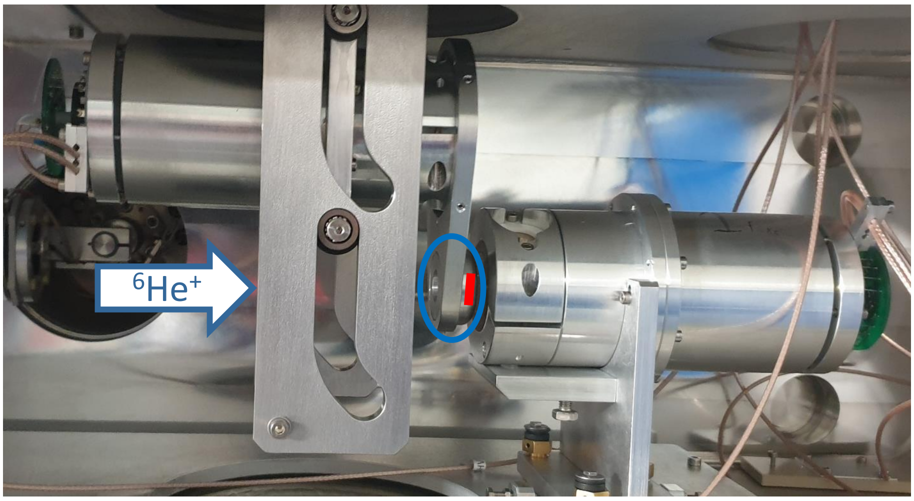

Figure 2.14: A picture of the experimental setup with the position of beam implantation phase. The red line represents the cap that was used to close the third collimator in order to get the background induced by ^{6}He$^+$ deposition on the collimator. The blue ellipse marks the area where the ^{6}He$^+$ deposition happens during Set4 and Set5.

For Set4 and Set5, a 0.4 mm thickness aluminum shutter was placed inside the collimator attached to Det2 as shown in Fig. 2.14. This shutter prevents the ^{6}He$^+$ ions from reaching the surface of Det1. These two sets provide the background induced by ^{6}He$^+$ deposition on the surface of the collimator. During Set4, the same configurations for polarization voltages, time cycles and beam intensity as for Set1 were used. While for Set5, the configurations of Set2 were applied. Table 2.1 summarizes the experimental conditions used for each set of measurements.

Set	Set name	T_{acq} (s)	$\langle N_0 \rangle$	ΔV_{PMT} (V)	Cycles
(1)	Short cycles	11	6130	0	3050
(2)	Long cycles	26	20900	0	620
(3)	Lower bias/Short	11	7140	-50	1930
(4)	Shutter/Short	11	–	0	200
(5)	Shutter/Long	26	–	0	115

Table 2.1: The five experimental conditions of the recorded data. T_{acq} is the duration of the measuring window; $\langle N_0 \rangle$ is the average number of detected ^{6}He decays per cycle with an energy threshold of 300 keV; ΔV_{PMT} indicates the difference in the PMT bias relative to the nominal voltage. The last column lists the number of recorded cycles.

A coincidence window of 200 ns wide for the PMTs signals was set during this experiment. This means that if two signals coming each from the PMT of each detector coincide within a window of 200 ns, these two signals are grouped together. This gives the possibility to eliminate any signal caused by electronic background, dark noise as well as events at super low energy that could trigger only one PMT. Otherwise, any energy deposition inside one of the scintillators above the energy threshold will be simultaneously detected by the two PMTs.

Prior to the beginning of data acquisition of each set, a one hour run was performed with ^{6}He implantation during which the signals traces were saved "Oscilloscope runs", to record the full digitized frames of all signals at a sampling rate of 10 Hz. These runs give access to the shapes of the signals and are used mainly to study after-pulses and pileups. Before and after the experiment, data were recorded with the nominal configuration using the ^{241}Am, ^{22}Na, ^{137}Cs and ^{60}Co sources to check the response function of the detectors. Background runs were also recorded without any sources in order to measure the ambient background. At the end of the experiment, a total number of about 4×10^7 detected ^{6}He decay events was achieved.

CHAPTER 3

First order calibration and the half-life measurement

In this chapter, we introduce a first analysis of the E815S experimental data which resulted in the determination of the most precise value of the ^{6}He half-life. The first order calibration in energy of the detection setup, correcting for relative gain and baseline fluctuations, as well as the effect of the other main sources of systematic error will be detailed.

3.1 Motivation for the half-life measurement

The extraction of the Fierz interference term b_{GT}, with very high precision from the analysis of the shape of the β-energy spectrum, requires both the high precision measurement of the shape of the spectrum and the high accuracy knowledge of all the theoretical components of the spectrum. One of the appealing aspects of the ^{6}He is that it decays to the ground state of ^{6}Li with a pure Gamow-Teller transition. This can be translated by the fact that the shape of the β-energy spectrum does not depend, to first order, on the dominant nuclear matrix element, denoted c in Ref. [61]. Conversely, this matrix element enters recoil order corrections in ratios with the weak magnetism form factor.

The extracted value of c from Ref. [1] has a relative uncertainty of 3.6×10^{-4}. Using only this value results in a negligible impact on the Fierz interference term extraction from the measurement of the energy spectrum. However, as mentioned in Ref. [1], the number of previous measurements of ^{6}He half-life with a relative uncertainty smaller than 1% is very poor. Figure 3.1 shows the large discrepancy of about 1% between two groups of measurements. This motivates the measurement of the half-life of ^{6}He with a total uncertainty similar to or better than that of Ref. [1], with a technique involving different sources of systematic effects, in order to resolve the discrepancy. The data of the E815S, with time stamped events with a precision

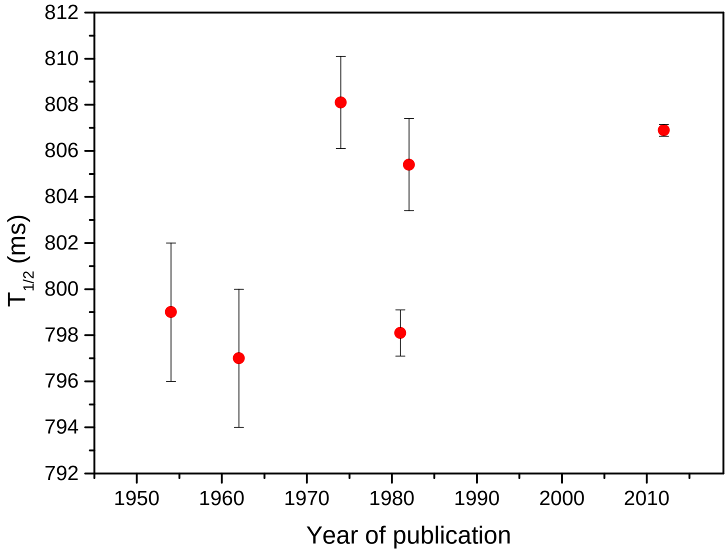

Figure 3.1: Comparison between the ^{6}He half-life results obtained by previous measurements having a relative precision smaller than 1%. The plotted values are from Refs.[2, 3, 4, 5, 6, 1].

of 2 ns, are very promising for such a measurement, which can be considered as a byproduct of the experiment, and only requires first order analysis of the data.

3.2 First order calibration and gain correction

A very accurate energy calibration of the β particle detectors is unnecessary for a precise half-life measurement. Nevertheless, it is crucial to control accurately the gain and baseline variations of the PMTs during each cycle and across the whole experiment. These variations modify the effective energy threshold as a function of time within the decay cycles, eventually leading to a systematic error/shift to the determination of the half-life [62]. In the following, we describe the energy calibration performed to compensate for these gain and baseline fluctuations, using the position of the 59.54 keV photopeak of the ^{241}Am calibration source as a reference. An equivalent but independent calibration was performed for Det1 as well as for Det2. When not specified, the figures shown in this section are for the calibration of Det1.

Prior to the calibration, the data from uncompleted cycles of each run were discarded. These are the first and last cycles of each run. The 59.54 keV γ rays of the ^{241}Am source interact mainly inside the YAP scintillator. Therefore, in order to reduce as much as possible the background contribution, the events with energy deposition in the YAP only are chosen. Those corresponds to a $\frac{Q_{fast}}{Q_{tot}}$ ratio between 0.5 and 0.62 (Fig. 3.2). Lastly, only the events that were recorded in coincidence within the two PMTs were selected for this calibration, in order to suppress further the background originating from the electronics and the PMTs.

Each recorded event was assigned with a time stamp relative to the start of the acquisition.

By comparing this time stamp to the time of the periodic signal reaching the DAQ system from the DG645 pulse generator, the relative time of each event inside each cycle is obtained. With this calculated time of each event, the decay histogram can be plotted (Fig. 3.3).

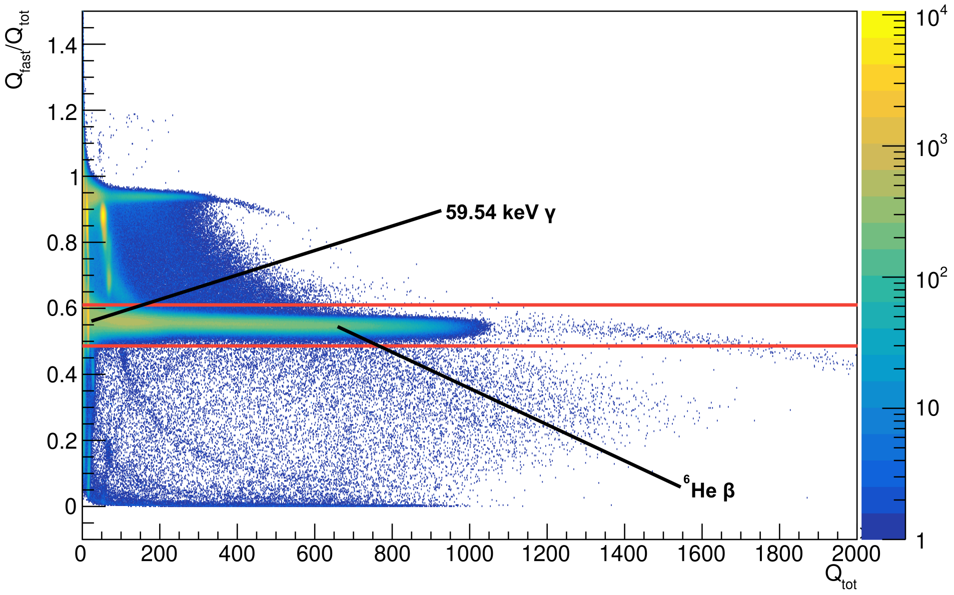

Figure 3.2: A plot of the Q_{fast}/Q_{tot} ratio vs Q_{tot} for a one hour run of the experiment. Only the events within the red lines are chosen for this calibration.

3.2.1 Sources of relative gain and baseline variations

The gain and baseline are expected to vary proportionally to the count rate variations. Two main causes for count rate variations within the acquisition phase of the cycles were observed. The first is the rate variation due to the ^{6}He decay itself. The number of detected β particles by the detectors decreases exponentially during each cycle (Fig. 3.3).

The second source of count rate variations is the change of the beam intensity from cycle to cycle due to the GANIL primary beam fluctuations or to sudden regime changes of the SPIRAL ion source. In other words, the initial rate of ^{6}He was not identical for all the cycles within the 3 sets of measurement. To identify this difference in the initial count rate, the SBR parameter was introduced, which stands for the "Signal to Background Ratio" defined as the ratio of the mean rate of ^{6}He decay events over the constant background rate detected within each cycle. It is calculated by fitting the decay spectrum for each cycle by an exponential function that considers the presence of a constant background:

$$f(t) = N_0 \times e^{-t/\tau} + B, \tag{3.1}$$

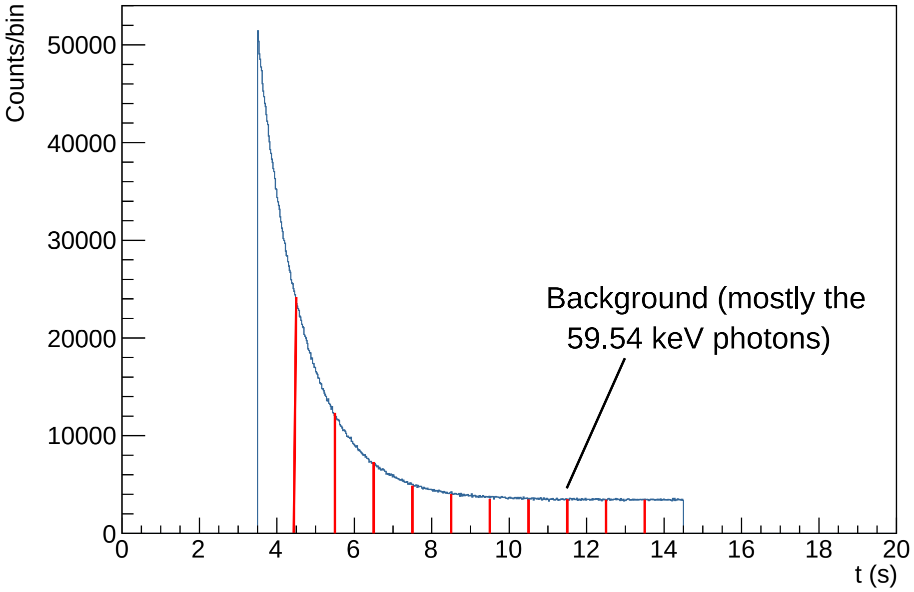

Figure 3.3: The decay spectrum for a one hour run of Set1 of measurement (only the acquisition phase of the cycle is shown here). The background here is dominated by the 59.54 keV γ particles. The vertical red lines represent the time intervals used to form the correction model.

where N_0 is the initial rate of ^{6}He for each cycle, τ is the decay constant and B is the present constant background. The SBR value for each cycle was obtained by dividing the total number of ^{6}He decay events in the cycle ($N_0 \times \tau$) by the constant background B (which in this case consists mostly of the 59.54 keV γ particles). Figure 3.4 shows the distributions of the SBR values for all the cycles of the three sets of measurements. These distributions show that the SBR and thus the initial rates of ^{6}He are not constant. The SBR values for the cycles are distributed along a large interval which is different for each of the 3 sets.

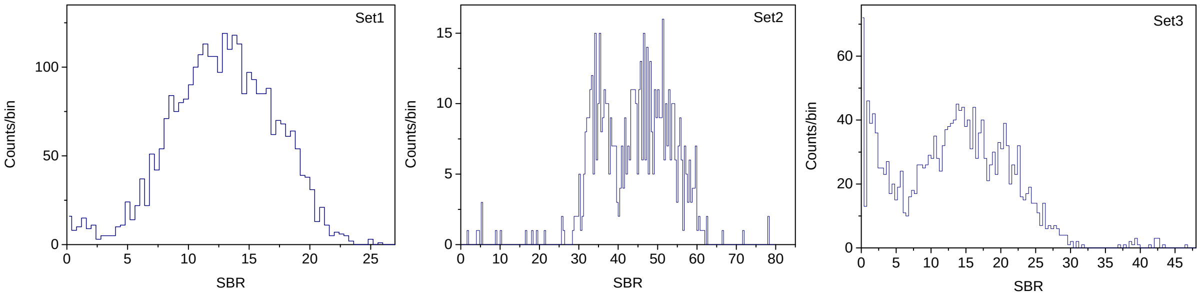

Figure 3.4: The SBR distribution for the three sets.

These two causes of the count rate variations lead to significant fluctuations of the gain and of the baseline of the detectors and should be accounted for prior to the determination of the half-life and the Fierz interference term.

3.2.2 Analytical correction model

Despite the fact of using two similar detectors, their gains are not necessarily identical. For this reason, the calibration should be done individually for each detector, to identically match their gains, before summing their signals.

The following text describes the method that was used for the calibration of Det1 for the data of Set1. The same method is used for the data of Set2 and Set3 as well as for Det2. The chosen correction model was a two-parameter model depending on the time in the decay cycle and on the SBR. As shown in the following, this is a simple phenomenological model based on observations but does not explain the physical reasons for the gain and baseline variations. First, all the cycles that have an SBR value below 5, whose statistics are too low to be analyzed properly, were excluded. Then, the rest of the cycles were sorted according to their SBR value from the lowest to the highest. Then, they were divided into 5 windows containing each the same number of cycles as shown in Fig. 3.5. For the time dependent count rate variation, the events were sorted according to their time within the cycles into 11 time intervals of 1 sec each between 3.5 sec (the start of the acquisition phase) and 14.5 sec (the end of the acquisition phase) as seen in Fig. 3.3. This selection of 5×11 sets of events allows to gather sufficient statistics per set.

For each SBR window and for each time interval, the histograms for both the total charge Q_{tot} and the baseline charge $Q_{baseline}$ were plotted. Afterward, the 59.54 keV photopeak and the baseline distribution were fitted with a Gaussian function. The interval $[\mu - \sigma;\ \mu + \sigma]$ was used as the interval for these fits, where μ is the mean value of the distribution and σ is its standard deviation (Fig. 3.6). This interval was chosen in order to reduce the effect of the superposition of the ^{6}He energy spectrum with the 59.54 keV photopeak. The mean values and their associated statistical uncertainties obtained by the fit correspond to the mean positions of the 59.54 keV photopeak and of the baseline within each SBR window and time interval. It is worth noting here, that the photopeak that was fitted corresponds to $\sim$80% of the total deposited energy, due to the fact that the other $\sim$20% of the energy is collected by the other detector's PMT. This will be accounted for later while summing the signals of the two detectors.

Figure 3.7 shows the variation of the positions of the 59.54 keV peak and baseline for the five windows of SBR for Det1. The variations shown in Fig. 3.7(a) correspond to a relative gain change of about 2%. The baseline variations in Fig. 3.7(b) correspond to a shift in energy of about 0.3 keV. The variations have the form of an exponential function:

$$g(t) = P_0 + P_1 \times e^{-t/\tau}, \tag{3.2}$$

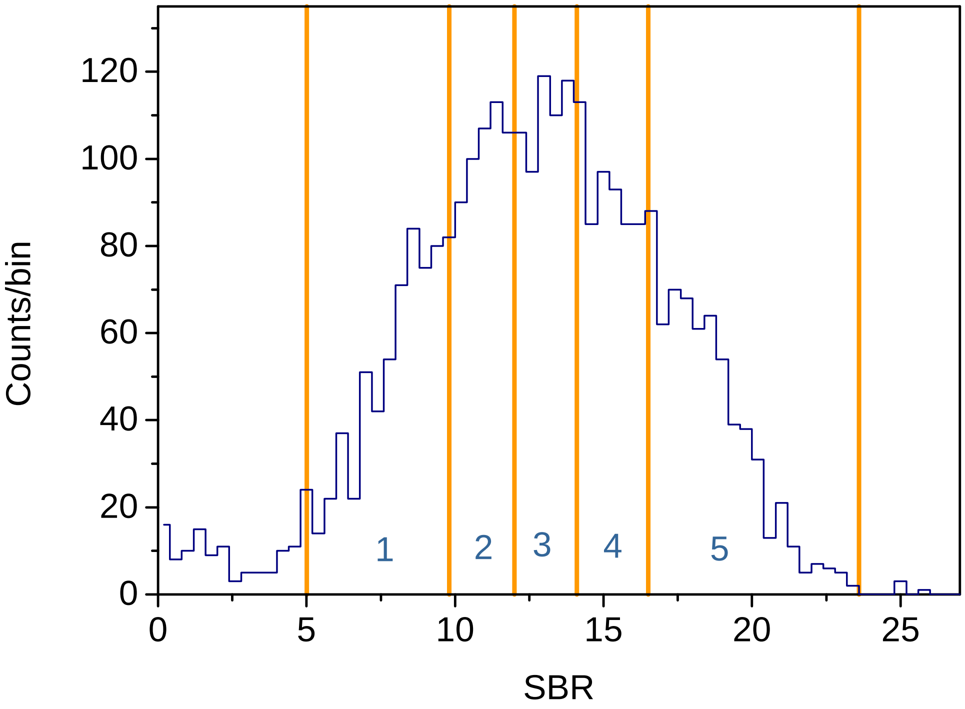

Figure 3.5: The SBR distribution for Set1. The vertical yellow lines define the five windows used for the calibration. The cycles with SBR < 5 are discarded

which was used to determine the parameters of the correction model. For the sake of simplicity, τ was assumed to be independent of SBR, while only P_0 and P_1 are functions of SBR values. For this reason, the variation plots obtained for the five SBR windows were fitted with Eq. (3.2) where P_0 and P_1 are free parameters of the fit function, and τ is fixed as a common value for the five distributions. With this fit, the values of P_0 and P_1 parameters as a function of SBR were obtained for the variations of the gain and the baseline.

This same procedure was also performed for Set2 and Set3 but with three SBR windows for Set2, and four SBR windows for Set3. This difference in the number of SBR windows is due to the different number of cycles in each set.

The values of P_0 (Fig. 3.9) and P_1 (Fig. 3.8) for each SBR window were then plotted against the mean value of each SBR window. The parameter P_1 is the most relevant one since it is the one causing the time dependence of the gain and of the baseline within the cycle. The plots of Fig. 3.9 suggest that the variation of P_1 as a function of SBR is linear for Set1, Set2 and Set3. The plots of Fig. 3.9 were thus fitted with a linear function:

$$P_1(SBR) = A \times SBR + B. \tag{3.3}$$

The higher values of P_1 are obtained for Set2, corresponding to the higher decay rates of about 21000 decays per cycle (Table 2.1). For Set1 and Set3, corresponding to decay rates of

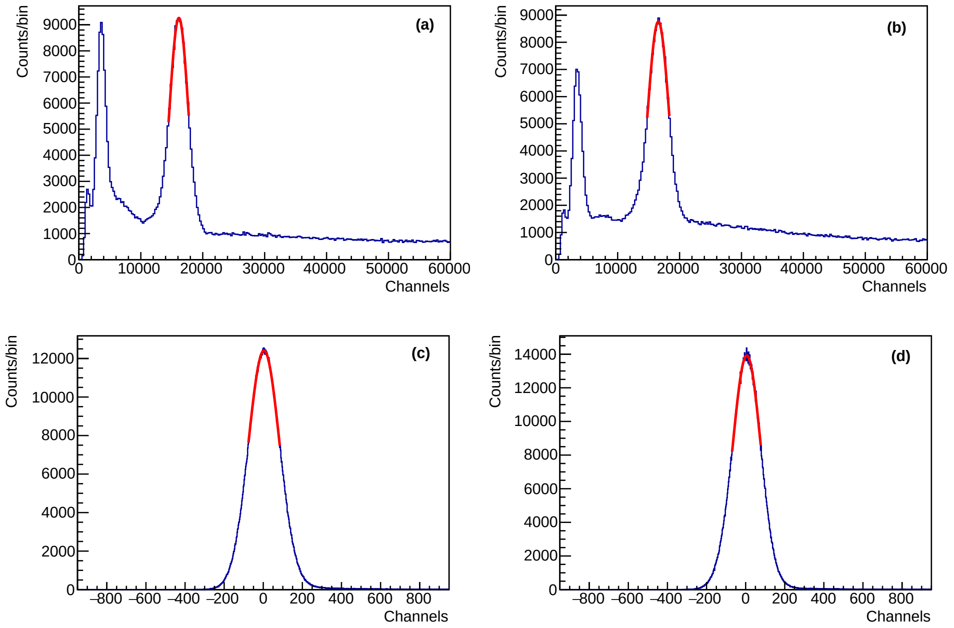

Figure 3.6: The 59.54 keV and baseline peaks and the fits used to measure their positions for two different time intervals and different SBR windows; (a) & (c): the 60 keV and baseline peaks respectively for the [3.5;4.5]s time interval and the SBR window 1. (b) & (d): the 60 keV and baseline peaks respectively for the [13.5;14.5]s time interval and the SBR window 1. The peaks below channel 10000 in (a) & (b) correspond to the ~20% collected light from energy deposition inside the other detector.

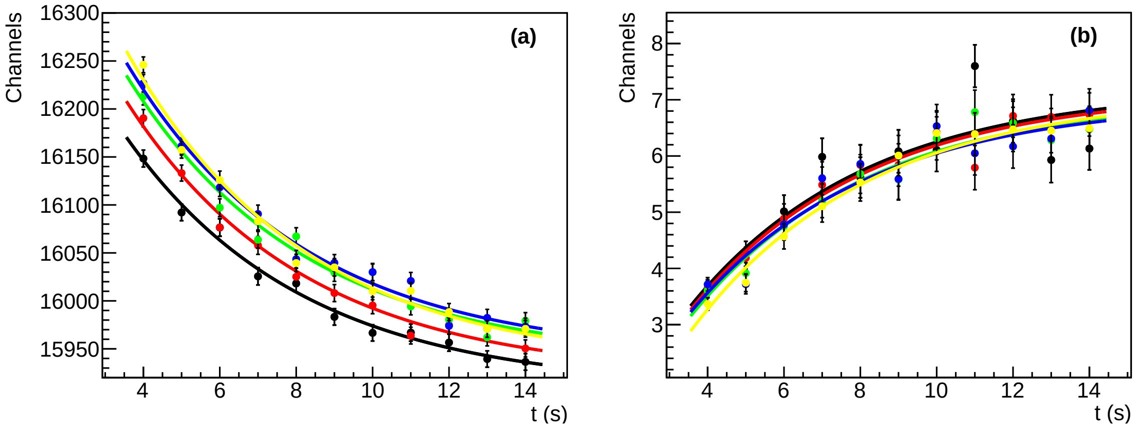

Figure 3.7: Variation of the 59.54 keV photopeak position (a) and of the baseline (b) in channels vs time *t* within the cycle, with the exponential fits used to extract the P_0 and P_1 parameters, for the 5 different SBR windows (SBR: 1-black, 2-red, 3-green, 4-blue, 5-yellow).

respectively ~6000 and ~7000, the P_1 values are similar but slightly lower than for Set3. This is most probably due to the PMT lower voltage used during Set3, leading to both a lower gain and thus a lower absolute gain variation. For the parameter P_0, Fig. 3.8 shows that the dependence on the SBR is not the same for the three sets. For Set1, P_0 was fitted with an exponential function:

$$P_0(SBR) = A + Be^{-SBR/C}, \tag{3.4}$$

and for Set2 and Set3, with a linear function:

$$P_0(SBR) = A \times SBR + B. \tag{3.5}$$

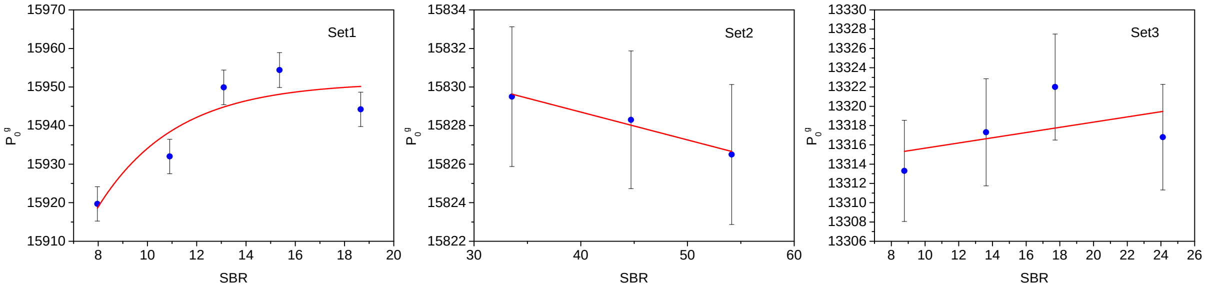

Figure 3.8: Variation of P_0^g for gain correction for the three sets of measurements.

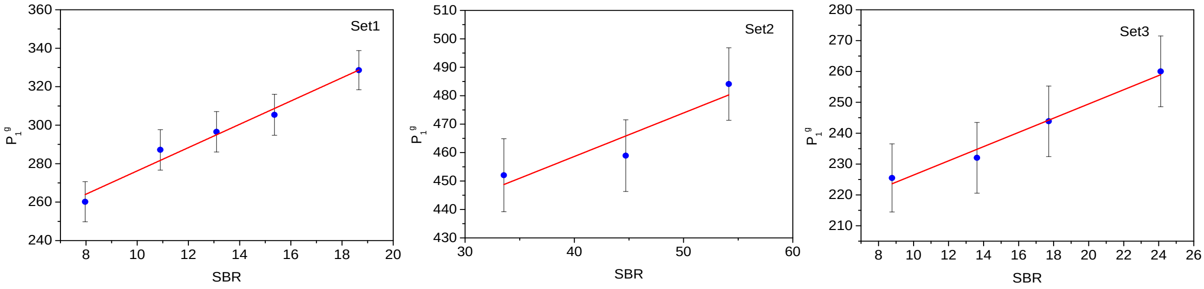

Figure 3.9: Variation of P_1^g for gain correction for the three sets of measurements.

The values of $P_0(SBR)$ and $P_1(SBR)$ were fitted for each set with the corresponding function, in order to obtain the analytical correction model used for the data calibration. For the gain and baseline variations, the correction functions are respectively:

$$C_{gain}(SBR,t) = P_0^g(SBR) + P_1^g(SBR) \times e^{-t/\tau}, \tag{3.6}$$

$$C_{baseline}(SBR,t) = P_0^b(SBR) + P_1^b(SBR) \times e^{-t/\tau}, \tag{3.7}$$

where $P_0^b(SBR)$ and $P_1^b(SBR)$ are linear functions for the three sets in the case of $C_{baseline}(SBR,t)$ (Appendix C).

In summary, Eqs. (3.6) and (3.7) describe respectively the variations of the gain and the baseline as a function of time within the cycle and of SBR for each detected event. With these two equations, the energy of each detected event, which is proportional to the integration charge Q_{tot}, can be calculated from the following expression:

$$E(keV) = 59.54 \times \frac{Q_{tot} - C_{baseline}(SBR,t) \times \alpha}{C_{gain}(SBR,t) - C_{baseline}(SBR,t) \times \alpha}, \tag{3.8}$$

where $\alpha = 306/24$ is the ratio of the baseline integration window for $Q_{baseline}$ over the total charge integration window for Q_{tot}. The calibration with Eq. (3.8) is a first order calibration for the collected events energies within each detector's PMT, using the position of the 59.54 keV photopeak as the only calibration reference.

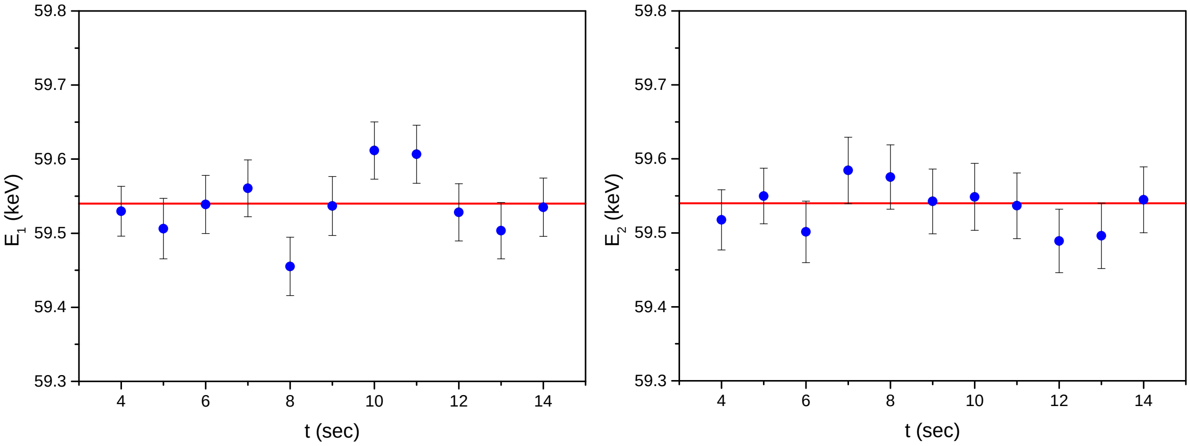

Figure 3.10: Centroïds of the 59.54 keV photopeak against time within the decay cycles after calibration with gain and baseline corrections for Det1 (left panel) and Det2 (right panel) for one run of Set1. The red line represents 59.54 keV

To test the validity of the individual gain and baseline corrections, the calibrated data of Det1 and Det2 with Eq. (3.8) were then sorted again with 11 time window selections. The 59.54 keV photopeaks were then fitted with Gaussian functions for each time selection. The values of the centroïds obtained for a one hour run of Set1 are displayed in Fig. 3.10. The results are consistent with 59.54 keV and do not exhibit the ~2% gain variation over the cycle duration shown in Fig. 3.7 anymore, proving the efficiency of the gain and baseline corrections. This calibration model was determined using all the events of a given measurement set. It does not account for slow gain variations that may occur from one run to another within the set. This slow gain variation over the sets was also determined using the average photopeak position for each run and corrected for (Appendix C). It was found to be below 1%.

3.2.3 Adding signals from both detectors

In the calibration and correction procedure described previously, the two detectors were treated independently using photopeaks where all the energy was deposited either in Det1 or in Det2 and using only the corresponding PMT signals. In the case of a ^{6}He decay, a significant part of the beta particles will deposit a fraction of the energy in one detector, scatter, and deposit the other fraction in the second detector. Even when all the energy of the β particle is deposited in only one detector, a fraction of the light will be collected by the other detector's PMT. It is thus important to sum the signals collected from both PMTs to get access to the total deposited energy. It has been shown in Chap. 2 that when energy is deposited in one of the two detectors, $\sim$80% of the collected scintillation light goes to its PMT while the other $\sim$20% goes to the other PMT. Summing the reconstructed energy from the two detectors after calibration with Eq. (3.8) would lead to an energy overestimated by about $\sim$20%. The last step of the calibration procedure consisted then into a re-scaling of the reconstructed energy. This scaling factor was again determined run by run in order to match the photopeak position with the expected 59.54 keV energy (Appendix C).

Figure 3.11 shows the 59.54 keV photopeak position against the decay time with and without applying the gain and baseline corrections for the energy calibration for Set1. The results shown in blue were obtained by fitting the photopeak after applying a complete calibration and correction model, summing the energy from the two detectors, and re-scaling for the light cross-talk. The results in orange were obtained without accounting for the dependence on the SBR and time t within the cycle. Without corrections, a $\sim$2% difference between the energy at the beginning and at the end of the decay is noticed.

The effect of the gain and baseline corrections on the extraction of the ^{6}He half-life is described in Sec. 3.5.4.2.

3.3 Other time dependent corrections

In addition to the gain and baseline variations, the two other time dependent effects that are known to affect the measurement of the half-life are the detector's dead-time and the pile-up of several signals within the same integration window.

3.3.1 Dead-time

The dead time of the detection system can be briefly defined as the smallest time difference between two consecutive signals, for which the DAQ can actually identify them as two separate individual signals. Here, the intrinsic dead-time corresponds to the length of the largest integration window which is 1 μs. The presence of this dead-time, leads to a loss of detected events. This loss of events is, in fact, time dependent, as its probability depends on the count rate. Basically, the higher the count rate, the higher the probability of having two or more events arising with a time difference smaller than the intrinsic dead-time. Therefore, this effect induces

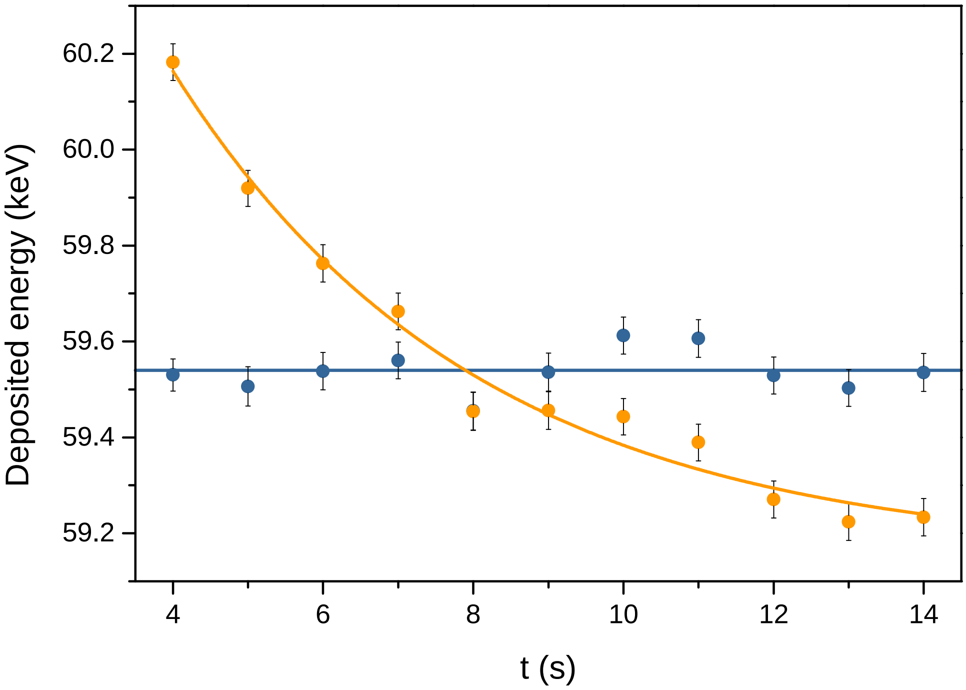

Figure 3.11: 59.54 keV photopeak position against time within the decay cycles, with and without applying the gain and baseline corrections for Set1. The blue line indicates the 59.54 keV energy and the orange one is just to guide the eyes. It is a fit of the non-corrected values with an exponential decay function.

a distortion of the shape of the detected decay scheme, since the count rate at the beginning of the cycle is exponentially higher than at the end of the cycle.

There are two types of dead-times conditions that can occur in measurements of rates [63]:

- The extensible dead-time (Fig. 3.12 (a)): An event is selected only if the time difference with any previous event is bigger than the dead-time. Therefore, each time an event is detected, the dead-time extends. In Fig. 3.12 (a), only the first and the last events produce a trigger.
- The non-extensible dead-time (Fig. 3.12 (b)): An event is selected only if the time difference with a previous event that produced a trigger is bigger than the dead-time. Thus, the dead-time between every two triggered events is fixed. In Fig. 3.12 (b), the first, the third and the fourth events produce a trigger. Therefore, using a non-extensible dead-time means keeping a higher number of events.

The DAQ system for this experiment was designed to have a non-extensible dead-time. For events selection with a non-extensible dead-time, the detected count rate can be expressed as [64]:

$$N_{DT}(t) = \frac{N_{decay}(t)}{1 + \tau_{DT} \times N_{decay}(t)}, \tag{3.9}$$

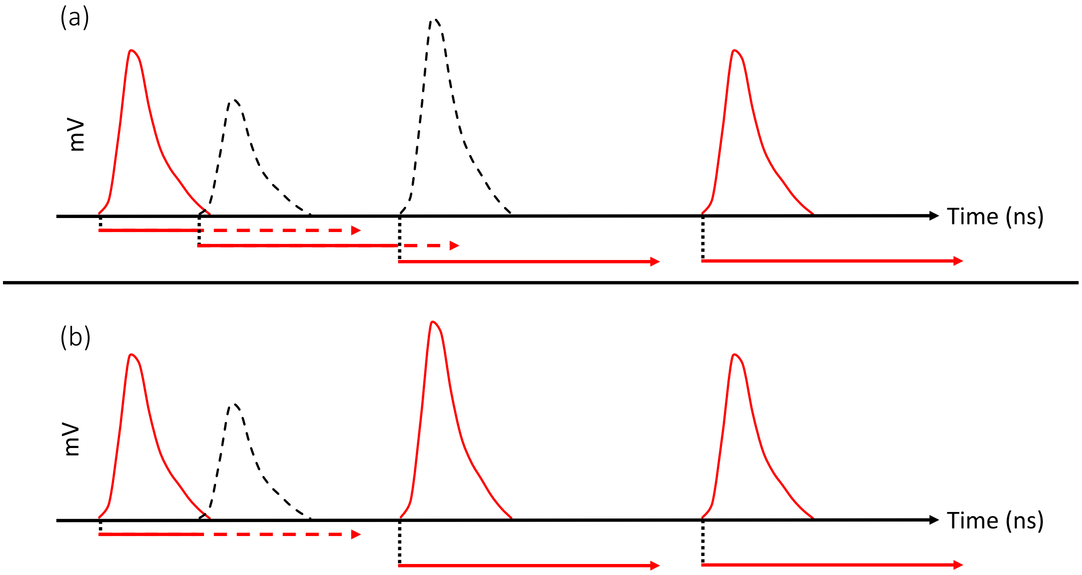

Figure 3.12: A figure showing the events selection while using an extensible dead-time (a), and a non-extensible dead-time (b). The red pulses represent the selected events, and the dotted black pulses represent the discarded events. The red arrows represent the dead-time length.

where $N_{DT}(t)$ is the detected count rate in the presence of a non-extensible dead-time, $N_{decay}(t) = N_0 e^{-t/\tau}$ is the expected detected count rate without dead-time, and τ_{DT} is the detector's intrinsic dead-time. This expression shows how the presence of the dead-time induces a time dependent change to the shape of the decay spectrum. Since the rate $N_{decay}(t)$ is larger at the beginning of the decay cycle, the relative loss of counts is also larger at the beginning of the cycle than at its end.

3.3.2 Pile-ups

Whenever two events arise simultaneously within one integration window, the pulses corresponding to those two events are piled-up and are considered as one single pulse with an integrated charge equal to the sum of the charges of the two initial signals, as shown in Fig. 3.13, where the dotted lines represent the two pulses and the red line is the resulting pile-up. The larger integrated charge and reconstructed energy due to the pile-up mean that for a selected energy threshold, the probability for a piled-up event to be above the selected threshold is higher than for a single event. Since the probability for a pile-up to occur is proportional to the instantaneous rate of detected events, it is a time dependent effect. The number of detected events as a function of time within the cycle for a selected energy threshold E in the presence of pile-ups is

$$N_{Pup}(E,t) = \frac{N_{decay}(t)}{1+\tau_{DT}\times N_{decay}(t)} \times [1+\alpha_E(t)], \tag{3.10}$$

where $N_{decay}(t)$ is the expected count rate without dead-time, τ_{DT} is the non-extensible dead-time, and $\alpha_E(t)$ is the relative rate excess of detected events as a function of time for a selected energy threshold E due to pile-ups.

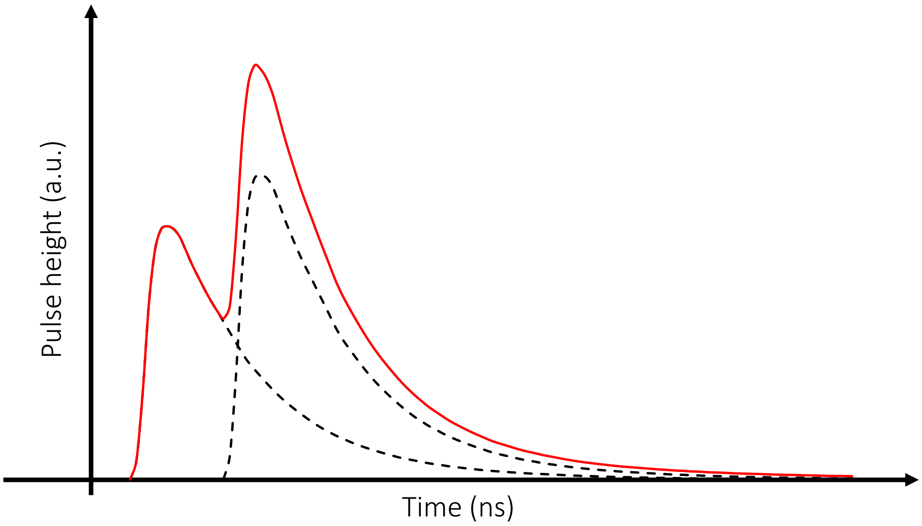

Figure 3.13: Illustration on the pile-up of two signals (the dotted black lines). The integral of the red line is the resulting charge of the pile-up.

3.4 Background sources investigation

3.4.1 Time dependent background

The presence of any background source with a decay time different from that of ^{6}He would introduce an error into the half-life estimate and the β-energy spectrum measurement. To search for such a background, the background contribution within the cycles was first assumed to be constant. This contribution is obtained by selecting the data that are recorded in the second half of the time window (Fig. 3.14). Hence, the energy spectrum of time dependent events was obtained by subtracting the background contribution from the data recorded in the first half of the time window.

Figure 3.15 shows the resulting energy spectra obtained from Set1 (nominal conditions) and Set4 (background with shutter) respectively in black and green lines. The spectrum of Set1 (the black line) shows two contributions: the full β-energy spectrum of the ^{6}He decay extending up to 3.5 MeV and a distribution with a peak at around 100 keV. This low energy peak was identified as Bremsstrahlung radiation due to β-decay of the ^{6}He$^+$ ions implanted on the third

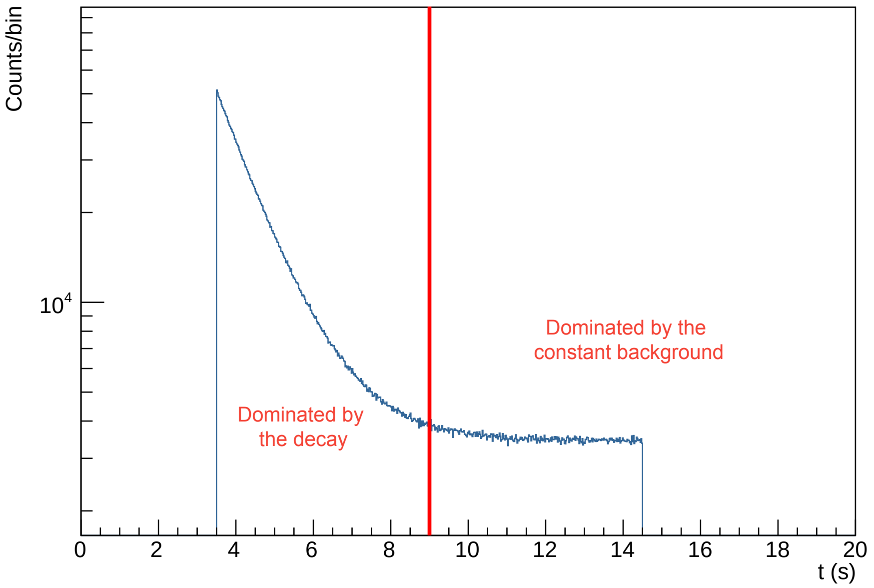

Figure 3.14: Decay rate histogram for one run of Set1. The red line represents the separation between the part of the cycle dominated by the ^{6}He decay events and the part dominated by the ambient background events.

collimator. This was confirmed by analyzing the data of Set4, which was collected using a block placed inside the collimator to prevent the direct implantation of ^{6}He on the face of the detector. The blue line represents the theoretical β-energy spectrum including the Fermi function (see discussion in Chap. 4) and convoluted with the detector's response function. The red distribution is the sum of the blue and the green spectra. The blue distribution seems to agree very well with the energy spectrum of Set1 (the black line). The decay time of the peak at 100 keV was extracted using a selection of events with deposited energies below 200 keV. It was found to be compatible with the half-life of ^{6}He, which confirms the identity of these Bremsstrahlung radiations. Bremsstrahlung events having the same time dependence as the ^{6}He events decaying at the surface of the detector, should not be a source of error for the half-life extraction. Furthermore, the relative contribution of these radiations represents less than 0.5% of the number of events associated with the ^{6}He decay on the detector for deposited energies above 500 keV. Thus, with an energy threshold of 500 keV or above, any error on the half-life measurement due to background can be safely neglected. The effect of this peak on the extraction of the Fierz term and the method used to deal with it is discussed in Chap. 4.

Another contribution was found by observing the runs of Set4 and Set5 (Fig. 3.16 left). It is a wide distribution of events between 1.5 MeV and 3 MeV, above the Bremsstrahlung peak at 100 keV. It was assigned to β particles emitted from ^{6}He nuclei implanted on the collimator's outer surface. These β particles can reach the detection volume through a hole in the lower

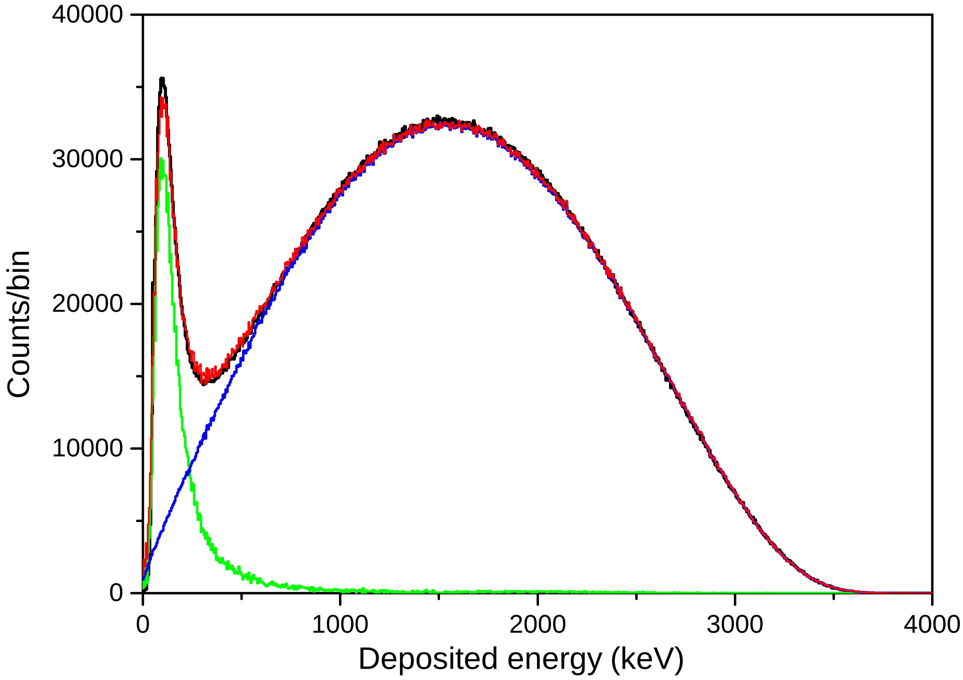

Figure 3.15: The energy spectra of Set1 (black line) and Set4 (green line) of measurements after subtracting the constant background contribution. The blue spectrum represents the theoretical β-energy spectrum including the Fermi correction and convoluted by the detector's response function. The red line is a fit of the spectrum of Set1 that combines both the blue and the green distributions. The green and blue distributions are normalized by using the parameters of the fit.

part of Det2, which leads to the YAP scintillator through the plastic PVT scintillator. The number of these events is very small and this source can't affect the half-life measurement since its detection rate is correlated to the decay rate of implanted ^{6}He$^+$ ions. The effect of this distribution on the Fierz term extraction is discussed in Chap. 4. To confirm the identity of the two contributions induced by the ^{6}He implantation on the collimator, the entire detection setup with the two detectors and the collimator attached to Det2 was built in GEANT4 (right panel of Fig. 3.16). Simulations were performed with events generated using the theoretical β-energy spectrum including the Fermi function, for ^{6}He implanted on the inner surface and on the outer surface of the collimator (respectively the orange and red areas of the right panel of Fig. 3.16). The calculated deposited energy within the two YAP scintillators in the simulations showed similar distributions as the ones obtained with Set4 and Set5 (center panel of Fig. 3.16). This confirms the origin of both the Bremsstrahlung peak at 100 keV and the distribution due to β particles emitted from the collimator. However, the simulations showed an overestimation in the number of counts assigned to electrons passing through the hole. This overestimation can be explained by the fact that in the simulations, the position of the source of events might not be perfectly identical to the position of the ^{6}He$^+$ beam implantation on the collimator. This shows that the simulations are not reliable for the subtraction of these beam induced contributions.

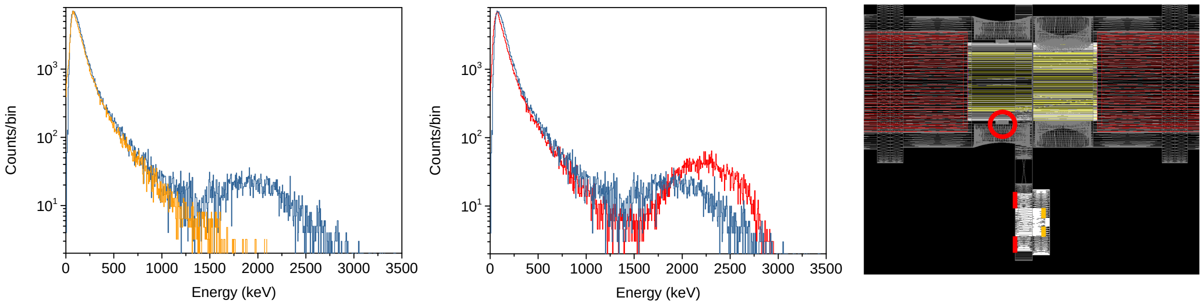

Figure 3.16: Left panel: experimental energy spectrum for one run where the ^{6}He was implanted on the collimator (blue). Deposited energy spectrum obtained by simulation for a source on the inner surface of the collimator, normalized to the experimental data (orange). Center panel: deposited energy spectrum obtained with a simulation where the source is located on the outer surface of the collimator, normalized to the experimental data (red) and experimental spectrum (blue). Right panel: drawing of the detection setup built in GEANT4. The orange and red lines represent respectively the position of the source of events on the inner and outer surface of the collimator. The red circle shows the position of the hole through which the electrons of the decay on the collimator were able to access the YAP scintillator.

3.4.2 Constant and long half-life background

This section focuses on the study of constant ambient background and long half-life (as compared to the ^{6}He half-life) sources of background. For simplicity, we will refer to this background using the term "constant background". The constant background energy spectrum is obtained by selecting events from the second half of the time window where short half-life contributions (such as from ^{6}He decay) are very small. Afterward, the energy spectrum obtained with the events of the first half of the time window, scaled by a normalization factor, was subtracted from the constant background energy spectrum. The value of the normalization factor was chosen to suppress the remaining contribution from ^{6}He decay in the constant background spectrum. It was obtained by assuming that all the events with energy above 2 MeV are solely due to ^{6}He decay. The resulting energy spectrum is shown in red in Fig. 3.17 for Set1. The black line corresponds to the spectrum obtained during dedicated background runs recorded before and after the online experiment. The first peak at 59.54 keV is due to the ^{241}Am calibration source. The photopeaks at 667 keV and 1460 keV are respectively from the ^{137}Cs source of a GANIL dose rate meter and from ^{40}K in the environment.

A discrepancy between the two spectra is observed with an excess of events below 0.6 MeV with the presence of a 511 keV photopeak. This excess of events, only observed when the beam is on, is probably caused by the presence of a β^+ emitter. This contaminant was not clearly identified, and its half-life was found to be too long to be measured within the cycle's duration. However, by selecting events with deposited energy between 150 keV and 600 keV, where this background dominates, one can study its time dependence over the second half of the decay cycles of Set2. This study did not allow us to determine its half-life but led to setting a minimum value for the half-life (90% CL) of $\sim$ 330 sec, which is very large in comparison

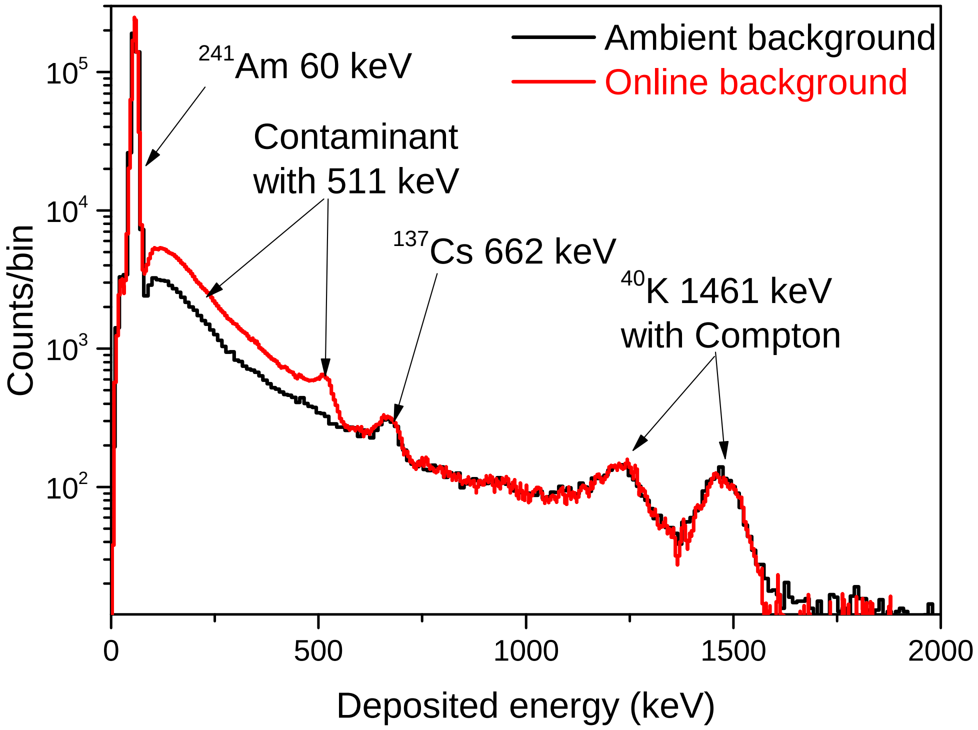

Figure 3.17: Energy spectrum for the ambient background (black line) and the background with long half-life that was recorded online (red line). The red line was normalized to the black line by using the ^{241}Am 59.54 keV photo-peak.

with the half-life of ^{6}He ($\sim$0.8 sec). The contribution of this unknown source of background corresponds only to 1.6% of the total β-decay events, and it can be fully suppressed by using an energy threshold of 0.6 MeV. The ambient background contribution is constant, thus it does not have any impact on the ^{6}He half-life extraction.

3.5 Half-life determination

The fact that each event was recorded with a 2 ns precision time stamp in addition to the charges obtained for four integration windows, gives a nice control on all potential systematic effects. This control resides in the ability to study those effects offline by changing either the dead-time or the energy threshold in the analysis. The half-life determination was performed using two different methods. The first is a cycle-by-cycle analysis. It consists in fitting the raw data of each cycle with a fit function accounting for the time dependent corrections due to dead-time and pile-up. The final half-life was then calculated from a weighted average of the results obtained for each individual cycle. The second is based on a weighted events analysis, where the events of all the cycles are weighted to account for the dead-time and pile-up effects. The histogram of the sum of weights as a function of time within a cycle will be then fitted with a simple decay function. The two methods should provide consistent results.

3.5.1 Offline events selections

With the acquisition configuration used for the detection setup, one can distinguish between two types of events: 1) the coincidences, coming from energy deposition inside one or more scintillators and producing enough light to trigger almost simultaneously (within a 200 ns window) the two acquisition channels of the PMTs, and 2) the singles, most probably generated by electronic noise or a very low deposited energy, triggering only one of the PMTs. When it comes to event loss due to the intrinsic non-extensible dead-time τ_{DT}, one must consider the presence of all the single and coincidence events. Figure 3.18 shows how events are either kept or lost due to the intrinsic dead-time of the acquisition, taking into account two independent detectors. Whenever an event has enough energy to trigger one of the PMTs at least, a time reference is set at the detection time of this event. Any event arriving with a time difference smaller than τ_{DT} is being skipped. The next detected event is the first one arriving with a time difference larger than τ_{DT} either if it is a single or a coincidence event. The events lost due to the dead-time must be accounted for in the half-life measurement. However, since it is not energy dependent, it has absolutely no effect on the shape of the β-energy spectrum. To correctly account for the loss of events due to dead-time, one has to consider the raw data without any offline cut that could modify the real rate of events triggering the detector channels.

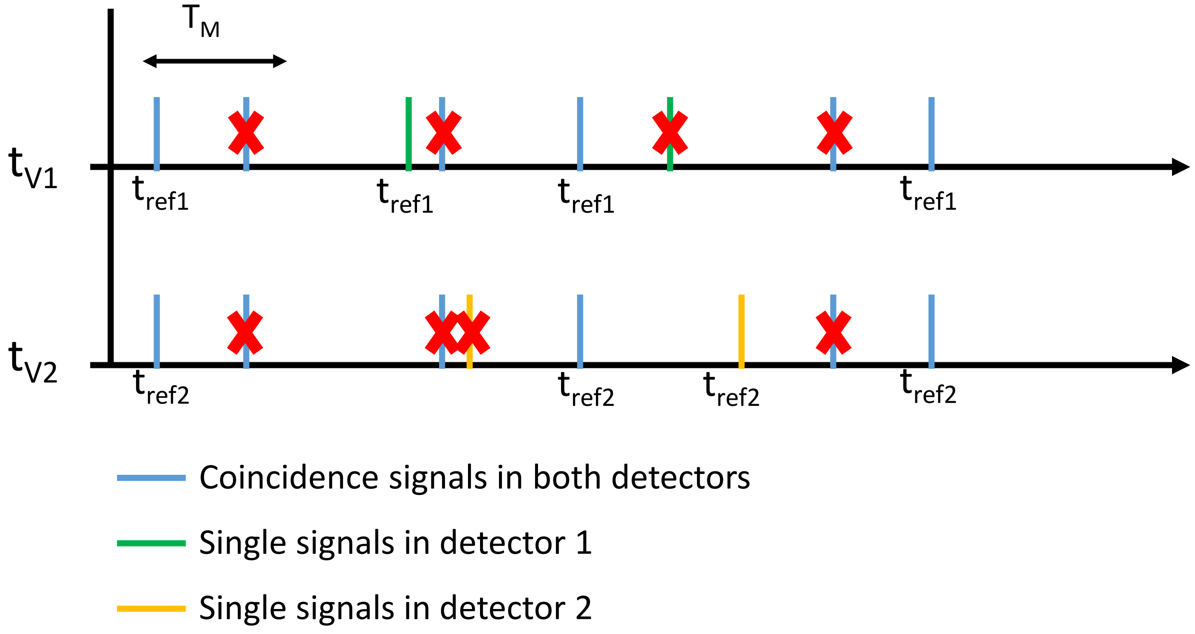

Figure 3.18: Sketch showing the selection of events using a non-extensible dead-time with two independent detectors.

As discussed earlier, the intrinsic dead-time τ_{DT} for the two PMT channels is 1 µs. This value cannot be reduced but it can be increased offline in order to reject spurious effects such as after-pulses or study the robustness of the dead-time correction. With the precise time-stamped events recorded by the DAQ system, the data were thus filtered offline by imposing several dead-times τ_{DT} ranging from 1 to 7 µs, using the procedure shown in Fig. 3.18. For the study of possible bias due to background contributions or imperfections of the gain and baseline corrections, several offline energy thresholds, ranging from 100 keV to 1200 keV, were also applied to the data.

3.5.2 Cycle-by-cycle analysis

The measurement of the half-life with a cycle by cycle analysis consists in fitting each decay cycle with a fit function accounting for all the time dependent corrections, in order to extract a half-life value for each cycle. The final half-life value for a given measurement set will then be obtained from the weighted average of the fit results of all cycles within the set.

3.5.2.1 Dead-time correction

The total instantaneous rate of events that could potentially trigger the PMT channels, at a time t within the decay cycle i in the presence of a constant background is expressed as:

$$r_T(t)_i = r_{0_i} e^{-t/\tau_i} + r_{b_i}, \tag{3.11}$$

where r_{0_i} is the total initial decay rate, τ_i is the decay lifetime and r_{b_i} is the total rate of the constant background. In the presence of a non-extensible dead-time τ_{DT}, the detection rate becomes [64]:

$$r_D(t)_i = \frac{r_T(t)_i}{1 + \tau_{DT} r_T(t)_i}, \tag{3.12}$$

where $\tau_{DT} r_T(t)_i$ represents the probability to miss an event as a function of time within a cycle i because of dead-time. The parameters r_{0_i}, τ_i and r_{b_i} were obtained by fitting the rate of detected events within each cycle with Eq. (3.12) (Fig 3.19), without any offline energy threshold. This first step is very important as it provides the parameters for $r_T(t)_i$ which enters the dead-time correction. This procedure must be applied for all the different imposed dead-time values used in the offline analysis.

3.5.2.2 Pile-up correction

By applying an energy threshold, labeled E_j, to the data, the total instantaneous rate of detected events given in Eq. (3.12) becomes:

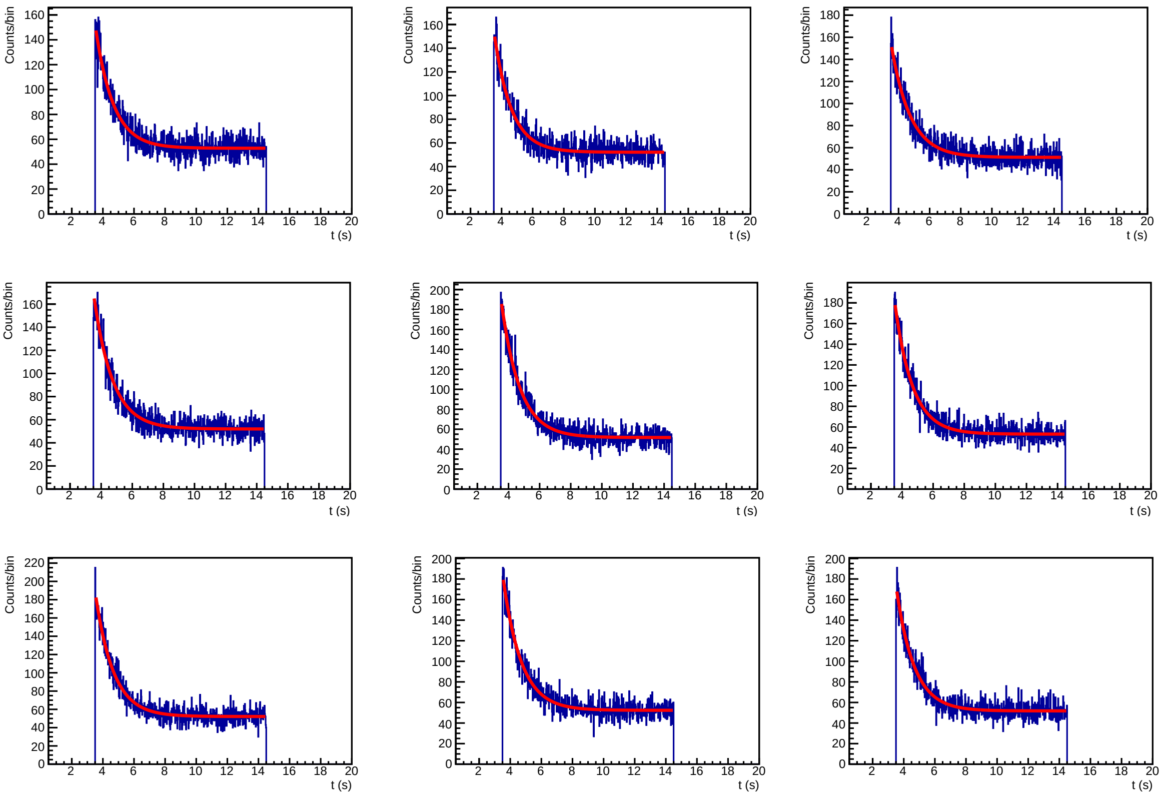

Figure 3.19: Decay histograms for several cycles of Set1, obtained by selecting all the recorded events with no offline energy threshold. The red lines represent the fit of each cycle with Eq. (3.12).

$$r_D(t)_{ij} = r_D(t)_i \cdot P_E(t)_j, \tag{3.13}$$

where $P_E(t)_j$ is the probability for an event to have an energy above the applied energy threshold E_j. This probability is mainly independent of time. However, it becomes time dependent in the presence of pile-up. The pile-up of two or more events within the same integration window leads on average to a larger reconstructed energy than for a single event, increasing thus the probability to cross the energy threshold. Therefore, the probability for an event to have an energy above the threshold is rate dependent, and thus time dependent. The presence of pile-up increases the number of detected events for a selected energy threshold E_j larger than zero. This excess of events is larger for higher count rates, resulting in an underestimation of the half-life if not properly corrected.

The instantaneous probability for two decay events to occur within the same integration window for each cycle is given by:

$$P_{\text{pu}}(t)_i = r_{0i} e^{-t/\tau_i} \Delta T, \tag{3.14}$$

where r_{0i} and τ_i are the parameters defined in Eq. (3.11) and $\Delta T = 300$ ns is the length of the total charge integration window (Q_{tot}).

The probability for three or more events to be found in the same integration window is very small, and its effect was estimated to be in the order of 10^{-7} s and hence negligible for the present measurement. Only the two-event pile-up hase a significant effect on the half-life determination. This effect is induced by the excess of events due to the difference between the probabilities to cross the energy threshold for two events pile-up, d_j, and for a single event, s_j. The excess of detected events due to pile-ups as a function of time can be written as:

$$r_E(t)_{ij} \approx P_{\text{pu}}(t)_i \cdot (d_j - s_j).r_{0i}e^{-t/\tau_i} \tag{3.15}$$

Both d_j and s_j are time independent probabilities. The probability for a single event to pass the energy threshold, s_j, is calculated by using the ^{6}He deposited β-energy distribution (Fig. 3.20). It is equal to the ratio between the integral of the spectrum beyond E_j and the integral of the entire spectrum.

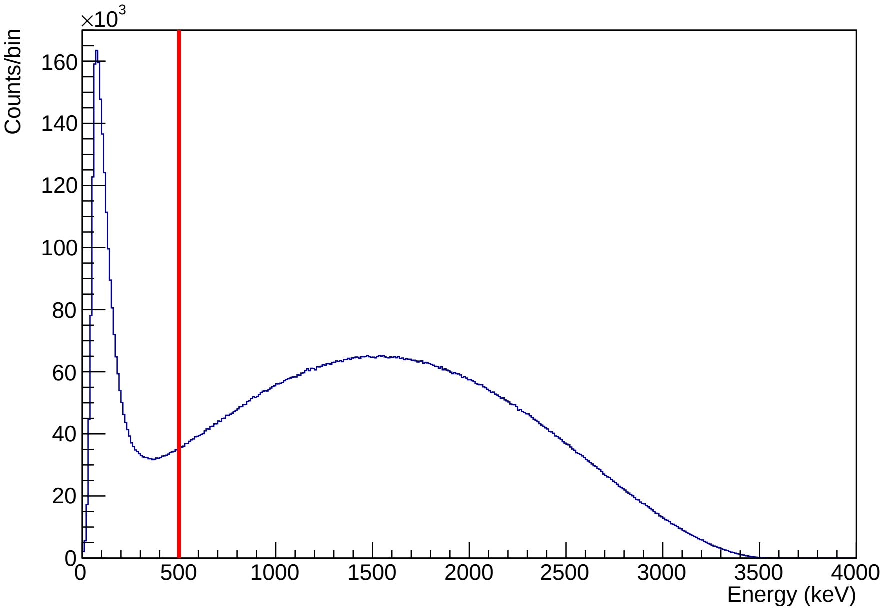

Figure 3.20: Deposited energy spectrum obtained for a one hour run of Set1. The red line represents an imposed energy threshold at 500 keV.

When it comes to the probability of a pile-up of two events to pass the energy threshold d_j, it was calculated with the following procedure. First, a typical PMT signal was generated by calculating the mean oscilloscope waveform of several thousands of signals which were saved in the oscilloscope runs. This PMT signal was then shifted in time from zero to 300 ns within the 300 ns integration window and the fraction of the charge R_I within this integration window was calculated. The charge fractions and corresponding delays are given in Table 3.1.

Arrival time (ns)	0	212	244	258	268	276	282	286	290	296	300
R_I	1	0.9	0.8	0.7	0.6	0.5	0.4	0.3	0.2	0.1	0

Table 3.1: Fraction of the charge of the second signal in the integration window and delay between the first and the second signal.

Afterwards, for each R_I, the probability for the corresponding pile-up event to be above the energy threshold E_j was calculated. This was done by using the convolution of the deposited energy spectrum of ^{6}He decay events with the same spectrum scaled by R_I (Fig 3.21).

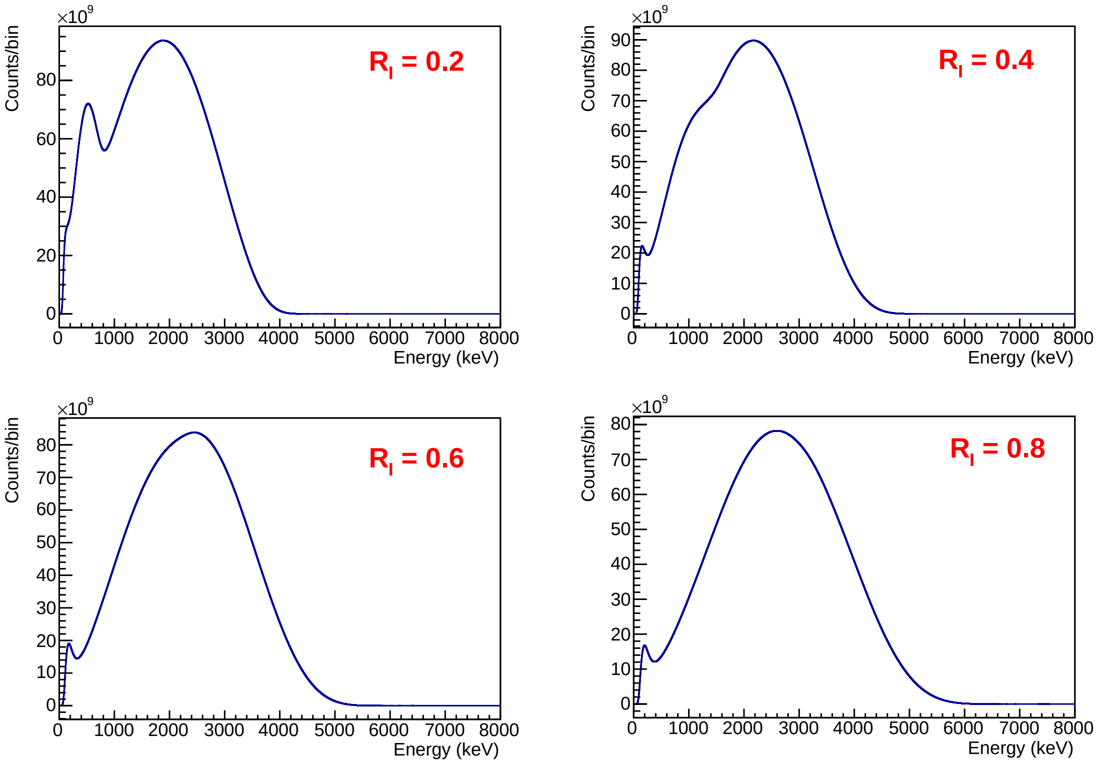

Figure 3.21: Spectra obtained by convoluting the experimental ^{6}He β-energy spectrum obtained within a 1 hour run of Set1 with the same spectrum scaled by the charge fraction R_I for several values.

Using these convolution spectra, the probability of the pile-up for each R_I to be above the selected energy threshold was obtained by calculating the ratio of the integral of the spectrum above the energy threshold E_j and the integral of the entire spectrum. Those values are plotted against the time of arrival of the second signal relative to the first one (Fig. 3.22). Finally, The mean probability for a pile-up event to cross the energy threshold, d_j, is obtained by calculating the integral covered by those values and normalized by the integration window length.

The expected rate of events without pile-up contribution is expressed as:

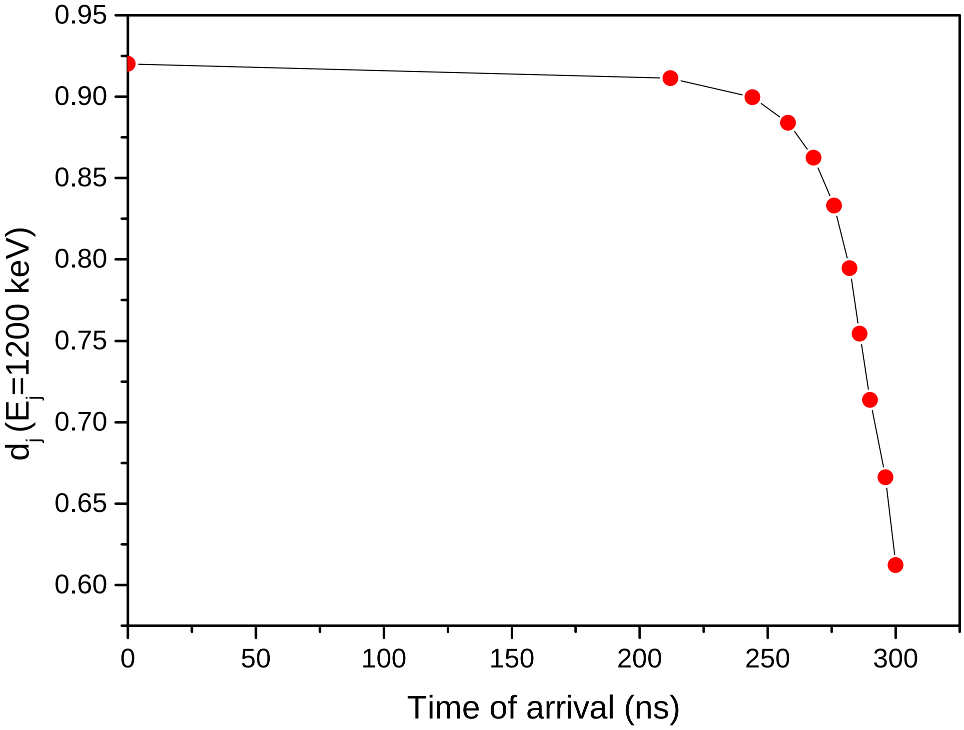

Figure 3.22: The probability of a pileup event to be above the energy threshold (1200 keV in this example) against the time of arrival of the second signal relative to the first one.

$$r_R(t)_{ij} = s_j r_{0i} e^{-t/\tau_i} + b_j r_{bi}, \tag{3.16}$$

where b_j is the time independent probability for background events to be above the threshold. b_j was obtained by using the deposited energy spectrum of background events (Fig 3.17). The relative excess of detected events due to pile-ups as a function of time within the cycle is then given by:

$$\alpha_E(t)_{ij} = \frac{r_E(t)_{ij}}{r_R(t)_{ij}}. \tag{3.17}$$

Finally, the function that describes the detected rate of ^{6}He decay events in a cycle for a non-extensible dead-time τ_{DT} and for an imposed energy threshold E_j is expressed as:

$$f_{ij}(t) = \frac{(A_{ij} \cdot e^{-t/\tau_{ij}} + B_{ij})[1 + \alpha_E(t)_{ij}]}{1 + \tau_{DT} \cdot r_T(t)_i}, \tag{3.18}$$

where A_{ij} and B_{ij} correspond respectively to the initial rate of ^{6}He decay events at the beginning of the cycle and the rate of background events in the cycle for an imposed energy threshold E_j.

3.5.2.3 Fit of the cycles

The fit procedure for each cycle comprehends three steps. First, the rate of detected events prior any energy threshold selection $r_T(t)_i$ was obtained by fitting each cycle without any applied energy threshold (Fig 3.19), with Eq. (3.12) where r_{0_i}, τ_i and r_{b_i} are free parameters of the fit function. The few cycles for which the fit was not able to converge properly (this was assessed by monitoring the χ^2 values of the fit) were discarded. Those represent less than 0.2% of the total number of cycles. Then, the excess rate of events due to pile-ups for every single cycle was estimated using the calculated probabilities d_j, s_j and b_j for the selected energy threshold E_j. Finally, the decay histogram for each cycle while imposing the selected τ_{DT} and E_j was built.

In the following, we discuss the fit procedure of the data with an imposed dead-time of 3 μs and an energy threshold E_j = 600 keV. The decay histogram for each cycle within each measurement set was built using the selected conditions on the data by selecting only the coincidences events. Afterwards, each cycle was fitted with Eq. (3.18), where A_{ij}, τ_{ij} and B_{ij} are free parameters of the fit function (Fig. 3.23). The fit was performed between 3.5 sec and 14.5 sec (29.5 sec for Set2) of each cycle, covering the whole acquisition phase.

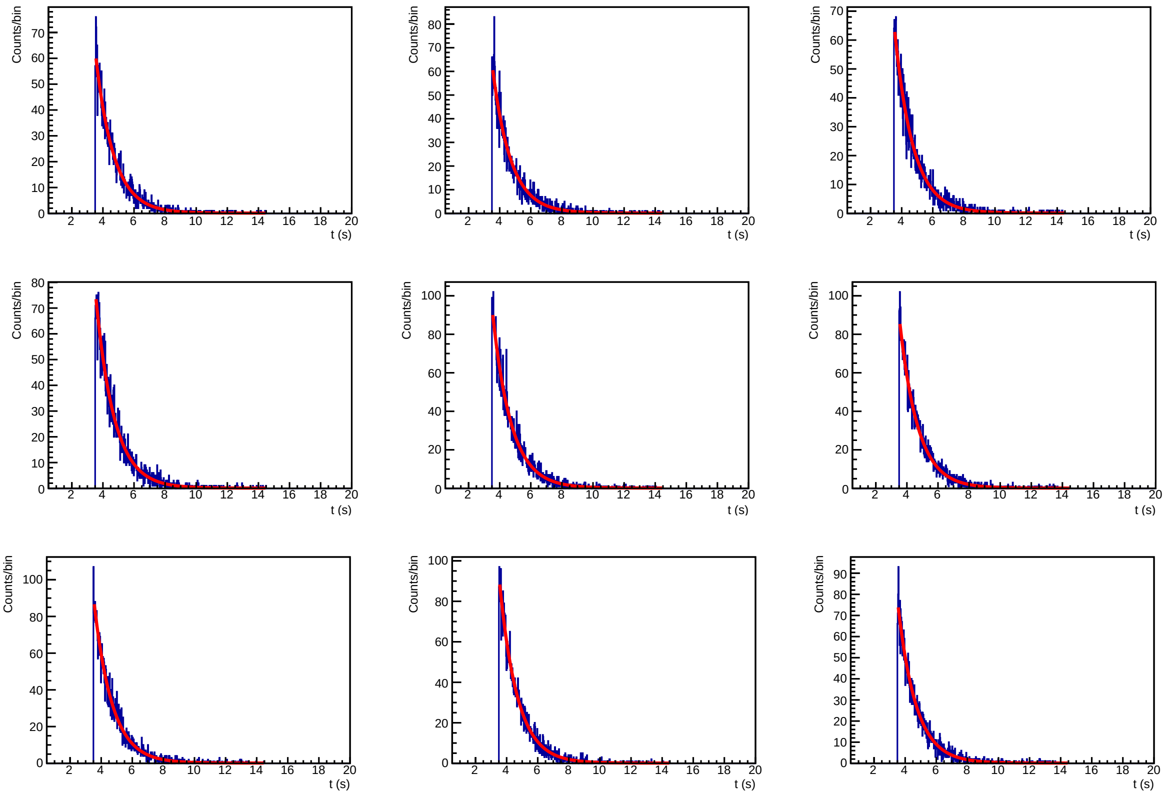

Figure 3.23: The decay histograms for several cycles of Set1. The red lines represent the fit with Eq. (3.18).

The goodness of the fit was tested by monitoring the obtained χ^2 values for each cycle. The distribution of χ^2 values shown in Fig 3.24 for Set1 shows that the values are well centered around the number of degrees of freedom "NDF" value. The study of p-values as well showed that the observed distribution of χ^2 is fully consistent with statistical fluctuations. The results of the fits for the two other sets showed similar χ^2 distributions.

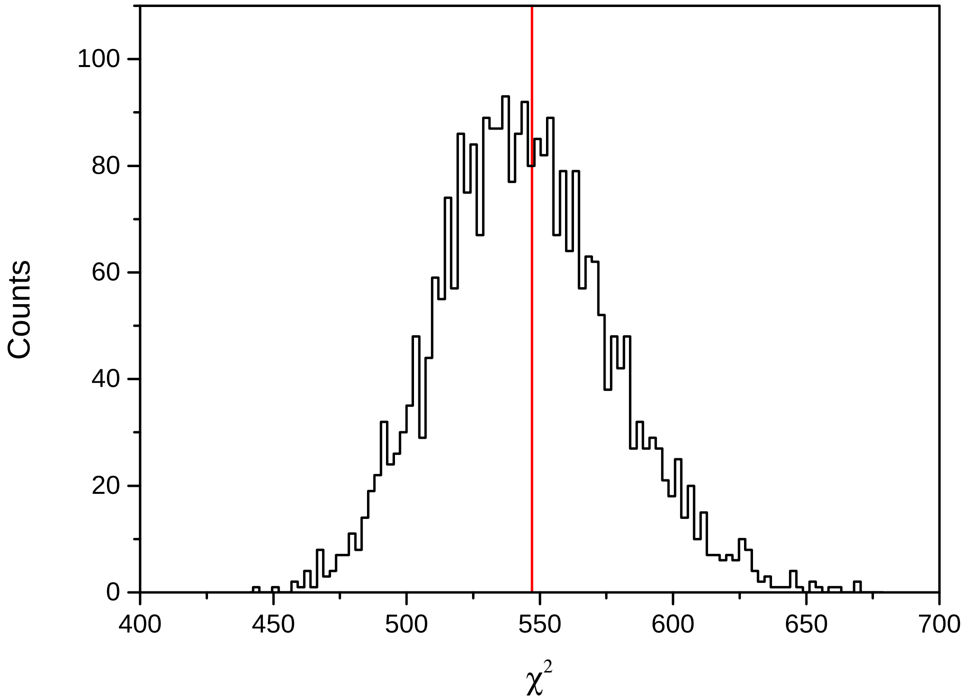

Figure 3.24: The χ^2 distribution for the fits of the cycles of Set1. The red line represents the number of degrees of freedom (NDF).

3.5.2.4 Test of the cycle-by-cycle analysis using MC simulations

The main problem with the analysis described above resides in the very low statistics recorded in each cycle, as shown in Fig. 3.19. For example, Set1 comprises 3050 cycles with an average number of decay events per cycle of only 6130. To check the validity of the cycle-by-cycle analysis method with a large number of cycles and low statistics in each cycle, Monte-Carlo simulations were performed. Three sets of 10000 statistically independent decay histograms were generated using the decay exponential distribution of Eq. (3.11) with a value of τ_i corresponding to the half-life obtained in Ref. [1]. For the three sets of MC simulations, the parameters r_{0_i} and rb_i were chosen so as to correspond to the mean values of the decay rates and background rates obtained for Set1, Set2, and Set3. In parallel, another histogram was generated with the total number of events of all the 10000 generated cycles for each of the three sets. Finally, all histograms were fitted with the exponential decay function of Eq. (3.11) with

$r0_i$, rb_i and τ_i as free parameters.

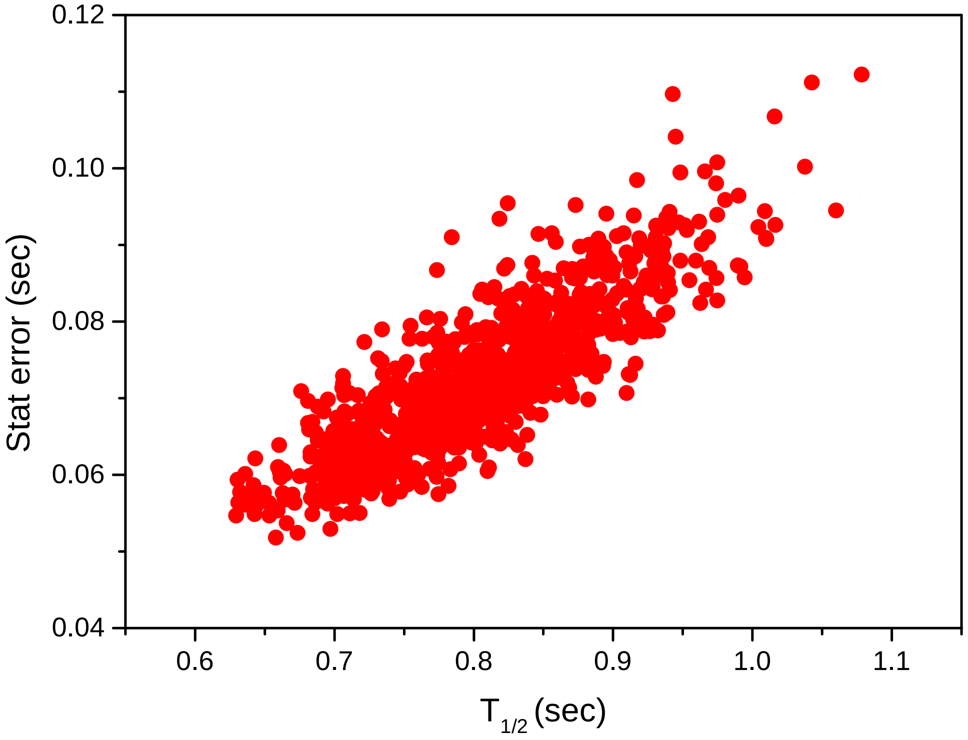

Figure 3.25: Statistical uncertainties against the half-life results for the fits of 1000 statistically independent decay histograms built using a Monte-Carlo simulation.

Many observations were made out of these fits. First, the half-life value obtained by the fit of the high statistics histogram was in agreement with the input value. Then, for the fits of the histograms with low statistics, the calculated weighted average was significantly lower than the input value. Considering this bias, the half-life values obtained from the fits of the low statistics histograms were plotted against their associated statistical uncertainties (Fig. 3.25). An unexpected linear correlation was observed between the resulting half-life values and their associated errors. As all cycles should have the same statistical weight, this correlation leads to a bias favoring fit results with a lower error and thus a lower half-life. However, this bias can be easily suppressed by using the inverse of the relative error (the ratio of the obtained half-life and its associated error) for the weighting of the half-life values when calculating the final weighted average. Using the relative error, the weighted average for the half-lives obtained by the fits of the low statistics histograms was calculated again. A significant improvement in the obtained half-life value was noticed for the three sets. However, the calculated weighted average showed an over-estimation by 9×10^{-5} s for the cycles with statistics similar to those of Set1 and Set3, and by 1.5×10^{-5} s for those of Set2. These biases are relatively small but not negligible. The cycle-by-cycle analysis can thus lead to a small systematic error due to the weighting and fitting procedures. Therefore, the Monte-Carlo simulations are crucial to account for this error.

3.5.2.5 Weighted average calculation

The half-life values and their associated statistical uncertainties were obtained from the fit of each cycle. The mean value of the half-life results and its associated statistical uncertainty for each set of measurements was calculated by the weighted average and weighted error as follows:

$$\begin{aligned} T_{1/2} &= \frac{\sum_{i=1}^{N} \omega_i T_i}{\sum_{i=1}^{N} \omega_i}, \\ \Delta T_{1/2} &= \sqrt{\frac{\sum_{i=1}^{N} T_i^2}{\sum_{i=1}^{N} \omega_i}}, \\ \omega_i &= \left[\frac{T_i}{\Delta T_i}\right]^2, \end{aligned} \tag{3.19}$$

where N is the number of cycles within each set of measurements, T_i is the obtained half-life value for each cycle, ΔT_i is the statistical error obtained by the fit, and ω_i is the associated weight given for each obtained half-life value. The inverse of the relative error was used to weight the half-life results in order to account for the correlation that was observed between the half-life results and their associated statistical uncertainties (Fig. 3.25). The obtained half-life results for an imposed energy threshold $E_j = 600$ keV and a non-extensible dead-time $\tau_{DT} = 3$ µs, for the three sets of measurement are displayed alongside their statistical uncertainties in Table 3.2.

	Set (1)	Set (2)	Set (3)
$T_{1/2}$ [ms]	807.41(25)	807.23(26)	807.14(34)

Table 3.2: Values of the ^{6}He half-life calculated by the weighted average of the half-life values obtained by the fits of each cycle, and corrected to account for the overestimation of the weighted results.

The results showed in Table 3.2 are corrected to account for the overestimation of the weighted results by 9×10^{-5} s for Set1 and Set3, and by 1.5×10^{-5} s for Set2.

3.5.3 Sum of weighted events analysis

The second method to extract the half-life from the experimental data is fully described in Ref. [48]. It consists in doing quite the opposite of what was done in the cycle-by-cycle analysis. Instead of fitting the raw data cycle by cycle with a fit function that accounts for the presence of dead-time and pile-ups, every single event was given a weight that accounts for these two effects, which is:

$$w(t)_{ij} = \frac{1+\tau_{DT}r_T(t)_i}{1+\alpha_E(t)_{ij}} \tag{3.20}$$

In order to simplify the explanation, a label k is introduced to express the use of a given dead-time value. Therefore, the associated weight for each event expressed in Eq. (3.20) becomes $w(t)_{ijk}$. Otherwise, to summarize the procedure, the instantaneous rate of detected events $r_T(t)_i$ and the rate excess of events due to pile-ups $\alpha_E(t)_{ij}$ for each cycle were calculated using exactly the same procedure as for the cycle-by-cycle analysis. Afterward, every single event in a measurement set was given a weight corresponding to its cycle i, the energy threshold E_j and the imposed dead-time τ_{DT}. Those events were then accumulated and binned into one histogram. The weighted number of counts in each bin corresponds to $n(t)_{jk} = \sum_i w(t)_{ijk}$ and the statistical uncertainty associated to each bin is $\sigma^2_{jk} = \sum_i w^2(t)_{ijk}$, where the sums run over the cycles and also overall events within each cycle. Afterward, the weighted data was fitted with an exponential decay function accounting for the presence of a constant background. The fit function can be expressed as follows:

$$f(t)_{jk} = A_{jk}e^{-t/\tau_{jk}} + B_{jk}, \tag{3.21}$$

where A_{jk} is the initial number of decay counts, τ_{jk} is the decay lifetime and B_{jk} is the present constant background. The three parameters A_{jk}, τ_{jk} and B_{jk} are free parameters of the fit function. The same conditions for the beginning and the ending time of the fit, applied for the cycle-by-cycle analysis, were used as well for this analysis.

Figure 3.26 shows the corrected decay histogram for Set2 with an imposed dead-time of 3 µs and an energy threshold of 600 keV, alongside the fit applied to the histogram (the red line) and the calculated standard residuals for each bin. It can be deduced from the standard residuals distribution that the weighting of events has been corrected accurately for the dead-time and pile-up effects.

	Set (1)	Set (2)	Set (3)
$T_{1/2}$ [ms]	807.42(25)	807.16(26)	807.10(35)
p-value	0.70	0.83	0.25

Table 3.3: Values of the ^{6}He half-life obtained from the fits of histograms for the three data sets along with their associated p-value.

The obtained values of half-life alongside their associated statistical uncertainties and their associated p-values for the three sets of measurements are displayed in Table 3.3. The results shown in Table 3.2 and in Table 3.3 shows that the two analysis gives approximately the same values. In addition, the results obtained for the three sets are statistically compatible with differences smaller than 1σ. Because of the lack of understanding of the causes behind the bias

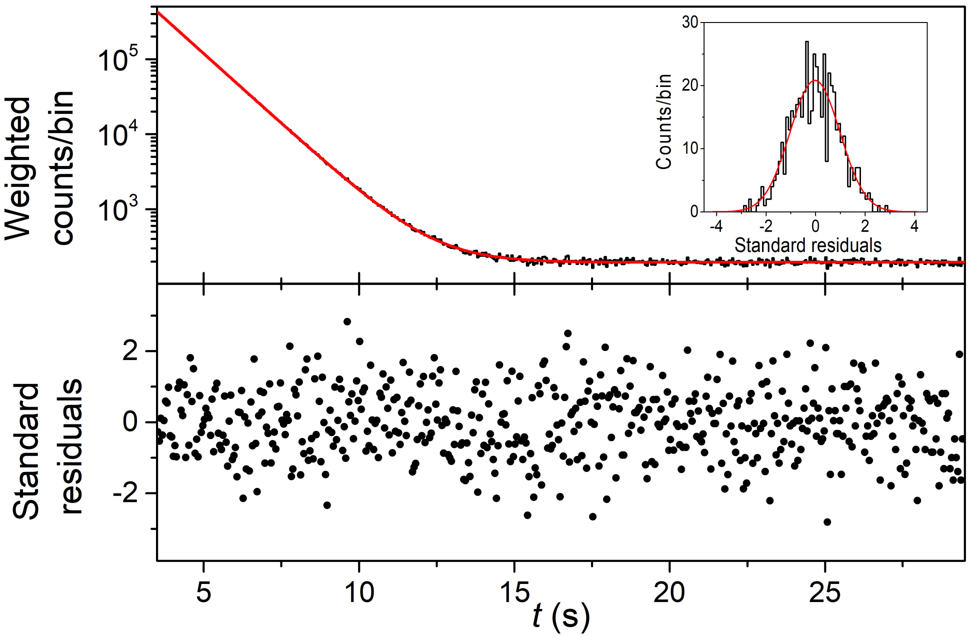

Figure 3.26: Upper panel: experimental decay spectrum from set (2) for a non-extensible dead time of 3 μs and an energy threshold of 600 keV (black) along with its fit function (red). Lower panel: standard residuals. The standard residuals distribution and its fit by a Gaussian are shown in the insert of the upper panel.

of the cycle-by-cycle method, we chose the "sum of weight" method for the rest of the analysis that is discussed in the following sections.

3.5.4 Systematic effects study

For the study of systematic effects involved in the half-life measurement, several data selections were made. For instance, seven imposed dead-times τ_{DT} ranging from 1 to 7 µs and twelve energy thresholds E_j ranging from 100 keV to 1200 keV were used. For each selection, the decay events were weighted with the corresponding weight accounting for the selected dead-time value and the selected energy threshold.

3.5.4.1 Dead-time selection effect

Figure 3.27 shows the obtained half-life values as a function of the imposed dead-time τ_{DT} for the three sets of measurement, while applying three energy threshold selections on the data (300, 600 and 900 keV). For the three sets, a small deviation for τ_{DT} = 1 µs can be noticed, but for values of 2 µs and above, the results are stable. This deviation can be explained by the presence of after-pulses in the 1-2 µs interval that was actually observed when looking at the recorded oscilloscope frames. The systematic uncertainty on the dead-time correction is obtained from the 2 ns resolution of the signals time stamp. This uncertainty is estimated to be smaller than 10^{-5} sec for the three sets.

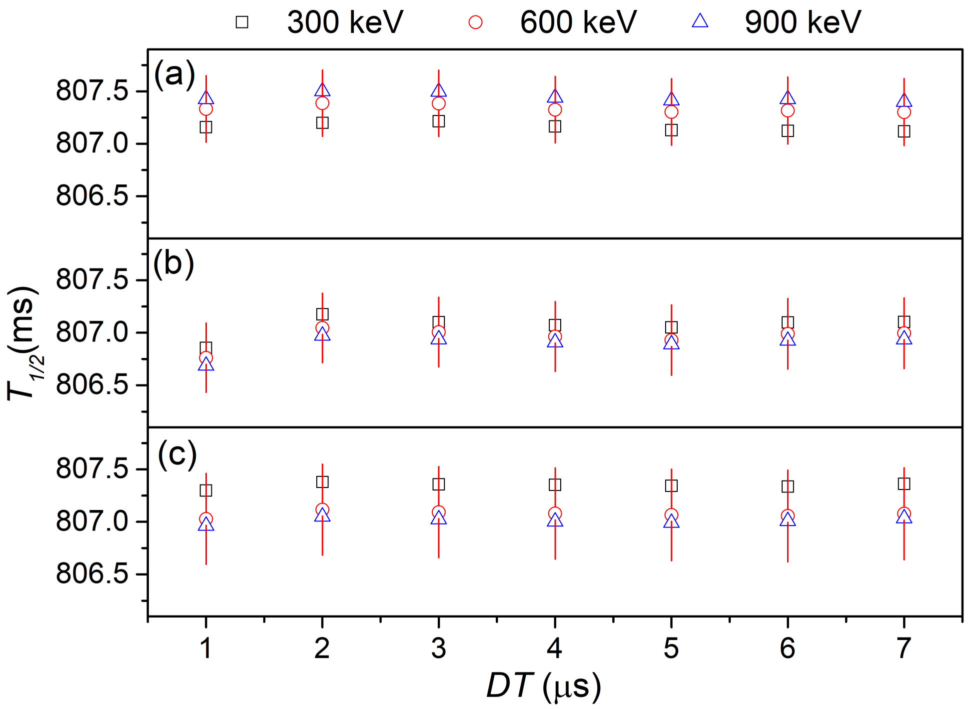

Figure 3.27: The measured half-life estimate for the three sets of measurements against the non-extensible dead-time: (a): Set1, (b): Set2 and (c): Set3. The black squares, red dots and blue triangles correspond respectively to offline energy thresholds of 300 keV, 600 keV and 900 keV. The statistical error bars for the 600 keV threshold are also plotted.

3.5.4.2 Gain and baseline corrections effect

An imperfect gain or baseline correction leads to an imperfect energy threshold selection, which induces a bias in the half-life estimate. This can be tested by monitoring the obtained half-life values for several threshold selections.

Figure 3.28 illustrates the half-life estimate as a function of the offline energy threshold selections between 100 keV and 1200 keV for the three sets of measurements. The blue dots represent the half-life values with gain correction, while the yellow dots are those without gain correction. The error bars represent the statistical uncertainty for each estimate, and the gray lines are the systematic uncertainty on the gain correction. This plot is a perfect way to check the validity of the gain correction. A bad gain correction will result in energy threshold dependent half-life values. This can be noticed clearly in the plot, where the corrected results seem to be quasi-independent of the threshold. By contrast, a clear dependence on the threshold is evidenced for the values with non-corrected gain, where the results appear to decrease as the selected threshold increases. The systematic uncertainties associated with the gain correction are presented by the gray lines in Fig. 3.28. They were calculated by accounting for the error on the fit parameters P_0 and P_1, which were used in Eq. (3.6) to form the correction model.

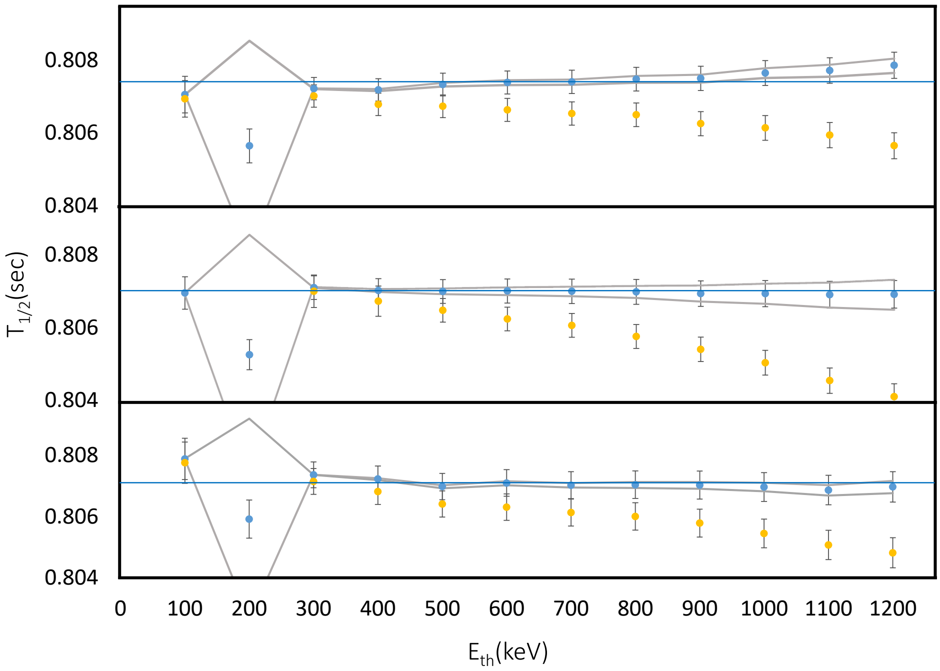

Figure 3.28: Half-life estimates obtained for the three sets of measurements as a function of the selected energy thresholds: (a): Set1, (b): Set2 and (c): Set3. Yellow dots are the half-life estimates without gain correction, while blue dots are those with gain correction. Error bars are statistical. The horizontal blue line shows the half-life value for an energy threshold of 600 keV. The grey lines represent the systematic uncertainty on the gain correction.

The systematic uncertainty on the gain correction increases with the energy threshold. It is remarkable that while accounting for both the systematic and statistical uncertainties, the half-life values for different energy thresholds between 300 keV and 1200 keV are consistent with a constant value for the three sets of measurements. The Bremsstrahlung peak's contribution dominates for energies below 300 keV (Fig3.15). This is why the values at 100 keV and 200 keV are shifted away from the rest. The most important bias can be noticed at 200 keV for the half-life estimates with and without gain correction, and even for the uncertainty on the gain correction. This can be explained by the presence of the right side of the Bremsstrahlung peak at 200 keV. Therefore, the half-life estimates for an energy threshold below 300 keV were discarded.

In order to reduce as much as possible the systematic and the statistical uncertainties, the chosen energy threshold should logically be either 300 keV or 400 keV. However, the unidentified background source shown in Fig. 3.17, whose half-life is unknown, and that extends up to 550 keV, made the E_{th} = 600 keV the most reasonable threshold to choose.

Figure 3.29 shows another comparison, this time between the half-life estimates with (blue dots) and without (yellow dots) the baseline correction. The same decreasing energy threshold dependence is also noticed for the half-life values without baseline correction, but one order of

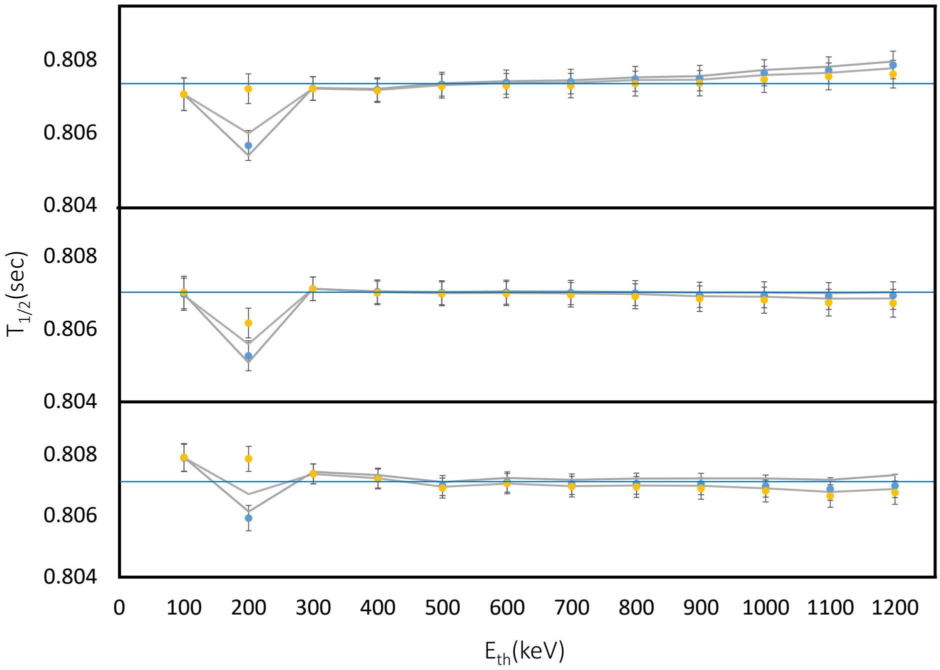

Figure 3.29: Half-life estimates obtained for the three sets of measurements as a function of the selected energy thresholds: (a): Set1, (b): Set2 and (c): Set3. yellow and blue dots are the half-life estimates respectively without and with baseline correction. Error bars are statistical. The horizontal blue line shows the half-life value for an energy threshold of 600 keV. The grey lines represent the systematic uncertainty on the gain correction.

magnitude lower than those without gain correction (Fig. 3.28). The systematic uncertainties increase also for higher thresholds.

The χ^2 and residuals distributions were also studied for the fits of the data for the three sets of measurements with and without the gain and baseline corrections. No significant deviation is noticed for the χ^2 values obtained by the two studies. This indicates that the analysis of χ^2 or p-values resulting from the fits fails to detect such systematic effects due to gain and baseline variations of the detection system. For the rest of this analysis, an energy threshold of $E_{th} = 600$ keV will be used in addition to a dead-time $\tau_{DT} = 3$ µs.

3.5.4.3 t_{min} effect

The half-life dependence on the lower bound of the fitting range t_{min} was also studied, by fitting the decay histogram using several values of t_{min} ranging between 3.5 s and 6.5 s (about 4 half-lives). The results of these fits for the three sets are shown in Fig. 3.30 illustrated by the statistical uncertainties.

When comparing the results obtained for $t_{min} = 4.5$ s, 5.5 s and 6.5 s with the initial value obtained for 3.5 s, the observed variations lead respectively to p-valuers of 0.51, 0.12 and 0.41, which were found to be totally compatible with the statistical fluctuations within the three sets of measurement.

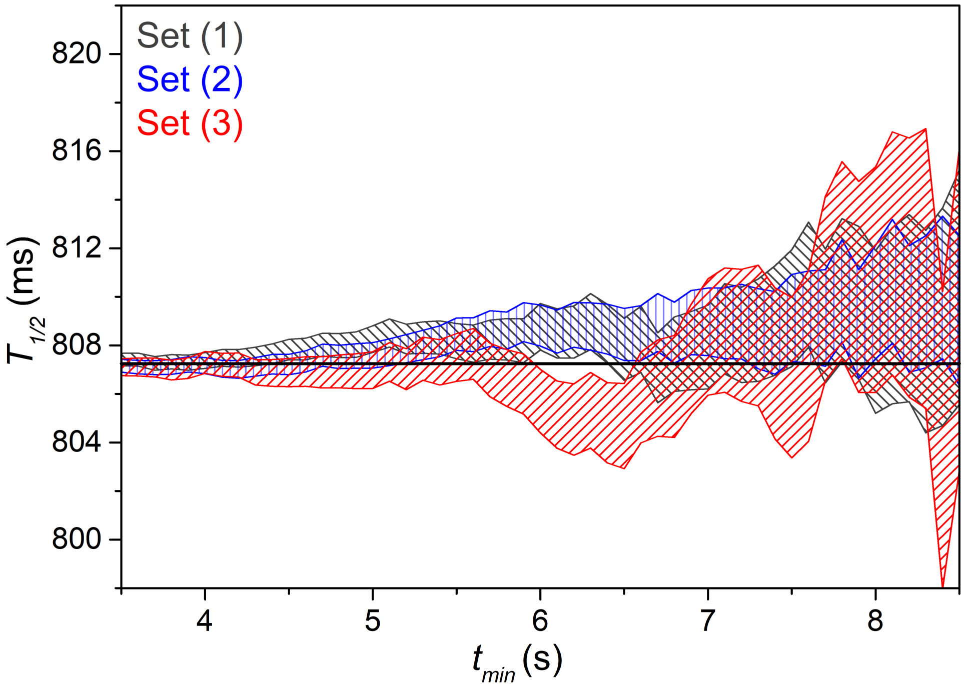

Figure 3.30: Half-life estimate obtained for Set1, Set2 and Set3 of measurements (respectively in grey, blue and red) as a function of the lower bound of the fitting range T_{min}^{Fit}. The colored areas indicate the values covered by the statistical error bars given at one standard deviation.

3.5.4.4 After pulses and Q4 study

Another common source of systematic uncertainty can arise from the after-pulses of the detection system. These after-pulses were actually found within the oscilloscope traces recorded within the oscilloscope runs in the region between 400 ns and 1000 ns of the fourth integration window (the 1 µs window). The presence of these after-pulses induces a bias to the results obtained while using the charges integration obtained by the fourth integration window. Therefore, the data obtained by this window were discarded, since they cannot be studied systematically due to the randomly generated after-pulses. Fortunately, such effect was not evidenced within the Q_{tot} window, thus no corrections related to after-pulses were needed while using the Q_{tot} window (Fig. 3.31).

3.5.4.5 Rapid diffusion

At last, the bias due to rapid diffusion of ^{6}He out of detector volume was investigated. The diffusion coefficients for Helium implanted inside the YAP could not be found in the literature. However, it is available for Helium implanted inside several other mineral materials such as Apatite, Garnet, Olivine, Quartz, Rutile, Titanite and Zircon [65]. All the diffusion coefficients for these materials were found to be smaller than $10^{-26}\text{m}^2\text{s}^{-1}$, which by using Fick's second

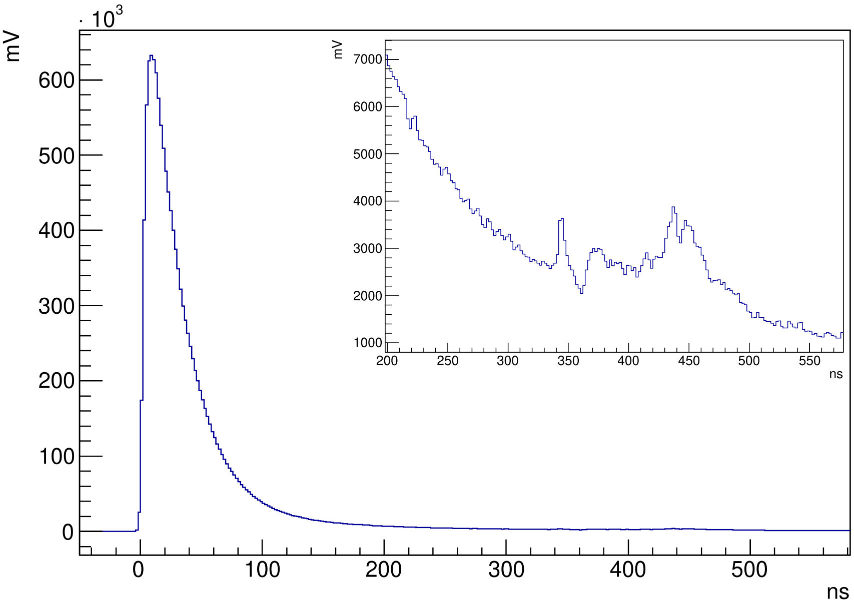

Figure 3.31: The sum of all the oscilloscope frames for YAP events obtained by one of the oscilloscope runs. The inner figure shows the zoom of the region between 200 and 550 ns. Several after-pulses contribution are evidenced in the region above 300 ns of the signals.

law with the present implantation depth of about 140 nm, leads to effusion time constants larger than 10^{11}s. These time constants are by far too large to have any significant effect on the half-life measurement of ^{6}He.

3.5.4.6 Other effects

The sensitivity of the obtained half-life to the binning of the histogram was studied by changing the bin width of the histogram between 20 ms, 50 ms and 100 ms. The resulting values of half-life were all compatible within 1×10^{-5}s. The gain and baseline correction model was also obtained by using the α particles deposited energy within the PVT as a reference instead of the 59.54 keV γ peak. The effect of using the α peak on the obtained half-life was found to be negligible.

3.6 Results and conclusions

Table 3.4 gives a summary of the obtained half-life estimates for Set1, Set2 and Set3 with their associated statistical uncertainties, alongside with the most important systematic corrections and their associated uncertainties. The combined uncertainties of the total correction were obtained by summation in quadrature. The results shown in the table were obtained by the sum of weighted events analysis while imposing a dead-time τ_{DT} = 3 µs and an energy threshold E_j

= 600 keV.

	Set1	Set2	Set3
$T_{1/2}$	807.42	807.16	807.10
Stat. error	0.25	0.26	0.35
Gain shift	0.75	0.77	0.78
Baseline shift	0.09	0.04	0.05
Pile-up shift	0.10	0.25	0.11
total shift	0.94	1.06	0.94
Gain error	0.07	0.10	0.06
Baseline error	0.03	0.02	0.09
Pile-up error	<0.01	<0.01	<0.01
Total syst. error	0.07	0.11	0.11

Table 3.4: Final results, in ms, for Set1, Set2 and Set3 along with the different systematic corrections and their associated uncertainties.

The obtained results for the cycle-by-cycle analysis were found to be compatible with those obtained by the sum of weighted events analysis. However, the correlation between the obtained half-life values and their statistical uncertainties must be studied more carefully in order to understand the overestimation of the weighted mean value. The gain shift correction is obviously the largest of all.

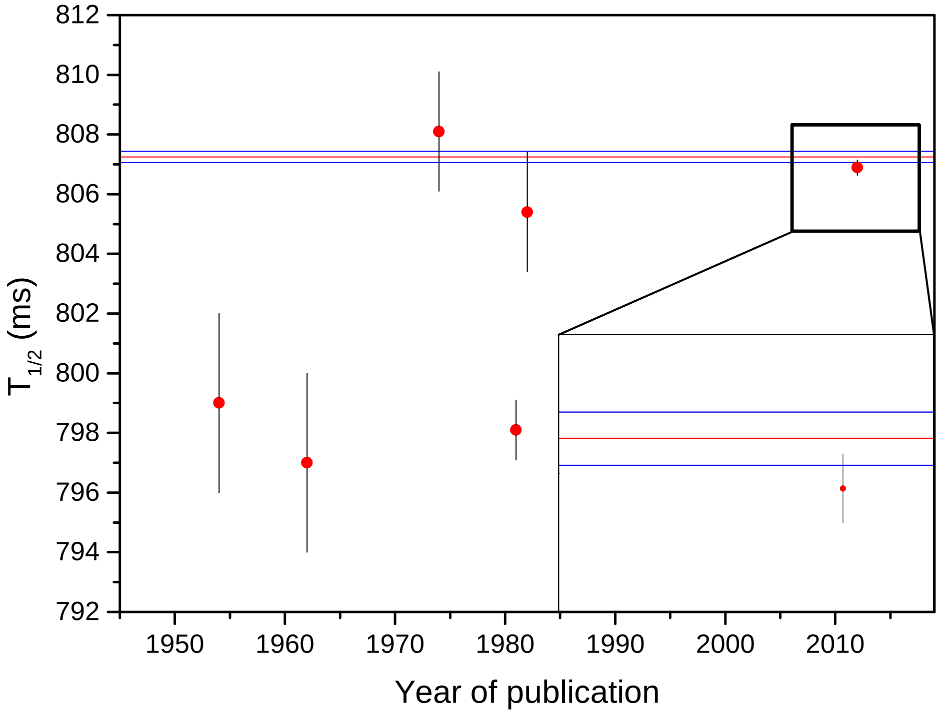

Figure 3.32: Comparison between the ^{6}He half-life value obtained from the present work (horizontal lines) and previous measurements having a relative precision smaller than 1%. The plotted values are from Refs.[2, 3, 4, 5, 6, 1].

The combined results for the three sets of measurements yield the value:

$$T_{1/2} = (807.25 \pm 0.16_{\text{stat}} \pm 0.11_{\text{syst}})\ \text{ms}, \tag{3.22}$$

where the systematic uncertainty corresponds to the largest of the three measurement sets. Figure 3.32 shows a comparison between the present result (horizontal lines) and the results that are shown in Fig. 3.1. The result obtained by this work is compatible with the last measurement of Ref. [1], which has a similar precision, with a difference of ∼1.2 combined standard deviations. It confirms the ^{6}He half-life results close to 807 ms and disfavors strongly alongside the result of Ref. [1] all the results below 800 ms.

CHAPTER 4

Fierz term analysis

In this chapter we delve into the extraction of the Fierz interference term, b_{GT} from the fitting of experimental β-energy spectra obtained from the data of the E815S experiment. Three main topics are discussed in the following sections. The first deals with the theoretical and instrumental components of the experimental energy spectrum. The second is the refined calibration matching the signals of ^{6}He decay obtained by the two detectors. Finally, the third describes the background subtraction, the data selections and the fitting of the spectra alongside the study of the systematic effects.

4.1 The components of the deposited energy spectrum

In Chap. 1, the full theoretical description of the allowed β-energy spectrum in ^{6}He decay was introduced in Eq. (1.24). The term $(1+\eta(W))$ corresponds to the product of several theoretical corrections, that were not discussed before, including the Fermi function $F(Z,W)$, the hadronic correction (spectral function) $f_1(W,b_{WM})$, the screening correction $S(Z,W)$, the electrostatic finite size correction $L_0(Z,W)$, the convolution finite size correction $C^A(Z,W,W_0)$, the finite mass correction $R_N(W,W_0)$, in addition to the radiative correction. Besides the theoretical corrections previously mentioned, there exists other instrumental effects entering the description of the shape of the β-energy spectrum, such as the resolution of the detection system and the distortion caused by the energy escape due to Bremsstrahlung radiations, which depends mainly on the geometry and the material of the scintillator in use. This distortion can be only estimated with enough precision through simulations.

In order to achieve the most precise measurement ever performed of the shape of the β-energy spectrum of ^{6}He, one must understand and determine all these effects with very high precision. Throughout this section, the variables are expressed in the natural unit (m_ec^2), with $\hbar = m_e = c = 1$. Here p is the momentum of the emitted electron, and W and W_0 correspond respectively to its total and endpoint energy in unit of electron mass.

4.1.1 Theoretical corrections

The theoretical corrections for the shape of the β-energy spectrum are detailed in Ref. [37]. A brief introduction to the Fermi function, the radiative correction and the hadronic correction is presented in this section. The other corrections (screening, electrostatic finite size, convolution finite size, and finite mass corrections) are too small to have a significant impact on the Fierz term extraction and can be found in Appendix D.

4.1.1.1 Fermi function

The Fermi function describes the effect of the Coulomb field of the daughter nucleus on the emitted β particle. It is derived from the solution to the Dirac equation for the electron wave function at a distance R (in this case it is the radius of ^{6}Li nucleus obtained as instructed in Ref. [66]) while assuming that the daughter nucleus is an infinitely heavy point-like particle. The Fermi function is given by Ref. [67]:

$$F(Z,W) = 2(\gamma+1)(2pR)^{2(\gamma-1)}e^{\pi y}\frac{|\Gamma(\gamma+iy)|^2}{[\Gamma(2\gamma+1)]^2}, \tag{4.1}$$

where Z is the atomic number of the daughter nucleus, $\gamma = \sqrt{1-(\alpha Z)^2}$, $y = \alpha ZW/p$, Γ is the complex gamma function and α is the fine structure constant.

4.1.1.2 Hadronic correction

The hadronic correction is due to induced recoil to first order, assuming the absence of second class currents. The description of Gamow-Teller transition to first order in recoil requires only three form factors [68, 61]. Those are the dominant Gamow-Teller strength c, the weak magnetism form factor b_{WM} and the induced tensor form factor d. The factor d is the sum of a first class part d^I and a second class part d^{II}. The second class part is absent in ^{6}He decay as shown in Ref. [61], where no evidence was found of a d^{II} term in $e-\nu$ correlation measurement for ^{6}He decay. For ^{6}He , the spectral function describing this correction has the following expression:

$$f_1(W, b_{WM}) = 1 + C_0 + C_1 W + \frac{C_{-1}}{W}, \tag{4.2}$$

with

$$C_0 = -\frac{2W_0 m_e}{3M}\left(1+\frac{b_{WM}}{c}+\frac{d^I}{c}\right), \tag{4.3}$$

$$C_1 = \frac{2}{3M}\left(5+2\frac{b_{WM}}{c}\right), \tag{4.4}$$

$$C_{-1} = -\frac{m_e}{3M}\left(2+\frac{d^I+2b_{WM}}{c}\right), \tag{4.5}$$

$$b_{WM} = \sqrt{\frac{6\Gamma_{M_1}M^2}{\alpha E_\gamma^3}} = 68.4(7)[69], \tag{4.6}$$

where Γ_{M_1} is the M_1 γ-decay width of the analog state within the isospin triplet [70], E_γ is the energy of the γ transition [71], M is the nuclear mass of the daughter nucleus ^{6}Li [72], $c = g_A M_{GT} = 2.7491(10)$ [69] and $d^I = 2.4$ [61]. The hadronic corrections are dominated by the weak magnetism form factor b_{WM}. The uncertainty induced by these corrections on the extracted b_{GT} is smaller than 10^{-3} [37].

4.1.1.3 Radiative correction

During the β-decay process, virtual and real photons can be emitted and change the decay kinematics. In contrast with all the above corrections, which could be simply added as a factor to the energy distribution function, the radiative correction effect can only be accessed through Monte-Carlo simulations because of the emission of real photons that may or not be detected. The radiative correction is treated similarly as in Refs. [73, 74]. It is split into two parts: the virtual-soft Bremsstrahlung, and the hard photon Bremsstrahlung.

The virtual and soft Bremsstrahlung correction of order α, which is characterized by the emission of a virtual photon (top row of Fig. 4.1), adds two terms to the β-energy distribution function as follows:

$$N(W) \propto F(Z,W)pW(W_0-W)^2\left[(1+z_{vs})\left(1+\frac{b_{GT}}{W}\right)+\tilde{\mathscr{M}}\right], \tag{4.7}$$

where $\tilde{\mathscr{M}}$ is defined as:

$$\tilde{\mathscr{M}} = -\frac{\alpha}{\pi}\frac{1-\beta^2}{\beta}\mathscr{N}(\beta), \tag{4.8}$$

α is the fine structure constant, $\beta = p_e/E_e$, and

$$\mathscr{N}(\beta) = \frac{1}{2}\ln\frac{1+\beta}{1-\beta}, \tag{4.9}$$

and z_{vs} is defined as:

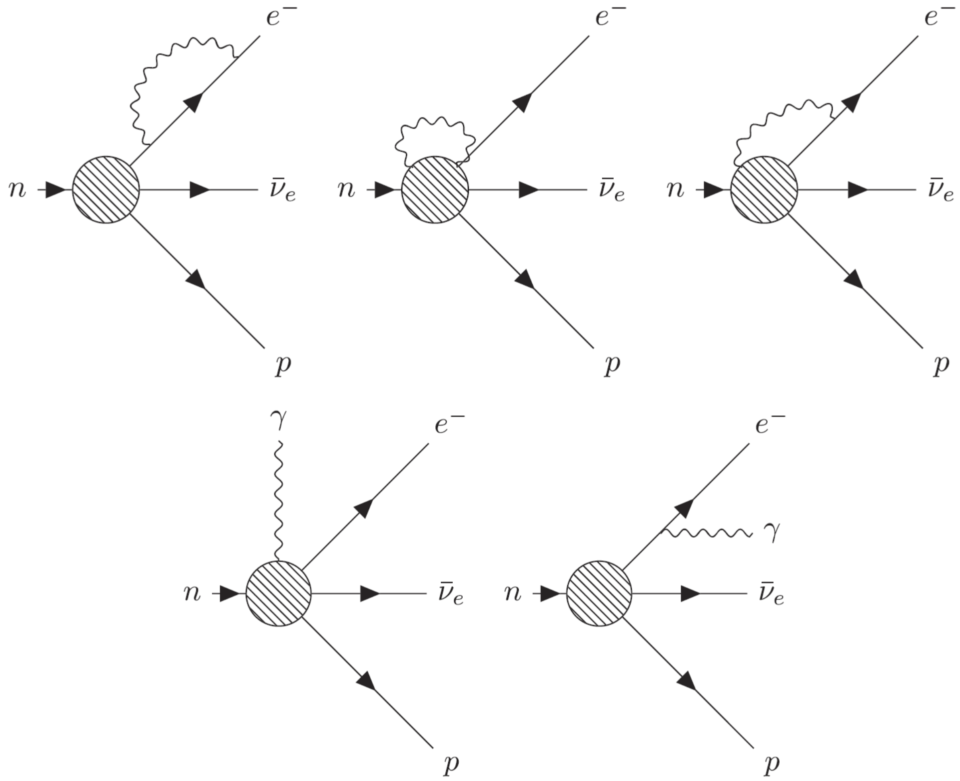

Figure 4.1: Feynman diagrams for the one-photon exchange processes associated with the order α radiative correction. The top row shows the processes involving virtual photon exchange, and the bottom row shows the processes involving real photon emission. Figure taken from Ref. [75].

$$
\begin{aligned}
z_{vs} =& \frac{\alpha}{\pi}\left[\frac{3}{2}\ln\left(\frac{m_p}{m_e}\right)+2\left(\frac{\mathcal{N}(\beta)}{\beta}-1\right)\ln\left(\frac{2\omega}{m_e}\right)\right. \\
&\left.+2\frac{\mathcal{N}(\beta)}{\beta}(1-\mathcal{N}(\beta))+\frac{2}{\beta}L\left(\frac{2\beta}{1+\beta}-\frac{3}{8}\right)\right],
\end{aligned}
\tag{4.10}
$$

where L is the Spence function defined as

$$
L(x)=\int_0^x dt\frac{\ln|1-x|}{x},
\tag{4.11}
$$

m_p is the proton mass and ω is the soft Bremsstrahlung cutoff energy.

On the other hand, the hard photon Bremsstrahlung correction, which is characterized by the emission of a real photon (bottom row of Fig. 4.1), changes the decay kinematics due to the additional photon in the final state. Therefore, in the case of the emission of a real photon, the β-energy distribution function becomes

$$
N(E_e)=F(Z,E_e)\cdot W_{Hg}(E_e,E_\nu,E_\gamma,\theta_{\beta\gamma}),
\tag{4.12}
$$

where

$$W_{Hg} = 2\mathcal{N}(\beta)E_\gamma E_\nu \left(E_e E_\gamma - p_e E_\gamma \cos\left(\theta_{\beta\gamma}\right)\right)\left(H_0 + a_{\beta\nu}H_1\right), \tag{4.13}$$

$$H_0 = E_\nu \left(-(E_e + E_\gamma)P^2 + \frac{1}{E_e - p_e \cos\left(\theta_{\beta\gamma}\right)}\right), \tag{4.14}$$

$$\begin{aligned} H_1 = &E_\nu p_e \cos\left(\theta_{\beta\nu}\right)\left(-P^2 + \frac{1}{E_e E_\gamma - p_e E_\gamma \cos\left(\theta_{\beta\gamma}\right)}\right) \\ &+ E_\gamma E_\nu \cos\left(\theta_{\nu\gamma}\right)\left(\frac{E_e + E_\gamma}{E_\gamma(E_e E_\gamma - p_e E_\gamma \cos\left(\theta_{\beta\gamma}\right))} - \frac{m_e^2}{\left(E_e E_\gamma - p_e E_\gamma \cos\left(\theta_{\beta\gamma}\right)\right)^2}\right), \end{aligned} \tag{4.15}$$

$$P^2 = \frac{1}{E_\gamma^2} + \frac{m_e^2}{\left(E_e E_\gamma - p_e E_\gamma \cos\left(\theta_{\beta\gamma}\right)\right)^2} - \frac{2E_e}{E_\gamma\left(E_e E_\gamma - p_e E_\gamma \cos\left(\theta_{\beta\gamma}\right)\right)}. \tag{4.16}$$

Here, E_ν is the energy of the emitted anti-neutrino, E_γ is the energy of the emitted Bremsstrahlung photon, p_e is the momentum of the β particle, and θ_{XY} is the angle between X and Y ($X,Y = \beta,\gamma,\nu$ and $X \neq Y$). We take here the SM value $a_{\beta\nu} = -1/3$ for pure Gamow-Teller decay.

The two expressions of Eqs. (4.7) and (4.12) can be used to generate events with Monte-Carlo simulations to study the effect of virtual and hard Bremsstrahlung photons emission on the shape of the β-spectrum. The details of the Monte-Carlo Simulation that generates the events are reported in Ref. [76]. The method used in this work to model the correction due to the generation of virtual and hard Bremsstrahlung photons on the detected β-energy spectrum will be discussed in Sec. 4.2.

4.1.1.4 Summary of the corrections to the β-energy spectrum in ^{6}He decay

The contribution of all the theoretical corrections to the β-energy spectrum of ^{6}He is calculated and presented in Fig. 4.2. It is clear that the dominant correction is the Fermi function, while the sizes of all the other corrections are below 2%.

4.1.2 Bremsstrahlung energy escape

The Bremsstrahlung process discussed in this section is due to the interaction of the emitted β particle with the surrounding matter (in the detector's bulk). It should not be mistaken with the soft and hard Bremsstrahlung discussed within the radiative corrections. The Bremsstrahlung radiation (or "breaking radiation") is electromagnetic radiation produced by a free electron that is deflected in the electric field of a charged particle (e.g. the atomic nucleus).

In our case, Bremsstrahlung radiation is produced by the interaction of the decay electrons and the nuclei of the YAP scintillator. The energy of these radiations extends almost up to the endpoint of the ^{6}He energy spectrum. As mentioned in Chap. 2, the YAP's properties lead to the re-absorption of a large part of the energy carried by these Bremsstrahlung photons, but a

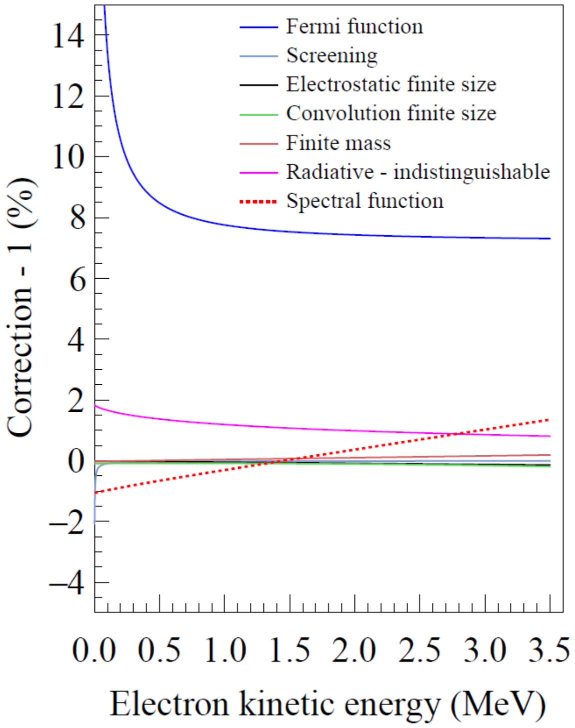

Figure 4.2: Calculated theoretical corrections to the β-energy spectrum in ^{6}He decay [37].

non-negligible amount of the photons escape the YAP scintillators without being detected. This means that the energy of the emitted β particles is not fully deposited in the detector. This effect distorts the shape of the detected β-energy spectrum. The distortion is mainly dependent on the scintillator material and on the geometry of the detector in addition to the energy of the β-particles. Therefore, the effect of the Bremsstrahlung energy escape can only be accessed through simulations.

4.2 Energy escape correction model and construction of the fit function

The energy distribution of the β particles emitted from ^{6}He decay given in Eq. (1.24) can be described by the following analytical expression that incorporates all the theoretical corrections except for the radiative ones:

$$N(W) \propto F(Z,W)pW(W-W_0)^2\left(\alpha_0+\alpha_{-1}\cdot\frac{1}{W}+\alpha_1\cdot W+\alpha_2\cdot W^2\right), \tag{4.17}$$

where α_{-1}, α_0, α_1 and α_2 are coefficients that can be chosen to include the relevant correction terms in W^i discussed in the previous section. Note that the coefficient α_{-1} includes both the Fierz term b_{GT} and the term C_{-1} from hadronic corrections. These coefficients can either be fixed or left free for the fitting of the experimental data. However, this function $N(W)$ does not include the effect of the Bremsstrahlung energy escape nor the radiative corrections leading to virtual or hard Bremsstrahlung photons. In the following, we introduce the method used to build an analytical model of the radiative corrections and of the Bremsstrahlung energy escape.

4.2.1 Events generation

Equation (4.17) shows that four terms with different energy dependence enter the expression of the electrons energy distribution. For each of these terms, the effect of the Bremsstrahlung energy loss was studied separately. The first step of the study consisted in using Monte-Carlo simulations to generate four sets of events S_i $(i = -1, 0, 1, 2)$ with energy distributions corresponding to each term described by the following functions:

$$g_i(W) = F(Z,W)pW(W-W_0)^2 \cdot W^i. \tag{4.18}$$

For the three terms dependent in W^i with $i \neq 0$, β-energy distributions were generated with the Von Neumann rejection method using directly the functions $g_{-1}(W)$, $g_1(W)$ and $g_2(W)$. For the term in W^0, the effect of virtual and hard Bremsstrahlung photons emission is significant and must be added independently as it is not included in the $g_0(W)$ function. The Monte-Carlo is more complicated and takes into account the probability that the emission is either a real photon or a virtual one. The probability that the emission is a real photon is calculated in Ref. [73] by comparing the decay rates noted ρ_H and ρ_{vs}. It was found that 2.955% of photon emission corresponds to real photons, while the rest corresponds to virtual photons. The generation of events is performed as follows:

First, the emitted photon is randomly chosen to be either real or virtual according to the probability of each type.

In the case of virtual photon emission, the energy of the electron E_e is uniformly generated between 0 keV and the endpoint energy of the decay E_0. Then, the Von Neumann rejection method is used with the function of Eq. (4.7) to decide whether this energy value is kept or discarded. This two-step process is repeated until the generation of a valid event with virtual photon emission. Note that in Eq. (4.7), the value of b_{GT} is here considered to be zero. The effect of b_{GT} will be included with the term $g_{-1}(W)$.

In the case of real photon emission, the energy of the electron E_e is uniformly generated between 0 and the endpoint energy of the decay E_0. Afterwards, the energy of the emitted photon and its direction relative to the direction of the electron are uniformly generated according to the following functions:

$$E_\gamma = \omega \exp\{(-u_1 \ln(C_S))\}, \tag{4.19}$$

$$\cos(\theta_{\beta\gamma}) = \frac{1-(1+\beta)\exp\{(-2\mathscr{N}(\beta)u_2)\}}{\beta}, \tag{4.20}$$

where u_1 and u_2 are two random numbers uniformly generated between 0 and 1, ω is the cut-off energy with $\omega = C_S \times (E_0 - E_e)$, where $C_S = 10^{-3}$ as prescribed by Ref. [73]. The azimuthal angle of the photon around β particle direction is uniformly generated between 0 and 2π. The energy of the emitted anti-neutrino is calculated as $E_\nu = E_0 - E_e - E_\gamma - E_r$, where E_r is the energy of the recoil ion. Then, the Von Neumann rejection method is used with the function of Eq. (4.12) to decide whether to keep or discard this energy value for the electron. If the energy value E_e is discarded, the process is repeated until the generation of a valid event with real photon emission. This event comprises both an electron and a photon of well defined energy and direction of emission. The advantage is that in this case (with real photon emission), the photon can also be tracked to account for the energy potentially deposited in the detector. For each set S_i associated with the the $g_i(W)$ functions, 10^8 events were generated for the GEANT4 simulation.

4.2.2 GEANT4 simulation

The second step consists in tracking the generated particles of each set of events S_i within the setup to determine the deposited energy in the YAP scintillator while accounting for Bremsstrahlung energy escape. The detection setup was built in GEANT4 including the two detectors placed in the full contact position (Fig. 4.3). In order to reproduce as well as possible the experimental conditions, the events were generated uniformly within a cylindrical volume with a radius of 2 mm, corresponding to the radius of the collimator attached to Det2, and a length of 47 nm, corresponding to the straggling length of $^6\mathrm{He}^+$ ions inside the YAP material obtained using SRIM (Fig. 2.9). The events generation volume is placed at 140 nm away from the surface of the YAP scintillator of Det1 which corresponds to the mean implantation depth of $^6\mathrm{He}^+$ ions as provided by SRIM simulations. Electrons defined in the sets S_i were generated inside this volume with random directions and energy distributions corresponding to each of the three $g_i(W)$ $(i = -1, 1, 2)$ functions defined in the previous section. In the case of hard Bremsstrahlung coming with the radiative corrections included in the set of events S_0, photons were generated and tracked alongside the electrons with their corresponding energies and directions.

For each set S_i, the total energy deposited inside the YAP volume by each event was computed with GEANT4. Then, histograms of the β-energy generated directly with the functions $g_i(W)$ (noted $Hinit_i(W)$) and histograms of the deposited energy as simulated by GEANT4 with the sets S_i (noted $Hgeant4_i(W)$) were built and compared. The left panel of Fig. 4.4 shows such histograms built with the Von Neumann method with the function $g_{-1}(W)$ (blue), and with the corresponding deposited energy inside the YAP obtained with the GEANT4 simula-

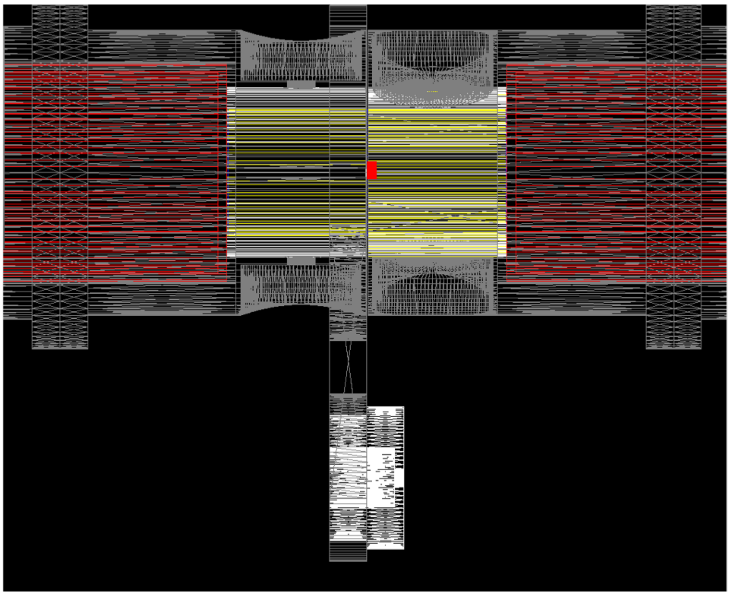

Figure 4.3: The detection setup built in GEANT4, showing the two detectors in full contact position, where the red lines are the two PMTs and the Yellow lines to the YAP and PVT scintillators. The red spot indicates (not to scale) the area of generation of events.

tion (red). The difference between the two histograms is here only due to the Bremsstrahlung energy escape. For the term in W^0 (right panel of Fig. 4.4), the difference between the histogram resulting from the GEANT4 simulation and the one built with the function $g_0(W)$ is due to both the Bremsstrahlung energy escape and radiative corrections.

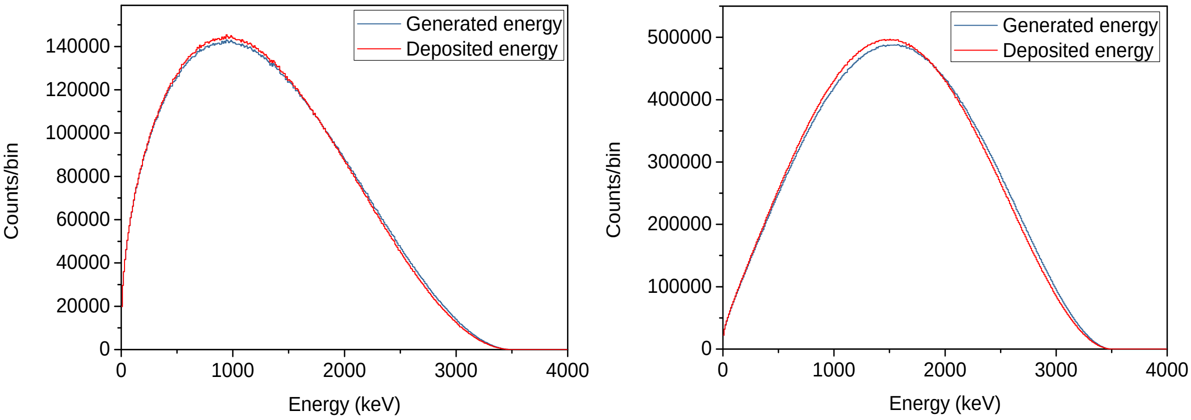

Figure 4.4: Blue lines: the generated energy spectrum with $g_{-1}(W)$ (left panel) and $g_0(W)$ (right panel). Red lines: the deposited energy within the YAP scintillators obtained by GEANT4 simulation.

4.2.3 Fit function

The next step consisted in building an analytical correction function $f_i(W)$ that models the effect of Bremsstrahlung energy escape (and of radiative corrections in the specific case of $g_0(W)$) for each $g_i(W)$ initial energy distribution. For this, we subtract the histograms $Hinit_i(W)$ from the histograms $Hgeant4_i(W)$ and scale this difference by the integral of the $g_i(W)$ function divided by the integral of the $Hinit_i(W)$ histogram. The resulting histogram was then fitted with a polynomial function $f_i(W)$ of order 9 (Fig.4.5).

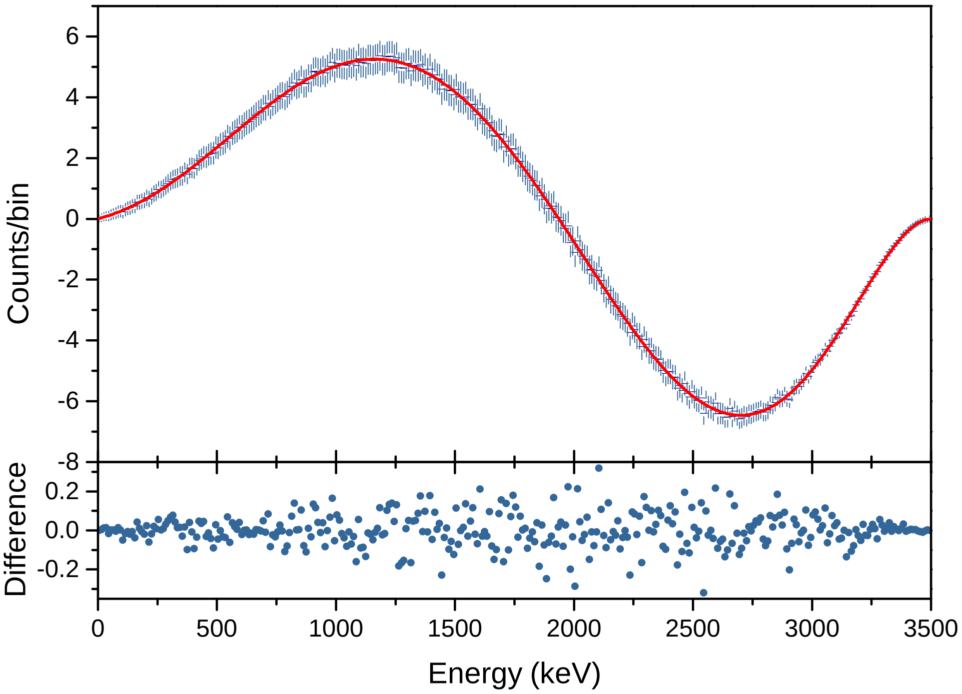

Figure 4.5: Top: the histogram of the normalized difference between the generated and deposited energy histograms (in blue). The fit of this histogram with a polynomial function (in red). Bottom: the residuals of the fit.

The deposited energy spectrum resulting from the decay function of Eq. (4.17) and accounting for both radiative corrections and Bremsstrahlung energy escape can then be expressed as:

$$F(W) = N \sum_{i=-1}^{2} \alpha_i \left[g_i(W) + f_i(W) \right], \tag{4.21}$$

where N is a normalization factor and $f_i(W)$ are the polynomial functions that describe the effect of Bremsstrahlung energy escape for each term of the β-energy spectrum ($f_0(W)$ includes as well the effect of the radiative correction). These functions were tested with several statistically independent sets of events generated by GEANT4 using Eq. (4.17), with different values for α_{-1}, α_0, α_1 and α_2. For these sets of events, the deposited energy spectra were built and fitted with the analytical function of Eq. (4.21) where α_0, α_1 and α_2 were fixed parameters, while N

and α_{-1} were free parameters of the fit. The left panel of Fig. 4.6 shows the results of the fit of the deposited energy spectra for 100 statistically independent sets of events. These events were generated with $\alpha_{-1} = 0.03$, $\alpha_0 = 1$, $\alpha_1 = 4$ and $\alpha_2 = 2$. These values were randomly chosen to test the fit function and have no physical meaning. The values of α_{-1} resulting from the fit are normally distributed around the input value within a range of $\pm 3\sigma$ as shown in the right panel of Fig. 4.6. The weighted average of these values of $\langle \alpha_{-1} \rangle = 0.028 \pm 0.001$ deviates by 2 sigmas $(2 \cdot 10^{-3})$ from the input value of 0.03. This deviation may either come from statistics or from the correction model. It is anyway small enough for this stage of the analysis, and additional simulations with higher statistics can be performed in the future if the precision must be improved.

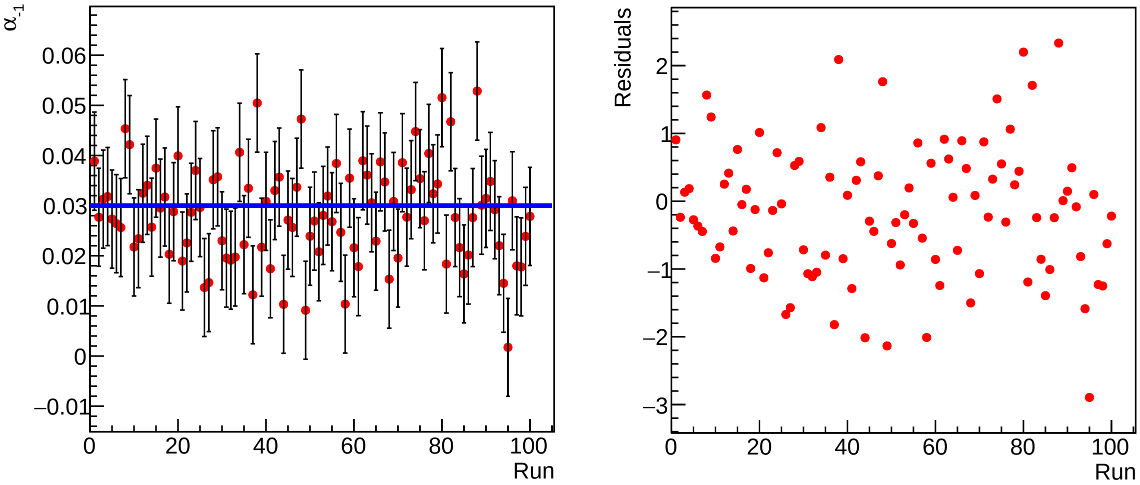

Figure 4.6: Left panel: the obtained values of α_{-1} by the fit of the deposited energy spectra of 100 statistically independent sets of events. The error bars are statistical. The blue horizontal line represents the input value of α_{-1}. Right panel: The residuals of the fits result away from the input value of α_{-1}.

With this model, we could build a combination of analytical functions including the relevant theoretical corrections and the effect of Bremsstrahlung energy escape. But if these functions can describe the energy deposited in the YAP, they do not include yet the response function of the detector. In order to fit the deposited energy spectrum built with experimental data, one has to account for the resolution in energy of the detector. This is done using a convolution with a Gaussian function whose width depends on the deposited energy, and leads to the fit function:

$$F(W) = N \sum_{i=-1}^{2} \alpha_i \left[g_i(W) + f_i(W) \right] \circledast \mathrm{Gaus}\left(0, \sigma(\mathrm{W})\right), \tag{4.22}$$

where $\sigma(W)$ represents the energy dependent resolution of the detection setup. This resolution will be discussed in more detail in the following sections.

4.3 Refined calibration

4.3.1 The unmatched spectra

For the half-life analysis, the calibration in energy was not crucial, as long as the fluctuations within the decay cycles were corrected to avoid any time dependent effect. This is not the case anymore for the extraction of the Fierz term. For the present setup, with two detectors, it is important to have a precise relative energy calibration between the two detectors. One of the difficulties with this setup comes from the fact that the scintillation photons generated in one YAP scintillator are not only detected by its associated PMT but also by the PMT coupled to the other YAP scintillator. In order to reconstruct the energy of a β particle that deposited its energy in both detectors, the signals from both PMTs need to be matched, and one must use the proper linear combination of these signals to determine the total deposited energy. The procedure that was used for this refined calibration is detailed in the following. Note that, at this stage, the goal is to determine a consistent relative calibration. As it will be seen later in the manuscript, the absolute calibration will be performed along with the final fitting of the spectra.

The first order calibration of the data, described in Chap. 3, was performed to correct for the relative gain and baseline fluctuations of the PMTs by matching the positions of the 59.54 keV photopeaks obtained in both detectors. However, this calibration did not account for the difference in light collection that could result from the different positions of the energy deposition of the 59.54 keV γ particles and of the β-decay electrons. The deposition of energy by the 59.54 keV photons happens mainly near the lateral surface of the YAP scintillators (near the location of the ^{241}Am sources), while for the electrons, it happens near the front surface of the two YAP scintillators (near the location of ^{6}He^{+} ions implantation). To study this effect, and for the sake of simplifying the analysis, only the events that deposited their entire energy inside one detector were used. These events can be isolated by selecting the events within the green/red lines for events depositing their whole energy in Det1 or Det2, as shown in Fig. 4.7.

The set of events that deposited their entire energy in Det1 will be noted "EV_1" and the set of events that deposited their entire energy in Det2 will be noted "EV_2". The PMTs attached to Det1 and Det2 will be noted respectively "PMT_1" and "PMT_2". The energy reconstructed for PMT_1/PMT_2 using the calibration with the 59.54 keV photopeaks will be noted E_1^{60keV}/E_2^{60keV}. With these notations the reconstructed energy in PMT_x by the set of events EV_y is noted $E_x^{60keV}(EV_y)$ (with $x, y = 1, 2$).

After the selection of EV_1 and EV_2, the reconstructed energy in both PMTs from these events was plotted. The left panel of Fig. 4.8 shows the spectra of $E_1^{60keV}(EV_1)$ (red) and $E_2^{60keV}(EV_2)$ (green) corresponding to the energy reconstructed using the light emitted within one scintillator and collected by its associated PMT. The right panel of Fig. 4.8 shows the spectra of $E_2^{60keV}(EV_1)$ (red) and $E_1^{60keV}(EV_2)$ (green) corresponding to the energy reconstructed using

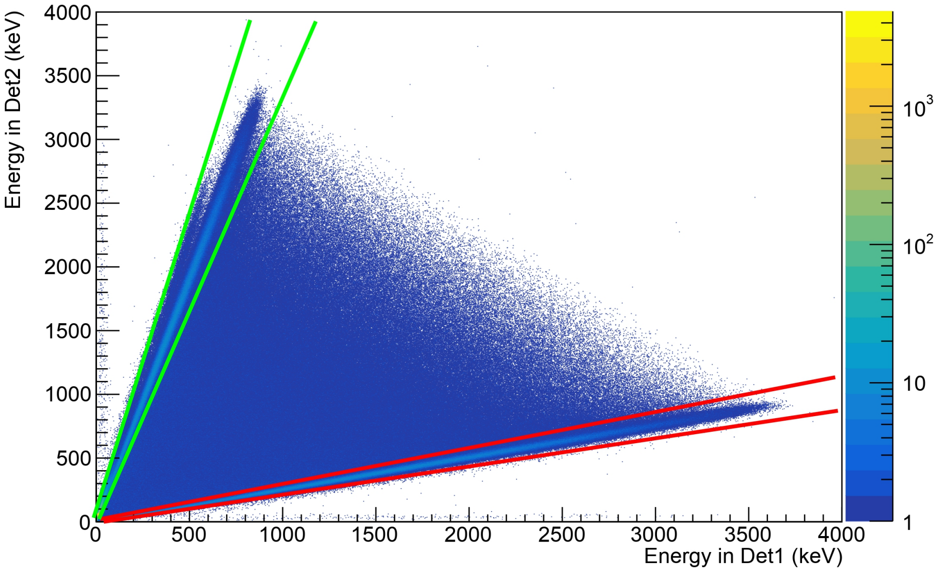

Figure 4.7: The collected energy in the PMT of Det2 plotted against the collected energy in the PMT of Det1 after the first calibration with the 59.54 keV photopeaks for one hour run of Set1. The events between the red (green) lines are the ^{6}He decay events that deposited their entire energy within the YAP of Det1 (Det2).

the light passing from one scintillator to the other and collected by the other PMT.

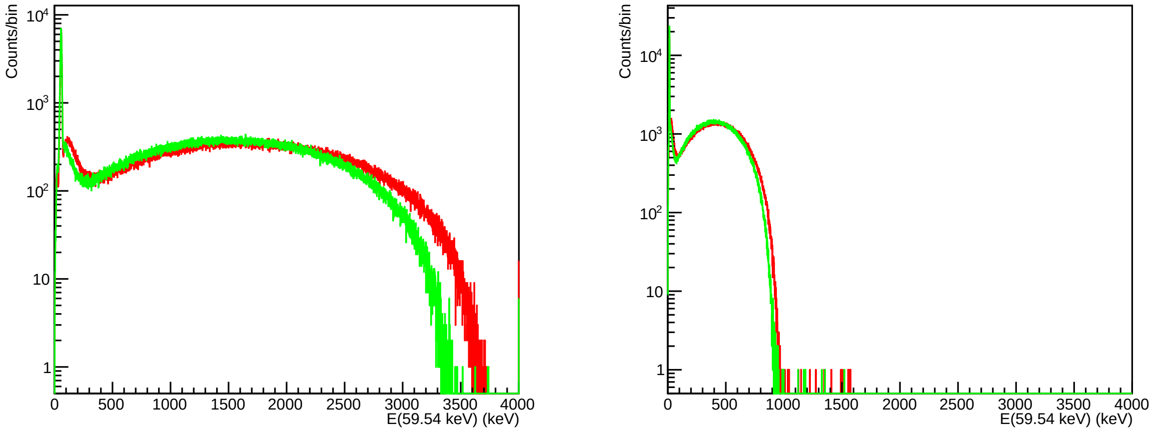

Figure 4.8: Left panel: spectra obtained from $E_1^{60keV}(EV_1)$ (red) and $E_2^{60keV}(EV_2)$ (green). Right panel: spectra obtained from $E_1^{60keV}(EV_2)$ (red) and $E_2^{60keV}(EV_1)$ (green).

A large discrepancy can be noticed between the spectra of the sets EV_1 and of EV_2, despite the good agreement for the position of the 59.54 keV photopeak. This discrepancy can be attributed to the difference in light collection by the two PMTs, which leads to a different ratio between photon collection efficiency from a ^{6}He decay and photon collection efficiency from a 59.54 keV photopeak. Therefore, a refined calibration is needed to match correctly the reconstructed energy in both detectors for β-decay electrons prior to the construction of the full energy for each event. The discrepancy was parameterized using the mean value of the ^{6}He energy distribution for $E_1^{60keV}(EV_1)$ and $E_2^{60keV}(EV_2)$ between 2700 keV and 3700 keV, noted respectively M_1 and M_2. The left panel of Fig. 4.9 shows these mean values M_1 and M_2 obtained for $E_1^{60keV}(EV_1)$ (red) and $E_2^{60keV}(EV_2)$ (green) for all the runs of the experiment. The right panel of Fig. 4.9 shows the mean position of the 59.54 keV photopeak obtained by fitting the photopeaks with EV_1 and EV_2 selections for all the runs. On the left panel, a discrepancy of about 3% is observed between the mean energies reconstructed with the two different detectors. Moreover, the mean values change from run to run, due to small modifications of the PMT gains and of light collection efficiency.

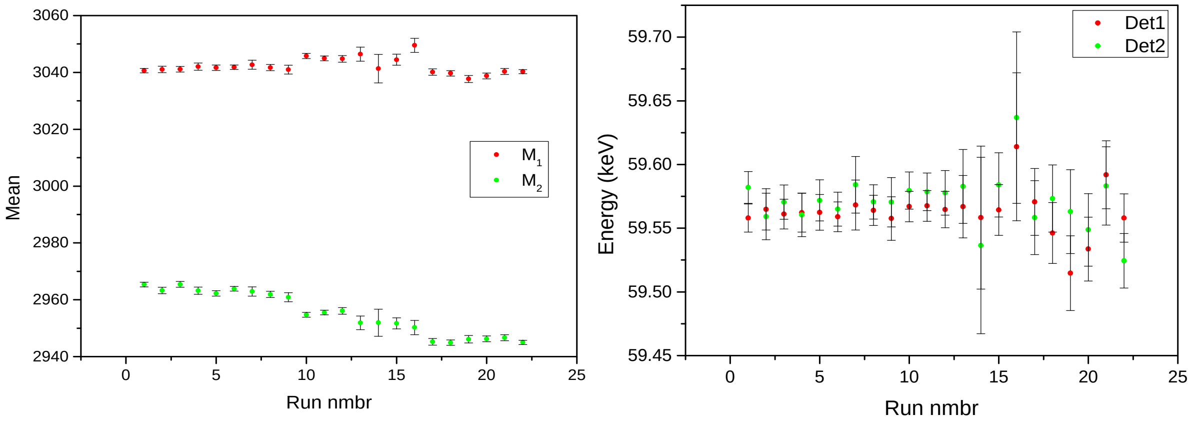

Figure 4.9: Left panel: The mean of the ^{6}He energy distribution for EV_1 (red) and EV_2 (green) collected respectively by PMT1 and PMT2. Right panel: The position of the 59.54 keV photopeak as seen by PMT1 and PMT2. In both panels, the error bars represent the statistical uncertainty.

4.3.2 The matching process

The refined calibration used to reconstruct the deposited energy inside the two YAP scintillators consisted of two steps. The first step was a calibration that considers that the discrepancy is due to different light collections and different gains of the PMTs. The purpose of this first step is to match the end of the two spectra of $E_1^{60keV}(EV_1)$ and $E_2^{60keV}(EV_2)$. It consisted in introducing two calibration coefficients, α_1 and α_2 ($\alpha_1 \times E_1^{60keV}$ and $\alpha_2 \times E_2^{60keV}$) for each run of data. These two coefficients were calculated to fix the mean values M_1 and M_2 at 3000 keV, which is arbitrarily chosen to perform a relative calibration. This calibration is therefore not an absolute energy calibration, but an intermediate calibration that ensures a matching of the reconstructed energy for both detectors. The values of α_1 and α_2 were obtained with an iterative process that stops only when the relative difference between M_1/M_2 and 3000 keV is smaller than 10^{-4}, which was found in Ref. [54] to be the required uncertainty on the gain to achieve an uncertainty of $\Delta b_{GT} = 2 \cdot 10^{-3}$. The calculation of α_1 and α_2 was done for each run separately. The calibrated energy with the obtained coefficients $E_1^{cal} = \alpha_1 \times E_1^{60keV}$ and $E_2^{cal} = \alpha_2 \times E_2^{60keV}$ was then calculated for all events and all runs.

The left panel of Fig. 4.10 shows the two spectra built with the energies of sets $E_1^{cal}(EV_1)$ and $E_2^{cal}(EV_2)$. The two spectra are now matched within statistical fluctuations starting from 500 keV (Right panel of Fig. 4.10). Below 500 keV, a small discrepancy can be noticed in the number of events forming the Bremsstrahlung peak. This is due to the fact that the Bremsstrahlung radiation from the ^{6}He implantation on the collimator attached to Det2 has a higher probability to be detected in Det1.

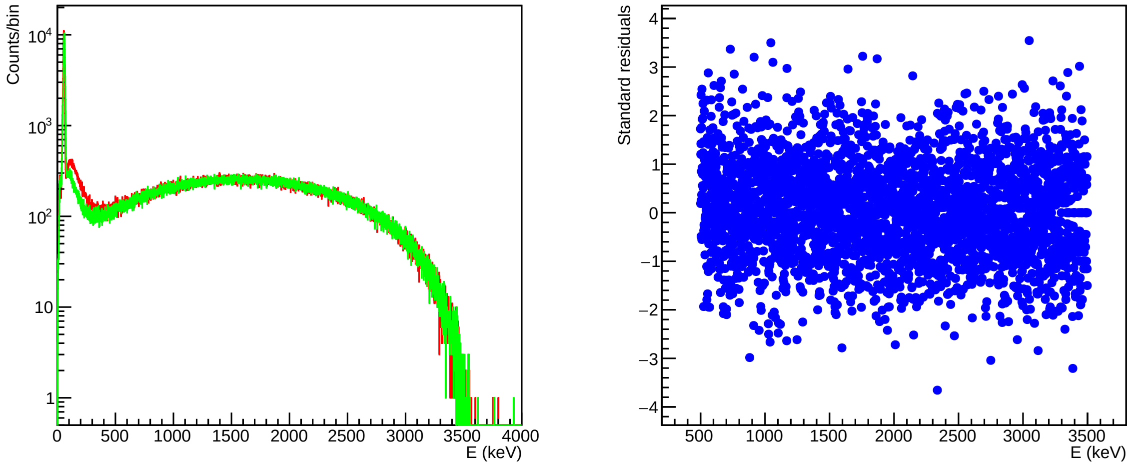

Figure 4.10: Left panel: spectra of EV_1 in PMT1 (blue) and EV_2 in PMT2 (red) after the matching of the mean values of the endpoints. Right panel: the residuals obtained from the two matched distributions.

However, the spectra obtained for $E_1^{cal}(EV_2)$ and $E_2^{cal}(EV_1)$ were not matched, and the reconstructed energy is about four times smaller due to the lower light transmission from a given YAP to the opposite PMT (Fig. 4.11). The presence of this discrepancy can be caused by different light transmissions from Det1 to Det2 and vice-versa. In the following, we consider β_1 and β_2 the coefficients that represent respectively the light transmission from Det1 to Det2 and vice-versa (Fig. 4.12).

During the first step of the calibration, only the sets EV_1 and EV_2 were used. For these sets of events, we consider that the calibrated energy is equal to the deposited energy in each detector, $E_1^{cal} = E_1^{dep}$ and $E_2^{cal} = E_2^{dep}$, since the energy deposition happens only in one detector.

If we now consider events with deposited energy in both detectors while assuming that the light generation in the two detectors is identical, we simply have:

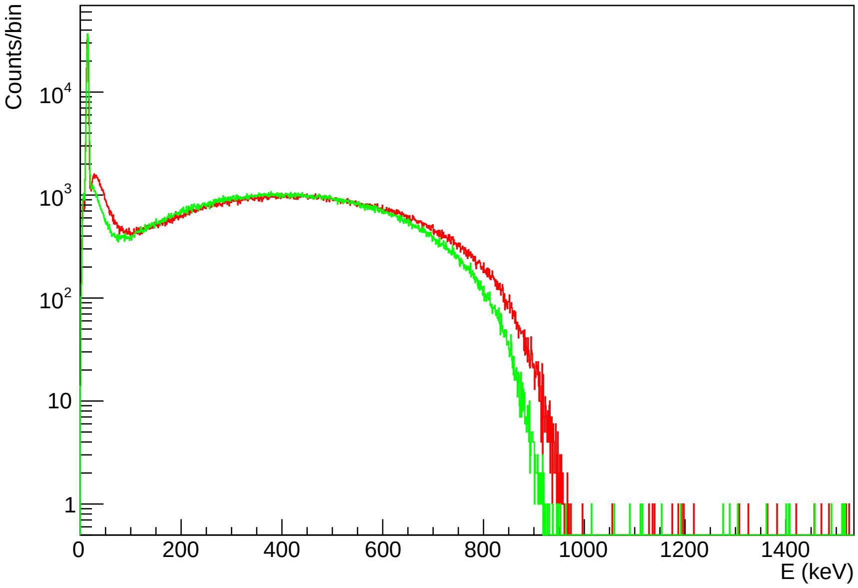

Figure 4.11: Spectra obtained by EV_1 (green) and EV_2 (red) with the collected energy respectively in PMT_2 and PMT_1 after the calibration with α_1 and α_2.

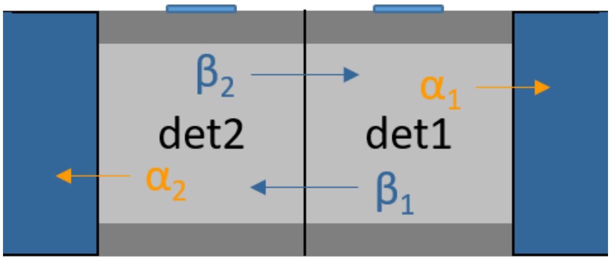

Figure 4.12: A sketch of the two detectors in contact position. The coefficients β_i correspond to the light transmission from one detector to the other. The coefficients α_i correspond to the correction in light transmission from one detector to its PMT for the ^{6}He β particles compared to the 59.54 keV γ particles.

$$E_1^{cal} = E_1^{dep} + \beta_2 E_2^{dep}, \tag{4.23}$$
$$E_2^{cal} = E_2^{dep} + \beta_1 E_1^{dep}. \tag{4.24}$$

Finally, the deposited energy in each detector can be calculated from Eqs. (4.23) and (4.24) as:

$$E_1^{dep} = \frac{E_1^{cal} - \beta_2 E_2^{cal}}{1 - \beta_1 \beta_2}, \tag{4.25}$$

$$E_2^{dep} = \frac{E_2^{cal} - \beta_1 E_1^{cal}}{1 - \beta_1 \beta_2}, \tag{4.26}$$

The values of β_1 and β_2 were calculated with a similar iterative process that matched the mean values of the spectra of $E_1^{cal}(EV_2)$ and $E_2^{cal}(EV_1)$ between 2700 keV and 3700 keV at 3000 keV (same as for the calculation of α_1 and α_2).

The deposited energy in each detector for each event of all the runs was obtained with Eqs. (4.25) and (4.26). The sum of E_1^{dep} and E_2^{dep}, noted E^{dep} corresponds to $c \cdot E$, where E is the real deposited energy by the β-decay electrons, and c is another calibration coefficient not yet determined.

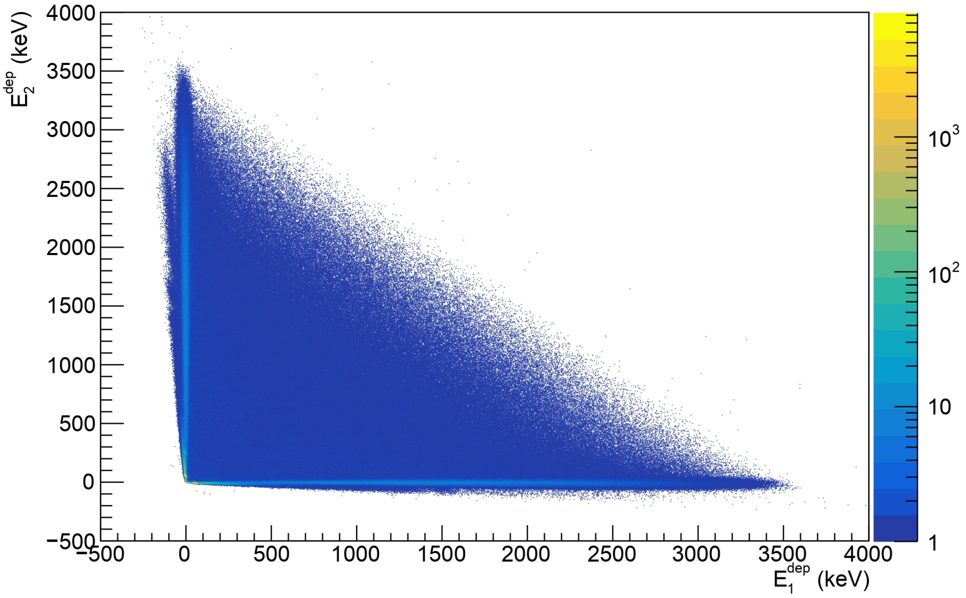

Figure 4.13: The distribution of E_2^{dep} vs. E_1^{dep}.

Figure 4.13 shows the distribution of E_2^{dep} against E_1^{dep}. In this plot, the events that deposited their entire energy inside Det1 are distributed along the horizontal axis, while the events that deposited their entire energy inside Det1 are distributed along the vertical axis. This shows that in case the event deposited its entire energy in Det1, $E_2^{dep} = 0$ and vice-versa. The events lying between these two lines correspond to β particles backscattering from one detector and depositing part of their energy in both detectors. For the calibration of the background data of Set4 and Set5, the parameters α_1, α_2, β_1 and β_2 cannot be calculated with the same procedure. Instead, their values were obtained by the average of the values of runs number 16 and 17, since

Set4 and Set5 were recorded between these two runs.

4.4 Resolution of the detection setup

The resolution of the detector can be characterized by the following expression:

$$\Delta E^2 = (\alpha\sqrt{E})^2 + (\beta E)^2 + \gamma^2. \tag{4.27}$$

Here, the term $\alpha\sqrt{E}$ corresponds to the statistical uncertainty induced by the number of scintillation photons, N_{ph}, collected by the PMTs. The linear term βE originates from the non-homogeneity of the YAP material causing a variation in light production and light collection from different spots within the scintillators. Finally, the constant term γ corresponds to fluctuations of the signals offset.

The resolution for the two detectors was studied prior to the E815S experiment using the detectors in full contact configuration with several calibration sources (Fig. 4.14). Data were taken with ^{22}Na, ^{137}Cs, ^{60}Co and ^{208}Tl calibration sources. The photopeaks of these sources were fitted with a Gaussian function that accounts for the presence of a superposing background (see Appendix C).

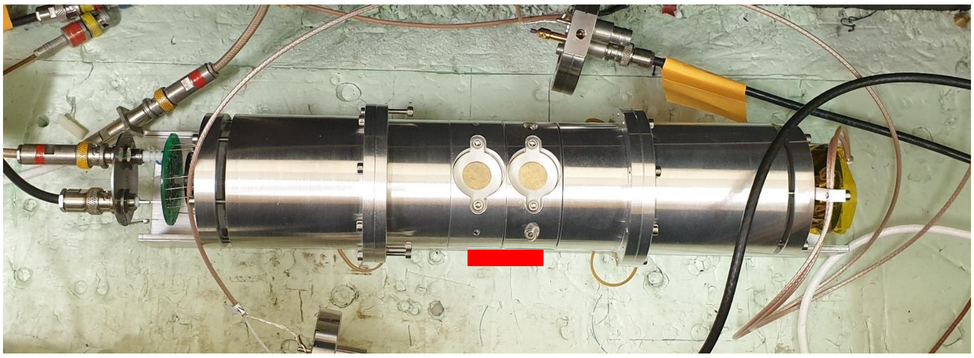

Figure 4.14: The setup used for the calibration tests prior to the E815S experiment. The two detectors are shown in full contact position with the two ^{241}Am sources mounted on top of each of them. The red rectangle represents the position of the gamma calibration source.

The values obtained by the fits for the mean position of each photopeak and its corresponding standard deviation σ were used to calculate the resolution R at each corresponding energy as:

$$R = \frac{FWHM}{mean} = \frac{2.35\sigma}{mean}. \tag{4.28}$$

Then, the resolution values for Det1 and Det2 were plotted against energy, and fitted with the following function derived from Eq. 4.27 (Fig. 4.15):

$$R = \frac{\Delta E}{E} = \sqrt{\left(\frac{\alpha}{\sqrt{E}}\right)^2 + \beta^2 + \left(\frac{\gamma}{E}\right)^2}, \tag{4.29}$$

where α, β and γ were free parameters of the fit function. For Det1, the obtained values by the fit for these parameters were $\alpha = (1.36 \pm 0.13)$ keV$^{1/2}$, $\beta = (0.036 \pm 0.002)$ and $\gamma = (6.96 \pm 11)$ keV.

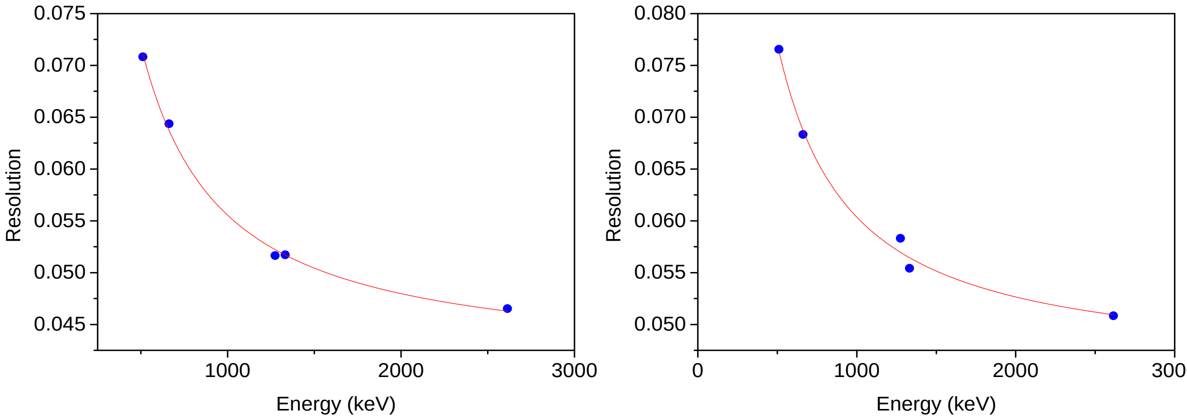

Figure 4.15: The resolution values obtained with the calibration sources for Det1 (left panel) and Det2 (right panel). The black line represents the fit using Eq. (4.29).

Figure 4.16 shows the three components of Eq. (4.27) ("$\alpha\sqrt{E}$", "βE" and "γ") plotted against energy up to 3.5 MeV while using the α, β and γ parameters obtained by the fit of the resolution of Det1. This plot shows that the impact of the term "γ" for energies above 100 keV is negligible relative to the other two terms. For energies below 100 keV, the term "βE" is also very small in comparison with the terms "$\alpha\sqrt{E}$" and "γ".

However, the optical coupling between the PMTs and the scintillators for the two detectors was modified between the off-line runs with calibration sources and the data taking during the experiment (The optical grease layer was changed for both detectors prior to the experiment). This change in the optical coupling means that for a given deposited energy, the number of scintillation photons collected by the PMTs is different. Therefore, the α parameter obtained from the calibration runs is not valid for the analysis of the data of E815S experiment. Additionally, the energy deposition of the ^{6}He decay electrons is very localized (3.5 MeV electrons range in the YAP scintillator is $\sim$ 5 mm) in comparison with the energy deposition of the γ particles of the calibration sources (almost uniformly covering the entire volume of the YAP scintillators). This means that the β parameter obtained by the calibration tests can be overestimated in comparison with the value of β induced by the ^{6}He decay electrons energy deposition inside the YAP. The γ parameter can also be linked to the width of the baseline peak obtained with the charge integration $Q_{baseline}$. This width was found to be similar during the online experiment

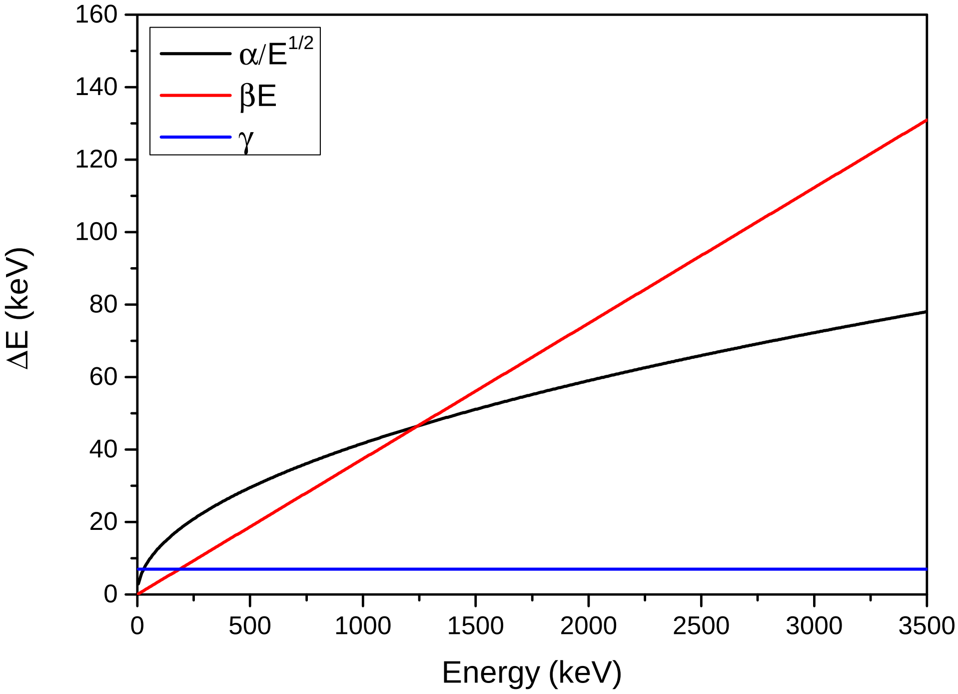

Figure 4.16: The three components of Eq. (4.27) plotted against energy using the α, β and γ parameters obtained by the fit of the resolution values for Det1.

and the calibration tests. In both cases, the baseline width indicates a γ value between 1 keV and 12 keV, depending on the noise model.

Fortunately, the 59.54 keV photopeak of the ^{241}Am source placed on each detector during the experiment can be used to determine an estimate for the α parameter for each detector, since the effect of the β parameter is negligible below 100 keV (Fig. 4.16). Therefore, at 59.54 keV the resolution function of Eq. (4.29) can be written as:

$$R = \sqrt{\left(\frac{\alpha}{\sqrt{E}}\right)^2 + \left(\frac{\gamma}{E}\right)^2}. \tag{4.30}$$

The method used to extract the α parameter from the 59.54 keV photopeaks is the following. First, only the events in the second half of each cycle were chosen to suppress the superposition of the 59.54 keV photopeaks with the ^{6}He decay events. Then, the events corresponding to energy deposited entirely in one of the detectors were selected using the cuts shown in Fig. 4.17. For each detector, the energy spectrum was built using the calibration detailed in the previous section. In summary, two energy spectra were built, with background events that deposited their full energy inside one detector only, corresponding to the energy collected in each PMT. These spectra were fitted at 59.54 keV with Gaussian functions (Fig. 4.18).

With the resolution at 59.54 keV, the parameter α was obtained for all the runs with ^{6}He using Eq. (4.30), where the γ parameter is known from the off-line calibration tests. Figure

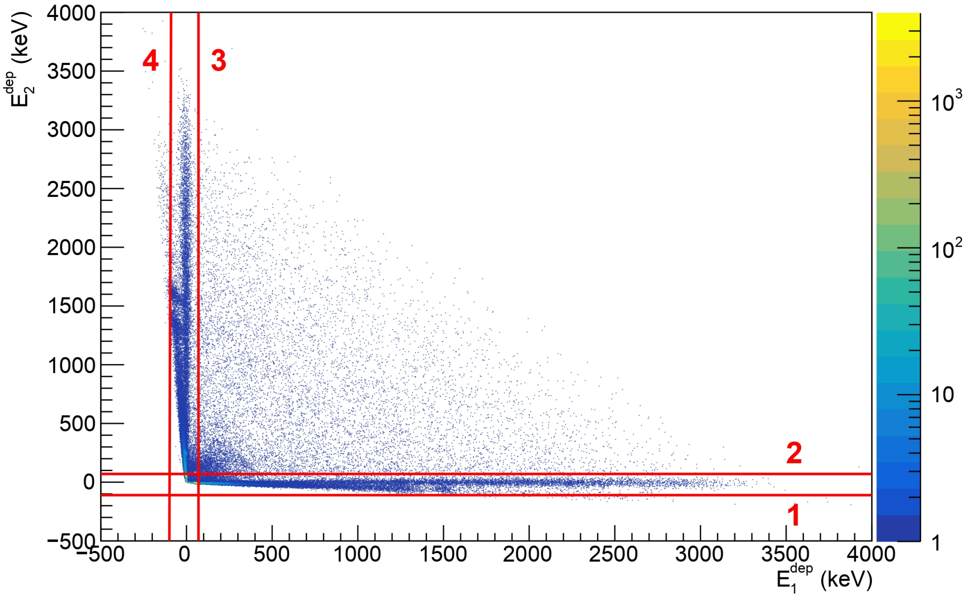

Figure 4.17: The distribution of E_2^{dep} vs. E_1^{dep} for the detected events in the second half of each cycle for one hour run of the experiment for Set1. The red lines represent the cuts used to isolate only the events for whom the energy is totally deposited inside Det1 (the zone between lines 1 and 2) and Det2 (the zone between lines 3 and 4).

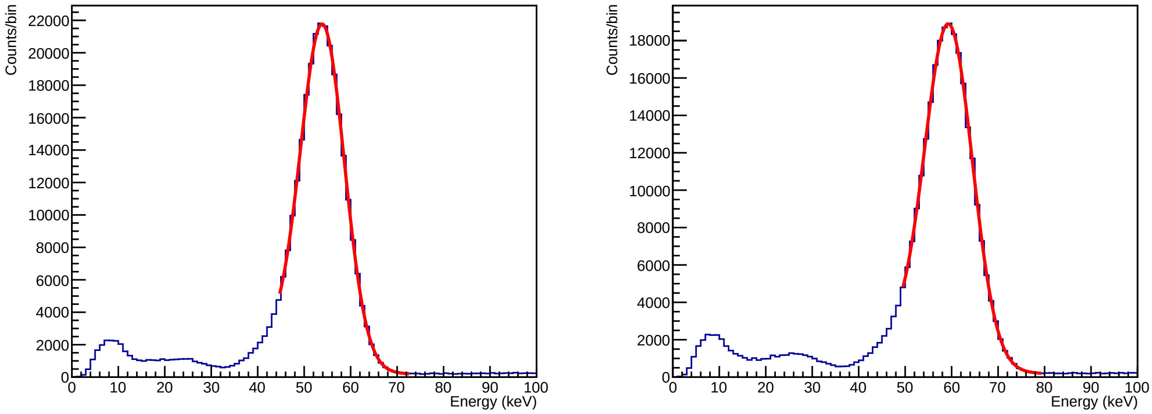

Figure 4.18: The energy spectra obtained for events happening in Det1 (left panel) and Det2 (right panel). The red lines represent the Gaussian fits.

4.19 shows the α parameter obtained for all the runs for the two detectors. It can be noticed that the values are relatively compatible for all the runs, except for some fluctuations within the runs of Set2, which can be explained by the low statistics in these runs. It can be also noticed that the values are not the same for the two detectors, which can be due to a different light collection efficiency.

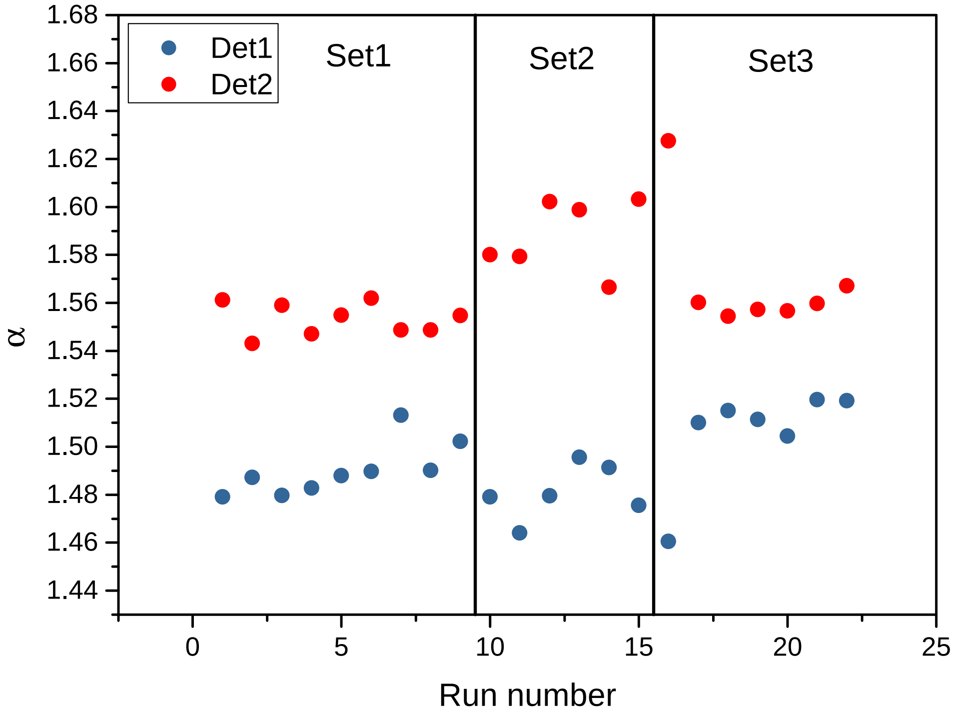

Figure 4.19: The α parameter for the two detectors obtained by the fit of the 59.54 keV photopeak for all the runs.

Finally, the mean value of all the runs for the two detectors, α_{Det1} and α_{Det2}, were calculated. The resolution of the detection setup, which was mentioned in Eq. (4.22), can thus be characterized as:

$$\sigma(E) = \frac{1}{2.35}\sqrt{\alpha^2 E + \beta^2 E^2}, \tag{4.31}$$

where α is the average of α_{Det1} and α_{Det2}. The value of β cannot be determined precisely for the β particles that are well localized in the center of the detection volume. It can be either fixed to zero or left as a free parameter of the fit function.

4.5 Events selection

Prior to the construction of the energy spectra, several event selections were applied to the data. These selections are reported in the following.

4.5.1 Data cleaning

First, all the events that belong to cycles with SBR smaller than 5 were discarded since those were not accounted for in the first calibration with the 59.54 keV photons. In addition, a dead-time of $\tau_{DT} = 3$ µs was imposed on the data in order to eliminate any effect of after-pulses.

Also, only the events that were detected in coincidence in the two detectors were chosen to eliminate the background due to dark noise.

Figure 4.20 shows the distribution of the baseline window integration $Q_{baseline}$ for a one hour run of Set1 with Det1. In addition to the expected normal distribution around zero, two other distributions to the right and to the left of the normal distributions were observed. These correspond to events for whom the BLR software has either overestimated or underestimated the background of the signal. These events must be discarded because the energy calibration is not valid for them. This was done by fitting the main $Q_{baseline}$ distribution around zero with a Gaussian function to obtain the standard deviation σ of the distribution. Then, the events with $|Q_{baseline}| > 2\sigma$ were discarded (outside the red lines in Fig. 4.20). These events correspond to $\sim 5\%$ of the total statistics.

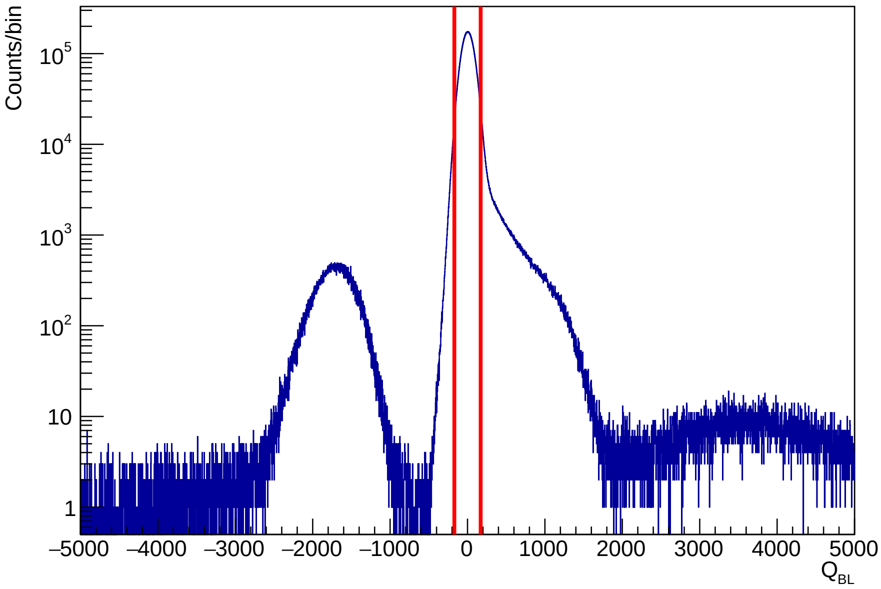

Figure 4.20: The baseline distribution obtained with Det1. The red lines represent the events selection on the baseline.

4.5.2 Q_{fast}/Q_{tot} selection

The selection of events based on their Q_{fast}/Q_{tot} ratio is very important to identify the β-decay events in the YAP. With this selection, the events with deposited energy in the YAP scintillators can be discriminated from those with deposited energy in the PVT. For the Fierz term analysis, a selection like the one shown in Fig. 3.2, which was used for the first calibration, cannot be used. With such a basic selection, a larger amount of the events at low energy are discarded, due to the shape of the distribution which is dependent on the energy. Therefore, in order to distinguish the β-decay events that deposited energy within the YAP scintillators, a selection that takes into account the shape of the Q_{fast}/Q_{tot} distribution as a function of E_{dep} must be used.

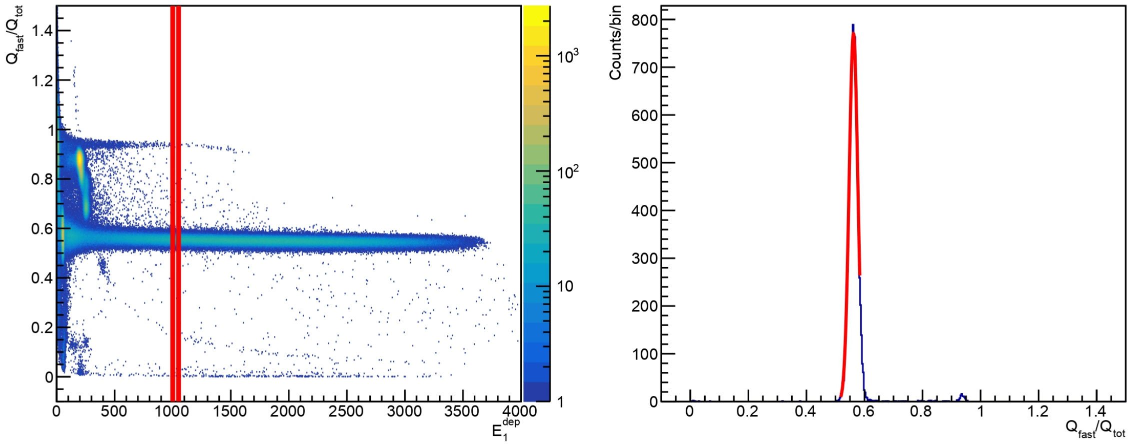

Figure 4.21: Left panel: the Q_{fast}/Q_{tot} distribution for a one hour run of Set1. The red lines represent one of the 50 keV intervals. Right panel: a histogram filled with the Q_{fast}/Q_{tot} values for the events within the red lines in the left panel. The red line is the Gaussian fit used to fit the distribution.

First, for each detector, the events were divided into 50 keV intervals in E_{dep} (left panel of Fig. 4.21). For each interval, a histogram was filled with Q_{fast}/Q_{tot} values for all the events within the interval. Then, these histograms were fitted with a Gaussian function in order to extract the mean value, μ, and the standard deviation, σ (right panel of Fig. 4.21). The interval of the fit was chosen to minimize as much as possible the effect of other contributions with larger Q_{fast}/Q_{tot}. With the obtained values of μ and σ, the limits of the selection were set at $(\mu \pm 4\sigma)$. These limits were chosen in order to ensure that more than 99.9% of the ^{6}He decay events were included.

Then, the calculated values of $(\mu + 4\sigma)$ and $(\mu - 4\sigma)$ were plotted against the mean value of each energy interval for the two detectors and fitted respectively with the following exponential functions (Fig. 4.22):

$$P^{+}_{Det1}(E_1^{dep}) = P_0^{+} e^{\left(-E_1^{dep}/P_1^{+}\right)} + P_2^{+} e^{\left(-E_1^{dep}/P_3^{+}\right)} + P_4^{+} E_1^{dep} + P_5^{+}, \tag{4.32}$$

$$P^{-}_{Det1}(E_1^{dep}) = P_0^{-} e^{\left(-E_1^{dep}/P_1^{-}\right)} + P_2^{-} e^{\left(-E_1^{dep}/P_3^{-}\right)} + P_4^{-} E_1^{dep} + P_5^{-}, \tag{4.33}$$

$$P^{+}_{Det2}(E_2^{dep}) = P_0^{+} e^{\left(-E_2^{dep}/P_1^{+}\right)} + P_2^{+} e^{\left(-E_2^{dep}/P_3^{+}\right)} + P_4^{+} E_2^{dep} + P_5^{+}, \tag{4.34}$$

$$P^{-}_{Det2}(E_2^{dep}) = P_0^{-} e^{\left(-E_2^{dep}/P_1^{-}\right)} + P_2^{-} e^{\left(-E_2^{dep}/P_3^{-}\right)} + P_4^{-} E_2^{dep} + P_5^{-}, \tag{4.35}$$

where P_i^{+} and P_i^{-} were free parameters of the fit for respectively the $(\mu + 4\sigma)$ and $(\mu - 4\sigma)$

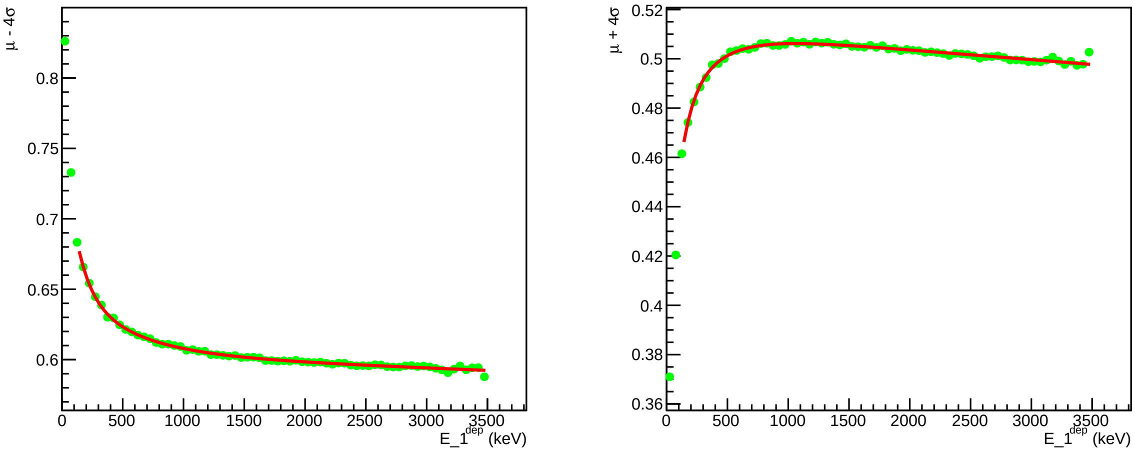

Figure 4.22: The values of $(\mu + 4\sigma)$ (left panel) and $(\mu - 4\sigma)$ (right panel) plotted against the mean value of the 50 keV energy intervals for Det1. The red lines represent the fit respectively with Eqs. (4.32) and (4.33).

distributions. Figure 4.23 shows the events that have a Q_{fast}/Q_{tot} ratio between P^{+}_{Det1} and P^{-}_{Det1} (left panel), and between P^{+}_{Det2} and P^{-}_{Det2} (right panel). However, due to the shape of these functions, some events can satisfy the selection of one detector without the other. Therefore, for each event, the energies E^{dep}_{1} and E^{dep}_{2} are compared. If E^{dep}_{1} was bigger than E^{dep}_{2}, the selections of Det1 are used. Otherwise, the selections of Det2 are the used ones.

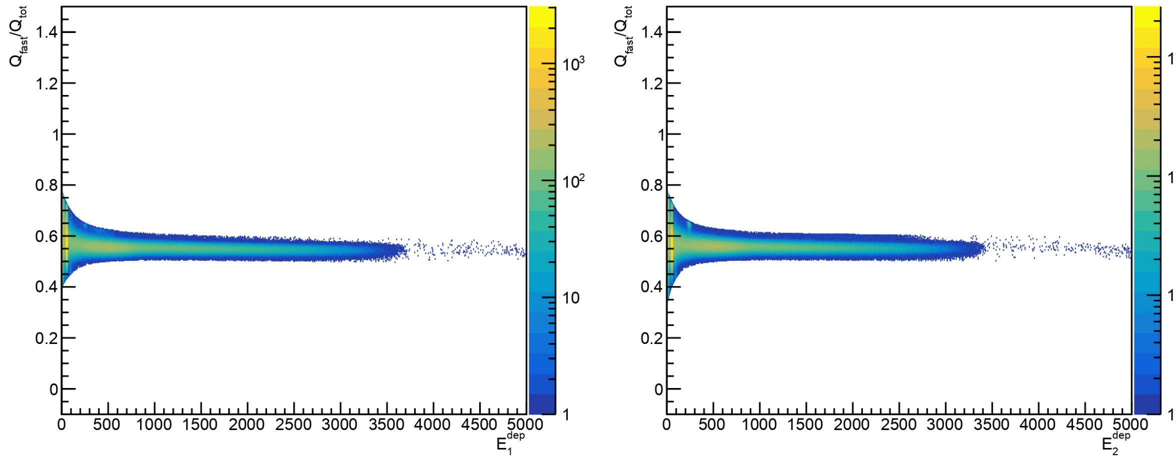

Figure 4.23: Distribution of Q_{fast}/Q_{tot} after the selection of events for Det1 (left panel) and Det2 (right panel).

4.5.3 E_2^{dep} vs. E_1^{dep} selection

The left panel of Fig. 4.24 shows a zoom on the E_2^{dep} vs. E_1^{dep} plot for a one hour run of Set1. This plot shows on the vertical axis the distribution of ^{6}He events that deposited their entire energy inside Det2 (EV_2). In addition, a distribution of events with a negative slope is observed to the left of the vertical distribution. The same distribution is also visible in the E_2^{dep} vs. E_1^{dep} plot for the runs of Set4 and Set5 (right panel of Fig. 4.24). This set of events can be attributed to background such as the Bremsstrahlung photons and the electrons produced by the ^{6}He implantation on the collimator attached to Det2 and to γ particles from the ambient background. The same distribution also exists on the side of the events that deposited their entire energy in Det1 (EV_1). Therefore, by applying appropriate selection limits, the effect of the collimator induced effects can be reduced.

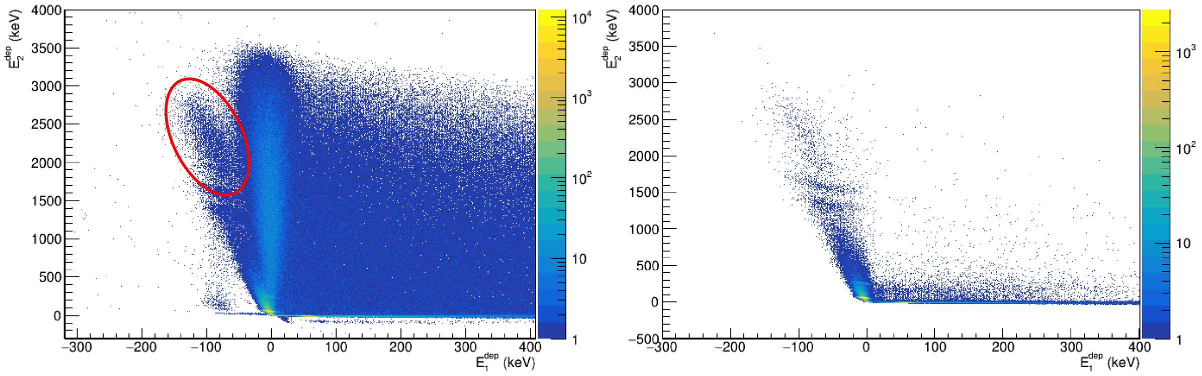

Figure 4.24: Left panel: a zoom on the E_2^{dep} vs. E_1^{dep} plot, for a one hour run of Set1, on the set of events that deposited their entire energy in Det2, showing in addition to this set another distribution of events with a different slope that was assigned to the induced Bremsstrahlung photons and the direct detected electron (inside the red ellipse) from ^{6}He implantation on the collimator. Right panel: the same zoom on the E_1^{dep} vs. E_2^{dep} for a run of Set4.

These limits were obtained with a method similar to the one used for the Q_{fast}/Q_{tot} selections, by dividing the events into 50 keV intervals of E_1^{dep} and E_2^{dep} (left panel of Fig. 4.25). Then, for each interval of E_1^{dep}, a histogram was build with the values of E_2^{dep} and vice-versa. These histograms were then fitted with a Gaussian function to obtain the mean value, μ and the standard deviation σ of the horizontal and vertical distributions (right panel of Fig. 4.25).

These limits will be set to remove part of the background events to the left of EV_2 and to the bottom of EV_1. The values of $(\mu - 4\sigma)$ for EV_1 and EV_2 were calculated and plotted against the mean values of the 50 keV energy intervals of E_1^{dep} and E_2^{dep} (respectively the left panel and right panel of Fig. 4.26). The $(\mu - 4\sigma)$ selection ensures that the majority of ^{6}He events are kept. These values were then fitted between 500 keV and 3000 keV with a second order polynomial function for EV_1 and EV_2, respectively noted $f_1\left(E_1^{dep}\right)$ and $f_2\left(E_2^{dep}\right)$, which were

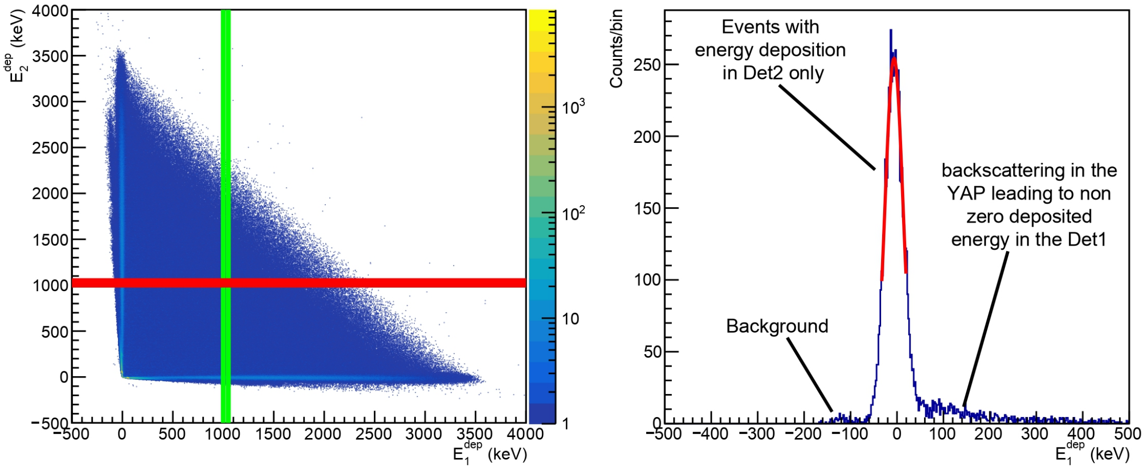

Figure 4.25: Left panel: E_2^{dep} vs. E_1^{dep} distribution for a one hour run of Set1. The green and red lines represent the 50 keV intervals of respectively E_1^{dep} and E_2^{dep}. Right panel: histogram filled with the E_1^{dep} values for the events within the green lines in the left panel. The red line is the Gaussian fit used to fit the distribution.

used for the selection of events. Below 500 keV, the presence of the Bremsstrahlung peak prevents a good separation of the ^{6}He events. Therefore, between 0 and 500 keV $f_1\left(E_1^{dep}\right)$ and $f_2\left(E_2^{dep}\right)$ were extrapolated from the fit above 500 keV.

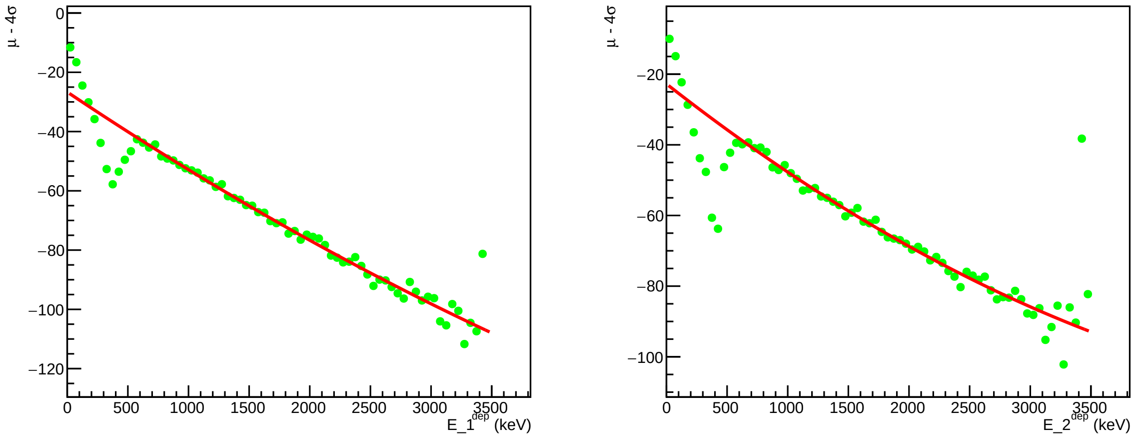

Figure 4.26: The values of $(\mu - 4\sigma)$ for the different intervals of E_1^{dep} (left panel) and E_2^{dep} (right panel) plotted against the mean value of the 50 keV energy intervals. The red lines represent the fit with a second order polynomial function.

Figure 4.27 shows the distribution of E_2^{dep} vs. E_1^{dep} values with the functions $f_1\left(E_1^{dep}\right)$ and $f_2\left(E_2^{dep}\right)$ represented by the red lines. The set of events between $f_1\left(E_1^{dep}\right)$ and $f_2\left(E_2^{dep}\right)$ will be noted EV_{in}, while the set of remaining events will be noted EV_{out}. The events of EV_{out}

will be used later as a normalization reference for the subtraction of the collimator induced background.

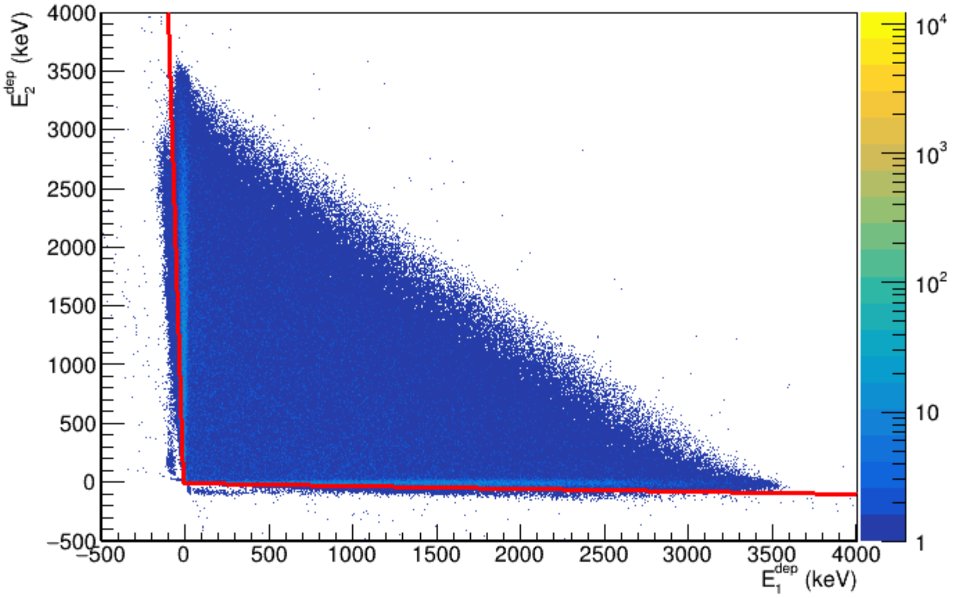

Figure 4.27: Distribution of E_2^{dep} vs. E_1^{dep} values for a one hour run of Set1. The red lines represent the selection cuts that separate the collimator induced background events.

4.6 Fitting procedure

4.6.1 Background treatment

The energy spectra for the events of each set must be obtained with a subtraction of all the background contributions. This background can be divided into two groups, the constant background and the collimator induced background. The constant background, shown in Fig. 3.17, is obtained from the selection of the second half of the cycles (between 8.5 sec and 13.5 sec for the cycles of Set1 and Set3, and 8.5 sec and 29.5 sec for Set2). It was subtracted for each set using the appropriate normalization factor given by the time duration of each selection window.

The subtraction of the collimator induced background is more complicated. The only way to determine precisely this background consists in using the data of Set4 and Set5, because it is impossible to estimate this background with enough precision from the simulations (as shown in Fig. 3.16). However, the precision on the background subtraction remains limited by the statistics within Set4 and Set5. This background includes the Bremsstrahlung photons noted EV_{Brem}, and the electrons reaching directly the detection volume noted EV_{e^-}. The ratio of these two contributions varies with the variation of the amount of ^{6}He$^+$ implantation on the inner and the outer surface of the collimator. Therefore, this ratio depends on the profile of the incident $^{6}\mathrm{He}^{+}$ beam which was not stable throughout the experiment.

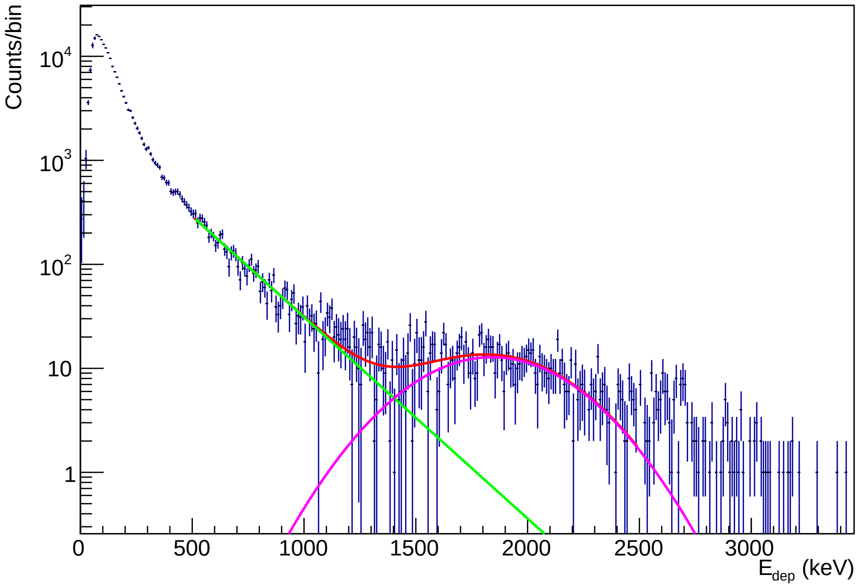

Figure 4.28: Spectrum of E^{dep} for a one hour run of Set4 with EV_{in} selection. The red line represents the fit of the histogram with a Gaussian function (magenta line) superimposed with an exponential function (green line).

The ratio of the remaining EV_{e^-} events inside the set EV_{in} is very small. These events were subtracted using an analytical function that estimates their distribution. This function was obtained by fitting the EV_{e^-} distribution inside EV_{in} from Set4 and Set5. This fit was performed using a Gaussian function superposed with an exponential background to reproduce the tail of the Bremsstrahlung peak (Fig. 4.28). Then, the function was normalized with the ratio of the integral of the energy distributions of EV_{out} between 1500 keV and 3000 keV (the energy interval that contains only the contribution of EV_{e^-}) (Fig. 4.29).

For the events of EV_{Brem}, an accurate normalization is not possible due to the very large amplitude of this background contribution within the EV_{in} selection and its small contribution within the EV_{out} selection. The normalization factor N_{Brem} needed for this background subtraction will thus be a free parameter of the final fit of the deposited energy spectrum. This will be discussed in more detail in Sec. 4.6.3.

4.6.2 Pileups simulation

One of the systematic effects that distorts the shape of the deposited β-energy spectrum is the effect of pile-ups. The estimation of the pile-ups contribution cannot be done with a simple convolution like the one used in Chap. 3 because of the Q_{fast}/Q_{tot} selection of events. The

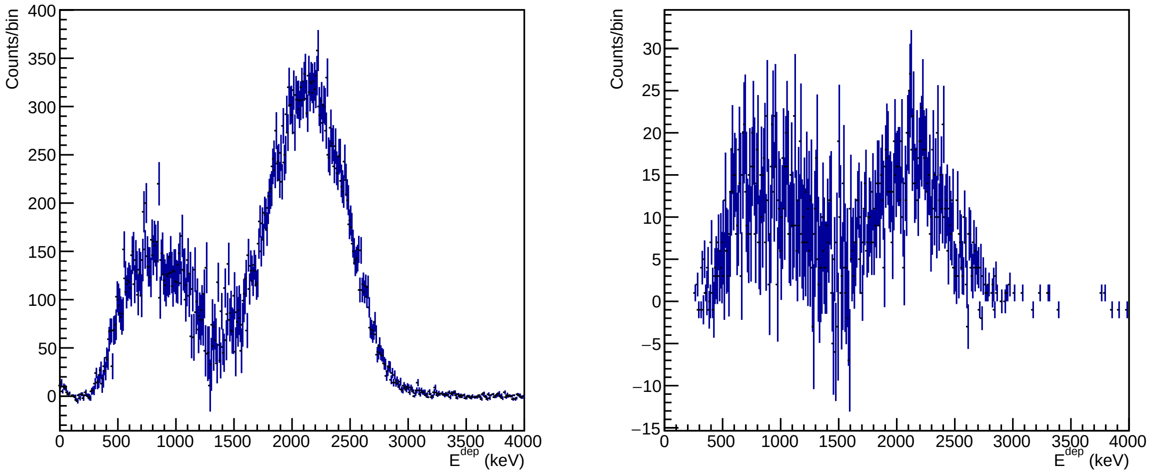

Figure 4.29: The distribution of E^{dep} for the events of EV_{out} for Set1 (left panel) and Set4 (right panel). The difference in the ratio between the two distributions below and above 1500 keV is due to the different implantation of $^{6}\mathrm{He}^{+}$ on the outer surface of the collimator.

ratio of the pile-ups events that enter the Q_{fast}/Q_{tot} selection and their deposited energies can only be estimated with a simulation which is described below.

First, the Von Neumann method is used to generate two energy values E_1 and E_2 between 0 and the endpoint energy E_0 using the experimental β spectrum to simulate two piled-up events. The integral of the PMT signal $R(T)$ obtained from the oscilloscope frames between 0 and 300 ns was calculated to determine the ratio of the second signal that is integrated in the integration window used for Q_{tot} (right panel of Fig. 4.30).

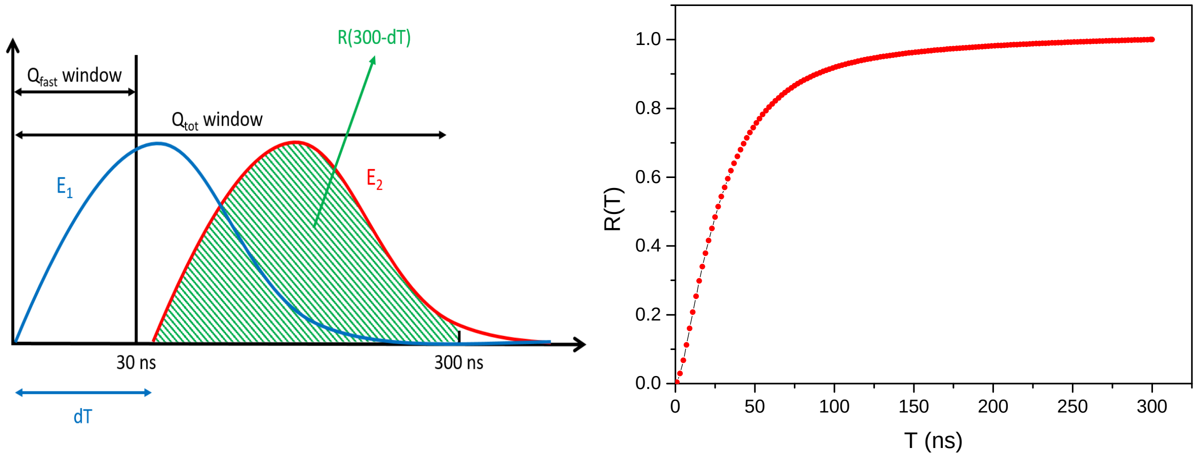

Figure 4.30: Left panel: a sketch explaining the generation of energies in the simulation. Right panel: the integration of the typical PMT signal, obtained from the oscilloscope traces, between 0 and 300 ns.

A dT value is then uniformly generated between 0 and 300 ns representing the time difference between the two events. The integration ratio of the second event is obtained by $R(300-dT)$ (left panel of Fig. 4.30). Then, the integration of the two events within the two integration windows of 30 ns and 300 ns, noted respectively E_{fast} and E_{tot}, were calculated in order to calculate the ratio E_{fast}/E_{tot} that represents the Q_{fast}/Q_{tot} ratio. Two equally probable cases must be considered. The first corresponds to two events with their full deposited energy inside the same detector. In this case, the fast and total components are calculated from:

$$E_{tot} = E_1 + E_2 \times R(300-dT), \tag{4.36}$$

$$E_{fast} = E_1 \times R(30) + E_2 \times R(30-dT). \tag{4.37}$$

where $E_2 \times R(300-dT)$ is the ratio between the integration of the second event's energy inside the 300 ns window, and $E_1 \times R(30)$ and $E_2 \times R(30-dT)$ are respectively the ratio of the integration of the first and second event's energy inside the 30 ns window.

The second case corresponds to two events with their full deposited energy inside each of the two detectors. In this case, one has to verify as well the ratio of light that is transmitted into the other detector. This is done by comparing the amount of collected light by each PMT $E_1^{col} = 0.8E_1 + 0.2E_2 \times R(300-dT)$ and $E_2^{col} = 0.2E_1 + 0.8E_2 \times R(300-dT)$, where the 0.8 and the 0.2 factors correspond to the ratio of light collected by the PMT of the detector where the energy deposition happened and the other detector's PMT. We remind that in the data cleaning procedure, the Q_{fast}/Q_{tot} selection is done using only one PMT signal corresponding to the detector with the higher reconstructed energy. The fast and total components of the simulation are thus calculated from:

$$E_{tot} = \left(r_1 E_1 + r_2 E_2 \times R(300-dT)\right)/0.8, \tag{4.38}$$

$$E_{fast} = \left(r_1 E_1 \times R(30) + r_2 E_2 \times R(30-dT)\right)/0.8, \tag{4.39}$$

where

$$\begin{cases} r_1 = 0.8 \text{ and } \mathrm{r}_2 = 0.2 & \text{if } \mathrm{E}_1^{\mathrm{col}} > \mathrm{E}_2^{\mathrm{col}} \\ r_1 = 0.2 \text{ and } \mathrm{r}_2 = 0.8 & \text{otherwise} \end{cases} \tag{4.40}$$

Then, the E_{fast}/E_{tot} ratio from the simulation was convoluted with a Gaussian function whose width $\sigma(E)$ was adjusted in order to reproduce the experimental data. Figure 4.31 shows the E_{fast}/E_{tot} ratio distribution obtained for the two cases (hits in the same or different detectors). In both cases, the Q_{fast}/Q_{tot} selections were applied to the two E_{fast}/E_{tot} distributions (the red lines) in order to obtain the ratio of pile-up events that enters the selections in both cases.

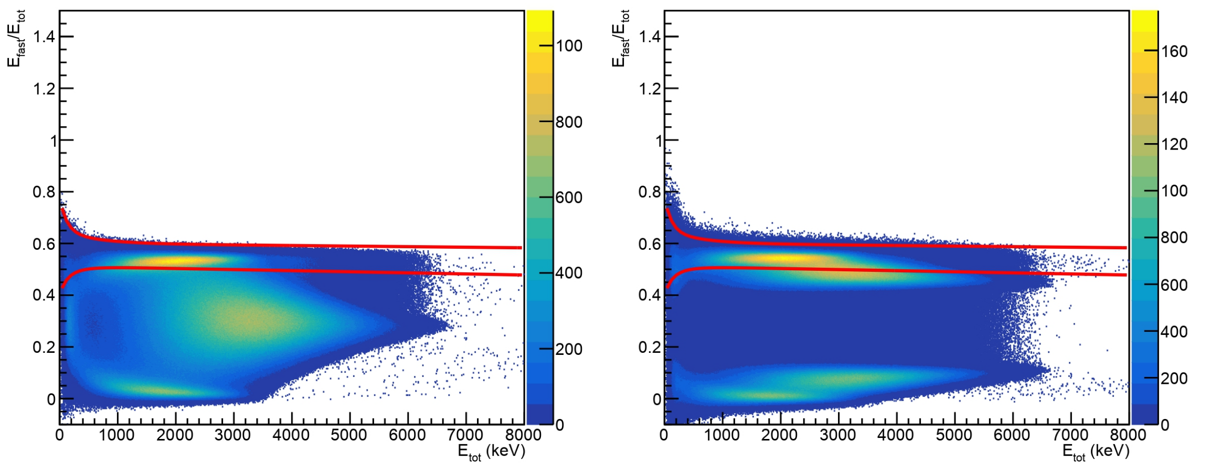

Figure 4.31: E_{fast}/E_{tot} vs. E_{tot} plots for the one detector case (left panel) and the two detectors case (right panel). The red lines represent the Q_{fast}/Q_{tot} selections.

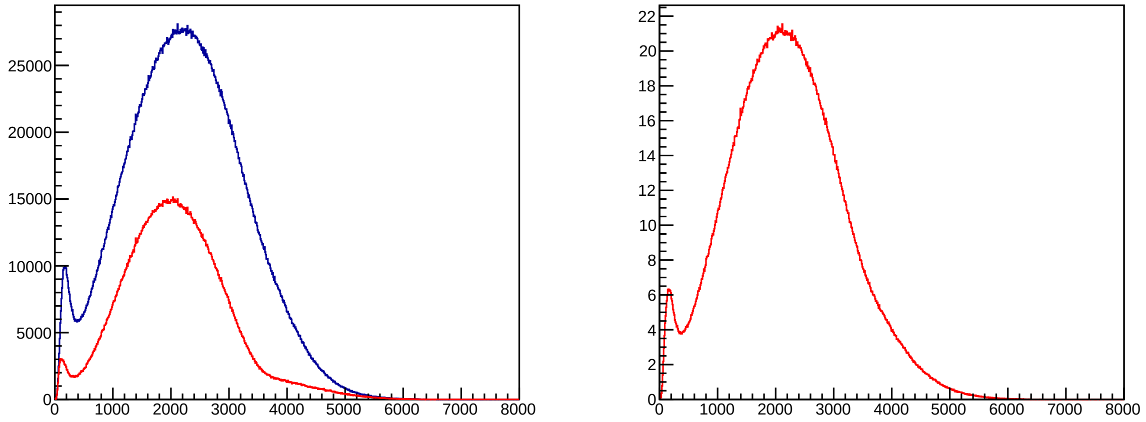

Figure 4.32: Left panel: the spectrum of E_{tot} obtained after applying the Q_{fast}/Q_{tot} selection for the pile-up in one detector (blue) and two detectors (red). Right panel: the pile-ups spectrum obtained by the sum of the two spectra of the left panel after normalization with the probability of having a pileup. The two plots were obtained with the rates of Set1.

The right panel of Fig. 4.32 shows a histogram filled with E_{tot} after the Q_{fast}/Q_{tot} selection for the case of pile-up in one detector (blue line) and in the two detectors (red line). The right panel shows the sum of the two histograms that accounted for the equal probability of the two cases and after normalization with the probability for pile-ups that was calculated from the rate of ^{6}He in each cycle using Eq. (3.14). In principle, this histogram shows the contribution of the pile-up of ^{6}He events to the shape of the experimental β-spectrum of Set1. The contribution of ^{6}He-α, and ^{6}He-γ pile-ups were estimated similarly while using the energy distribution respectively of the α particles in the PVT, and the constant background (Fig. 3.17) for the generation of E_2.

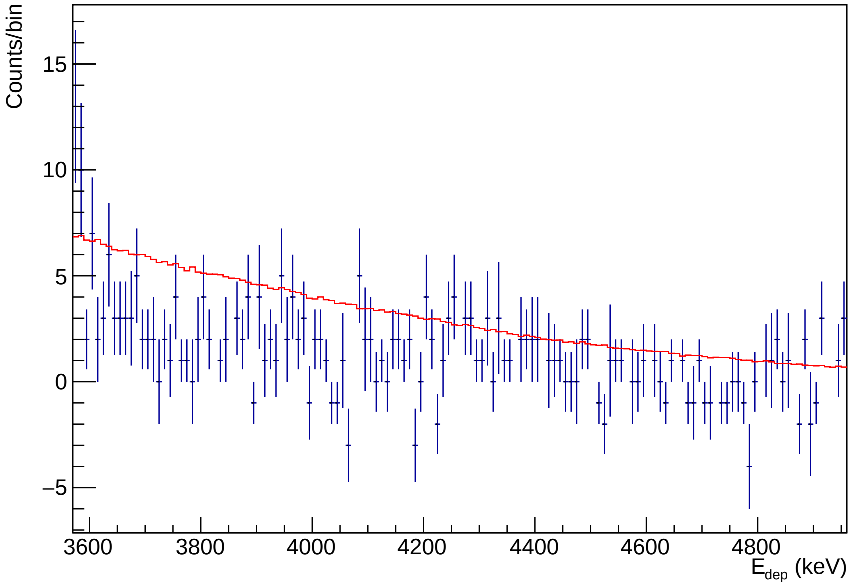

Figure 4.33: The experimental deposited β-energy spectrum obtained by Set1 (blue) with the statistical error bars on each bin, with the pile-ups from simulation (red).

However, a comparison between the pile-ups spectrum and the experimental spectrum of Set1, above 3600 keV (Fig. 4.33) shows a slight discrepancy. This means that our pile-ups simulation fails to estimate properly the number of pile-up events, and needs to be studied in more detail.

4.6.3 Fitting the spectra

The experimental β-energy spectrum for each set is constructed with the calibrated energies E_{dep}, for the events EV_{in} after the subtraction of all backgrounds. These spectra will be fitted within the interval [100;3500] keV with the following function:

$$F(W) = N\left\{\sum_{i=-1}^{2} \alpha_i \left[g_i(c\cdot W) + f_i(c\cdot W)\right] + b_{GT}\left[g_{-1}(c\cdot W) + f_{-1}(c\cdot W)\right]\right\} \circledast \mathrm{Gaus}\left(0, \sigma(\mathrm{c}\cdot\mathrm{W})\right), \tag{4.41}$$

which is adapted from Eq. (4.22) to include a calibration coefficient c that was mentioned in Sec. 4.3.2. The parameters α_i were calculated with the known theoretical corrections mentioned in Sec 4.1. The expression of $\sigma\left(c\cdot W\right)$ was obtained from Eq. (4.15), where β was at this stage fixed to zero (because of the interactions of the very well localized electrons inside the YAP).

The parameters N, c, b_{GT} and the α coefficient involved in the resolution $\sigma(c \cdot W)$ (Eq. (4.31)) were free parameters of the fit function. The bin width in the experimental histogram was fixed to 10 keV resulting in a number of degrees of freedom for the fits of 337.

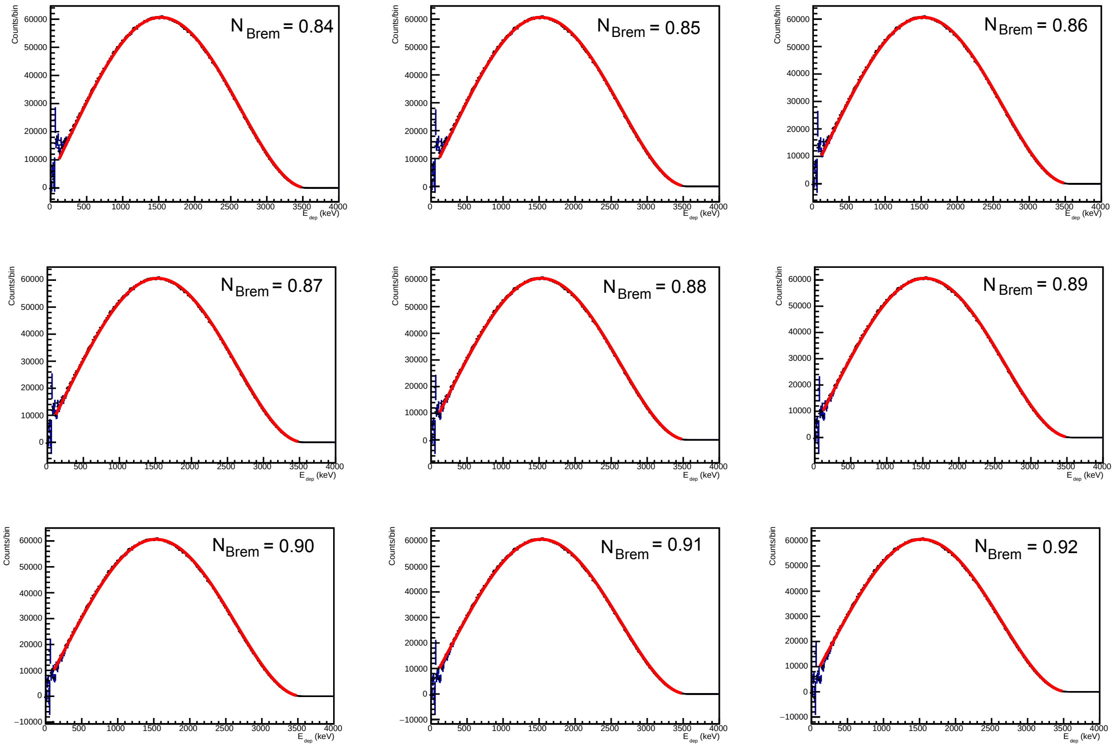

Figure 4.34: The β-energy spectrum obtained after the subtraction of the Bremsstrahlung peak with several normalizations. The red lines represent the fit of the spectra with Eq. (4.41).

The contribution of EV_{Brem} inside the set EV_{in} was subtracted with the data of Set4 and Set5. The set EV_{out} was used for the normalization by calculating the integral of the distribution of events in EV_{out} between 500 and 1200 keV (the energy interval that contains the contribution of EV_{Brem}) (Fig. 4.29). However, this normalization is not precise enough to have a clean subtraction of EV_{Brem} events. This is due to the different implantation area of $^{6}\text{He}^{+}$ on the collimator, in addition to the limited statistics within Set4 and Set5 ($\sim$300 acquisition cycles out of a total of $\sim$6000). Therefore, several normalization coefficients, N_{Brem}, were used for each set to normalize the distribution of EV_{Brem} within EV_{in} for the data of Set4 and Set5 prior to the subtraction of these events from the EV_{in} distribution of Set1, Set2, and Set3. Then, each of the resulting spectra was fitted with Eq. (4.41) (Fig. 4.34). Note that the statistical uncertainty from the Bremsstrahlung data was properly accounted for in the final spectra.

For each fit, the χ^2 value was calculated and plotted against the coefficient N_{Brem} used for the subtraction of EV_{Brem}, alongside the values of b_{GT} (Fig. 4.35). The distribution of the χ^2 values was then fitted with a second order polynomial function. The best N_{Brem} coefficient and b_{GT} values were obtained from the minimum of the function (the value with the lower χ^2 value noted "χ^2_{min}"). The statistical uncertainty due to the subtraction of EV_{Brem} was obtained by calculating the difference between the two values of b_{GT} corresponding to $\chi^2_{min}+1$.

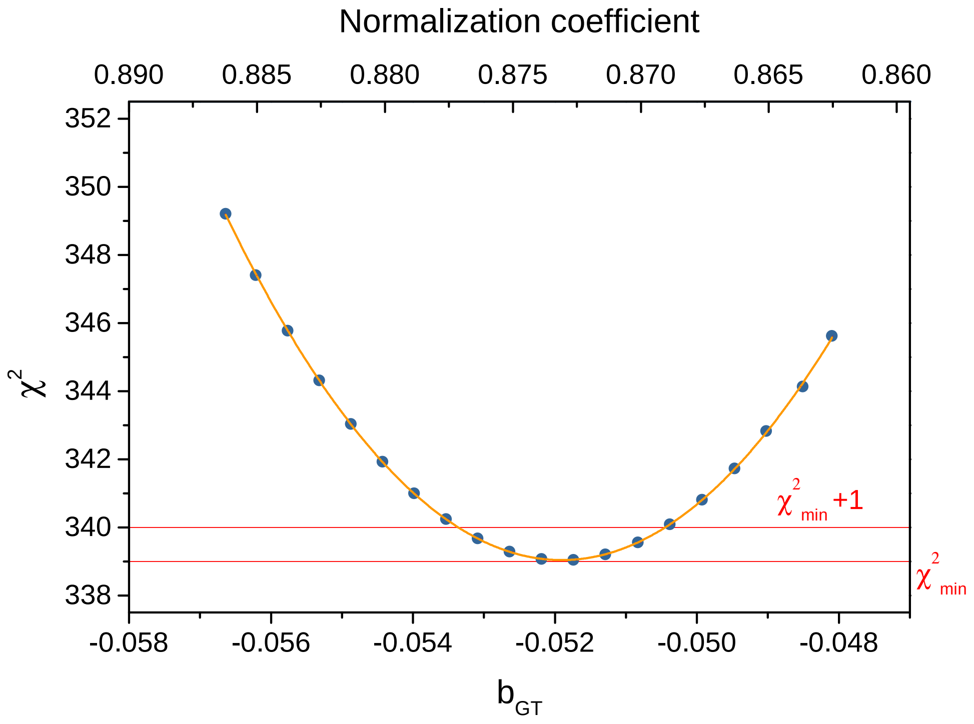

Figure 4.35: The χ^2 values obtained from the fit of the spectra plotted against the obtained results of b_{GT} and the normalization coefficients. The yellow line is a fit with a second order polynomial function. The horizontal lines corresponds to χ^2_{min} and $\chi^2_{min}+1$ values.

The goodness of the fits was validated with the χ^2 values and the standard residuals. Figure 4.36 shows the fits of the β-energy spectrum obtained for Set1, Set2 and Set3 after the subtraction of EV_{Brem} with the normalization coefficient N_{Brem} that corresponded to χ^2_{min}, in addition to the distribution of the standard residuals. These do not show any evidence of a bad fitting of the spectra.

4.7 Study of systematic effects

In this section, we give an overview of the potential systematic effects entering the extraction of the Fierz interference term by the fit of the experimental deposited β-energy spectra. The energy range of the fit function was also set between 100 keV and 3500 keV for the study of the systematic effects. The effect of the theoretical corrections, of the Bremsstrahlung escape correction, and of the convolution with the detector's resolution were studied with simulated data. For this purpose, several sets of 10^8 events were generated for GEANT4 with Eq. (4.17),

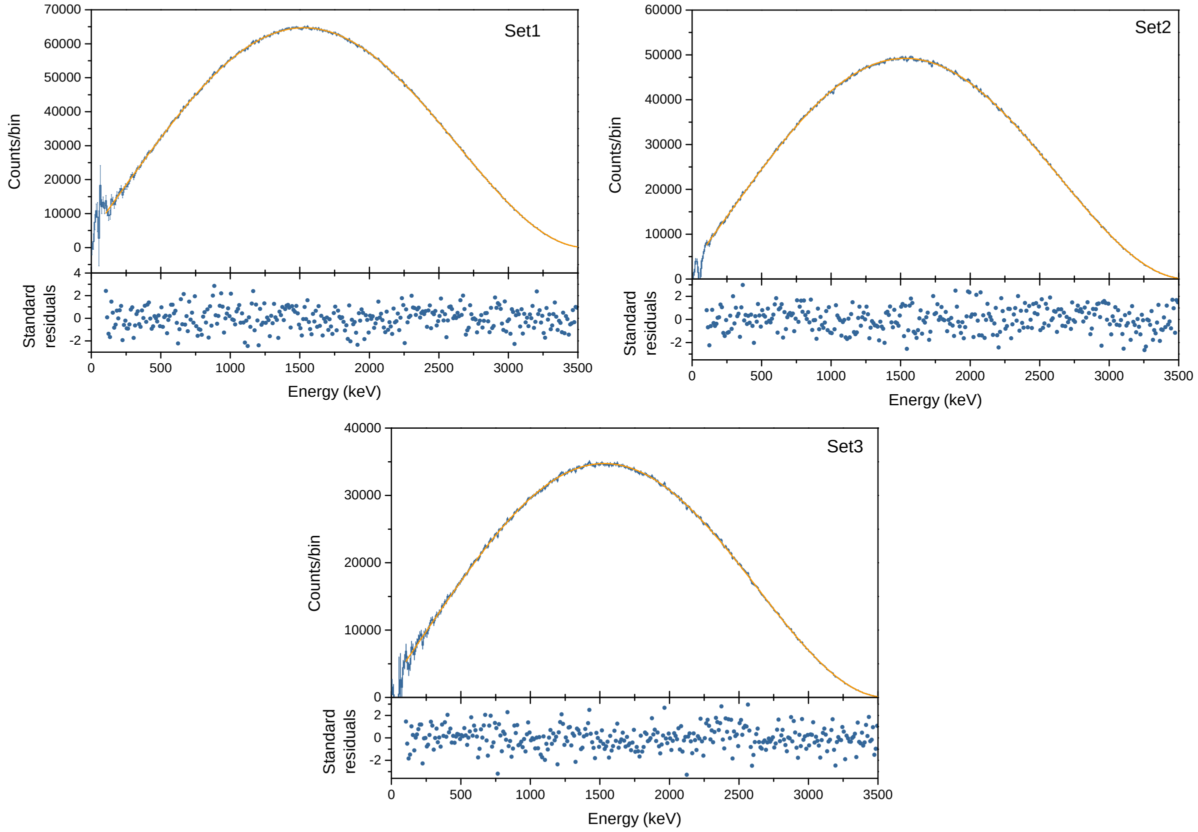

Figure 4.36: The experimental β-spectrum obtained for all the events of each set, after subtraction of backgrounds and the Bremsstrahlung peak with the normalization coefficient obtained for the lowest χ^2, with the standard residuals of the fits.

where the parameters α_i $(i = -1, 0, 1, 2)$ were fixed to the calculated values with the theoretical corrections introduced in Sec. 4.1.

4.7.1 Theoretical corrections

The largest theoretical corrections to the shape of the β-energy spectrum are the hadronic and radiative corrections. The effect of these corrections on the extracted value of b_{GT} is described below.

4.7.1.1 Weak magnetism form factor b_{WM}

The largest parameter entering the hadronic corrections is the weak magnetism form factor b_{WM}, which was fixed to the reported value in Ref. [69] noted here $b_{WM\mathrm{ref}}$. The effect of fixing the value of b_{WM} used in the fit function on the resulting b_{GT} was studied with simulated data. The deposited energy spectrum obtained by the simulation, with $b_{GT} = 0$, was fitted with Eq. (4.41) while fixing the value of b_{WM} with several values ranging between $b_{WM} \pm 20\%$. Figure (4.37) shows the values of b_{GT} obtained by these fits. These values show a linear dependence between the obtained b_{GT} and the fixed value of b_{WM}. The ratio of the change in b_{GT} relatively to the change in $\Delta b_{WM} = \frac{b_{WM}}{b_{WM\text{ref}}}$ is given by $\frac{\Delta b_{GT}}{\Delta b_{WM}} = 0.026$. Here Δb_{GT} corresponds to the absolute uncertainty on b_{GT}. The relative uncertainty of b_{WM} is in the order of about 1% (Eq. (4.6)), which corresponds to an absolute systematic uncertainty of $\Delta b_{GT} = 2.6 \cdot 10^{-4}$.

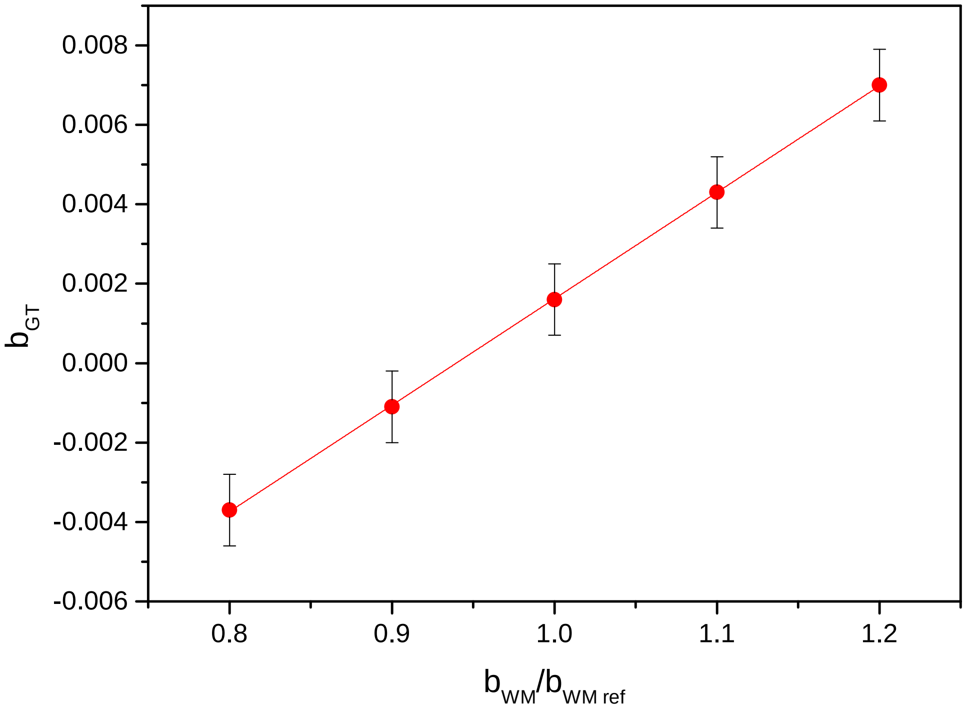

Figure 4.37: The obtained values of b_{GT} from the fits of the simulated data against the values of b_{WM} fixed within the fit function. The red line is a linear fit.

4.7.1.2 Radiative corrections

The radiative corrections to the shape of the β-spectrum were obtained with a simulation. The effect of including these corrections to the fit function on the resulting value of b_{GT} was studied by fitting the simulated deposited energy spectrum with the function of Eq. (4.41), where the function $f_0(W)$ was calculated to include only the Bremsstrahlung energy escape, without taking into account the effect of the generation of virtual and hard Bremsstrahlung photons. The left panel of Fig. 4.38 shows the deposited energy spectrum obtained from the simulation, with the fit function (the red line), and the right panel of Fig. 4.38 shows the distribution of the residuals. The obtained χ^2 in addition to the distribution of the residuals show the sensitivity of the fit to the radiative corrections. The value of b_{GT} obtained from this fit was deviated by $3.7 \cdot 10^{-2}$ from the value obtained by the fit of the same histogram with a fit function that accounts for the radiative corrections. The order α radiative corrections are calculated very precisely ($\mathcal{O}(10^{-2})$). This means that the uncertainty induced by the radiative corrections on the extraction of the Fierz term is in the order of $3.7 \cdot 10^{-4}$.

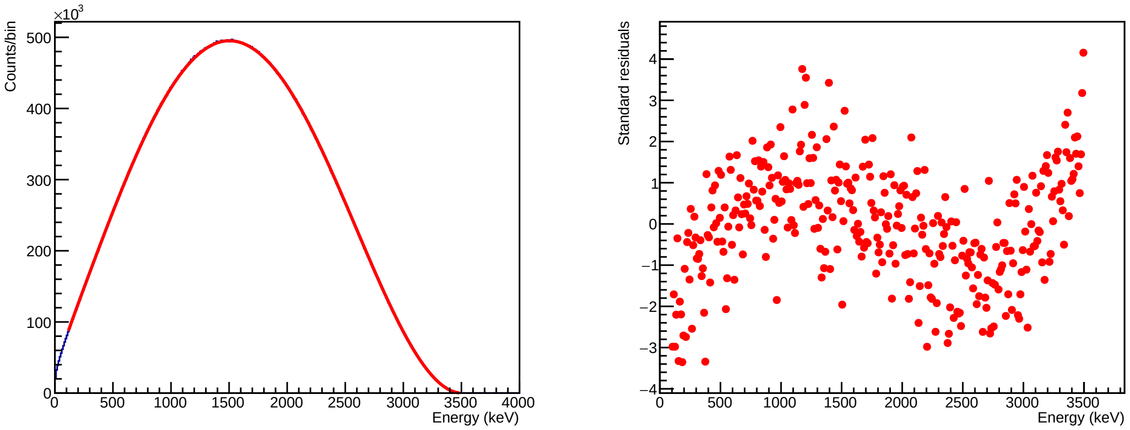

Figure 4.38: Left panel: the simulated energy spectrum with the fit function that does not include the effect of radiative corrections. Right panel: the standard residuals of the fit.

4.7.2 Bremsstrahlung escape correction model

The Livermore, Penelope, and Option4 constructors are optimized for low energy processes. According to Ref. [77], the Option4 physics constructor uses "the best set of electromagnetic physics models selected from the low energy and standard packages". It was used in this work to obtain the Bremsstrahlung escape model. The systematic uncertainty on the choice of this physics constructor was obtained with the simulation. This simulation was performed with the same set of events using the three physics constructors for the computation of the deposited energy inside the detection volume by GEANT4. The three obtained deposited energy spectra were then fitted with Eq. (4.21), where b_{GT} was a free parameter of the fit. The results of the fit are shown in Table 4.1. If one considers the difference between these three models as a reference for the estimate of the uncertainty, the associated error on b_{GT} is in the order of 0.7×10^{-3}.

Physics constructor	b_{GT}	χ^2
G4EmStandardPhysics_option4	$(1.6 \pm 0.9)10^{-3}$	348
G4EmLivermorePhysics	$(2.3 \pm 0.9)10^{-3}$	332
G4EmPenelopePhysics	$(1.9 \pm 0.9)10^{-3}$	342

Table 4.1: The values of b_{GT} obtained by fitting the simulated data using the three physics constructors that are optimized for low energy processes, with the χ^2 values for each fit. The input value of b_{GT} is, and the number of degrees of freedom is $NDF = 346$.

The effect of an imperfect correction model was also studied by fitting the deposited energy spectrum obtained with the Option4 constructor, using the function of Eq. (4.21) for the fit while modifying the amplitude of the correction function $f_i(W)$ by ±10%. The fit results are shown in Table 4.2.

Correction	b_{GT}	χ^2
$1.1 f_i(W)$	$(-2.8 \pm 0.9)10^{-3}$	522
$0.9 f_i(W)$	$(6.9 \pm 0.9)10^{-3}$	655
No correction	$(68.6 \pm 0.9)10^{-3}$	>20000

Table 4.2: The values of b_{GT} obtained by fitting the simulated data using the correction function $f_i(W)$ modified by ±10% and without any correction, with the χ^2 values for each fit. The input value of b_{GT} is 0, and the number of degrees of freedom is $NDF = 346$.

The results presented in Table 4.2 show that for a change of 10% in the model, the effect on the obtained value of b_{GT} from the fit is of the order of $5 \cdot 10^{-3}$. This means that the correction due to Bremsstrahlung has to be known with a relative precision of 2% or better to obtain an uncertainty on b_{GT} below $1 \cdot 10^{-3}$. One can also note that the goodness of the fit is severely deteriorated as shown by the values of χ^2, which can be a helpful indication of a bad correction for this effect.

4.7.3 Detector's resolution effect

The effect of the convolution of the fit function with the detector's response function was studied with simulated data. This was done by generating 20 statistically independent sets of events using the following function:

$$G(W) = F(Z,W)pW(W-W_0)^2\left(1 + b_{GT}\frac{1}{W}\right), \tag{4.42}$$

where $b_{GT} = 0.03$. The generated events were convoluted with the response function, characterized by Eq. (4.31), to generate another 20 sets of events that include the effect of the response function of the detection setup. Then, the convoluted sets were fitted with the following expression

$$C(W) = F(Z,W)pW(W-W_0)^2\left(1 + b_{GT}\frac{1}{W}\right). \circledast \mathrm{Gaus}\left(0, \sigma(\mathrm{W})\right), \tag{4.43}$$

while the non-convoluted sets were fitted directly with Eq. (4.42). Figure 4.39 shows the obtained values of b_{GT} with and without the convolution for each set of events. It shows that the results are compatible in the two cases, proving the validity of the convolution method.

Another aspect to be studied is the effect of fixing the parameters α and β of Eq. (4.31). To study this effect, a set on 10^8 events was generated with Eq. (4.42) where $b_{GT} = 0.03$. For the α parameter, the generated events were convoluted with the response function with $\alpha = 1.52$ and $\beta = 0$. Then, the resulting spectrum was fitted with Eq. (4.43) where β was fixed to zero,

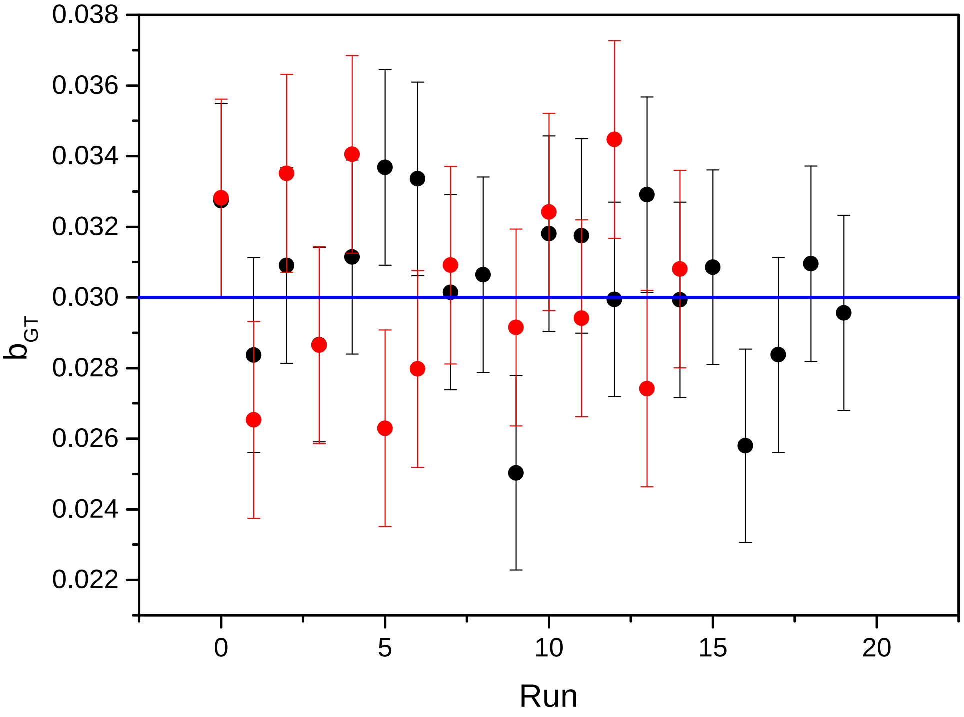

Figure 4.39: The values obtained from the fit of the 20 sets of events with convolution (red) and without convolution (black). The blue line represents the input value of b_{GT}.

and α was fixed to several values ranging between 0.91 and 2.13 (corresponding to $\alpha \pm 40\%$). The left panel of Fig. 4.40 shows the values of b_{GT} obtained for the different fixed values of α. This plot shows that even for a change of 40% on the value of α, the value of b_{GT} was biased by less than 2σ. The slope of the plot in Fig. 4.40 also indicates that to reduce the uncertainty induced by the contribution of the α parameter on b_{GT} below 10^{-3}, α must be known with a precision of about 0.09. In the present analysis, α is a free parameter of the fit and does not enter into the sources of systematic errors.

To study the effect of the β parameter, the generated events were convoluted with the response function with $\alpha = 1.36$ and $\beta = 0.01$ (the value obtained by the analysis of the runs with γ calibration sources). Then, this spectrum was fitted with Eq. (4.43) where α was either fixed to 1.52 or left as a free parameter and β was fixed to several values ranging between 0 and 0.04. The right panel of Fig. 4.40 shows the values of b_{GT} for the different fixed values of β while α is fixed (in blue) or left as a free parameter (in red). If we consider that offline calibrations with γ sources give an upper limit to the β parameter, the expected error is given by the points with values of β^2 below 0.001 in the right panel of Fig. 4.40. It shows an error of about 1.2×10^{-2} when α is fixed, and below 2×10^{-3} with α as a free parameter.

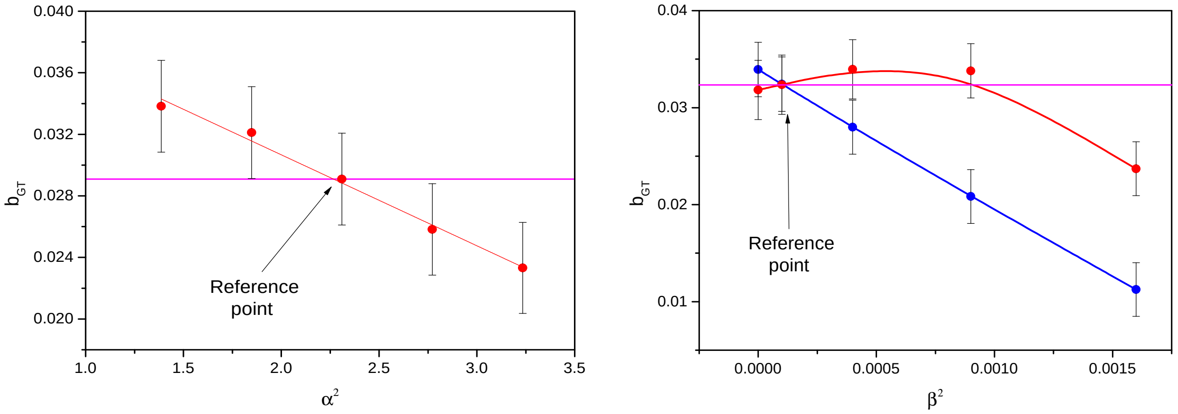

Figure 4.40: Left panel: the values of b_{GT} obtained by the fit while fixing α to several values and β fixed to zero. Right panel: the values of b_{GT} obtained by the fit while fixing β to several values when α is fixed (blue) or left as a free parameter of the fit function (red). The magenta line indicates the b_{GT} value of the reference point.

4.7.4 Subtraction of EV_{e^-} and pile-ups contributions

The error due to the subtraction of the contribution of EV_{e^-} was studied by fitting the experimental deposited energy spectrum for each set with and without the subtraction of this contribution. It was found to be in the order of 4×10^{-3}. The amount of EV_{e^-} contribution to be subtracted can be estimated with a relative precision better than 10% for each set, which leads to an error on b_{GT} below $5 \cdot 10^{-4}$.

The effect of the estimation of the pile-ups contribution was obtained by fitting the deposited β-energy spectrum for each set with and without the subtraction of the pile-ups distribution. It was found that the effect of this subtraction on the extracted value of b_{GT} was of the order of 4×10^{-4} for Set1 and Set3, and of the order of 6×10^{-3} for Set2. It is worth noting, though, that the estimation of pile-ups distribution needs to be studied in more detail in order to understand the reason behind the discrepancy shown in Fig. 4.33.

4.7.5 Other systematic effects

Several systematic effects were not studied yet. Those include for instance the linearity of the detectors response function. For the extraction of b_{GT}, the response function of the YAP was considered to be perfectly linear (Fig. 2.11). The effect of the deviation from linearity can be estimated by using several non-linear functions to fit the response function, and then using these functions for the fit of the deposited β-spectra. Another effect that must be studied is the presence of a calibration offset caused by the energy threshold of the detection setup.

As mentioned in Sec. 4.3, the refined calibration of Set4 and Set5 was done by using the average values of the calibration coefficients (α_1, α_2, β_1 and β_2) obtained for the runs number 16 and 17. The systematic uncertainty of this choice will be obtained by using the values of each of these two runs for the calibration of Set4 and Set5. The difference obtained with these calibration coefficients will be considered as the systematic uncertainty due to the calibration of Set4 and Set5.

Another thing that needs to be studied is the effect of the selections on both the Q_{fast}/Q_{tot} and on the E_2^{dep} vs. E_1^{dep} distributions. The study can be done by constructing and fitting the β-spectra while using several selection intervals.

4.8 Preliminary results

The results for the three sets are displayed in Fig. 4.41. These were obtained after the subtraction of the pile-ups contribution and of the contribution of EV_{e^-}. The statistical uncertainties obtained for the three sets are displayed in Table 4.3. The total uncertainty indicated for each set was obtained by summation in quadrature for the statistical uncertainty obtained by the fit and the statistical uncertainty induced by the subtraction of EV_{Brem}. The pure statistical uncertainty for the sum of the three sets on the value of the Fierz interference term is of the order of $\Delta b_{GT\ \mathrm{stat}} \simeq 1.6 \times 10^{-3}$, which is within the uncertainty goal of this experiment. However, the uncertainty resulting from the subtraction of EV_{Brem} events ranges between 3.9×10^{-3} and 6.5×10^{-3}, which increases the total statistical uncertainty to a value slightly above the uncertainty goal.

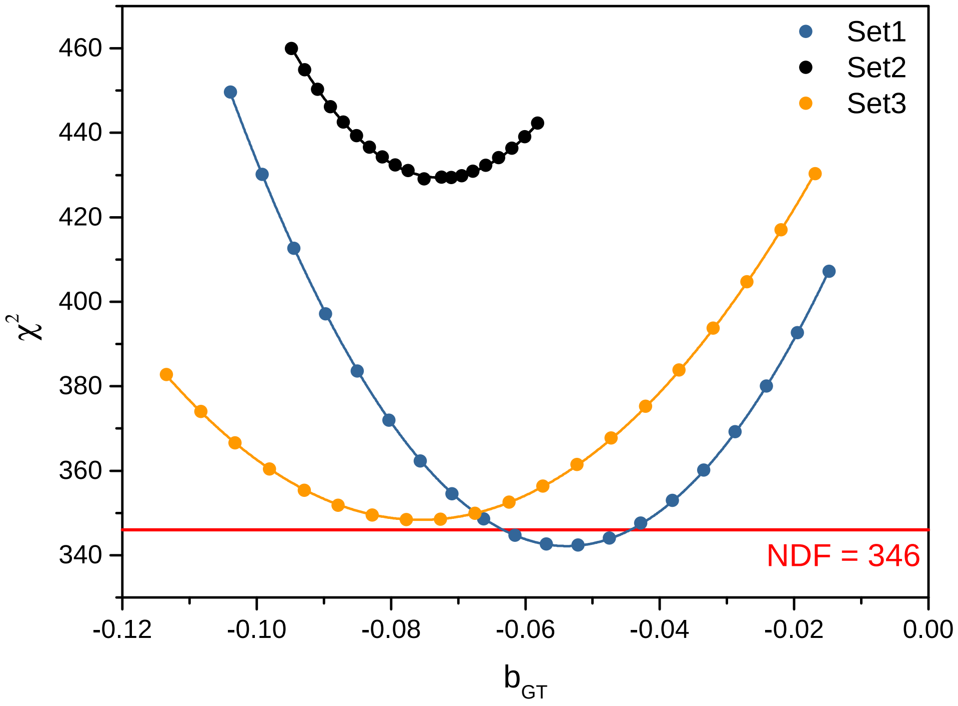

Figure 4.41: The values of b_{GT} obtained by the fits for the three sets. The red line represents the NDF value.

	Set1	Set2	Set3
Stat	$2.6 \cdot 10^{-3}$	$2.5 \cdot 10^{-3}$	$3.5 \cdot 10^{-3}$
EV_{Brem} subtraction	$4.8 \cdot 10^{-3}$	$3.9 \cdot 10^{-3}$	$6.5 \cdot 10^{-3}$
Total	$5.4 \cdot 10^{-3}$	$4.7 \cdot 10^{-3}$	$7.3 \cdot 10^{-3}$

Table 4.3: The statistical uncertainty obtained for each set.

The preliminary results obtained for the three sets are not compatible with each other within the limits of the statistical uncertainty. A discrepancy of about 0.02 exists between the values obtained for Set1 and for Set2 and Set3. In addition, the χ^2 values obtained for Set2 are significantly larger than the two other sets in comparison with the NDF value (the green line in Fig. 4.41), meaning that the fit function was unable to fit correctly the spectrum for Set2. However, these results are still very preliminary. As mentioned in Sec. 4.7, many systematic effects contributing to the extraction of the Fierz term have not yet been studied.

CHAPTER 5

Summary and conclusions

This thesis reported the high precision measurement of the half-life and the β-energy spectrum for the decay of ^{6}He from the analysis of the data of the E815S experiment. Because of the ambitious precision goals and of the large statistics that were collected, the data analysis had to be performed very carefully. A large part of the work described in this manuscript was thus dedicated to the details of this analysis, which includes many aspects such as: gain and baseline variation corrections, background studies, accurate calibrations, tests of the fit functions, implementation of theoretical corrections, and a study of the main sources of systematic errors.

The half-life measurement reported in this work is the most precise measurement of the ^{6}He half-life ever performed. The result obtained from this measurement is consistent with the one reported in Ref. [1], resolving therefore the longstanding discrepancy of about 1% between two sets of previous measurements with relatively high precisions.

For the extraction of the Fierz term, the pure statistical uncertainty was found to be in the order of $1.6 \cdot 10^{-3}$, which remains within the uncertainty goal of the experiment. However, the subtraction of EV_{Brem} events, an unanticipated background due to Bremsstrahlung radiation, increases significantly the total uncertainty.

The study of sources of systematic error is still in progress for the measurement of the Fierz term, and several effects are not yet estimated. Table 5.1 summarizes the systematic effects that have been studied or that will be studied later on, with the estimated uncertainty induced by each of them. The systematic effects investigated so far lead to systematic errors that are below or in the order of 10^{-3}, which remains compatible with our precision goal.

The results of the Fierz term reported in this work are still very preliminary ($b_{GT} \simeq -6 \cdot 10^{-2}$) and not yet reliable. The distributions of the residuals did not show any clear sign of a

Systematic effect	Δb_{GT}
EV_{e^-} subtraction	5×10^{-4}
β parameter	$<2\times10^{-3}$
b_{WM}	2.6×10^{-4}
Radiative	3.7×10^{-4}
Bremsstrahlung escape	7×10^{-4}
Pile-ups	?
Selections	?
Calibration offset	?
Non-linear response function	?
Total	?

Table 5.1: The error budget for the extraction of b_{GT} from the measurement of the β-spectrum shape.

problem with the fit procedure. However, a discrepancy larger than the combined statistical and systematic uncertainties exists between the results of the fits obtained with three independent sets of data. Hopefully, this problem may be solved by the study of the remaining systematic errors that will be performed in the next few months.

For instance, the selections performed on the E_2^{dep} vs. E_1^{dep} distributions could have a significant effect on the result of the fit since these have a direct influence on the amount of EV_{Brem} events that are discarded by the selection. Other effects that need to be studied as well are the calibration of the data of Set4 and Set5, the non-linearity of the detector's response function (including a possible offset), and the imperfection of the reconstruction of the deposited energy. This last point can be studied with a run by run analysis by monitoring the fluctuations of the calibration parameter c of the fit function. Another step in the analysis that must be refined is the calculation of the parameters α_1, α_2, β_1 and β_2 that were used for the calibration. The method reported in Sec. 4.3, to match the end of the histograms, does not take into consideration the difference in the resolution between the distributions of ($E_1^{cal}(EV_2)$ and $E_2^{cal}(EV_1)$) and ($E_1^{cal}(EV_1)$ and $E_2^{cal}(EV_2)$). The matching of all the histograms must be redone using a fit that includes the resolution.

Concerning the long term perspectives, the largest contribution to the uncertainty budget was found to be the subtraction of the EV_{Brem} contribution. In a future experiment, this contribution can be largely reduced by shielding the detection setup with a few millimeters of lead. In addition, it would be very useful to have background data acquisition with the conditions of Set4 and Set5 more consistently and with much higher statistics. For the Bremsstrahlung escape correction, we rely on the GEANT4 simulations and it would be very useful to compare these simulations with independent measurements. This could be done using an offline β source and a large total absorption spectroscopy detector surrounding our YAP detector, in order to detect directly escaping photons in coincidence with the β particles. Our offline calibrations using γ sources and previous studies indicate a very good linearity of the YAP detector. However, it will be important to complete these studies with other sources and with conversion electrons to ensure that non-linearity effects are negligible or known with sufficient precision.

APPENDIX A

Other properties of the Standard Model

A.1 Symmetries

Symmetry is one of the fundamental pillars on which our knowledge of particle physics is built. A symmetry of a physical system is a feature of this system that remains conserved under a certain transformation. Symmetry is described by group theory. When a group governs a physical system, the Lagrangian remains invariant under the group of transformations, implying the existence of a conserved quantity. The symmetries of a system can be continuous or discrete.

In the case of a continuous symmetry, Noether's theorem [78] guarantees the existence of conserved physical quantity. For instance, an invariance under translation in time, translation in space and rotation implies respectively the conservation of energy, momentum and angular momentum of the system.

In addition to the continuous symmetries, there exists other discrete symmetries, each associated to a fundamental property of the physical system. The most important of those are; The Parity P, that shows how the system evolves when every particle, interaction and decay is replaced by its mirror counterpart. The Charge conjugation C, that shows how the system evolves when replacing every particle with its anti-particle (and vice-versa). The Time reversal T, that shows how the system evolves if it goes backward in time, i.e. by reversing the direction of motion within the process.

It was always assumed that the individual discrete symmetries were preserved by the four forces of nature. This assumption was proven to be wrong in 1957 when Wu et al. discovered the parity violation in the weak interaction with the famous ^{60}Co experiment [79]. Today we know that the strong and electromagnetic forces conserve the three discrete symmetries, while both parity and charge conjugation symmetries are broken by the weak interaction, as well as the combination of them both (*CP*-symmetry). There are, however, very good theoretical reasons to believe that the combined *CPT*-symmetry is conserved by all the forces. This is called the *CPT* theorem. One consequence of this theorem is that for every particle, its associated anti-particle must have exactly the same mass and lifetime, which is found to be true so far. Another consequence of this theorem is that for every broken individual symmetry, there should be a compensating asymmetry in the remaining operation(s) to ensure the conservation of the *CPT*-symmetry.

A.2 CKM matrix

For quarks, The weak eigenstates u', d', c', s', t' and b' are not the same as the mass eigenstates u, d, c, s, t and b. If one considers only the symmetries and ignores the masses of the particles, the u', c', and t' would look and behave exactly the same for all the interactions. The same is true for their partners d', s' and b' as well as for the charged leptons e, μ and τ and their neutrinos. However, the fact that particles do have masses resulted in including a symmetry breaking mechanism to the SM, known as the Higgs mechanism. This mechanism, which assigns to the quarks their masses, mixes the quarks weak states to give the mass states. In other words, the weak interaction, governed by the emission of a $W^{\pm}$ boson, rotates the quark states. The mixing between the quarks generations is given by the unitary matrix derived by Cabibbo-Kobayashi-Maskawa [80, 81] (CKM matrix) that rotates the set of quark mass states into the quark weak states and vice-versa. By convention, the mixing is done for the members of the generations with charge (-1/3) i.e. the d, s, and b quarks are each a mixing of d', s', and b'. The mixing of the quark mass and weak states in terms of the CKM matrix is given by:

$$\begin{pmatrix} d' \\ s' \\ b' \end{pmatrix} = \begin{pmatrix} V_{ud} & V_{us} & V_{ub} \\ V_{cd} & V_{cs} & V_{cb} \\ V_{td} & V_{ts} & V_{tb} \end{pmatrix} \begin{pmatrix} d \\ s \\ b \end{pmatrix} \tag{A.1}$$

where the V_{ij} are the CKM matrix elements representing the transition probabilities from the i quark to the j quark due to the rotation of the states of the j quark. Moreover, the CKM matrix is unitary, meaning that the sum of the square of the modules of each row of the matrix is equal to 1 as shown in the following equation:

$$\sum_{j=d,s,b} \left|V_{ij}\right|^2 = 1, \qquad i = u,c,t \tag{A.2}$$

The values of the CKM matrix elements are not fixed by theory but are determined with experiments. The most stringent limits on the magnitudes of the elements of V_{CKM} are [7]:

$$V_{CKM} = \begin{pmatrix} 0.97435 \pm 0.00016 & 0.225 \pm 0.00067 & 0.00369 \pm 0.00011 \\ 0.22486 \pm 0.00067 & 0.97349 \pm 0.00016 & 0.04182^{+0.00085}_{-0.00074} \\ 0.00857^{+0.00020}_{-0.00018} & 0.0411^{+0.00083}_{-0.00072} & 0.999118^{+0.000031}_{-0.000036} \end{pmatrix} \tag{A.3}$$

The most striking observation of the matrix elements values is that the elements on the diagonal are dominant. This shows that the weak transitions between different quark generations are strongly suppressed. The test of the unitarity of the CKM matrix is an essential tool for the search of BSM physics.

APPENDIX B

YAP's response function

Prior to the E815S experiment, several tests with γ calibration sources (^{22}Na, ^{137}Cs, ^{60}Co and ^{208}Tl) were performed to study the response function of the detection setup. Figure 4.14 shows the setup used for these tests.

This was done by fitting the photopeaks of these sources with the functions of Eqs. (B.1) and (B.2) that take into account the presence of another contribution superposing with the photopeak (the tail of the Compton edge) (Fig. B.1).

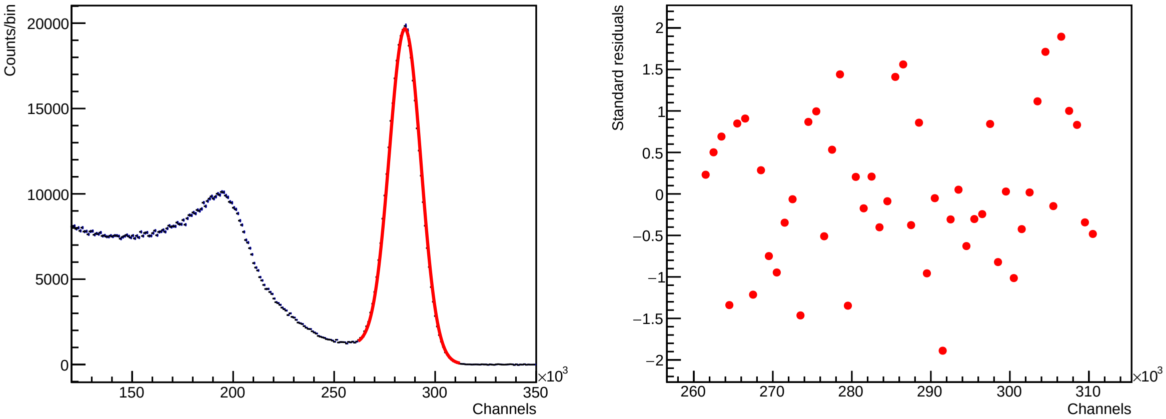

Figure B.1: Right panel: the photopeak of the 662 keV γ particles of the ^{137}Cs source. The red line represents the fit with the function f_1. Left panel: The standard residuals of the fit.

$$f_1 = Gauss(N,\mu,\sigma) + \frac{N_0}{1+e^{\frac{Ch-\mu}{\sigma}}}, \tag{B.1}$$

$$f_2 = Gauss(N,\mu,\sigma) + \frac{N_0}{2}\left(1 - erf(\frac{Ch-\mu}{\sqrt{2}\sigma})\right). \tag{B.2}$$

Table B.1 shows the resulting reduced χ^2 values for the fits of the photopeaks while using the functions f_1, f_2, and an ordinary Gaussian function. The χ^2 values obtained for the fits with the functions f_1 and f_2 are significantly better than those for the fits with the ordinary Gaussian function that does not account for the tail contribution within the photopeak. The χ^2 values obtained by the fits with the function f_1 were slightly better than those for the fits with f_2. Therefore, the results of the fits with f_1 were used for the study of the resolution.

	Det1			Det2		
χ^2/NDF	f_1	f_2	Gaus	f_1	f_2	Gaus
^{241}Am (59.54 keV)	0.941518	0.95878	41.0262	1.03388	1.10035	20.4343
^{22}Na (511 keV)	1.08126	1.06729	384.174	0.513743	0.520857	29.3089
^{137}Cs (661.66 keV)	0.890062	1.25972	33.4084	1.26423	1.3193	37.6431
^{22}Na (1274.54 keV)	0.827281	0.831834	4.5137	1.4367	1.46508	13.2936
^{60}Co (1332.49 keV)	1.11574	1.14345	234.758	1.39516	1.47362	9.9319
^{208}Tl (2614.51 keV)	1.56978	2.41701	3.72435	1.68374	1.87318	6.32137

Table B.1: The values of reduced χ^2 obtained by the fits of the calibration sources photopeaks with the functions f_1, f_2, and with a normal Gaussian function.

The peak of the α particles that deposited their entire energy inside the PVT was used as a reference point to match the gain of the PMTs between the runs. Table B.2 shows the correction coefficients obtained by fitting the peak of the α particles for each run.

	Det1	Det2
^{241}Am	1	1
^{22}Na	0.997	1.004
^{137}Cs	0.999	0.997
^{60}Co	0.988	0.996
^{208}Tl	0.985	0.987

Table B.2: The gain correction coefficients obtained by the fit of the ^{241}Am 5.5 MeV α particles peak for each run.

The mean μ and the standard deviation σ for each photopeak obtained by the fits were corrected with the coefficients displayed in Table B.2. Figure B.2 shows the distribution of the mean values μ against the energy of the γ particles, with a linear fit (red line), and the residuals away from the linear model for the two detectors. The two detectors show a linear response with a deviation of about 2 keV for Det1 and 4 keV for Det2 from the linear model. The resolutions were then calculated for each photopeak using Eq. 4.28, and were fitted with Eq. 4.29 to obtain the parameters α, β and γ (Fig. 4.15).

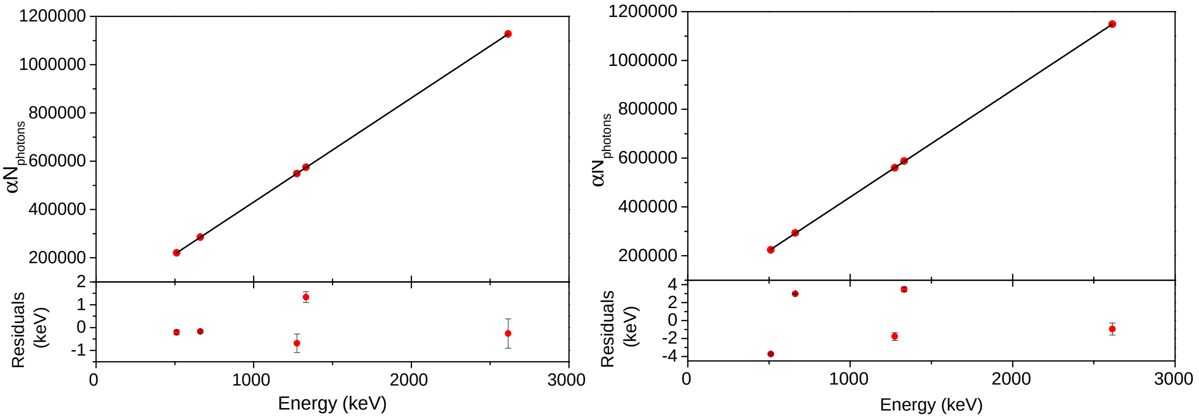

Figure B.2: The distribution of the mean values of the photopeaks μ, with linear fits (red lines) and the residuals away from the linear model for Det1 (left panel) and Det2 (right panel).

APPENDIX C

Gain and baseline correction model

Figures C.1 and C.2 show the distribution of the parameters P_0^b and P_1^b with the linear functions used to fit them in order to construct the gain and baseline correction model.

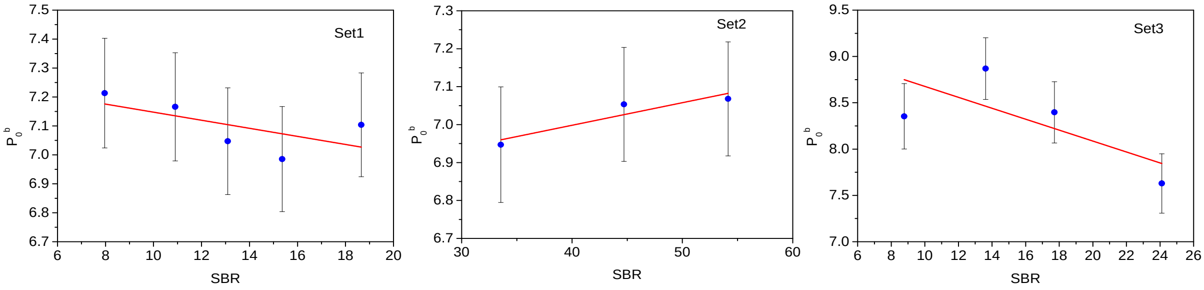

Figure C.1: Variation of P_0^b for baseline correction for the three sets of measurements.

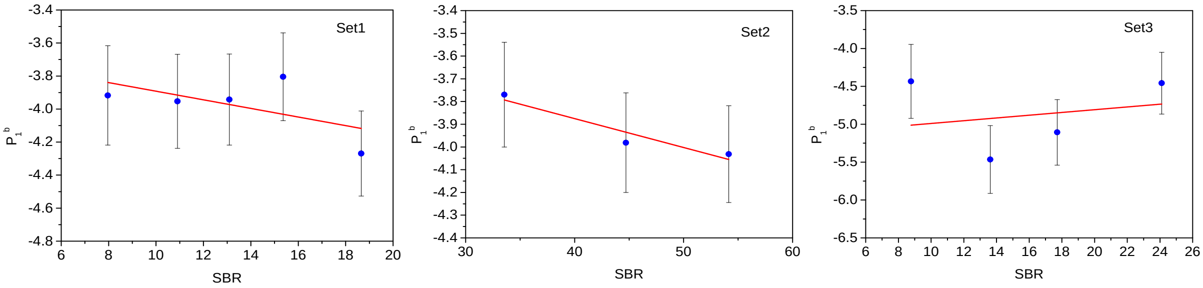

Figure C.2: Variation of P_1^b for baseline correction for the three sets of measurements.

The slow variation between the runs was not accounted for with the calibration performed with the expression of Eq. (3.8). This variation is shown in Fig. C.3 for the runs of Set1. It can be noticed that this variation is smaller than 1% for the two detectors and that it has a completely opposite behavior for the two detectors. This variation was then corrected for each run to match the expected value of 59.54 keV.

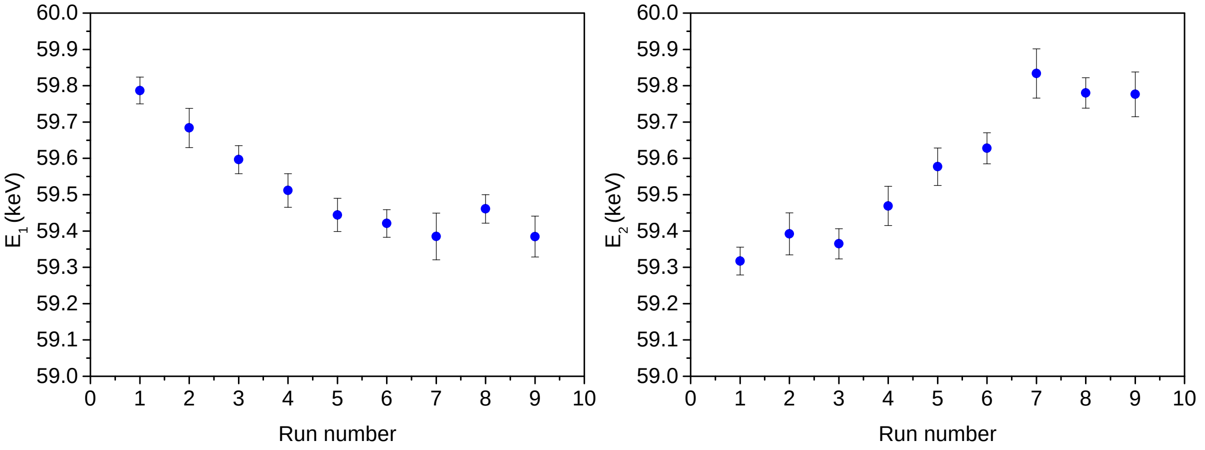

Figure C.3: The position of the 59.54 keV photopeak obtained for each run after the calibration with Eq. (3.8) for Det1 (left panel) and Det2 (right panel).

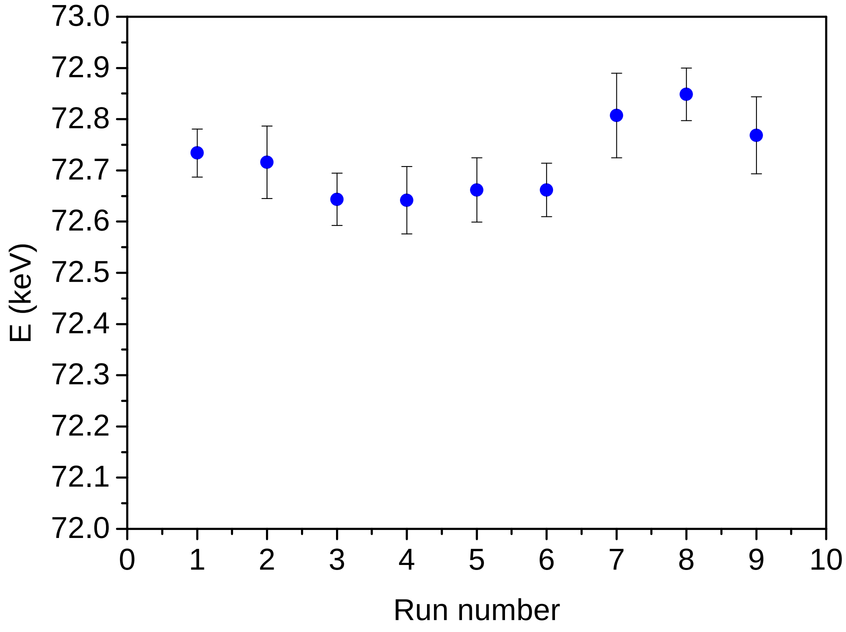

Figure C.4: The position of the 59.54 keV photopeak after the summation of the signals of each detector. An overestimation by about 20% can be noticed, caused by the light cross-talk between the two detectors that was not taken into account during the relative gain and baselined corrections.

After this gain correction, which was performed run by run and independently on each detector, the reconstructed energies from both detectors were summed event by event. This allowed to account for the events with part of the energy deposited in each detector. But because of the light cross-talk between the two detectors, this summation leads to an overestimation of the energy by about 20%, as shown in Fig. C.4. A scaling coefficient is thus calculated run by run to correctly reconstruct the energy of each event using the position of the 59.54 keV photopeak.

APPENDIX D

Smaller theoretical corrections

D.1 Screening correction

The Fermi function doesn't take into consideration the effect of the presence of electrons in the atom of the daughter bound state on the departing β particle. This presence produces a screening of the nuclear charge which effectively reduces the nuclear charge felt by the departed β particle. This description of the electromagnetic field induces a distortion to the shape of the β-energy spectrum and can be taken into consideration by a screening correction. There exists in the literature several methods to calculate the screening correction, such as Rose's formula [67] and Bühring's formula [82]. In this work, the Bühring's formula is used, which represents a significant improvement compared with Rose's formula [83].

The description of the screening correction requires the knowledge of the screening potential. One of the simplest models describing a screened Coulomb potential is the Hulthén potential [83]:

$$V(r) = \frac{\alpha Z \beta_s}{e^{\beta_s r} - 1}, \tag{D.1}$$

which becomes near the origin as follows [84]:

$$V(r) = -\frac{\alpha Z}{r} + \frac{1}{2}\alpha Z \beta_s + \mathcal{O}(r), \tag{D.2}$$

The term $\frac{1}{2}\alpha Z \beta_s$ is a shift of the potential near the nucleus due to screening. It is referred to as the screening potential V_s and is negative for β^- decay [83]:

$$V_s = -\frac{1}{2}\alpha Z \beta_s, \tag{D.3}$$

$$\beta_s = 2C\left(|\tilde{Z}|\right)\alpha|\tilde{Z}|^{1/3}, \tag{D.4}$$

where $\tilde{Z} = 2$ is the atomic number of the mother nucleus (^{6}He), and the value of $C(2) \simeq 1.386$ is calculated in Ref. [37].

Bühring studied the Hulthén potential and derived a close evaluation of the wave function normalization factor of the Dirac equation for a semi-realistic case [82]. The resulting expression for the screening correction is as follows [83, 66]:

$$S(Z,W) = X\frac{\tilde{W}}{W}e^{-\pi y}\left(\frac{2p}{\beta_s}\right)^{2(1-\gamma)}\left|\frac{\Gamma(\gamma+i\tilde{y})}{\Gamma(\gamma+iy)}\right|^2\left|\frac{\Gamma(\gamma+2i\tilde{p}/\beta_s)}{\Gamma(1+2ip/\beta_s)}\right|^2, \tag{D.5}$$

where

$$\begin{aligned} X = &\left[1+\frac{1}{4}\left(\frac{\beta_s}{p}\right)^2\right]^{-1} \times \left\{1+\frac{1}{8}\left(\frac{\tilde{W}+\gamma}{\tilde{W}}\right)\left(\frac{\beta_s}{p}\right)^2\right. \\ &\left.\frac{1}{2}\gamma^2\left[1+\left(1-\frac{\alpha Z\beta_s}{W+1}\right)^{1/2}\right]^{-2}\frac{W-1}{\tilde{W}}\left(\frac{\beta_s}{p}\right)^2\left[1-\frac{1}{8}(1-\gamma)\frac{1}{\gamma}\left(\frac{\beta_s}{p}\right)^2\right]\right\}, \end{aligned} \tag{D.6}$$

$$\tilde{p} = \frac{1}{2}p+\frac{1}{2}\left[p^2-2\alpha Z\tilde{W}\beta_s\right]^{1/2}, \tag{D.7}$$

$$\tilde{y} = \frac{\alpha Z\tilde{W}}{\tilde{p}}, \tag{D.8}$$

D.2 Electrostatic finite size correction

The assumptions made to construct the Fermi function include the point-like size of the daughter nucleus. However, in reality, the daughter nucleus has a finite charge distribution, which affects the solutions to the Dirac equation. Solving the Dirac equation in the field of the real charge distribution of the daughter nucleus introduces the electrostatic finite size correction $L_0(Z,W)$ to the Fermi function.

H. Behrens and J. Jänecke [85] calculated the values of $L_0(Z,W)$, for $Z < 30$, using numerical computation while assuming that the daughter nucleus is a uniformly charged sphere of radius R. Wilkinson [86] used these values to perform an empirical fit and obtained an analytical expression of $L_0(Z,W)$ for $Z < 40$:

$$L_0(Z,W) = 1+0.206(\alpha Z)^2-1.039WR\alpha Z-0.0058(pR)^2-0.54\frac{R\alpha Z}{W}, \tag{D.9}$$

	b_1	b_2	b_3	b_4	b_5	b_6
a_{-1}	0.115	-1.8123	8.2498	-11.223	-14.854	32.086
a_0	-0.00062	0.007165	0.01841	-0.53736	1.2691	-1.5467
a_1	0.02482	-0.5975	4.84199	-15.3374	23.9774	-12.6534
a_2	-0.14038	3.64953	-38.8143	172.1368	-346.708	288.7873
a_3	0.008152	-1.15664	49.9663	-273.711	657.6292	-603.7033
a_4	1.2145	-23.9931	149.9718	-471.2985	662.1909	-305.6804
a_5	-1.5632	33.4192	-255.1333	938.5297	-1641.2845	1095.358

Table D.1: Coefficients for the parameterization of $L_0(Z,W)$ for electrons copied from Ref. [66].

Wilkinson then used the same values and improved the fit to include nuclei with $Z \leq 60$ [66], and obtained the following expression:

$$\begin{aligned} L_0(Z,W) =& 1+\frac{13}{60}(\alpha Z)^2 - WR\alpha Z\frac{41-26\gamma}{15(2\gamma-1)} - \alpha ZR\gamma\frac{17-2\gamma}{30W(2\gamma-1)} + a_{-1}\frac{R}{W} \\ &+ \sum_{n=0}^{5} a_n (WR)^n + 0.41(R-0.0164)(\alpha Z)^{4.5}. \end{aligned} \tag{D.10}$$

In the above expression the a-values are given by the parametrization:

$$a = \sum_{x=1}^{6} b_x (\alpha Z)^x, \tag{D.11}$$

where the b_x-values are different for each a_n, and are given in the following table.

D.3 Convolution finite size correction

Another effect related to the finite nuclear size is the convolution of the leptonic and nucleonic wave functions through the nuclear volume. For Gamow-Teller transitions it has the following form [66]:

$$C^A(Z,W,W_0) = 1 + C_0^A + C_1^A W + C_2^A W^2, \tag{D.12}$$

where

$$C_0^A = -\frac{233}{630}(\alpha Z)^2 - \frac{(W_0 R)^2}{5} + \frac{2}{35} W_0 R\alpha Z, \tag{D.13}$$

$$C_1^A = -\frac{21}{35} R\alpha Z + \frac{4}{9} W_0 R^2, \tag{D.14}$$

$$C_2^A = -\frac{4}{9} R^2. \tag{D.15}$$

Here the superscript A indicates the Axial-Vector nature of the Gamow-Teller transition.

D.4 Finite mass correction

To construct the Fermi function, two assumptions were made considering the masses of the daughter nucleus and the emitted neutrino. For the neutrino, its mass was considered to be null. The effect of a non-zero mass of the emitted neutrino on the β-energy spectrum can be safely neglected considering the very low neutrino mass (below 30 eV) [66]. For the daughter nucleus, its mass was considered to be infinitely large. However, the effect of a finite mass for the daughter nucleus on the β-energy spectrum is significant and requires a recoil correction. The correction for Gamow-Teller decays can be included to the phase space through a factor $R_N(W, W_0)$ provided in Ref. [66]:

$$R_N(W, W_0) = 1 + r_0^A + \frac{r_1^A}{W} + r_2^A W + r_3^A W^2, \tag{D.16}$$

where

$$r_0^A = -\frac{2W_0}{3M} - \frac{W_0^2}{6M^2} - \frac{77}{18M^2}, \tag{D.17}$$

$$r_1^A = -\frac{2}{3M} + \frac{7W_0}{9M^2}, \tag{D.18}$$

$$r_2^A = -\frac{10}{3M} - \frac{28W_0}{9M^2}, \tag{D.19}$$

$$r_3^A = \frac{88}{9M^2}, \tag{D.20}$$

with M is the nuclear mass of the ^{6}Li in natural unit [72], and A is a superscript corresponding to the axial-vector nature of the Gamow-Teller transition.

Bibliography

[1] A. Knecht, R. Hong, D. W. Zumwalt, B. G. Delbridge, A. García, P. Müller, H. E. Swanson, I. S. Towner, S. Utsuno, W. Williams, and C. Wrede. Precision measurement of the ^{6}He half-life and the weak axial current in nuclei. *Phys. Rev. C*, 86:035506, 2012.

[2] R. M. Kline and D. J. Zaffarano. Decay Characteristics of Some Short-Lived Nuclides of Low Atomic Number. *Phys. Rev.*, 96:1620, 1954.

[3] J. K. Bienlein and F. Pleasonton. The half-life of ^{6}He. *Nucl. Phys.*, 37:529, 1962.

[4] D. H. Wilkinson and D. E. Alburger. Half-lives of ^{6}He, ^{19}Ne, and ^{42}Sc^{m}. *Phys. Rev. C*, 10:1993, 1974.

[5] P. H. Barker, T.B. Ko, and M.J. Scandle. The half-life of ^{6}He. *Nucl. Phys. A*, 372:45, 1981.

[6] D. E. Alburger. Half-life of ^{6}He. *Phys. Rev. C*, 26:252–253, 1982.

[7] R. L. Workman et al. Review of Particle Physics. *Prog. Theor. Exp. Phys.*, 2022:083C01, 2022.

[8] E. Fermi. An attempt of a theory of beta radiation. 1. *Z. Phys.*, 88:161–177, 1934.

[9] S. Weinberg. A Model of Leptons. *Phys. Rev. Lett.*, 19:1264–1266, 1967.

[10] A. Salam. Weak and Electromagnetic Interactions. *Conf. Proc. C*, 680519:367–377, 1968.

[11] S. L. Glashow. Partial-symmetries of weak interactions. *Nucl. Phys.*, 22:579–588, 1961.

[12] G. Aad et al. Observation of a new particle in the search for the Standard Model Higgs boson with the ATLAS detector at the LHC. *Phys. Lett. B*, 716:1–29, 2012.

[13] J. Suhonen. *From Nucleons to Nucleus*. Springer Berlin, Heidelberg, first edition, 2007.

[14] K. S. Krane. *Introductory Nuclear Physics*. John Wiley, third edition, 1987.

[15] V. Cirigliano, M. Gonzalez-Alonso, and M. L. Graesser. Non-standard Charged Current Interactions: beta decays versus the LHC. *J. High Energy Phys.*, 02:046, 2013.

[16] A. Falkowski, M. González-Alonso, and O. Naviliat-Cuncic. Comprehensive analysis of beta decays within and beyond the Standard Model. *J. High Energy Phys.*, 04:126, 2021.

[17] M. González-Alonso and J. Camalich. Isospin Breaking in the Nucleon Mass and the Sensitivity of β Decays to New Physics. *Phys. Rev. Lett.*, 112:042501, 2014.

[18] M. González-Alonso, O. Naviliat-Cuncic, and N. Severijns. New physics searches in nuclear and neutron β decay. *Prog. Part. Nucl. Phys.*, 104:165–223, 2019.

[19] J. D. Jackson, S. B. Treiman, and H. W. Wyld. Possible Tests of Time Reversal Invariance in Beta Decay. *Phys. Rev.*, 106:517–521, 1957.

[20] N. Severijns. *Weak Interaction Studies by Precision Experiments in Nuclear Beta Decay*, pages 339–381. Springer Berlin, Heidelberg, 2004.

[21] M. González-Alonso and O. Naviliat-Cuncic. Kinematic sensitivity to the Fierz term of β-decay differential spectra. *Phys. Rev. C*, 94:035503, 2016.

[22] J. C. Hardy and I. S. Towner. Superallowed $0^+ \to 0^+$ nuclear β decays: 2020 critical survey, with implications for V_{ud} and CKM unitarity. *Phys. Rev. C*, 102:045501, 2020.

[23] A. Gorelov, D. Melconian, W. P. Alford, D. Ashery, G. Ball, J. A. Behr, P. G. Bricault, J. M. D'Auria, J. Deutsch, J. Dilling, M. Dombsky, P. Dubé, J. Fingler, U. Giesen, F. Glück, S. Gu, O. Häusser, K. P. Jackson, B. K. Jennings, M. R. Pearson, T. J. Stocki, T. B. Swanson, and M. Trinczek. Scalar Interaction Limits from the $\beta-\nu$ Correlation of Trapped Radioactive Atoms. *Phys. Rev. Lett.*, 94:142501, 2005.

[24] E. G. Adelberger, C. Ortiz, A. García, H. E. Swanson, M. Beck, O. Tengblad, M. J. G. Borge, I. Martel, H. Bichsel, and the ISOLDE Collaboration. Positron-Neutrino Correlation in the $0^+ \to 0^+$ Decay of ^{32}Ar. *Phys. Rev. Lett.*, 83:1299–1302, 1999.

[25] V. Araujo-Escalona, D. Atanasov, X. Fléchard, P. Alfaurt, P. Ascher, B. Blank, L. Daudin, M. Gerbaux, J. Giovinazzo, S. Grévy, T. Kurtukian-Nieto, E. Liénard, G. Quéméner, N. Severijns, S. Vanlangendonck, M. Versteegen, and D. Zákoucký. Simultaneous measurements of the β-neutrino angular correlation in ^{32}Ar pure Fermi and pure Gamow-Teller transitions using β-proton coincidences. *Phys. Rev. C*, 101:055501, 2020.

[26] H. Saul, C. Roick, H. Abele, H. Mest, M. Klopf, A. K. Petukhov, T. Soldner, X. Wang, D. Werder, and B. Märkisch. Limit on the Fierz Interference Term b from a Measurement of the Beta Asymmetry in Neutron Decay. *Phys. Rev. Lett.*, 125:112501, 2020.

[27] P. Müller, Y. Bagdasarova, R. Hong, A. Leredde, K. G. Bailey, X. Fléchard, A. García, B. Graner, A. Knecht, O. Naviliat-Cuncic, T. P. O'Connor, M. G. Sternberg, D. W. Storm, H. E. Swanson, F. Wauters, and D. W. Zumwalt. β-Nuclear-Recoil Correlation from ^{6}He Decay in a Laser Trap. *Phys. Rev. Lett.*, 129:182502, 2022.

[28] B. M. Rustad and S. L. Ruby. Gamow-Teller Interaction in the Decay of ^{6}He. *Phys. Rev.*, 97:991–1002, 1955.

[29] D. W. Hetherington, A. Alousi, and R. B. Moore. The shape factor of the ^{20}F beta spectrum. *Nucl. Phys. A*, 494:1–35, 1989.

[30] G. W. Severin, L. D. Knutson, P. A. Voytas, and E. A. George. ^{66}Ga ground state β spectrum. *Phys. Rev. C*, 89:057302, 2014.

[31] L. D. Knutson, G. W. Severin, S. L. Cotter, Li Zhan, P. A. Voytas, and E. A. George. A superconducting beta spectrometer. *Rev. Sci. Instrum.*, 82:073302, 2011.

[32] David E. Alburger. Intermediate-Image Pair Spectrometer. *Rev. Sci. Instrum.*, 27:991–1004, 2004.

[33] E. A. George, P. A. Voytas, G. W. Severin, and L. D. Knutson. Measurement of the shape factor for the β decay of ^{14}O. *Phys. Rev. C*, 90:065501, 2014.

[34] P. A. Voytas, E. A. George, G. W. Severin, L. Zhan, and L. D. Knutson. Measurement of the branching ratio for the β decay of ^{14}O. *Phys. Rev. C*, 92:065502, 2015.

[35] K. P. Hickerson, X. Sun, Y. Bagdasarova, D. Bravo-Berguño, L. J. Broussard, M. A.-P. Brown, R. Carr, S. Currie, X. Ding, B. W. Filippone, A. García, P. Geltenbort, J. Hoagland, A. T. Holley, R. Hong, T. M. Ito, A. Knecht, C.-Y. Liu, J. L. Liu, M. Makela, R. R. Mammei, J. W. Martin, D. Melconian, M. P. Mendenhall, S. D. Moore, C. L. Morris, R. W. Pattie, A. Pérez Galván, R. Picker, M. L. Pitt, B. Plaster, J. C. Ramsey, R. Rios, A. Saunders, S. J. Seestrom, E. I. Sharapov, W. E. Sondheim, E. Tatar, R. B. Vogelaar, B. VornDick, C. Wrede, A. R. Young, and B. A. Zeck. First direct constraints on Fierz interference in free-neutron β decay. *Phys. Rev. C*, 96:042501, 2017.

[36] M. Hughes, E. A. George, O. Naviliat-Cuncic, P. A. Voytas, S. Chandavar, A. Gade, X. Huyan, S. N. Liddick, K. Minamisono, S. V. Paulauskas, and D. Weisshaar. Measurement of the ^{20}F half-life. *Phys. Rev. C*, 97:054328, 2018.

[37] X. Huyan. *PRECISION MEASUREMENT OF THE β-ENERGY SPECTRUM IN ^{6}HE DECAY*. PhD thesis, Michigan State University, 2019.

[38] O. Naviliat-Cuncic. Private communication 2023.

[39] W. Byron, H. Harrington, R. J. Taylor, W. DeGraw, N. Buzinsky, B. Dodson, M. Fertl, A. García, G. Garvey, B. Graner, M. Guigue, L. Hayen, X. Huyan, K. S. Khaw, K. Knutsen, D. McClain, D. Melconian, P. Müller, E. Novitski, N. S. Oblath, R. G. H. Robertson, G. Rybka, G. Savard, E. Smith, D. D. Stancil, M. Sternberg, D. W. Storm, H. E. Swanson, J. R. Tedeschi, B. A. VanDevender, F. E. Wietfeldt, A. R. Young, and X. Zhu. First Observation of Cyclotron Radiation from MeV-Scale $e^{\pm}$ following Nuclear β Decay. *Phys. Rev. Lett.*, 131:082502, 2023.

[40] K. Łojek, D. Rozpędzik, K. Bodek, M. Perkowski, and N. Severijns. Front-end electronics and data acquisition system for a multi-wire 3D gas tracker. *Nucl. Instrum. Meth. Phys. Sect. A*, 802, 2015.

[41] L. De Keukeleere. *Measuring the ^{114}In $\rightarrow$ ^{114}Sn β-spectrum shape using a Multi-Wire Drift Chamber*. PhD thesis, KU Leuven, 2023.

[42] S. Vanlangendonck. *The effect of weak magnetism on the shape of the ^{114}In beta energy spectrum*. PhD thesis, KU Leuven, 2023.

[43] O. Naviliat-Cuncic and M. González-Alonso. Prospects for precision measurements in nuclear decay in the LHC era. *Annalen Phys.*, 525:600–619, 2013.

[44] C. H. Johnson, Frances Pleasonton, and T. A. Carlson. Precision Measurement of the Recoil Energy Spectrum from the Decay of ^{6}He. *Phys. Rev.*, 132:1149–1165, 1963.

[45] J. B. Vise and B. M. Rustad. Electron-Neutrino Angular Correlation in the Decay of ^{6}He. *Phys. Rev.*, 132:2573–2581, 1963.

[46] M. González-Alonso and O. Naviliat-Cuncic. Kinematic sensitivity to the Fierz term of β-decay differential spectra. *Phys. Rev. C*, 94:035503, 2016.

[47] O. Naviliat-Cuncic, X. Fléchard, E. Liénard, X. Mougeot, G. Quéméner, and J.C. Thomas. Improved Search for Tensor Interactions in Nuclear Beta Decay. *Proposal to the AAPG-CE31*, 2020.

[48] M. Kanafani, X. Fléchard, O. Naviliat-Cuncic, G. D. Chung, S. Leblond, E. Liénard, X. Mougeot, G. Quéméner, A. Simancas Di Filippo, and J.-C. Thomas. High-precision measurement of the ^{6}He half-life. *Phys. Rev. C*, 106:045502, 2022.

[49] A.C.C. Villari, C. Eleon, R. Alves-Condé, J.C. Angelique, C. Barué, C. Canet, M. Dubois, M. Dupuis, J.L. Flambard, G. Gaubert, P. Jardin, N. Lecesne, P. Leherissier, F. Lemagnen, R. Leroy, L. Maunoury, J.Y. Pacquet, F. Pellemoine, M.G. Saint-Laurent, C. Stodel, and J.C. Thomas. Spiral at ganil: Latest results and plans for the future. *Nuclear Physics A*, 787:126–133, 2007.

[50] Hamamatsu. Photomultiplier Tube R7723, R7724, R7725. https://www.hamamatsu.com/.

[51] Eljen-Technology. General purpose plastic scintillator ej-200, ej-204, ej-208, ej-212. (888), 2016. https://eljentechnology.com/.

[52] Crytur spol.s.r.o. YAP :Ce. https://www.crytur.com/.

[53] Saint-Gobain Crystals. Physical properties of common inorganic scintillators. https://www.saint-gobain.com/.

[54] G. D. Chung. Precision Measurement of the Fierz Term in ^{6}He Decay: Fast Beam Detector Monte-Carlo Simulation. Master's thesis, Université de Caen Normandie, 2022.

[55] G. F. Knoll. *Radiation Detection and Measurement.* John Wiley, fourth edition, 2010.

[56] http://www.srim.org/.

[57] W. Mengesha, T. D. Taulbee, B. D. Rooney, and J. D. Valentine. Light yield nonproportionality of CsI(Tl), CsI(Na), and YAP. *IEEE Trans. Nucl. Sci.*, 45:456–461, 1998.

[58] M. Kapusta, M. Balcerzyk, M. Moszyński, and J. Pawelke. A high-energy resolution observed from a YAP : Ce scintillator. *Nucl. Instrum. Meth. Phys. Sect. A*, 421:610–613, 1999.

[59] M. Moszyński, A. Syntfeld-Każuch, L. Swiderski, M. Grodzicka, J. Iwanowska, P. Sibczyński, and T. Szczęśniak. Energy resolution of scintillation detectors. *Nucl. Instrum. Meth. Phys. Sect. A*, 805:25–35, 2016.

[60] https://faster.in2p3.fr/.

[61] F. P. Calaprice. Second class interactions and the electron-neutrino correlation in nuclear beta decay. *Phys. Rev. C*, 12:2016, 1975.

[62] C. Fontbonne, P. Ujić, F. de Oliveira Santos, X. Fléchard, F. Rotaru, N. L. Achouri, V. Girard Alcindor, B. Bastin, F. Boulay, J. B. Briand, A. M. Sánchez-Benítez, H. Bouzomita, C. Borcea, R. Borcea, B. Blank, B. Carniol, I. Čeliković, P. Delahaye, F. Delaunay, D. Etasse, G. Fremont, G. de France, J. M. Fontbonne, G. F. Grinyer, J. Harang, J. Hommet, A. Jevremović, M. Lewitowicz, I. Martel, J. Mrazek, M. Parlog, J. Poincheval, D. Ramos, C. Spitaels, M. Stanoiu, J. C. Thomas, and D. Toprek. High precision measurement of the ^{19}Ne β-decay half-life using real-time digital acquisition. *Phys. Rev. C*, 96:065501, 2017.

[63] C. Fontbonne. *Acquisition multiparamétrique de signaux de décroissance radioactive pour la correction des défauts instrumentaux : application à la mesure de la durée de vie du* ^{19}Ne. PhD thesis, Normandie Université, 2017.

[64] A. P. Baerg. Dead time, decay and background effects in counting. *The Intern. J. Appl. Radi. and Isot.*, 24:401–405, 1973.

[65] P. Trocellier, S. Agarwal, and S. Miro. A review on helium mobility in inorganic materials. *J. Nucl. Mater.*, 445:128, 2014.

[66] D. H. Wilkinson. Evaluation of beta-decay: II. Finite mass and size effects. *Nucl. Instrum. Meth. Phys. Sect. A*, 290:509–515, 1990.

[67] K. Siegbahn. *Beta- and Gamma-ray Spectroscopy*. Series in physics. North-Holland Publishing Company, 1955.

[68] Barry R. Holstein and S. B. Treiman. Tests for Second-Class Currents in Nuclear Beta Decay. *Phys. Rev. C*, 3:1921–1926, 1971.

[69] A. Knecht, R. Hong, D. W. Zumwalt, B. G. Delbridge, A. García, P. Müller, H. E. Swanson, I. S. Towner, S. Utsuno, W. Williams, and C. Wrede. Precision Measurement of the ^{6}He Half-Life and the Weak Axial Current in Nuclei. *Phys. Rev. Lett.*, 108:122502, 2012.

[70] J. C. Bergstrom, I. P. Auer, and R. S. Hicks. Electroexcitation of the 0^+ (3.562 MeV) level of ^{6}Li and its application to the reaction ^{6}Li(γ, π^+)^{6}He. *Nucl. Phys. A*, 251:401–417, 1975.

[71] D. R. Tilley, C. M. Cheves, J. L. Godwin, G. M. Hale, H. M. Hofmann, J. H. Kelley, C. G. Sheu, and H. R. Weller. Energy levels of light nuclei A = 5, 6, 7. *Nucl. Phys. A*, 708:3–163, 2002.

[72] B. J. Mount, M. Redshaw, and E. G. Myers. Atomic masses of ^{6}Li,^{23}Na,^{39,41}K,^{85,87}Rb, and ^{133}Cs. *Phys. Rev. A*, 82:042513, 2010.

[73] F. Glück. Order-α radiative correction calculations for unoriented allowed nuclear, neutron and pion β decays. *Comp. Phys. Commu.*, 101:223–231, 1997.

[74] F. Glück. Order-α radiative correction to ^{6}He and ^{32}Ar β decay recoil spectra. *Nucl. Phys. A*, 628:493–502, 1998.

[75] L. Hayen, N. Severijns, K. Bodek, D. Rozpedzik, and X. Mougeot. High precision analytical description of the allowed β spectrum shape. *Rev. Mod. Phys.*, 90:015008, 2018.

[76] R. Hong. *Developments for a measurement of the $\beta - \nu$ correlation and determination of the recoil charge-state distribution in* ^{6}He *β decay*. PhD thesis, University of Washington, 2016.

[77] Physics list electromagnetic physics constructors in Geant4 11.1. https://geant4-userdoc.web.cern.ch/UsersGuides/PhysicsListGuide/html/electromagnetic/Opt4.html.

[78] E. Noether. Invariant variation problems. *Trans. Theor. Stat. Phys.*, 1:186–207, 1971.

[79] C. S. Wu, E. Ambler, R. W. Hayward, D. D. Hoppes, and R. P. Hudson. Experimental Test of Parity Conservation in Beta Decay. *Phys. Rev.*, 105:1413–1415, 1957.

[80] N. Cabibbo. Unitary Symmetry and Leptonic Decays. *Phys. Rev. Lett.*, 10:531–533, 1963.

[81] M. Kobayashi and T. Maskawa. CP-Violation in the Renormalizable Theory of Weak Interaction. *Prog. Theor. Phys.*, 49:652–657, 1973.

[82] D. H. Wilkinson. Methodology for superallowed Fermi beta-decay Part II. Reduction of data. *Nucl. Instrum. Meth. Phys. Sect. A*, 335:182–200, 1993.

[83] W. Bühring. The screening correction to the Fermi function of nuclear β-decay and its model dependence. *Nucl. Phys. A*, 430:1–20, 1984.

[84] W. Bühring. Approximate, non-relativistic scattering phase shifts, bound state energies, and wave function normalization factors for a screened Coulomb potential of the Hulthén type. *Z. Phys. A*, 310:255–262, 1983.

[85] H. Schopper, H. Behrens, and J. Jänecke. *Numerical Tables for Beta-Decay and Electron Capture*. Landolt-Börnstein: Numerical Data and Functional Relationships in Science and Technology - New Series. Springer Berlin, Heidelberg, 1969.

[86] D. H. Wilkinson. The sensitivity of allowed β-decay to the nuclear radius. *Nucl. Phys. A*, 205:363–366, 1973.